Morris, J.D., Villinger, H.W., Klaus, A., et al., 2003
Proceedings of the Ocean Drilling Program, Initial Reports Volume 205

4. Site 1253[1]

Shipboard Scientific Party[2]

SITE SUMMARY

Site 1253 is located ~200 m seaward of the deformation front in the deepest part of the Middle America Trench (Figs. **F1, F2**). Operationally, one primary goal for this site was to recore the sediments immediately above the sill encountered during Leg 170, drill and core for the first time through the sediments below the sill, and core >100 m into the oceanic section. The other major task was to install a CORK-II observatory in the deep igneous section (Fig. **F3**), where coring and logging were used to identify depths at which to set the packer and osmotic fluid and gas samplers.

There were two primary science objectives for this site. The first goal was to determine the bulk composition and distribution within the incoming plate of key element and isotopic tracers; this would provide a baseline in physical, mineralogical, and chemical characteristics against which changes during shallow subduction processes may be measured or inferred. The bulk composition and distribution of key element and isotopic tracers also provided a starting point from which to examine the recycling from subduction trench to volcanic arc (or deeper mantle) of important components such as CO_2. The second major objective at this site was to investigate the hydrology and thermal structure of the igneous section entering the trench. This objective will be addressed using temperature and pressure data and fluid and gas samples recovered from the observatory 1–2 yr and 5–6 yr postcruise. Interstitial water chemistry analyzed aboard ship during Leg 205, together with that from Leg 170, provides evidence for contemporary flow of seawater at depth at both reference sites.

The seismic record (Fig. **F2**) in the vicinity of Hole 1253A (common midpoint [CMP] number 3210) images the sedimentary sequence of middle Miocene age with a clear change in seismic reflectivity at ~6.1 s two-way traveltime (TWT). This represents the top of the calcareous

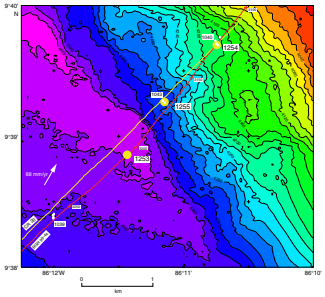

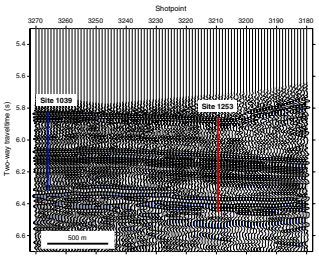

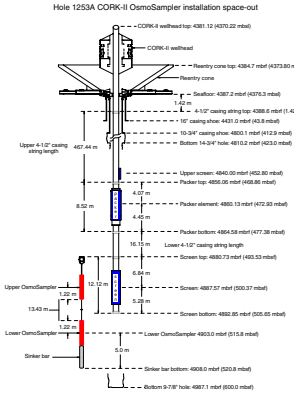

[1]Examples of how to reference the whole or part of this volume.
[2]Shipboard Scientific Party addresses.

Unit U3 (Kimura, Silver, Blum, et al., 1997) at ~180 meters below seafloor (mbsf). Beneath the sedimentary sequence, the strong reflector at 6.34 s TWT images the top of a gabbro sill as revealed by drilling results from Leg 170 at Site 1039. The coherent reflection pattern below the top of the sill is difficult, if not impossible, to interpret below the drilled depth of 600 mbsf (Fig. F2).

One hole was drilled at Site 1253, which was partially cored and into which we installed a long-term hydrologic borehole observatory (Fig. F3). After setting a reentry cone and 16½-in casing into the seafloor, we reentered this hole with the rotary core barrel (RCB) and drilled without coring to ~370 mbsf. RCB coring below 370 mbsf penetrated 30 m of calcareous and locally clay-rich sediments with intermittent ash layers (average recovery = 75%) before encountering a gabbro sill between 400 and 431 mbsf (average recovery = 74%). Below the sill were ~30 m of partially lithified calcareous sediments with intermittent ash layers (average recovery = 20%). This interval was followed by coring ~140 m into a second igneous unit (average recovery = 75%), with local zones of 30%–50% recovery.

After coring, operations focused on preparing the hole for logging and a CORK-II installation. The hole was opened to 14¾ in; 10¾-in casing was installed to a depth of ~413 mbsf and cemented in place to inhibit communication between the borehole and the formation. After drilling out the cement shoe and drilling a rathole with an RCB bit, we logged the hole. Because we conducted operations at or very near Leg 170 drill sites where logging while drilling was conducted, our logging focused on the igneous section at Site 1253. Here, we ran the triple combination (triple combo) and Formation MicroScanner (FMS)-sonic tool strings to determine physical properties, fracture distribution, and structure of the basement rocks. After an initial logging run encountered an impassable bridge in the shallow sediment section, casing was run into the uppermost part of the sill to stabilize the hole for subsequent CORKing operations. The subsequent logging run encountered a bridge at 530 mbsf that limited the triple combo and first FMS-sonic run to the interval between 530 and 413 mbsf; on a second pass, the FMS-sonic tool passed below the bridge and the hole was logged upward from 564 mbsf. A miniaturized temperature logger was run along with the Lamont-Doherty Earth Observatory (LDEO) Temperature/Acceleration/Pressure (TAP) tool.

After logging, we assembled the CORK-II components, including a 4½-in casing screen, casing packer, and casing made up to the instrument hanger (Fig. F3). The entire assembly was then lowered into the hole and latched in to seal the borehole outside of the 4½-in casing. The OsmoSampler with integral temperature sensors was lowered through the center of, and latched into the bottom of, the 4½-in casing. The final operation was to inflate the packers and shift spool valves that would connect the CORK-II pressure monitoring system to the formation, which would completely seal the zone to be monitored. Problems with the "go-devil" used for this step made it difficult to determine whether the packer had inflated or the valves had turned for pressure monitoring. Dives of the deep-sea submersible *Alvin* have since confirmed that the installation is fully operational. Three absolute pressure gauges including a data logger are installed within the instrument hanger head. One sensor monitors pressure within the sealed-off fluid sampling zone at the bottom of the hole; one monitors pressure variations present within the borehole above the sealed-off section; and the third sensor provides seafloor reference pressures. One additional sam-

pling line extends from the CORK-II head all the way down to the screened interval below the packer and is available for future pressure/fluid sampling purposes. The specifics of the CORK-II installation, relative to the structure and petrology of the igneous sections, are discussed in more detail below.

Lithostratigraphy and Sediment Geochemistry

Sediment coring began at Site 1253 at 370 mbsf, where nannofossil chalks with minor clay interlayers were recovered, closely similar to those at Leg 170 Site 1039. Other significant grains identified are siliceous sponge spicules, diatoms, and zeolites derived from the degradation of volcanic glass shards. Volcanic detritus (glass, altered glass, and mineral fragments) is ubiquitous, varying between ~3% and 10% of the total. Tephra layers (<1% of total stratigraphic thickness) are typically thin (<5 cm), with mafic layers accounting for >70% of the layers identified. A thick (8 cm) siliceous white tephra was recovered at 398.8 mbsf. Diagenesis has resulted in moderate lithification in the section, except immediately above the gabbro sill, where the sediment is much more clay rich, laminated, and lithified. This section (Core 205-1253-4R) is less calcareous (<2 wt% $CaCO_3$). Clays and zeolites form increasingly large volumes of the sediment in the last 3 m above the gabbro sill, and quartz from diatom and/or spicule opal recrystallization to quartz is seen as thin chert layers at 395.4 mbsf (interval 205-1253A-4R-1, 53–61 cm). Below the gabbro sill, in Core 205-1253A-10R, less lithified nannofossil chalks were recovered. These are identified as the same lithologic unit as above the sill, but they are dominated by a clastic granular limestone defined as packstone with clay. Minor amounts of baked sediments, usually inferred to be out of place, were recovered within and below the gabbro sill. Bulk sediment chemistry, by inductively coupled plasma–atomic emission spectroscopy (ICP-AES), largely map the minor variations in lithology, with SiO_2 increasing and CaO and Sr decreasing in the more clay-rich interval immediately above the sill. The TiO_2 and Al_2O_3 in the sediments are largely controlled by the ash contribution; relatively constant Ti/Al ratios through the calcareous and clay sediment sections suggest relatively homogeneous amounts of volcanic detritus throughout the section. Baked sediments have chemistry similar to the dominant lithology. No appreciable increases in Fe, Mn, or transition metal concentrations were noted above the sill, in contrast to the increases in Cu, Ni, Zn, and V observed for ~80 m above the sill at Site 1039.

Biostratigraphy

Because of the small amount of new sediment recovery expected during Leg 205, the shipboard science party did not include a micropaleontologist. Samples were taken for a shore-based participant. Results are expected to help constrain the ages of the gabbro sill and the lower igneous unit.

Igneous and Metamorphic Petrology

Coring at this site penetrated two separate igneous subunits. The upper subunit is a gabbro sill and is similar to that encountered at Leg 170 Holes 1039B, 1039C, and 1040C. The sill (Subunit 4A) has been further subdivided tentatively into two subsections, Subunits 4A-1 and 4A-2,

based on the distribution of voids, veins, grain size variation with depth, and the proportions of plagioclase to pyroxene. The lower igneous subunit (Subunit 4B) has been tentatively subdivided into seven subsections using the same criteria. Both the upper and lower igneous sections contain plagioclase and clinopyroxene phenocrysts, with rare olivine, orthopyroxene, and ilmenite and magnetite. Subunit 4B, particularly below 513 mbsf, is more glass rich and more altered. Phenocrysts are set in a groundmass that typically varies between microcrystalline and fine grained, with occasional medium-grained horizons. A 1.3-m-thick interval of cryptocrystalline material is present at 513 mbsf, where larger amounts of glass and a greater degree of alteration are observed. The petrologic data suggest that Subunit 4B is either a sill complex with multiple intrusions or a series of thick and slowly cooled lava flows. It is possible that changes in petrology and physical properties at ~513 mbsf mark the change from a sill complex to basement; postcruise dating and detailed analysis will be necessary to evaluate the two possible origins of Subunit 4B. Note that some characteristics of Subunit 4B are similar to those seen in some horizons recovered during Leg 206 coring, which intersected thick ponded lava flows (Shipboard Scientific Party, 2003; Wilson, Teagle, Acton, et al., in press).

Discrete alteration is highest at the tops of the subunits, is generally higher in the lowermost cores, but is generally low (1%–5%) overall. Veins sampled below 485 mbsf in Subunit 4B contain up to ~11 wt% carbonate, although quantification is difficult because vein material is mixed with various amounts of igneous rock. Diffuse alteration of the bulk rock, in the form of zeolite formation and clay replacement of minerals and glass, ranges from ~10%–50%, with higher levels of alteration seen below 513 mbsf. Chemically, all rocks from both subunits are of basaltic composition (46–49 wt% SiO_2 and 6–9 wt% MgO), with compositional variation in part due to olivine, clinopyroxene, and plagioclase fractionation. Variations in elements such as Ti, V, Ba, and Zr indicate that Subunits 4A and 4B are not comagmatic and possibly could have been derived from different mantle sources. Chemical and isotopic analyses beyond those available shipboard will be necessary to determine whether these mantle sources are associated with the Galapagos hotspot, the East Pacific Rise, or both.

Structural Geology

The most evident feature of the sediments above the magmatic intrusion (in cores firm enough to preserve original structures) is the tilted bedding with 30° average dip; paleomagnetically reoriented dip azimuths cluster at 221°, similar to the geometry observed at Sites 1039 and 1040. Small normal faults perpendicular to bedding, with millimeter-scale offsets are common throughout, as are pressure solution structures 3–10 cm long. The close association of reworked pelagic sediment in the lower part of Subunit U3C, westward-tilted bedding, and the magmatic intrusion suggest that the lowermost part of the sedimentary section was deformed during the gabbro emplacement. At Site 1253, the sediments do not exhibit subhorizontal shortening related to incipient subduction, despite the location of the deformation front only several hundred meters to the east.

The igneous units were carefully analyzed with respect to the CORK-II experiment and to provide data for comparison to the FMS data. A sediment/gabbro contact was recovered in interval 205-1253A-27R-1, 1–6 cm, and it dips 72°, although this piece sits at the top of the core

and may not have been recovered in place. The igneous units are commonly cut by magmatic veins. Dilational joints are also frequent, usually filled with a film of green minerals (clay and zeolite?), and rarely are present as open fractures. The paleomagnetic reorientation of the fractures to the real geographical coordinates has been done with particular care; some joints share preferred orientations with magmatic veins, but many do not. Overall fracture density increases with depth. Brittle shear zones, represented by en echelon Riedel shears, are common in the lower part of the deeper igneous unit (Core 205-1253A-36R and below) and usually show a reverse sense of movement.

Physical Properties

Variations in physical properties correlate with major lithologic changes between sediments and igneous units. A limited number of measurements indicate decreased porosity and increased grain density and *P*-wave velocity within sediments immediately above and between the igneous units; these differences may reflect alteration (recrystallization) and porosity reduction caused by emplacement of the igneous units.

Clear trends in the physical property data are (1) the small but systematic increase in velocity, bulk density, and grain density and the decrease in porosity within the lower igneous unit and (2) the higher natural gamma radiation (NGR) in the upper igneous unit and the clear shift in NGR emissions at 512 mbsf within the lower igneous unit. The cause of these trends in porosity, density, grain density, and velocity with depth in the lower igneous unit is unclear. The differences in NGR emissions suggest chemical differences between and within the igneous units, which may reflect primary compositional differences or varying degrees of alteration within igneous units that were initially chemically similar. The fact that the trends in porosity, density, and velocity are not correlated with the NGR trend suggests that the processes that control porosity, density, and *P*-wave velocity are separate from the chemical or lithologic processes that affect the NGR emissions.

Paleomagnetism

Shipboard magnetic studies on the archive-half sections and discrete samples established a reliable set of magnetic polarity changes and investigated rock magnetism, especially mineral composition and the domain state of magnetic minerals in the sediments and igneous rocks. The small amount of coring above the sill yielded at least two reversed polarities consistent with those seen in Holes 1039B, 1039C, and 1040C during Leg 170. Sediments below the sill generally showed negative polarity, but low recovery and high drilling disturbance preclude identification of a magnetic chron or subchron. Good recovery in the gabbro sill allows identification of several intervals of normal and reversed magnetic polarity. In the lower igneous unit, the upper part (between 450 and 513 mbsf) is primarily within an interval of reversed polarity. Two brief intervals of possibly normal polarity are identified, but discrepancies between archive-half and discrete sample results preclude firm identification. Below this depth, multiple intervals of normal and reversed polarity are observed. Postcruise age dating will be necessary to provide an absolute framework for this chronostratigraphy. Saturation isothermal remanent magnetization and Lowrie's test of the sediments show three separate unblocking temperatures, interpreted to reflect the

presence of goethite, pyrrhotite (or greigite), and magnetite. In the igneous section, magnetization is often unstable and appears to reflect largely multidomain (>100 µm) magnetic minerals, presumed to be magnetite. Intervals of more stable magnetization and high magnetic intensity are observed at 400 mbsf in the upper unit and at 462–474, 513–523, and 572–593 mbsf in the lower unit.

Inorganic Geochemistry

Interstitial water chemistry of sediment pore fluids was used to investigate in situ diagenetic reactions and the possibility of fluid flow in basement. Several features in the pore water chemistry suggest a role for enhanced ash alteration and associated authigenic mineral formation above and below the sill. Higher Na and much lower K and Si are observed just above the sill, and the Ca and Sr gradients remain constant at this depth. Cl concentrations are very slightly freshened (1.5%) relative to seawater, which may reflect opal-A or clay dehydration reactions immediately above the sill. The implied liberation of Na, Ca, and Sr to the fluids suggests ash alteration and carbonate recrystallization. The sharp decrease in K and Si is consistent with the uptake of these liberated elements via the authigenic formation of clays, zeolites, and quartz, also observed lithologically. Just below the sill, the Mg concentration in the fluid is quite low, consistent with the authigenic formation of more Mg-rich clays associated with ash alteration. Clear overall gradients with depth are noted for calcium, strontium, sulfate, silica, and lithium. The gradients parallel those measured during and after Leg 170 (Kimura, Silver, Blum, et al., 1997) but are shifted deeper by ~40 m, thus maintaining the same depth relationship to the top of the sill. The gradients trend toward values typical of modern seawater in the intervals just above and below the sill.

Organic Geochemistry

Organic geochemistry at this site reflects the low heat flow of the incoming plate, with all hydrocarbon concentrations measured for shipboard safety requirements being below the detection limit of the gas chromatographs. Calcium carbonate concentrations in the sediments above and below the sill range from 32 to 65 wt% and overlap those of Site 1039, except in the laminated, clay-rich sediments just above the sill, where values drop to <2 wt%. $CaCO_3$ in the igneous rock is low, (<0.4 wt%, except in veins) even in the top and bottom of Subunit 4A and the top of Subunit 4B, immediately adjacent to the sediment section. Veins below 485 mbsf typically contain carbonate (<11 wt%), where some of the differences may be due to variable dilution with matrix igneous material. Total organic carbon is low, and frequently below detection limit, throughout. Sulfur concentrations are low in the sediment sections and near zero in the igneous section, except for one vein sampled at 546.1 mbsf.

Microbiology

Sediment whole rounds (5 cm) were taken for contamination testing (microspheres and perfluorocarbon tracers) and postcruise microbiological measurements (adenosine triphosphate [ATP] assay, cell counts, and deoxyribonucleic acid [DNA] extractions and analysis). As expected with RCB coring in partially lithified sediments, contamination was sig-

nificant and variable. In the igneous section, veined intervals were taken as whole rounds (up to 40 cm) and split under sterile conditions. Aliquots will be used for DNA extraction and analysis, culturing experiments and cell counts, fluorescent in situ hybridization studies, and for studies of mineral alteration and chemical change associated with microbial activity. Contamination tests, although difficult to use quantitatively, indicate that the tracers were delivered to all but one cored interval. Interior tracer concentrations are variable, but microsphere concentrations are lower to very low in the interiors.

Downhole Measurements

At Site 1253, the Davis-Villinger Temperature-Pressure Probe (DVTPP) was deployed twice in an attempt to determine the in situ temperature and pressure of the formation. The first measurement was performed directly beneath the casing of the reentry cone at a depth of 60 mbsf; the second was at a depth of 150 mbsf. Prior to these measurements, the bottom water temperature was determined using a high-resolution and calibrated miniaturized temperature data logger (Pfender and Villinger, 2002) attached to the video system during reentry, giving a bottom water temperature of 1.989°C at Site 1253. At Site 1039, the bottom water temperature was 1.81°C, as measured by two different tools (water-sampling temperature probe and the Adara temperature tool). The cause of this difference is not clear. The miniaturized temperature data logger was also affixed to the triple combo logging tool near the TAP tool and run during logging. Unfortunately, thermal changes attributed to the curing of the cement used to tag the casing to the formation created a large signal visible in the temperature record in the upper logged interval, and temperature differences recorded between the two runs indicate that equilibrium formation temperatures had not been attained. The two DVTPP runs encountered difficulties with electronic noise and excessive tool motion, precluding their use to provide high-quality temperature or pressure measurements at this site.

Downhole Logging

The hole was logged upward with one pass of the triple combo and one pass of the FMS from 530 mbsf to the bottom of the casing shoe at 413 mbsf. On the second pass, the FMS slid past the obstruction at 530 mbsf and the hole was logged upward from 564 mbsf, where a second bridge was encountered. The measured inclination of the hole was very small (0.5°–1.6°). The caliper data indicate that the hole diameter in the logged portions of the upper and lower igneous units (423–431 and 461–561 mbsf) was relatively uniform, ranging mostly between 10 and 12 in. Thin intervals of increased hole diameter were present at 482, 485, 487–489, and 502–504 mbsf. The caliper reached maximum extension between 435 and 461 mbsf, corresponding to the sedimentary section between the igneous units.

The logs can be clearly separated into three intervals on the basis of obvious changes in hole diameter, velocity, resistivity, bulk density, and porosity, corresponding to the upper igneous subunit (Subunit 4A: gabbro sill), the sediments below, and the lower igneous subunit (Subunit 4B). In the logged part of sill (413–431 mbsf, with a 14¾-in hole above 423 mbsf and a 9⅜-in hole below), porosities are low and densities, resistivities, and *P*-wave velocities are high. In the sedimentary section of enlarged borehole (431–461 mbsf) high porosities and low bulk densi-

ties, resistivities, and *P*-wave velocities identify sediments. A return to high bulk densities, resistivities, and *P*-wave velocities at 461 mbsf indicates the top of the lower igneous subunit. The logs better identify the exact depth of the lower igneous subunit than do core depths, because of partial recovery and the standard curatorial practices of moving any recovered material to the top of the core. The NGR intensity is distinctly higher in Subunit 4A than in the sediments and Subunit 4B. Natural gamma logs are not available below 513 mbsf, where NGR emissions measured on cores using the multisensor track (MST) suggest a small increase in K, U, or Th concentrations in the lower part of the lower igneous subunit.

The logging data identify a change in the character of the resistivity and *P*-wave velocity logs in Subunit 4B at ~491–493 mbsf. Above this depth in the lower subunit, values are relatively homogeneous; below, the logs have similar average values but a more spiky character. FMS images indicate a change in character at a depth of ~508 mbsf. Above that depth, conductive features are generally discontinuous. Below, more closely spaced, thin, near-horizontal to slightly dipping conductive features are present in several intervals that are separated by intervals of poor images and irregular borehole size that could be fractured material or sediment interlayers. Intervals of decreased bulk density but no corresponding velocity decrease may indicate a fractured interval rather than sediment interlayers, which should cause a velocity decrease. Based on the bulk density and sonic logs, potential fractured intervals are inferred at 466–468, 484–486, 490–493, and 506–508 mbsf. Sediment interlayers thinner than the vertical resolution of the sonic tool (107 cm), would not be clearly distinguishable in this log, but the general high density and low porosity in areas of smaller borehole diameter preclude the presence of any significant sediment layers.

FMS images can be used to characterize structure and fabric in the igneous units. The gabbro sill (Subunit 4A) between 419 and 426 mbsf exhibits a blocky texture with an ~0.5-m size to the blocks. Between 426 and 432 mbsf, the formation appears more massive with thin conductive features at a 0.5- to 2-m spacing, although it is difficult to trace the conductive features across the four FMS pads. At the very top of Subunit 4B (463–467 mbsf), curved conductive features (fractures or irregularities in the borehole wall) are common. Between 467 and 493 mbsf, the formation appears more massive to blocky, with 0.5- to 1-m spacing between thin conductive features. These conductive features can be clearly traced across the four pads only between ~472 and 478 mbsf. Between 487 and 493 mbsf, irregular to curved vertical conductive features are present, representing possible fractures or irregularities in the borehole wall. From 493 to 498 mbsf, conductive features are rare, becoming more common again between 498 and 508 mbsf. At 508 mbsf, the character of the FMS image changes to more closely spaced conductive features (<0.5-m spacing). In rare cases, such as at 513–514 mbsf, these conductive features can be traced across the four pads and suggest a low dip angle. Image quality between 514.5 and 518 mbsf is poor because of an enlarged borehole. Relatively low (3800–4000 m/s) *P*-wave velocities and low (5–15 Ωm) spherically focused resistivities occur at similar depths. Below 518 mbsf, the layered character returns, but the absolute value of resistivity increases. Imaging is poor from 525–527, 534–539, and 542–555 mbsf. From 539 to 541 and 555 to 563 mbsf, the image is characterized by more closely spaced (<0.5 m) thin, nearly horizontal conductive features. These conductive features appear to dip to the southwest. The static FMS images indicate that both intervals have

high resistivity. Therefore, it appears unlikely that these are sediment layers.

Synthesis Topics

Fluid Flow in the Incoming Plate

As at Site 1039, 1.4 km to the west, interstitial water chemistry determined at Site 1253 is also indicative of fluid flow in or below Subunit 4B, where the chemical composition of the fluid is inferred to approach values typical of modern seawater. Figure F4 shows depth profiles for major, minor, and biogeochemical components determined aboard ship in the sediment interval above and below the sill. In the limited sediment interval cored, Site 1253 profiles for Ca and Sr mimic those at Site 1039 (see Fig. F20, p. 62, in the "Leg 205 Summary" chapter). High Ca values (~18.5 mM) seen at ~300 mbsf at Site 1039 likely reflect the effects of mafic ash alteration, which liberates Ca. Mg calcite and dolomite production are also suggested by Mg and Mg/Ca profiles at Site 1039 (Kimura, Silver, Blum, et al., 1997). In the pore waters from the deeper sediments at Site 1253, Ca and Sr decrease by ~20%–30%, toward, but not to, values typical of seawater. A similar magnitude change is seen in the Si content of the pore fluids above and below the sill, excluding the exceptionally low values seen at the immediate boundary with the sill (where quartz precipitation was noted). Li contents increase by ~60% over the lowermost 30 m of the section above the sill. Sulfate concentrations in the pore waters from Site 1253 are relatively uniform (27.2–28.6 mM, with no clear depth variation) and nearly of seawater composition. This contrasts with values of 12–20 mM measured higher in the section at Site 1039. These gradients are in directions opposite to those expected for most biogeochemical and fluid/rock reactions in deep siliceous and calcareous sediments at either low or elevated temperatures, which would be expected to reduce sulfate and to release Si, Ca, and Sr while consuming Mg and Li. The gradients observed at Site 1253, like those at Site 1039, suggest communication with a fluid of nearly seawater composition presumably flowing at depths below those from which interstitial waters have been recovered. At Site 1039, residence time calculations based on Sr and Li isotopes and concentrations (Silver et al., 2000) indicate that the gradients toward seawater are maintained by flow within the last 15–20 k.y. The gradients at Site 1253 are closely similar to those at Site 1039, supporting an argument for recent flow here also, which may have extracted heat from the plate to produce the unusually low heat flow in this region. The nature of this large regional-scale flow system, presumed responsible for the large heat flow anomalies as well as the chemical gradients, remains enigmatic; the CORK-II was installed at this site in hopes of providing necessary new information for better understanding the flow system.

F4. Pore fluid chemical data, p. 70.

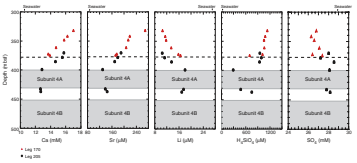

Igneous Stratigraphy

The petrology of the igneous units can be combined with paleomagnetic and rock magnetism studies and logging results to better understand the nature of the two units and their internal structure (Fig. F5). Paleomagnetic results show that the sill (Subunit 4A) spans several polarity reversals, implying multiple pulses of magma intrusion, although the elapsed time cannot be evaluated until age dating is completed

F5. Selected logging data, p. 71.

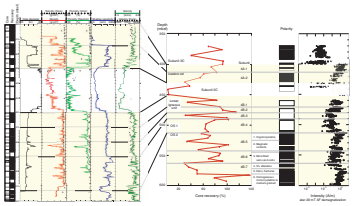

postcruise. Magnetic intensity is highest at the top of the sill, indicating more stable magnetization, probably because of the presence there of finer-grained magnetite than at deeper levels in the sill. The petrologic boundary between Subunits 4A-1 and 4A-2 approximately corresponds to a polarity reversal boundary. Subunit 4A-2 is composed entirely of microcrystalline gabbro. Logging results show a large hole diameter at the top of Subunit 4A-2, which corresponds to the 14¾-in hole drilled to provide a rathole for the casing installation. Seismic velocity and shallow resistivity (considered more reliable in the igneous units; see **"Downhole Logging,"** p. 58) are relatively high and uniform, and the cores recovered are massive in appearance, breaking into large pieces (see **"Site 1253 Visual Core Descriptions"**). At the base of the sill, recovery drops, the hole size increases, and velocity and resistivity decrease in general and exhibit a more spiky character, suggesting that fractured rock is present or possibly thin (<1 m) sediment interlayers.

The lower igneous subunit (Subunit 4B) begins at a depth of 450 mbsf in the core reference frame, which was used for petrologic and paleomagnetic work, and at ~460 mbsf in the logging data. A depth of 460 mbsf for the top of Subunit 4B is considered more reliable, given the very low recovery at the top of the subunit and the standard curatorial practice of moving all recovered material to the top of the core. Subunit 4B was subdivided into seven subsections, using the same criteria used for Subunit 4A. Within each subsection, multiple alternations between microcrystalline and fine-grained material may indicate the presence of multiple cooling units. Subunits 4B-1 through 4B-3 all formed during what may be a single reversed polarity interval, although dating is required. Magnetic intensity is again high at the top of Subunit 4B, and decreases with depth. The logging data show that Subunits 4B-1 through 4B-3 are characterized by high, and relatively uniform, resistivity and *P*-wave velocity. There is a marked increase in resistivity at the top of Subunit 4B-4, which corresponds to a short massive interval that was drilled very slowly (0.75 m/hr) with high recovery. In this interval, conductive features are rare in the FMS data (see **"Downhole Logging,"** p. 58). There is a hint of increased *P*-wave velocity at and below this interval, as seen in the logging data and measured in the cores. From ~490 mbsf to the base of the logged section, the borehole character becomes more heterogeneous, with intermittent highs and lows in resistivity and seismic velocity. Below 508 mbsf, FMS images change to more closely spaced conductive features, which are continuous across all four pads at rare intervals, such as 513–514 mbsf. This is an interesting depth, as it corresponds to a thin layer of rock with true basaltic texture and a return to high magnetic susceptibility, similar to that seen at the top of the sill and the top of Subunit 4B, and interpreted as indicating single-domain (<100 µm) magnetite. Below this depth, several clear sets of polarity reversals are seen, indicating multiple periods of magmatic activity. The MST natural gamma measurements on the core suggest increased K, U, or Th concentrations in this lower part of Subunit 4B. Glass is more abundant below this depth, discrete and diffuse alteration is more extensive, and carbonate-bearing veins are present. Despite these differences, the generally microcrystalline and fine-grained material below this depth shares many textural, mineralogical, and chemical similarities to the overlying sections.

CORK-II Installation

Details of the core and borehole at the levels of the CORK-II installation in Hole 1253A are shown in Figure F3, with the petrological and structural character of key depths shown in Figures F5 and F6. The center of the packer was set at ~473 mbsf, with the inflatable element being between 471.5 and 475.5 mbsf (Fig. F3). The cores indicate that this is an interval of high recovery of massive rock with relatively few fractures. The logging results (see "Downhole Logging," p. 58) show this to be in an area of relatively uniform physical properties (high resistivity, bulk density, and *P*-wave velocity). Interpretation of FMS images indicates a massive blocky formation, with 0.5- to 1-m spacing between thin conductive features, which can be traced across the four pads. The upper OsmoSampler, located inside a 7.35-m-long screen in the 4½-in casing, is set between 496.7 and 504 mbsf (Fig. F3). A 2-m pressure screen is located within the casing screen, and a fluid sampling line runs from this screen to the CORK-II wellhead. Figure F6 shows this to be an interval of modest recovery of moderately fractured rock composed of alternating microcrystalline and fine-grained material (see "Igneous and Metamorphic Petrology," p. 3). Logging data in Figure F6 show this to be an interval of generally uniform hole diameter, with minor variations in bulk density and *P*-wave velocity. FMS images show closely spaced conductive features. The lower sampler is dangled in the open hole between 512.1 and 519.5 mbsf. This is again a zone of moderate recovery and fracture density in a cryptocrystalline (basaltic) to microcrystalline part of the section, with relatively high concentration of voids and 10% to locally 50% secondary mineral formation. The logging data (Fig. F6) show this to be an interval of decreased resistivity and sonic velocity and variable hole diameter. In the upper part of this interval, FMS images show closely spaced (<0.5 m) shallowly dipping conductive features that are continuous and can be traced across the four FMS pads. The intervals for the osmotic samplers were chosen using a combination of scientific and operational constraints. Originally, the intervals between 513–521 (now OsmoSampler 2) and 560–568 mbsf were targeted, where the latter is a zone of high fracture density and maximum alteration in largely microcrystalline rock. However, the bridge encountered by the logging tools at 530 mbsf restricted the OsmoSampler deployment to shallower levels. The upper pressure screen, located above the packer, was set into the sediments between the two igneous subunits, where sediments collapsing around the screen are expected to make an effective seal. The final installed configuration for this modified CORK-II geochemical and hydrologic borehole observatory is shown in Figure F3. For details of the postcruise submersible visit to this site, see "Postcruise *Alvin* Submersible Visit to Site 1253 and 1255 CORK-IIs," p. 36, in the "Leg 205 Summary" chapter.

F6. Fracture distribution, core recovery and petrologic observations, and detailed FMS images, p. 73.

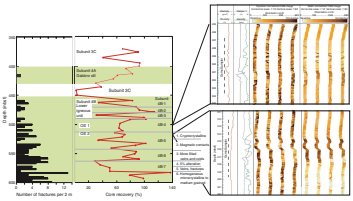

OPERATIONS

Leg 205 was originally scheduled to begin in San Diego, California, on 6 September 2002. Because of the threat of a dockworker strike in the western United States, the port call was changed to Victoria, Canada. As a result, the start of the Victoria port call changed to 2 September.

Victoria, Canada, Port Call

Leg 205 officially began with the first line ashore at 0900 hr 2 September. A number of changes resulted from the short time between the decision to change the port call and the start of the port call: (1) the Ocean Drilling Program (ODP) technical staff crossover occurred on 4 September; (2) the Transocean staff crossover took place on 6 September; and (3) the Leg 205 science party boarded the ship on 17 September in Acapulco, Mexico, during the transit from Victoria to proposed Site 1039R-A.

Prior to the loading of the Leg 205 supplies, a substantial amount of equipment used to support the Leg 204 gas hydrate objectives had to be taken off the ship. Pressurized gas hydrate samples, gas hydrate samples immersed in liquid nitrogen, and 340 boxes of core samples were off-loaded. A 20-ft refrigerated van used for processing and storing the gas hydrate samples on board was also removed from the ship. A number of special coring tools and special laboratory equipment for gas hydrate research also were off-loaded.

Immediately upon arrival in Victoria, 1095 metric tons of marine gas oil was taken on board and we started to load 60 metric tons of barite and 80 metric tons of sepiolite. After the food for Leg 205 was loaded, the following equipment was loaded: (1) seven joints of 16-in casing, (2) 30 joints of 10¾-in casing, (3) 139 joints of 4½-in casing, (4) a new spool of core winch wire, (5) four standard reentry cones, (6) four CORK-II wellheads and associated instruments, (7) four 16-in casing hangers, (8) two 10¾-in casing hangers, (9) a new bicentered hole opener, and (10) other miscellaneous hardware.

An essential element of the long-term geochemical observatories to be installed during the leg was the downhole water, gas, pressure, and temperature sampling/monitoring equipment. During the port call, six downhole OsmoSamplers were assembled and stored in a water bath in the downhole measurements laboratory so that they would be completely prepared for deployment later in the leg. During assembly, temperature sensors were placed inside the OsmoSamplers. The pressure meters and data logger units were checked out and programmed in preparation for deployment.

At the request of the port authority, starting on 4 September, loading operations had to be suspended at 1700 hr each day for noise abatement. The ship left Victoria at 0754 hr on 7 September and began the transit to Acapulco to pick up the Leg 205 science party.

Transit from Victoria, Canada, to Acapulco, Mexico

Because of Leg 204 operations continuing to the last possible minute and a very short (39 hr) transit to Victoria, Leg 204 personnel had only minimal time for the routine end-of-leg maintenance of the drilling equipment; much of this activity took place during the transit. In addition, the new core winch wireline was installed and some minor plumbing runs associated with the CORK-II wellheads were made during the transit.

Calm seas were encountered during the initial portion of the transit. On 15 September, however, the vessel began passing through the edge of a tropical depression (36- to 42-nmi/hr winds and 20-ft seas) which reduced the ship's speed. The weather moderated during the day of 16 September, and moderate seas were encountered for the rest of the transit to Acapulco.

The transit ended with the first line ashore at 1030 hr on 17 September in Acapulco. The total transit was 2636 nmi and took 239.4 hr at an average speed of 11.0 nmi/hr.

Acapulco, Mexico, Port Call

The primary objective of the brief Acapulco port call was to board the Leg 205 scientists and load a few pieces of equipment that were essential for Leg 205 operations but did not make the Victoria port call. This included two 10¾-in casing hangers and the 32-in vibration-isolated television (VIT) camera guide sleeve.

Because the weather forecast for the transit to Site 1253 (proposed Site 1039R-A) did not look favorable for using the cranes while under way, we decided to assemble the Site 1253 reentry cone while in port. Work on the reentry cone began at 1200 hr. By 1700 hr the reentry cone had been bolted together and tack welded enough to make it secure for the transit, and a pilot was requested for departure. During this time, a required safety briefing on the vessel's survival gear was given to the science party. In addition, we also took advantage of the fact that the vessel was moored with the starboard side to the dock and lowered lifeboats 2 and 4 to the water and started their engines. With all tasks completed in Acapulco, the last line was released at 1738 hr on 17 September and we began the transit to Site 1253.

Transit from Acapulco, Mexico, to Site 1253 (Proposed Site 1039R-A)

The final welding of the reentry cone was completed (at 0600 hr on 18 September; all times given are local ship time which was Universal Time Coordinated [UTC] – 5 hr) during the transit to Site 1253. We also held additional safety meetings, introduced key Transocean personnel and the ODP operations manger to the science party, and gave science party members tours of the ship to familiarize them with the vessel.

At 1053 hr on 19 September, we changed course toward shore to disembark one of the ship's stewards because of a family emergency. At 1830 hr on 19 September, the vessel was positioned just off the south breakwater at Puerto Madero, Mexico. A small fishing boat arrived from Puerto Madero and took the steward to shore. At 1845 hr, the vessel resumed the transit to Site 1253.

At 1400 hr on 21 September, the vessel arrived at Site 1253.

Site 1253 (Proposed Site 1039R-A)

The thrusters were lowered and the vessel was placed in dynamic-positioning mode at 1431 hr on September 21, and we deployed a seafloor positioning beacon at 1620 hr. The upper guide horn was then laid out and the reentry cone moved to the center of the moonpool doors. Drill collars were picked up for the bottom-hole assembly (BHA), assembled, and stored in the derrick. Three joints of 16-in casing (42.5 m) were assembled, and a 16-in casing hanger was made up to the casing string. The casing running tool was then attached to the casing string, and the casing string was lowered into the reentry cone until the casing hanger latched into the reentry cone. The weight of the reentry cone was picked up to verify it had latched properly. We then released the casing running tool and pulled out of the reentry cone. A visual in-

spection confirmed that the casing hanger latch ring was properly seated in the reentry cone landing ring latch ring groove.

The next step was to attach a 14¾-in tricone bit to the stinger below the casing running tool. The rest of the BHA was then made up and lowered into the reentry cone until the running tool landed. The running tool was latched into the 16-in casing hanger, and the entire assembly (16-in casing, reentry cone, and BHA) was picked up off the moonpool doors. The moonpool doors were opened, and at 2100 hr on 21 September, the reentry cone was lowered below the keel. The moonpool doors were then closed, and the pipe trip to the seafloor began.

At 0745 hr on 22 September, with the 16-in casing shoe and bit near the seafloor, the jetting-in process began, initiating Hole 1253A. At 0945 hr, the reentry cone mud skirt landed on the seafloor and the running tool was released. This was verified using the VIT camera system. The seafloor depth was determined to be 4387.1 meters below rig floor (mbrf) (4376.3 meters below sea level [mbsl]), and the bottom of the 16-in casing shoe was at 43.82 mbsf. We then retrieved the drill string in preparation to assemble an RCB BHA.

After installing the reentry cone and 16-in casing, we assembled an RCB BHA with a 9⅞-in bit and bit release. The bit was lowered to the seafloor, and Hole 1253A was reentered at 0555 hr 23 September. We then drilled ahead without coring from 4431.0 to 4444.0 mbrf (43.8 to 56.8 mbsf), where a DVTPP measurement was taken. The temperature and pressure data appeared to indicate that the tool moved while in the formation.

When the DVTPP was recovered, the colletted delivery system (CDS) was jammed with rust and sediment. This created a seal inside the upper barrel above the collets, trapping pressure inside the barrel. A vent hole was drilled in the upper barrel to prevent this from recurring, and the CDS was cleaned up and redressed with a new set of collets. After stroking the tool to verify performance, the CDS was set aside for use at a later time.

We continued to drill ahead without coring from 4444.0 to 4537.2 mbrf (56.8 to 150 mbsf) when the DVTPP was deployed a second time. Unfortunately, this run of the DVTPP also experienced tool movement while in the formation, resulting in poor data. A review of the tool and deployment procedures is under way.

We then drilled ahead without coring to 4757.1 mbrf (369.9 mbsf), where we started RCB coring. Cores 205-1253A-1R through 4R, consisting of nannofossil chalk and claystone, were taken from 4757.1 to 4787.6 mbrf (369.9 to 400.5 mbsf). The rate of penetration (ROP) in the sediments was 23 m/hr, and we had a core recovery of 73%.

Cores 205-1253A-5R through 9R were cut from 4787.6 to 4817.0 mbrf (400.5 to 429.9 mbsf) in a very dense and hard gabbro sill. The ROP in the gabbro was 1.7 m/hr, and core recovery was 70.3%. Another change in the drilling occurred when we encountered sediments in Cores 205-1253A-10R through 13R. The ROP was 18.2 m/hr, and core recovery dropped to 17%.

We encountered more gabbro in Cores 205-1253A-14R through 28R from 4817.0 to 4916.0 mbrf (429.9 to 528.9 mbsf). A few thin sediment layers were present in the gabbro, but these were only minimally recovered. The ROP dropped to 1.4 m/hr, and core recovery rate was 50%. At the end of cutting Core 205-1253A-25R, a small amount of erratic torque in the drill string was observed. With 53.2 total rotating hours on the bit, 45.2 hr of which was in hard rock, the decision was made to trip the drill string for a bit change. The bit cleared the seafloor at 1950

hr on 27 September. During the trip out of the hole, tight spots were noted at 4816, 4734, and 4647 mbrf. The bit cleared the rig floor at 0245 hr on 28 September. The used drill bit was in good condition but was slightly reduced in gauge.

A new 9⅞-in RCB bit was made up to the BHA. Because of the length of time drilling in hard rock, the mechanical bit released was also replaced. The BHA was spaced out for the RCB and lowered to the seafloor.

Hole 1253A was reentered at 1108 hr on 28 September. The bit was lowered into the hole to 4816 mbrf (429 mbsf), where excessive drag was encountered. We picked up the top drive and washed/reamed from there to the bottom of the hole at 4903.1 mbrf (516 mbsf). Once the 32 m of fill in the bottom of the hole was cleaned out, we resumed RCB coring.

After the bit change, we continued RCB coring from 4903.1 to a total depth of 4987.1 mbrf (515.9 to 600.0 mbsf) and recovered 59.6 m (71%). The penetration rate through this hard gabbro section was only 1 m/hr. The lowermost 6 m of the hole appeared to have numerous ledges and may be deviated. Because of the slow penetration rate and no clear indication that we were close to the bottom of the gabbro, we decided to stop coring.

Next, we circulated 30 barrels of sepiolite to clean out the hole and made a wiper trip in preparation for logging. While the pipe was lowered back to bottom during the wiper trip, an obstruction was encountered at 4920 mbsf (533 mbsf). The top drive was picked back up and used to rotate and wash to the bottom of the hole. Several ledges were reamed on the way back to total depth. Torque in the bottom 6 m of the hole led us to speculate that this section may be deviated. As this section is so close to the bottom of the hole, there was no way to confirm this with a survey.

After 2 m of fill in the hole was washed out, 30 barrels of sepiolite was circulated to ensure that all the debris was washed out of the hole. Then, in preparation for logging, the entire borehole volume was displaced with 185 barrels of sepiolite. The bit was pulled out of the hole, and the ship was offset 50 m north to drop the bit on the seafloor. At 2308 hr on 2 October, the pipe reentered Hole 1253A and the end of the pipe was positioned at the 16-in casing shoe at 4431 mbrf (44 mbsf).

The logging equipment was rigged up, and the triple combo tool string was lowered into the hole. The tools would not penetrate past a bridge at 4537 mbrf (150 mbsf). Because the upper sediment section had been logged previously during ODP Leg 170 and our primary logging objective was the deeper part of the section, we decided to postpone logging until after we set the 10¾-in casing into the top of the first sill.

We retrieved the drill string, and the bottom of the BHA was back on the rig floor at 1615 hr on 3 October. To prepare for the installation of the 10¾-in casing, we needed to widen the 9⅞-in hole to 14¾ in. We attached a 14¾-in reaming bit to the BHA, lowered it to the seafloor, and reentered Hole 1253A at 0044 hr on 4 October. We then drilled (without coring) from the 16-in casing shoe (4431 mbrf; 44 mbsf) to 23 m into the top of the upper gabbro (4810 mbrf; 422.8 mbsf). To make sure the hole was in the best condition possible to install the 10¾-in casing, the entire borehole volume was circulated two times, a wiper trip was made (without any significant hole problems), the borehole volume was circulated again, and then the hole was filled with sepiolite. The 14¾-in reaming bit was then pulled out of the hole; it reached the rig floor at 1345 hr on 5 October.

After assembling 30 joints of 10¾-in casing (411 m) and a cementing shoe, we lowered it to the seafloor and reentered Hole 1253A at 0210 hr

on 6 October. We picked up the top drive with a cementing manifold and landed the 10¾-in casing hanger in the reentry cone at 0445 hr on 6 October. The casing was cemented in place with 40 barrels of cement (15.8 lb/gal). The cementing was completed at 0650 hr, the casing running tool was released, the cementing manifold was laid out, the top drive was racked back, and the drill string was pulled out of the hole. The camera system was recovered while the pipe was pulled out of the hole, and the drill string was back on the rig floor at 1530 hr on 6 October.

Our next step was to drill out the cement plug at the bottom of the casing as well as clean out the hole to total depth (600 mbsf) in preparation for logging and installing the CORK-II. We assembled the BHA with a tricone bit (Reed HP21 9⅞-in mill tooth), ran it down to the seafloor, and reentered the hole at 0011 hr on 7 October. The top of the cement was encountered at 4795 mbrf (407.8 mbsf), which is ~5 m above the bottom of the 10¾-in casing shoe.

The cementing plug and cement inside the casing were drilled out in 45 min, and then the hole was cleaned to 4987.1 mbrf (600.0 mbsf). The hole was swept clean with 30 barrels of sepiolite, and we started a wiper trip by raising the bit up to the 10¾-in shoe. On the way back down to 600 mbsf, 20,000 lb of weight was taken at 4976 mbrf (588.8 mbsf), so we rotated and washed the hole from there to total depth. We found 7 m of fill in the bottom of the hole. The hole was swept again with 50 barrels of sepiolite and then displaced with 60 barrels of sepiolite in preparation for logging.

Before we could log, we had to drop the bit on the seafloor. The bit was pulled clear of the reentry cone at 1630 hr on 7 October, and the vessel was offset 50 m north. The rotary shifting tool (RST) was deployed on wireline to release the bit. The mechanical bit release (MBR) shifted smoothly; however, the bit did not drop off. The RST was picked up and then dropped on top of the MBR support bearing, knocking the bit free at 1840 hr.

We reentered Hole 1253 (at 2027 hr), positioned the bottom of the pipe near the 10¾-in casing shoe at 4798 mbrf (410.8 mbsf), racked back the top drive, and started to rig up for logging. After assembling the triple combo tool string and lowering it into the hole to 4917 mbrf (530 mbsf), we lost communication with the tool and it had to be pulled out of the hole. The Hostile Environment Litho-Density Sonde was leaking oil; it was replaced with the Hostile Environment Litho-Density Tool. The reconfigured triple combo tool string was lowered down the drill string until it landed on a bridge at 4917 mbrf (530 mbsf). The tools could not be worked past the bridge, so the hole was logged from that point up to the seafloor and then pulled out of the hole.

The FMS-sonic velocity tool string was assembled and lowered into the hole until it landed on a bridge at 4917 mbrf (530 mbsf). The tools would not pass the bridge, and we logged from there up to the 10¾-in casing shoe (4798 mbrf; 411 mbsf). The FMS was lowered for a second pass, and this time it passed through the bridge at 4917 mbrf, coming to rest on another bridge at 4951 mbrf (564 mbsf). We logged from that point up to the 10¾-in casing shoe and then pulled the tools out of the hole. Once we had disassembled the logging tools, we pulled the drill string out of the hole, clearing the reentry cone at 2215 hr on 8 October. After the bottom of the pipe was back on the rig floor (0515 hr on 9 October), the drill line was slipped and cut.

The next operational step at Hole 1253A was to deploy the CORK-II observatory. After preparing the rig floor and all the tools required, the 4½-in casing screen was picked up and hung off at the rotary table. A latch nipple for landing/latching the OsmoSampler inside the casing was attached to the screen. To the top of the screen, we attached one full joint of 4½-in casing, one 2-m-long piece of 4½-in casing, and one 3-m-long piece of 4½-in casing. The screen was lowered into the moonpool, where the flat umbilical was connected to the two ¼-in pressure monitoring hydraulic lines extending from the top of the screen. The screen was then lowered through the moonpool as the umbilical was strapped to the 4½-in casing.

A CORK-II inflatable packer was picked up next and attached to the top of the 4½-in casing. The packer was lowered into the moonpool, where the umbilical was severed and connected to the two ¼-in pressure monitoring hydraulic pass-through lines extending from the bottom of the packer. The packer was then lowered through the moonpool, and the umbilical was connected to the two ¼-in pressure monitoring hydraulic pass-through lines extending from the top of the packer.

We then attached 33 joints of 4½-in casing, one 2-m-long piece of 4½-in casing, and one 3-m-long piece of 4½-in casing (467.44 m total length) to the top of the packer. The umbilical was strapped to the 4½-in casing and centralizers attached to the casing as the screen/packer subassembly was lowered through the moonpool.

During deployment of the 4½-in casing string and umbilical, at ~16 m above the packer, one of the three umbilical ¼-in hydraulic lines was severed and split out of the umbilical. A ¼-in pressure monitoring line termination screen was connected to the split-out umbilical hydraulic line. The termination screen will be used to monitor the pressure above the packer and below the 10¾-in casing shoe. The termination screen was banded to the 4½-in casing, and centralizers were positioned at the top and bottom of the termination screen to protect it.

The CORK-II running tool was latched onto the CORK-II wellhead. The wellhead was then picked up and made up to the top of the 4½-in casing string. The wellhead was lowered into the moonpool where the umbilical was severed and connected to the bottom of the wellhead. The packer setting hose was made up between the CORK-II running tool and the top of the wellhead, completing the assembly.

All of the sampling valves and bleed valves on the wellhead were opened, and the wellhead was lowered into the water to purge the hydraulic lines of air. The 1/16-in hydraulic lines connecting the pressure meter control valves to the pressure meters were filled with water before the wellhead was picked up. The wellhead was raised back to the moonpool level, where all valves were closed. Large rubber bands were then attached to the individual valve handles such that they would hold the valves in the closed position during the deployment. This was done to prevent the valves from partially opening during the deployment as happened with the ACORK valves deployed during Leg 196. With all hydraulic lines purged, all valves closed, and a last-minute inspection of the wellhead completed, the CORK-II assembly was lowered to the seafloor.

Hole 1253A was reentered at 0320 hr on 10 October. The 4½-in casing screen shoe was lowered to 4874 mbrf (487 mbsf), where we picked up the top drive and lowered the wireline sinker bar assembly into the hole for a sounding run. The wireline sinker bar assembly reached 4915

mbrf (527.8 mbsf), which was 7 m below the OsmoSampler sinker bar's final position.

The lower weak link (900 lb) was made up to the top of the OsmoSampler sinker bar. This subassembly was then picked up and landed in the top of the drill string. The upper OsmoSampler was attached to the latch/running tool subassembly with 4.88 m of ⅜-in braided nylon rope. The upper weak link (1500 lb) was attached to the bottom of the upper OsmoSampler followed by 13.4 m of ⅜-in braided nylon rope. The lower OsmoSampler was then attached to the rope.

The Hole 1253A OsmoSampler subassembly (23.61 m overall length) was picked up, and the bottom of the lower OsmoSampler was connected to the lower weak link on top of the sinker bar that hung off in the drill pipe. The entire assembly (27.31 m overall length) was then lowered down the drill string until the latch/running tool subassembly landed on the drill string. The wireline sinker bar assembly was made up to the latch/running tool subassembly, and then the entire assembly was slowly lowered down the drill string in steps to prevent differential pressure from damaging the osmotic pumps.

The OsmoSampler assembly was lowered until the latch/running tool subassembly landed in the latch nipple on top of the 4½-in casing screen. The latch/running tool was jarred down on to set and lock the latch (lock mandrel) in the latch nipple. A 3000 lb overpull with the wireline confirmed that the latch was locked in place. The latch/running tool was then jarred up on, shearing the running tool release pin and releasing the running tool from the latch at 1110 hr on 10 October. The running tool and wireline were then pulled out of the hole.

The packer setting go-devil was then dropped down the inside of the drill string. The CORK-II wellhead was then lowered into the hole until it landed and latched into the reentry cone. A 5000 lb overpull with the drill string confirmed that the wellhead was latched into the reentry cone.

The drill string was pressured up to 800 psi and held for 30 min to set the packer. While the drill string was being pressurized, the pressure gauge fluctuated once as if there was a sudden small change in volume. Also, occasionally while holding the 800-psi pressure, the pump had to be engaged at 2–3 strokes per minute to maintain the pressure. After 30 min, the drill string pressure was increased to 1800 psi and held for 10 min to activate the spool valves (to connect the pressure sensors in the wellhead to the downhole screens). Finally, all of the drill string pressure was bled off through the rig floor standpipe manifold relief valve.

The final step was to install the remotely operated vehicle platform around the wellhead on top of the reentry cone. The landing platform and deployment bridle were assembled in the moonpool and then lowered down the drill string to the reentry cone on the logging line. After landing the platform on top of the reentry cone, the deployment bridle acoustic releases were activated at 2245 hr on 10 October. The logging line was raised, and the weight indicator showed a reduction in weight of 800 lb, confirming that the platform had been released. The logging line and platform deployment bridle were then pulled out of the hole.

We then deployed the camera system to visually inspect the installation. No problems were observed during the visual inspection, so the CORK-II running tool was released from the wellhead at 0050 hr on 11 October.

The wireline sinker bar assembly was deployed to recover the packer setting go-devil to prevent having to retrieve the drill string when it was full of water. However, the go-devil was encountered at 400 mbrf in-

stead of down near the seafloor at the CORK-II running tool, where it should have been. It took 1.5 hr and jarring with 8000 lb of overpull to recover the go-devil. When it was recovered, the go-devil seals were missing. The top drive was racked back, and the drill string and camera system were pulled out of the hole. The CORK-II running tool cleared the rig floor at 0945 hr on 11 October (Table T1).

While the drill string was being retrieved, the ship moved in dynamic-positioning mode to Site 1254 (1.1 nmi). The beacon from Site 1253 was recovered at 0430 hr on 11 October and redeployed at 0945 hr on 11 October in Hole 1254A.

The Site 1253 CORK-II was visited by *Alvin* ~1 month following installation. This visit confirmed that despite the failure of the go-devil, the CORK-II installation had been successful and was property functioning. For details of the *Alvin* dive and videos of the CORK-II, see **"Postcruise *Alvin* Submersible Visit to Site 1253 and 1255 CORK-IIs,"** p. 36, in the "Leg 205 Summary" chapter.

T1. Coring summary, Site 1253, p. 169.

LITHOSTRATIGRAPHY

Coring at ODP Site 1253 during Leg 205 was directed at completing recovery of the sediment section overlying the igneous oceanic crust initially cored during ODP Leg 170 at Site 1039. Consequently, we choose to assign the sediments and sedimentary rocks recovered at Site 1253 to the existing stratigraphic framework. All the sediment recovered above the gabbro sill at 400 mbsf was assigned to Subunit U3C (Fig. F7). Below this level there were a number of thin (<6 cm) baked crystalline sediment layers between igneous rock in the lower igneous unit (Subunit 4B), as well as between this complex and the upper gabbro sill (Sections 205-1253A-10R-2 to 12R-1, 26 cm; 431–442 mbsf) (see **"Petrology,"** p. 26). In zones of low core recovery, the thickness of sediment within Subunit 4B is not clear. Zones of faster than normal drilling penetration rate within the lower unit may represent additional sedimentary intervals, but could also be simply more fractured igneous rock. Baked sedimentary rocks were recovered from within Subunit 4B in intervals 205-1253A-25R-1, 0–1 cm (513 mbsf), 26R-1, 17–18 cm (516 mbsf), and 27R-1, 1–6 cm (519 mbsf). These intervals form part of Unit U4, although the lithologies are the same as those seen in Subunit U3C.

Sediments cored in Hole 1253A are dominated by a mixture of nannofossil chalks and varying but subordinate proportions of clay. The facies are typically fine grained and massive with few identifiable sedimentary structures apart from bioturbation (Fig. F8). The light color reflects the dominant biogenic carbonate origin of the sediments. Prominent dark green clay layers constitute <5% of the section and are massive, commonly burrowed, and usually <1 cm thick. They are interpreted as primary sedimentary deposits. Going downsection from Cores 205-1253A-1R to 4R, there is an increase in the proportion of clay in the sediment and in the degree of lithification, changing from a firm chalk in Core 1R (Fig. F8) to a hard mudstone in Core 4R (Fig. F9). At the same time, the facies become more laminated downsection, suggesting less bioturbation, although this is occasionally observed over narrow intervals between laminated intervals. Although these changes occur as the contact with the gabbro sill is approached, there is no indication that the presence of the sill has caused these changes in facies. Rather, it is likely that the sill exploited a change in sediment composition as a place for intrusion.

F7. Stratigraphic log, Sites 1039 and 1253, p. 74.

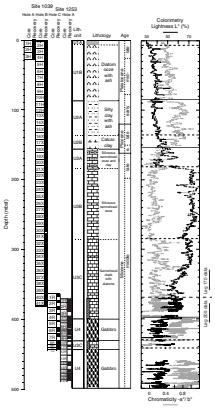

F8. Nannofossil chalk with diatoms, p. 75.

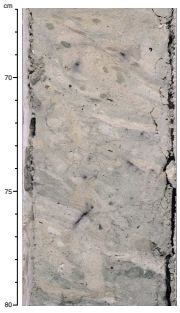

F9. Calcite-rich claystone, p. 76.

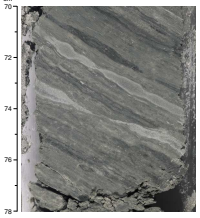

Below the gabbro sill (Subunit 4A), in Section 205-1253A-10R-2 (430.72 mbsf), the sediment returns to softer carbonate lithologies. However, unlike the nannofossil chalks seen higher in the section within Subunit U3C, this core is dominated by a clastic granular limestone, defined as packstone with clay. The sediment shows an original sedimentary fabric that is interpreted to reflect lamination during deposition under the influence of moderate current activity. A minor amount of micritic nannofossil chalk is interbedded and represents sedimentation during lower-energy episodes. Downsection in Core 205-1253A-11R (436 mbsf), chalk dominates and appears to be more similar to those lithologies recovered from the top of Hole 1253A (<396 mbsf). There is no convincing evidence to indicate that the sediment between Subunits 4A and 4B differs in a significant fashion from that above the sill.

Redeposited Intervals

Although the facies are typically pelagic, there are a number of minor redeposited intervals that are still carbonate dominated but contain elevated clay concentrations. An example is seen in interval 205-1253A-1R-1, 78–104 cm (Fig. F10), where a brownish gray bed shows parallel laminations and a graded base, suggestive of redeposition. However, the graded layer accounts for only 2–3 cm of the total bed thickness of 26 cm. Additional clastic sections are seen within the bed, indicating that the flow was not a single pulse but instead involved a series of closely spaced events or, perhaps, pulses within a single mass flow event.

Tephras

Volcanic ash layers represent an important minor lithology but account for <1% of the total stratigraphic thickness. They are typically thin (<5 cm) and structureless, with grading only rarely apparent. Mafic layers account for >70% of the layers identified, but there is no variation with depth in the bulk composition. Lighter-colored siliceous ashes are seen as far downsection as Core 205-1253A-4R. Alteration is variable, with some shards found in some intervals appearing to be clear and very fresh under microscopic examination (Fig. F11C), whereas others are almost entirely converted to zeolites. Individual tephra shards are commonly found in minor quantities throughout the section (Fig. F12), with the exception of Subunit U3B, suggesting that originally there may have been many more thin tephra layers that have been disrupted by bioturbation after deposition. Indeed, smear slide analysis shows that volcanic glass shards are scattered through the background pelagic sediments.

Whereas most volcanic ashes alter to a dark gray color, the most lithified Core 205-1253A-4R contains a bright white altered ash layer (Fig. F13) that contains fine sand- and silt-sized particles of cloudy, partially palagonitized glass. Identified tephras appear to be totally dominated by volcanic glass and degraded glass shards, with no feldspar, hornblende, or pyroxene grains identified. The evidence strongly points to these layers being the product of primary air fall events followed by settling through water. There is no support for redeposition as volcaniclastic turbidites or as hyaloclastites.

F10. Clay and spicules interbedded in nannofossil chalk with foraminifers, p. 77.

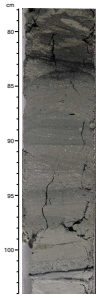

F11. Clay and grain types, Hole 1253A, p. 78.

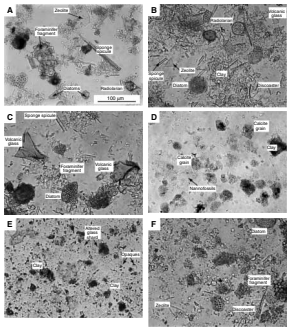

F12. Various sedimentary components, Sites 1039 and 1253, p. 79.

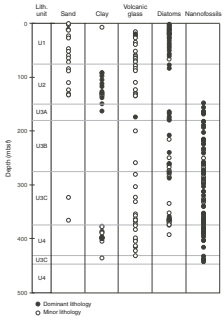

F13. Altered volcanic ash layer within claystone with zeolites, p. 80.

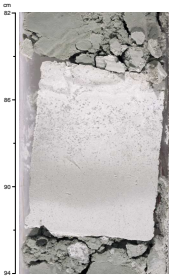

Breccias

Minor breccia layers, up to 3 cm thick, are observed, especially in the more carbonate-rich intervals in Cores 205-1253A-1R and 2R, although these always represent <1% of the total stratigraphy. We interpret these as being related to neptunian diking, because they crosscut horizontal bedding markers in the core and do not show a simple flat-bedded geometry. The clasts comprise pieces of broken nannofossil chalk, indicating intraformational reworking. These breccia could have formed far from the trench as a result of intraplate stress, although the stresses acting on the sequences would have increased as the site approached the deformation front. We suggest that these breccia are probably linked to deformation in front of the forearc wedge, although the exact timing of their emplacement cannot be definitively constrained from this work.

Trace Fossils

Trace fossils are developed through much of the cored interval, testifying to well-oxygenated bottom water conditions. Trace fossils of the *Zoophycos* ichnofacies were identified, including *Zoophycos, Planolites,* and *Chondrites,* consistent with deposition in lower bathyal to abyssal water depths (>2000 m) (Ekdale et al., 1984). The degree of bioturbation is strongest in the lighter carbonate-rich intervals and becomes less common in the clay-rich laminated sedimentary rocks of Core 205-1253A-4R (395–400 mbsf). Trace fossils are especially apparent where they disrupt the occasional dark green clay-rich layers (Fig. **F14**).

F14. *Zoophycos* ichnofossils disturbing a clay-rich interval, p. 81.

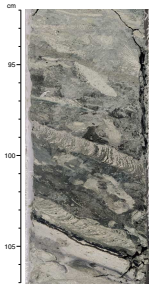

Diagenesis

Diagenesis has resulted in a moderate lithification to a chalky strength, except in Core 205-1253A-4R, lying immediately above a gabbro sill where the sediment is much more lithified. This section is also much less carbonate rich than other cores examined, with clays and zeolites forming increasing large volumes of the sediment in the 3 m above the upper gabbro sill. Thin chert layers are also seen in interval 205-1253A-4R-1, 53–61 cm, indicating mobilization and precipitation of silica in the sediment, likely derived from the abundant sponge spicules. As noted at Site 1039, the carbonate sediments are occasionally stained by a fine dark purple lamination that may cut across bedding fabrics and is often developed as a halo around larger burrows. Termed Liesegang rings, these features reflect mobilization of metals in the sediments during early diagenesis. It should, however, be emphasized that the overall composition of the sediment stained in this fashion does not appear to be significantly changed, and they cannot be considered as metalliferous sediments in the normal usage of the term.

Smear Slide Analysis

Smear slide analysis allows the variation in major sedimentary components to be analyzed and their variation with depth to be assessed (see **"Site 1253 Smear Slides"**) (Fig. **F12**). Apart from nannofossils and clay minerals, other grain types that contribute significantly to the sediments include siliceous sponge spicules, foraminifer test fragments, diatoms, opaque minerals, volcanic glass shards, and zeolites derived from the degradation of volcanic glass shards (Fig. **F11**). Minor, albeit common, components include radiolarian tests and fragments of tests,

grains of crystalline calcite, and occasional silicoflagellates. There is no evidence of terrestrial grain types, such as quartz, feldspars, or micas.

Plotting the new Site 1253 smear slide data with that collected at Site 1039 during Leg 170 allows total sedimentary variations with depth to be assessed. The microscopic analysis shows that grain sizes are fine throughout the core, with minor amounts of sandy material preferentially preserved in uppermost lithostratigraphic Units U1 and U2 (Fig. F12). This is consistent with a model in which the oceanic crust into which Site 1253 penetrates originated in a pelagic environment at a ridge crest and then approached the trench through time. Only when the site came close to the active continental margin was it in a position to receive coarser clastic material. Clay minerals are rare in the carbonate-rich Subunits U3B and U3C and are especially common in Unit 2 and Subunit U3A. Of the biogenic components, diatoms are seen in significant volumes throughout the section, but are most numerous in Unit U1, possibly reflecting the arrival of the drill site within the high-productivity upwelling zone along the Costa Rica margin. Abundance of diatoms is typically considered to indicate high biogenic productivity in nutrient-rich conditions. Nannofossils conversely show the opposite trend to decreased relative concentrations in Units U2 and U1, while being very abundant lower in the core. The trend in nannofossil abundance may partly reflect dilution by diatoms in these upper units and also corrosion and dissolution by colder, nutrient-rich waters in the coastal upwelling zone.

X-Ray Diffraction Mineralogy

X-ray diffraction (XRD) analyses were performed routinely. The results of XRD analyses of randomly oriented bulk sediment powders are summarized in Tables T2 and T3. Site 1253 peak intensity and peak area data are listed in Table T2, and peak ratio data are listed in Table T3.

T2. XRD analysis, p. 170.

T3. Peak area ratios of dominant minerals, p. 171.

The sample suite considered here includes dominant lithology carbonate sediments, minor lithology clay-rich sediments, and several tephras. A representative carbonate Sample is 205-1253A-4R-1, 14–15 cm, for which the calcite to quartz peak area ratio is 265, the clay to quartz peak area ratio is 10, and the plagioclase to quartz ratio could not be determined because of the absence of the plagioclase peak. Cristobalite/quartz peak area ratio data are typically used to monitor opal diagenesis. The cool temperatures (<10°C) encountered at this site render such considerations moot.

As expected, investigation of the peak area data shows that calcite peaks dominate the diffractogram data for samples of the major lithology (Subunit U3C). Three samples of carbonate sediments at baked contacts near and within gabbro sills (intervals 205-1253A-5R-1, 0–1 cm; 25R-1, 10–12 cm; and 27R-1, 4 cm) and seven tephras (intervals 205-1253A-2R-1, 49–50 cm; 2R-3, 101–102 cm; 4R-1, 86–87 cm; 4R-3, 87–88 cm; 4R-3, 90–92 cm; 10R-2, 85–87 cm; and 11R-2, 42–44 cm) were also analyzed to constrain finer-scale mineralogic variation at this site.

The baked sediments in contact with the gabbro intrusions are not identical. At interval 205-1253A-5R-1, 0–1 cm, at the top of the gabbro sill, bulk XRD data show a clay-rich mineralogy with abundant amorphous glass and suggest that illite is present. Sample 205-1253A-25R-1, 10–12 cm, is nearly pure calcite. At Section 205-1253A-27R-1, 4 cm, XRD data show a clay-rich mineralogy with abundant amorphous glass, and smectite and mixed layer smectite-illite clays dominate the clay component.

Tephra mineralogy also varies with stratigraphic depth as a function of initial composition, alteration, and extent of mixing with background sediment. Samples 205-1253A-2R-1, 49–50 cm, and 2R-3, 101–102 cm, show very little clay, abundant calcite, and minor plagioclase and quartz presence. Samples 205-1253A-10R-2, 85–87 cm, and 11R-2, 42–44 cm, are similar to those tephras just described, but also contain a smectite clay, likely saponite. Smectite may be present as a volcanic glass alteration product. Samples 205-1253A-4R-1, 86–87 cm, and 4R-3, 90–92 cm, have weak calcite peaks; these tephras consist mainly of plagioclase, quartz, and detrital hornblende. Compared to the dark, mafic tephras that dominate the section, the tephra at 205-1253A-4R-3, 87–88 cm, is in its own category, being a white siliceous ash. Mineralogically, the composite clay peak area at d ≈ 4.5 Å is greater than that in any other tephra and appears to represent smectite.

Sediment Chemical Analyses

Major and trace element analyses of 20 sediments, volcanic ashes, and baked sediments found intercalated between the divisions of the igneous subunits of Hole 1253A were conducted shipboard following the methods described in "Inorganic Geochemistry," p. 24, in the "Explanatory Notes" chapter. Major, minor, and trace element analyses are presented in Table T4. The tephras and baked sediments are analyzed by the ICP-AES separately from the sediments. Cerium, copper, and nickel values are near detection limits and are not reliable in those sediments overlying Subunit 4B that were analyzed. Copper, however, was above the detection limit in the tephras and baked sediments analyzed. Analyses were made on freeze-dried bulk samples that are a mixture of sediment particles and sea salts (see "Inorganic Geochemistry," p. 24, in the "Explanatory Notes" chapter). The data have not yet been corrected for porosity and pore water contribution to the bulk sediment composition.

T4. Bulk sediment analyses, Hole 1253A, p. 172.

The ICP-AES geochemical data at this reference site can be useful for (1) tracking the lithologic and sedimentologic variations within the sedimentary section, (2) determining the average composition of the sediment column for key elements entering the subduction zone for further recycling studies, and (3) helping to constrain estimates of tectonic underplating under the forearc.

Figure F15 shows variations in TiO_2, Al_2O_3, SiO_2, and Ti/Al with depth below seafloor. Titanium and aluminum show similar trends in the sediments overlying igneous Subunit 4B at Site 1253, and concentrations remain fairly constant with depth. The baked sediments within Subunit 4B have similar aluminum and titanium concentrations to the sediments above it. Ash layers are common at Site 1253, and volcanic detritus is nearly ubiquitous at low concentrations in much of the sediment recovered. The tephras analyzed from Site 1253 have consistently higher aluminum and titanium concentrations than the surrounding pelagic sediments. Consequently, the proportion of volcanic material in the sediments will tend to control the bulk sediment Ti/Al ratios. The small range in Ti/Al ratios (0.1–0.01) in the sediments overlying igneous Subunit 4B suggests that the percentage of volcanic ash in the sediments analyzed is fairly constant.

F15. TiO_2, Al_2O_3, SiO_2, and Ti/Al depth profiles, p. 82.

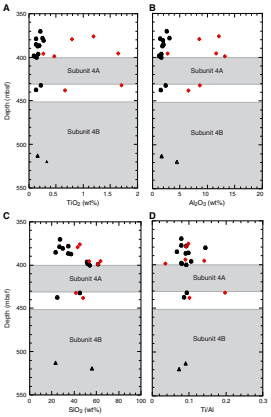

Silica concentrations within the section at Site 1253 reflect the lithologic change from a carbonate-rich nannofossil chalk down into a calcareous claystone immediately above the gabbro sill. Silica concentrations increase with depth as a result of the formation of clay minerals

and zeolites associated with sill emplacement and subsequent sediment diagenesis. Furthermore, XRD data indicate diatom and radiolarian recrystallization to quartz in the sediments above the sill. The authigenic formation of clay minerals and zeolites is also responsible for the uptake of dissolved potassium in the sediments immediately above the sill (Fig. F72) (see "Inorganic Geochemistry," p. 45). Below the sill, the sediments are composed mainly of nannofossil chalk, resulting in the lower silica concentrations observed (Fig. F15).

In Figure F16, CaO, MgO, strontium, and barium are plotted against depth for the sediments, volcanic ash, and baked sediments within Subunit 4B at Site 1253. Decreases in calcium and strontium with depth in the sediments above the sill reflect the reduction in carbonate content. In general, the calcium and strontium concentrations in the tephras are less than those of the background sediments overlying Subunit 4B. The baked sediments have concentrations similar to the sediments above the sill. Calcium and strontium concentrations increase between the sill and Subunit 4B because of the dominant nannofossil chalk lithology. Magnesium concentrations, like silica, increase with depth and reflect decreasing carbonate content immediately above the sill. Formation of in situ magnesium-bearing clays is also responsible for the increase in magnesium concentrations and the decrease in dissolved magnesium immediately adjacent to the sill. The incompatible element barium is highly enriched in these sediments (Fig. F16D), but concentrations decrease with depth to ~200 µg/g above the sill. Interestingly, dissolved barium concentrations are highest in this same region of only moderate barium concentration in the sediment. The maximum value observed in the basal sediment section is 3136 µg/g, whereas the maximum value observed in the volcanic ash samples is 1254 µg/g. This pattern suggests that the barium enrichment in the sediment is not entirely characteristic of the volcanic detritus and is largely the result of barium accumulation in barite.

F16. CaO, MgO, Sr, and Ba depth profiles, p. 83.

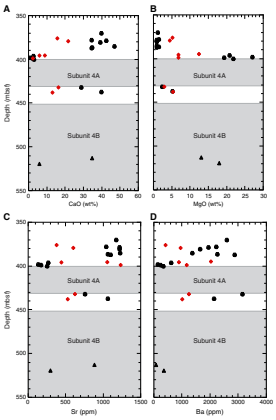

Figure F17 shows variations in Na_2O and K_2O with depth. Sodium concentrations in the sediments above the sill are fairly constant with depth and range between 1.06 and 1.97 wt%. The baked sediments analyzed have similar concentrations to the sediments recovered above the sill; however, there is a marked increase in sodium concentrations with depth in the tephras above the sill, which corresponds to an increase in dissolved sodium concentrations within the same interval (see "Pore Water Results," p. 46, in "Inorganic Geochemistry"). Potassium concentrations decrease with depth from 0.511 to 0.133 wt% between the sill and Subunit 4B (Fig. F17B). The baked sediments and the sediments above the sill have similar potassium concentrations, likely reflecting mobilization of this element during diagenesis, synchronous with and after sill emplacement.

F17. Na_2O and K_2O depth profiles, p. 84.

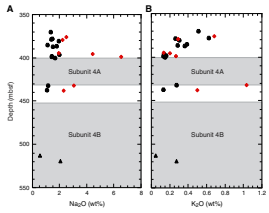

Both MnO and Fe_2O_3 concentrations remain fairly constant with depth (Table T4) and have maximum values of 0.38 and 3.39 wt%, respectively. Iron concentrations in the tephras are typically higher and range between 1.44 and 9.5 wt%. P_2O_5, vanadium, yttrium, zirconium, and chromium all remain fairly constant with depth within the sediments above the sill and in the baked sediments.

Tephra Geochemistry

The seven tephra layers chosen for chemical analyses were selected to span a range of colors, from white to dark gray, presumed to reflect sig-

nificant differences in the major element chemistry. Low analytical totals of 84–97 wt% indicate a significant degree of alteration, consistent with the observation of advanced diagenesis in the drilled section, especially immediately above the gabbro sill. Microscopic analysis shows that although clear fresh-looking glass shards can be found in the ash layers, these are largely outnumbered by glass in moderate to advanced stages of palagonitization (Fig. F18). The range of silica contents (42–65 wt%) shows a wide spread, with a dominance of basaltic tephra, that typically appears dark in the cut core surface. The bright white tephra observed in interval 205-1253A-4R-3, 85–93 cm, is also chemically distinctive in being the second most siliceous layer (62 wt% SiO_2) and having a much lower Fe_2O_3/MgO ratio than the other ashes. Because of the advanced state of alteration, little useful information concerning petrogenesis can be derived from study of the major elements. The tephra in interval 205-1253A-4R-2, 100–122 cm, differs from the nearby tephras in being thick (22 cm), with an anomalous major element chemistry (e.g., low TiO_2, Al_2O_3, and Fe_2O_3).

F18. White tephra layer, p. 85.

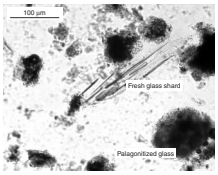

This interval is a light gray laminated clay-rich bed that is quite distinct from the laminated dark claystone facies that dominate the sequence from 395 to 399 mbsf. We suggest that this clay unit represents material that was originally mostly volcanic ash. However, the great thickness, darker color, and laminations indicate that this unit has been reworked and is not a primary volcanic sediment. Nonetheless, this deposit further contributes to the idea of explosive Galapagos volcanism, placing significant quantities of volcanic ash into the Pacific Ocean at this time.

The middle Miocene was singled out as a period of strong explosive volcanic activity by Kennett et al. (1977) and Kennett and Thunell (1977) for the Circum-Pacific region. Hein et al. (1978) demonstrated that the middle–late Miocene was a period of powerful volcanism in the Aleutians. In the Americas, Perkins et al. (1998) have shown that ~17 Ma was a time of extensive ignimbrite eruption in the western United States, whereas closest to Site 1253, Sigurdsson et al. (2000) documented a maximum in explosive tephra sedimentation in the Caribbean at 15–20 Ma presumed to be derived from Central America. The tephras recovered in the Miocene section at Site 1253 now show that the Galapagos hotspot was also very active at this time.

It is noteworthy that the white tephra was not recovered at Site 1039; because the relevant Core 170-1039C-4R reached only 18% recovery, it is likely that the tephra was simply not recovered at that locality. In addition, the white and mafic tephras are deposited at Site 1253 within a laminated sequence. The very fact that the tephras lie in such a sequence of laminated low-$CaCO_3$ sediment is itself of note when compared to the bioturbated nannofossil chalks above and below. We speculate that this period of low pelagic biogenic production and cessation of seafloor burrowing may be the product of the regional volcanism in the Galapagos and in Central America, causing widespread collapse of the ecology through the eastern central Pacific Ocean, much as has been recorded from the aftermath of the Toba eruption (Rampino and Ambrose, 2000).

Conclusions

We conclude that the sedimentary section recovered at Site 1253 is dominated by nannofossil chalks with minor amounts of clays and te-

phras. These were deposited at lower bathyal to abyssal water depths within a pelagic environment, remote from any continental mass. Deposition occurred above the calcite compensation depth in a well-oxygenated environment, interrupted by a relatively brief phase of more reducing bottom water conditions, allowing laminated clay-rich mudstone to form. In the middle Miocene (~17 Ma) the region received tephra deposits from the Galapagos hotspot during part of a major regional phase of tectonic and magmatic activity. Volcanism is also associated with synchronous seafloor anoxia. Shortly afterward, the section was intruded by a gabbro sill and Subunit 4B that caused advanced diagenesis and lithification, extending ~10 m above the top of the sill. Subsequent diagenesis has resulted in the hydration of volcanic glass shards distributed through the section to form zeolites and palagonite.

PETROLOGY

During coring at Site 1253, we encountered two igneous units. The upper unit, Subunit 4A, is a gabbro sill between 400 and 431 mbsf and is further subdivided into two subunits on petrologic grounds. Below this unit, ~30 m of sediment was recovered. Subunit 4B (450 mbsf curated depth to the bottom of the hole at 600 mbsf) was subdivided into seven subunits. Both Subunits 4A and 4B are plagioclase- and clinopyroxene-phyric with microcrystalline, fine-grained, and, rarely, medium-grained groundmasses. At 513 mbsf, a thin basaltic (cryptocrystalline) interval was recovered, and Subunit 4B is more glass rich and altered below this depth. These features are generally similar to those described during Leg 206 (Holes 1256C and 1256D) when thick ponded lava flows were encountered in basement (Shipboard Scientific Party, 2003, in press). The data suggest that Subunit 4B is either a series of thick and slowly cooled lava flows formed at the East Pacific Rise, oceanic crust intruded by mutliple gabbro sills generated by the Galapagos hotspot, or a combination of the two. It is possible that the drill string passed from a sill complex to basement at a depth of ~513 mbsf. Postcruise dating and detailed geochemical and isotope analysis will be necessary to discern between the possibilities.

Subunit U4A: Gabbro Sill

Interval: 205-1253A-4R-CC to 10R-1, 78 cm
Depth: 401–432 mbsf
Thickness: 31 m
Age: maximum age of 16.726 Ma

General Description

An igneous formation of gabbroic texture was first encountered at 401 mbsf in Hole 1253A during RCB coring. We recovered gabbro from 401 to 432 mbsf before intercepting a layer of clastic, granular limestone, defined as packstone with clay.

Subunit 4A is composed of microcrystalline to fine-grained plagioclase-pyroxene gabbro with plagioclase aggregates or, more rarely, plagioclase with pyroxene aggregates in a holocrystalline groundmass (Fig. F19). The contact between sediment and gabbro was not recovered in place. The maximum age of the gabbroic sill is constrained by the Mio-

F19. Microcrystalline to fine-grained holocrystalline gabbro, p. 86.

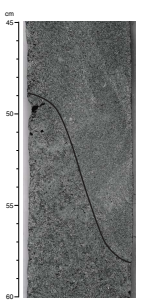

cene ooze and clastics from Subunit 3C and based on paleomagnetism data at post–16.726 Ma in age (see "Paleomagnetism," p. 41).

The principal features observed in core hand specimen of the gabbroic sill are summarized in Figure F20. This is presented in terms of structures such as veins, fractures, magmatic contacts, and voids and textures along with the proportion of each mineral phenocryst and the groundmass characteristics. Several observations can be made: (1) voids are solely located at the top of Sections 205-1253A-4R-CC, 5R-1, and 8R-2; (2) veins are more frequent for Core 205-1253A-5R and the bottom of 8R; (3) magmatic contacts are located at the top of Core 8R; and (4) plagioclase phenocrysts are more abundant than pyroxene phenocrysts except at the top of Core 8R. We tentatively interpret these textural and structural variations as features defining two different parts of the sill. The upper Subunit 4A-1 extends from 401 to 415.2 mbsf (Sections 205-1253A-4R-CC to 7R-2) and the second Subunit 4A-2 from 415.2 to 430.8 mbsf (Sections 205-1253A-8R-1 to 10R-1). The core recovery is >85% within the first subunit, whereas it drops to ~50% in the second subunit. In addition, the ratio of the natural remnant magnetization (NRM) over the magnetic intensity varies from 0 to 1.5 within Subunit 4A-1, whereas it remains close to 0 within Subunit 4A-2 (see Fig. F65). This indicates that the magnetization is stronger and more stable within the upper part than the lower part of the gabbro sill. This could be related to the variation of gabbro grain size as illustrated in Figure F20, where it is possible to distinguish, on a centimeter scale, changes in phenocryst abundance and groundmass grain size. The downhole logging data indicate high Th, U, and K gamma ray counts throughout the gabbro sill.

F20. Structural, textural, and mineralogical features of Subunit 4A, Cores 205-1253A-4R through 10R, p. 87.

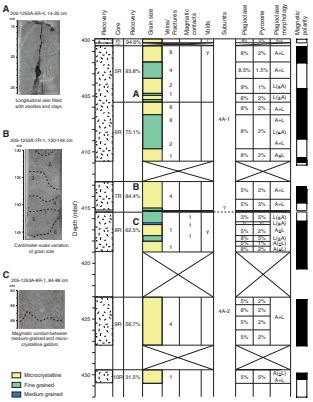

Microscopic Description

Eighteen thin sections from the gabbro sill were examined, and Figure F21 shows a typical example of microcrystalline gabbro. Plagioclase ($An_{>50}$) is present either as aggregates up to 7 mm in size or as several millimeter-sized laths. The proportion of laths and aggregates are related to the groundmass grain size, where smaller phenocrysts are observed in microcrystalline groundmass and larger ones in fine- to medium-grained groundmass. Phenocrysts of clinopyroxene (augite) up to 1.6 mm in size show anhedral to subhedral morphology and are present sometimes with plagioclase aggregates. The groundmass is mainly composed of ~300-µm euhedral to subhedral plagioclase, ~100-µm anhedral clinopyroxene, a rare amount of glass (<2%), palagonite, and clay. Rarely, we observed <1% of anhedral orthopyroxene and/or olivine phenocrysts. Ilmenite and opaque minerals, such as magnetite, up to 15% in total, are observed as either phenocrysts or as small minerals within the groundmass. Finally, we observed elongated and xenomorphic glass, altered glass, and mineral inclusions within plagioclase and sometimes within clinopyroxene as shown in Figure F22. Most of the inclusions are located in phenocryst centers, indicating their incorporation at early stages of mineral crystallization. Detailed thin section descriptions are presented in the thin section description log (see the "Site 1253 Thin Sections").

F21. Microcrystalline gabbro, p. 89.

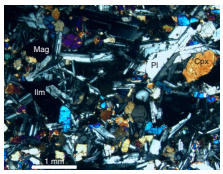

F22. Glass inclusions, altered glass, and clinopyroxene in plagioclase phenocrysts, p. 90.

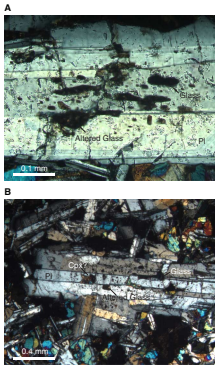

Alteration

Alteration in the gabbro sill is characterized by weathering, replacement of primary minerals, and precipitation of secondary minerals in

voids, veins, and the groundmass. Voids are elongated (up to 1.2 mm wide) and are present only at the top of each "subunit" and close to veins that are located throughout the full thickness of the sill. Veins, <1 mm wide, are also filled with a mixture of very fine grained cryptocrystalline groundmass (Fig. F23) and altered glass (palagonite). Because of thin section preparation difficulties, most of the vein and void filling material was lost and could not be identified by microscopic studies. However, macroscopic observations show that clay is the main secondary mineral precipitating in voids and veins. Zeolites could not be identified in the XRD pattern of samples taken from veins; however, macroscopic observations show the presence of white secondary minerals in voids that are believed to be zeolites. XRD analyses identified a trioctahedral smectite (saponite) in Sections 205-1253A-5R-2, 5R-3, and 6R-3. Based on thin section observations, it is difficult to clearly identify the presence of minerals from the chlorite group (corrensite and chamosite?, although they are tentatively identified as present). An overview of the minerals identified by XRD analyses is given in Table T5. The main alteration feature observed in thin sections is the replacement of primary minerals by clay, as shown in Figure F24A. Olivine is identified by the shape of the crystal (Fig. F24B), which is completely replaced by clay and remnants of the primary mineral (Fig. F24C). An example of altered plagioclase is shown in Figure F24D, where it is replaced by a mixture of secondary minerals, partly clays. Similar alteration is also observed for other primary minerals. However, most of the phenocrysts remain unaltered and the groundmass shows only a modest amount of clays (~5%–10%).

F23. Cryptocrystalline to holocrystalline groundmass in microcrystalline gabbro, p. 91.

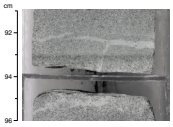

T5. Mineralogical assemblages determined by XRD, p. 173.

F24. Alteration of primary minerals in Subunit 4A, p. 92.

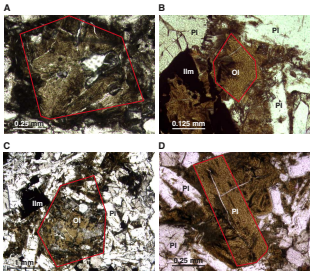

Subunit U4B: Gabbro

Interval: 205-1253A-12R-1, 26 cm, to 43R-4, 80 cm
Depth: 452–600 mbsf
Thickness: >148 m
Age: undetermined

General Description

A second igneous formation is present at 452 mbsf (curated depth) in Hole 1253A below a >30-m-thick layer of clastic, granular limestone or packstone with clay. Logging results indicate that Subunit 4B begins at ~461 mbsf, where the depth difference reflects the standard curatorial practice of moving any recovered material to the top of the core.

Subunit 4B is composed of microcrystalline to fine-grained and, occasionally, medium-grained plagioclase-pyroxene gabbro with plagioclase aggregates or, more rarely, plagioclase with pyroxene aggregates in a holocrystalline groundmass. Very rare horizons of cryptocrystalline igneous rock, with clear basaltic texture, are present within the 148 m of recovered igneous rocks (Cores 205-1253A-12R to 43R). However, we observed textural, structural, and mineralogical features identical to those of Subunit 4A, a gabbroic sill. We terminated Hole 1253A at 600 mbsf without reaching the lower edge of Subunit 4B. As a consequence, it remains unclear whether the gabbro of Subunit 4B is an igneous intrusion within the basement related to the magmatic activity of the Galapagos hotspot or represents a coarser part of the basement of the Cocos plate formed by slow cooling of thick lava flows, similar to the ponded flows observed in basement samples from Holes 1256C and 1256D during ODP Leg 206 (Shipboard Scientific Party, 2003, in press).

The main structural, textural, and mineralogical characteristics seen in core hand specimen of Subunit 4B are summarized in Figures F25, F26, F27, F28, F29, and F30. Representative close-up photographs of cores are added to the figures to illustrate the main macroscopic features. We described the 33 cores (205-1253A-12R through 43R) following the scheme used for Subunit 4A. We used the following criteria to subdivide the cored section:

1. Voids solely located at the top of a subunit;
2. Higher vein abundance at the top of a subunit;
3. Increasing groundmass grain size toward the bottom of a subunit associated with increasing abundance of plagioclase aggregates instead of laths; and
4. Pyroxene percentage higher than or equal to plagioclase, associated with higher abundance of plagioclase laths than aggregates are present at the top of a subunit.

Using these criteria, we distinguish seven different subunits, which are characterized as follows.

Subunit 4B-1

Subunit 4B-1 occurs in Cores 205-1253A-12R through 15R, extending from 450.6 to 470.9 mbsf. It is a 20.3-m-thick microcrystalline gabbro with 2 m of fine-grained gabbro at the top of Core 205-1253A-13R. Voids filled with sediment and/or clays are present throughout Subunit 4B-1 as shown in Figure F25. Recovery was generally low (below 20%) except for Core 205-1253A-14R in which recovery was 87%. Paleomagnetism data indicate that the formation of Subunit 4B-1 took place during an interval of reversed polarity.

Subunit 4B-2

Subunit 4B-2 extends from Cores 205-1253A-16R through 17R (470.9 to 480.5 mbsf) (see Figs. F25, F26). A 3.5-m-thick fine-grained gabbro is present at the center part of the subunit and is overlain and underlain by microcrystalline gabbro. Veins <1 mm wide are present throughout the subunit, whereas magmatic contacts are concentrated at the top of Core 205-1253A-16R and at middle of Core 17R. Recovery was excellent (>89%), and paleomagnetism data indicate a reversed polarity for the emplacement of Subunit 4B-2.

Subunit 4B-3

Subunit 4B-3 is present in Cores 205-1253A-18R and 19R (480.5 to 490.33 mbsf) and is composed of 10-m-thick microcrystalline gabbro. By comparison, Subunits 4B-1 and 4B-2 exhibit a higher proportion of voids, a larger number of magmatic contacts at the top (see Fig. F26A), a higher amount of veins toward the bottom (Fig. F26B), and a higher proportion of pyroxene phenocrysts. Coring recovery was variable (32.6% and 115.9%).

Subunit 4B-4

Cores 205-1253A-20R through 24R constitute Subunit 4B-4, which extends from 490.3 to 513 mbsf. It is essentially composed of fine-

F25. Structure, texture, and mineralogy of Subunit 4B, Cores 205-1253A-12R through 16R, p. 93.

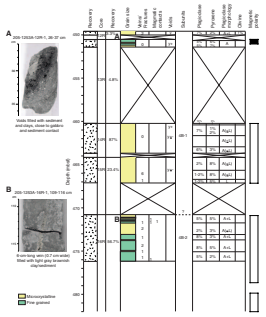

F26. Structure, texture, and mineralogy of Subunit 4B, Cores 205-1253A-16R through 22R, p. 95.

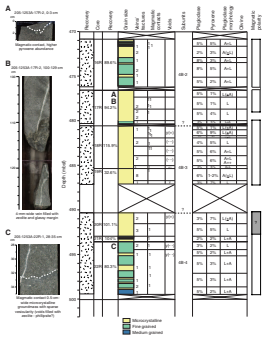

F27. Structure, texture, and mineralogy of Subunit 4B, Cores 205-1253A-23R through 28R, p. 97.

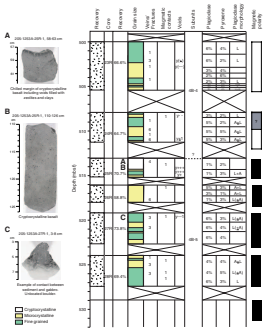

F28. Progressive increase of groundmass grain size, p. 99.

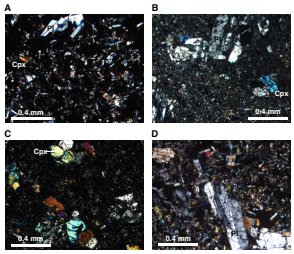

grained gabbro with some interlayering of microcrystalline gabbro. At the bottom of Core 205-1253A-22R, we observed a 0.5-m-thick medium-grained gabbro. Magmatic contacts are not frequent. However, veining and void presences are more concentrated at the top and bottom of Subunit 4B-4. Coring recovery was excellent, averaging 83%. Downhole logging data show a resistivity and velocity decrease at 513 mbsf, which is the depth of the petrological boundary between Subunits 4B-4 and 4B-5.

Subunit 4B-5

Subunit 4B-5 (513–543 mbsf; Cores 205-1253A-25R through 31R) is characterized by an upper 1.26-m-thick cryptocrystalline basalt (Figs. F27A, F27B, F28). The contact between cryptocrystalline basalt (Subunit 4B-5) and the overlying microcrystalline gabbro (Subunit 4B-4) was not recovered. The cryptocrystalline basalt grades progressively into microcrystalline gabbro without any compelling evidence of contact (Fig. F28). In Piece 8 of Section 205-1253A-25R-1, we observed a dark gray 0.5-cm-wide margin mainly composed of very cryptocrystalline groundmass rather than a glassy chilled margin. Fine-grained gabbro is the most abundant grain size groundmass with intercalation of microcrystalline gabbro at the top (apart from the 1.26 m of cryptocrystalline basalt) and bottom of Subunit 4B-5. The number of magmatic contacts increases within the coarser grained part of the subunit (Fig. F29). The lowest coring recovery (35.2%) was obtained in Core 205-1253A-29R, where the recovered material is mainly composed of the coarsest groundmass of the entire Subunit 4B, which does not contain any veins or fractures. Apart from the 1.26-m-thick cryptocrystalline groundmass, Subunit 4B-5 does not differ from previous subunits. No downhole logging data are available below 550 mbsf. However, paleomagnetism data indicate that a magnetic polarity reversal occurs at the transition between Subunits 4B-4 and 4B-5.

Subunit 4B-6

Cores 205-1253A-32R through 36R compose Subunit 4B-6 which extends from 543.2 to 566 mbsf (Figs. F29, F30). It is essentially microcrystalline gabbro with a few intervals of fine-grained gabbro. Subunit 4B-6 shows an increase in small-scale veining (Fig. F30B, F30C) and clustering of magmatic contacts within Core 205-1253A-33R (549.2–552.9 mbsf). The recovery is lower (53.2%) at the top of Subunit 4B-6, whereas it averages ~86% to its base.

Subunit 4B-7

Subunit 4B-7 extends from 566 to 600 mbsf and is mainly composed of microcrystalline and fine-grained gabbro (Figs. F30, F31). The first four cores (Cores 205-1253A-37R through 40R) are mainly composed of microcrystalline gabbro, with a larger number of fractures on a centimeter scale (Fig. F30C) and low recovery between 30.8% and 52%. In contrast, Cores 205-1253A-41R, 42R, and 43R are very homogeneous fine-grained gabbro that exhibits some magmatic contacts as well as large veins as illustrated in Figure F31A.

Figure F32 shows the variation of core recovery along with the lithostratigraphy from 370 to 600 mbsf, as well as the main features in each subunit. These observations were used to summarize observations from

F29. Structure, texture, and mineralogy of Subunit 4B, Cores 205-1253A-28R through 35R, p. 100.

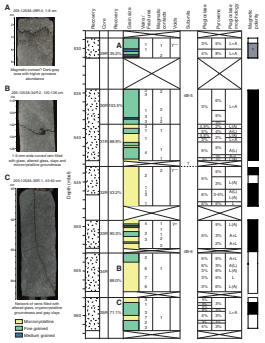

F30. Structure, texture, and mineralogy of Subunit 4B, Cores 205-1253A-36R through 40R, p. 102.

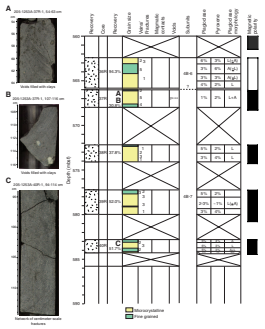

F31. Structure, texture, and mineralogy of Subunit 4B, Cores 205-1253A-41R through 43R, p. 104.

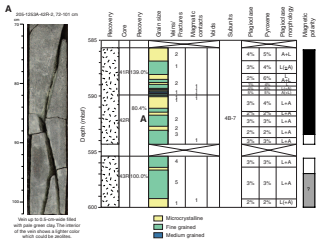

F32. Core recovery plot, Hole 1253A, p. 105.

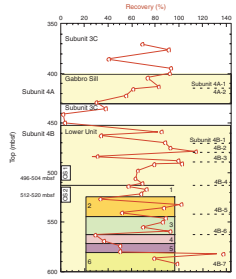

180 m of igneous rock and to guide the emplacement of two OsmoSamplers. The first OsmoSampler is centered at 500.37 mbsf in the microcrystalline to fine-grained gabbro of Subunit 4B-4. The second OsmoSampler is centered at 515.8 mbsf, within the upper 10 m of Subunit 4B-5, including the basaltic horizon. Their positions are sketched in Figure F32.

Microscopic Description

We examined 61 thin sections from Subunit 4B, and we present six photomicrographs of microcrystalline (Fig. F33A, F33B, F33E), fine-grained (Fig. F33C, F33D) and medium-grained gabbro (Fig. F33F) to illustrate the groundmass grain size observed over the entire Subunit 4B. The full set of thin section descriptions are presented as a thin section description log (see the "Site 1253 Thin Sections"). Phenocrysts are plagioclase, clinopyroxene, olivine, and orthopyroxene. Plagioclase ($An_{>55}$) is present either as aggregates up to 1 cm in size in medium-grained gabbro or as several-millimeter-sized laths. We also observed plagioclase growth zoning, indicating magma differentiation during crystallization of plagioclase phenocryst (Fig. F34). The proportion of laths and aggregates are related to the groundmass grain size. Phenocrysts of clinopyroxene (augite to titanoferrous augite) up to 2.6 mm in size show anhedral to subhedral morphology. Orthopyroxene phenocrysts are less abundant than 1% and are present as up to 1.3-mm-sized anhedral crystals within the groundmass. The abundance of olivine phenocrysts (up to 1.2 mm in size) varies significantly throughout Subunit 4B. This mineral is typically altered as explained in detail in "Alteration," p. 27, and its shape is generally anhedral. We encountered difficulties in certain thin sections distinguishing olivine from clinopyroxene, as we did not systematically observe clinopyroxene cleavage and olivine morphology has been destroyed by alteration. However, we distinguished each mineral based on crystallographic features such as pleochroic color, extinction sector, and biaxial figure. Ilmenite and magnetite (<7% in total) are present either as anhedral phenocrysts up to 0.7 mm in size or within the groundmass. Groundmass is mainly composed of ~300-µm euhedral to subhedral plagioclase, ~200-µm anhedral clinopyroxene, glass, altered glass (palagonite), and clays. Subunit 4B contains a greater abundance of glass (several percent) than Subunit 4A (<2%).

Melt as glass or altered glass is found as inclusions at the center of plagioclase (Fig. F35), pyroxene, and olivine phenocrysts. They do not present any specific morphology, but they are always located at the center of phenocryst before extensive magma differentiation as shown from plagioclase growth zoning.

Another feature of Subunit 4B is the large number of magmatic contacts. The contacts are defined by a sharp increase in groundmass grain size and phenocrysts. Plagioclase and clinopyroxene exhibit euhedral morphology in the smaller groundmass size, whereas they are anhedral and intergrown with each other in the coarser groundmass size as illustrated in Figure F36. Such features are consistent with injection/intrusion of melt within microcrystalline gabbro, with recrystallization of the groundmass on the microcrystalline side and slow growth of plagioclase and clinopyroxene within the medium-grained groundmass. Such characteristics do not fit with crystallization segregation processes, as intergrowth of minerals will not occur in such a case. In addition, we also observed a higher abundance of glass or altered glass (palagonite)

F33. Microcrystalline and fine- and medium-grained gabbro, p. 106.

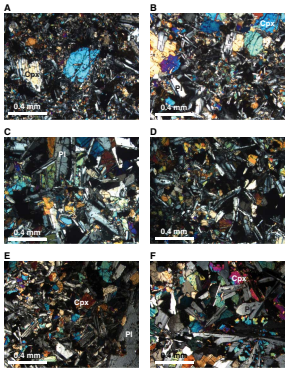

F34. Growth zoning within plagioclase, p. 107.

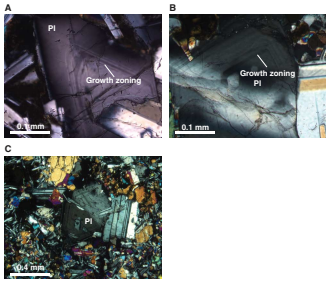

F35. Glass and altered glass inclusions, p. 108.

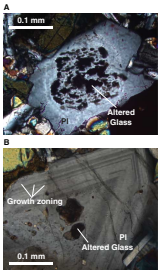

F36. Groundmass size and plagioclase and clinopyroxene intergrowth, p. 109.

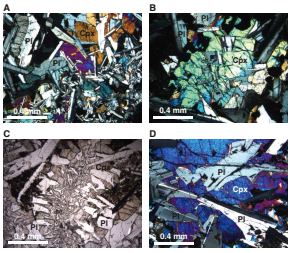

at the magmatic contact than within the gabbro groundmass. However, glass does not define a continuous chilled margin but is present as small accumulations <0.5 mm across. Within these areas, ilmenite and opaque minerals are highly concentrated (up to 20%). Such features support an injection crystallization/recrystallization rather than a crystallization segregation magmatic process. It is also possible that the magmatic contacts represent the location of fluid addition or circulation at high temperature, which implies coarse mineral crystallization.

Alteration

The degree of alteration is determined by macro- and microscopic observations combined with onboard XRD analyses. Because of the relatively rare abundance of veins and voids and, as a consequence only small amounts of discrete alteration material, only a few XRD analyses of separated vein and void material were conducted. Additionally, whole-rock samples with and without void and vein material were analyzed. An overview of the results is given in Table **T5.** The identification of different types of zeolites has to be confirmed by onshore microprobe analyses because many relevant peaks occur close to each other, making conclusive identification by XRD difficult.

Subunit 4B is characterized by a higher amount of alteration compared to the gabbro sill (Subunit 4A). However, the discrete alteration still remains low, giving the rocks a relatively fresh appearance in hand specimen. Below Core 205-1253A-24R, which also marks the border of a "subunit," thin sections show an increased percentage of glass as fragments within the groundmass (up to 10% in Sections 205-1253A-34R-2 and 41R-2 in contrast to very rare amounts of glass in the first subunits). Glass remains fresh or is partly altered to palagonite. Clay minerals, originating from palagonite or as alteration products from primary minerals, are common secondary minerals (10%–20%) and can make up as much as 50% in Section 205-1253A-33R-1.

Observations of the primary minerals indicate that olivine is the most altered mineral (up to 100%). In many cases only the shape of olivine can be identified, filled by clay, which is believed to be saponite. Saponite precipitates also in veins as a green mineral. XRD patterns show clear evidence of saponite. The (060) reflection at 1.541 Å and peaks at 1.749, 2.65, 3.14, and 4.64 Å demonstrate the presence of a trioctahedral smectite (Sample 205-1253A-42R-2, 94–99 cm, separated vein material). A glycol-saturated sample shows a shift of the 13.0-Å peak to 14.6 Å, also indicating the presence of saponite. Because of the similar occurrence of peaks, the presence of nontronite is also possible.

Plagioclase is generally more altered than pyroxene; the average of plagioclase alteration is ~10%, and pyroxene alteration is ~5%. However, in rare cases, both minerals can be altered up to 30%–40% or even totally replaced by clay. The alteration of primary minerals starts at glass inclusions or intramineral fissures and, along the rim, weathering to clay minerals. The surfaces of fissures cause the mineral to be divided into several fragments, where the alteration continues until the whole primary mineral is replaced (e.g., Fig. **F37** for olivine). Clays are also abundant close to opaque minerals (magnetite and ilmenite), suggesting that some of the opaque minerals that are also found in replaced primary minerals could be alteration products. Chlorite is identified in only a few thin sections (e.g., Sample 205-1253A-42R-3), but XRD analyses indicate the presence of minerals from the chlorite group (probably chamosite and corrensite). The lack of iron oxyhydroxides

F37. Altered primary minerals by clay, p. 110.

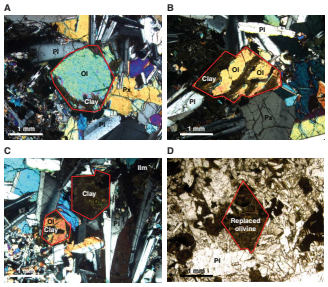

and the weak appearance of celadonite in XRD patterns could be related to more reducing conditions or their replacement during a later alteration stage.

Only trace amounts of zeolites are found in cavities, voids, and veins in thin sections, as most material is lost because of difficulties in thin section preparation. The identification of zeolites in Section 205-1253A-22R-2 is shown in Figure F38. XRD patterns show distinct reflections at 6.56, 5.91, 5.42, 4.39, and 2.87 Å, indicating the presence of mesolite and scolecite. Other zeolites that are in this sample are thomsonite and phillipsite, although their identification is equivocal in terms of XRD pattern. Nevertheless, laumontite, mesolite, thomsonite, and scolecite, which all belong to the same zeolite group, are common in the upper part of Subunit 4B above Core 205-1253A-25R, whereas phillipsite and stilbite can be identified only below Core 24R (Fig. F39). Stilbite is also identified in Sample 205-1253A-33R-1 (Piece 8A, 132–134 cm) by the characteristic sheaflike aggregates and radiating masses (Fig. F40A, F40B, F40C). Other zeolites are found in thin sections from the upper part of the unit (Fig. F40D, F40E, F40F). The reason for the different types of zeolites in relation to depth could be changing alteration conditions due to changes in fluid flow, temperature, abundance and chemical composition of primary minerals, chemical composition of the groundmass, and different redox conditions.

The presence of calcite is restricted to veins and is clearly identified by XRD pattern with representative peaks at 3.86, 3.03, 2.495, 2.281, 2.090, 1.908, and 1.869 Å in Samples 205-1253A-39R-1, 130–131 cm, and 27R-1, 94–98 cm. In thin sections, calcite could not be identified. However, not all veins were selected for XRD or thin section observations, allowing the possibility that calcite may also be present in other veins of Subunit 4B.

The presence of different secondary mineral assemblages probably reflects different stages in the progressive alteration. Clay minerals are the most abundant secondary minerals and are believed to precipitate first. It is unclear how many clay alteration stages are present. Empty alteromorphs of primary minerals are sometimes replaced with an isotropic alteration mineral and clay, which in terms of olivine alteration is believed to be saponite. At an advanced weathering stage, primary minerals are partly replaced by chlorite, whereas zeolite and calcite precipitate in voids and veins.

Geochemistry

Geochemistry of the gabbro sill (Subunit 4A) and the gabbro (Subunit 4B) has been investigated by ICP-AES analyses. The results are presented in Table T6. Issues of data quality are discussed in the "Explanatory Notes" chapter. Major element totals vary between 96.45 and 102.12 wt% with loss on ignition ranging from 0.17 to 3.16 wt%. The principal objectives are (1) to decipher primary geochemical characteristics from those produced by fluid/rock interaction, (2) to examine the extent to which fractional crystallization processes have modified the chemical composition of the melt before emplacement, and (3) to begin the identification of the mantle source of Subunits 4A and 4B.

Figure F41 shows the variation of major and trace element concentration vs. depth (in mbsf). Geochemical variation within and between the gabbro sill and the gabbro is generally small, which is not unusual for rocks of 46–49.5 wt% SiO_2. The gabbro sill is nearly holocrystalline and may not represent original liquid composition, whereas we observe

F38. XRD pattern with mesolite and scolecite peaks, p. 111.

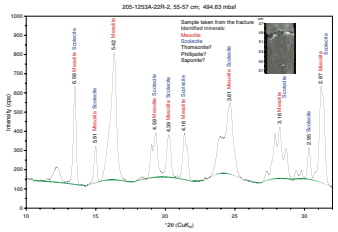

F39. XRD pattern with peaks for phillipsite and stilbite, p. 112.

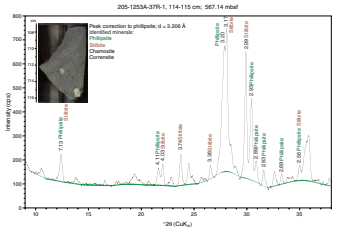

F40. Zeolites, p. 113.

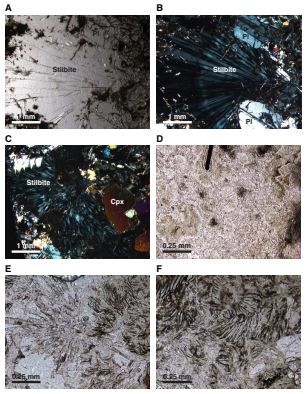

T6. ICP-AES data for the gabbro sill and Subunit 4B, p. 174.

F41. Major and trace elements as a function of depth, p. 114.

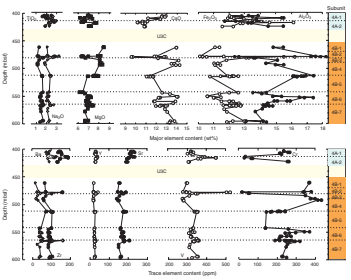

more glass and palagonite in Subunit 4B, suggesting that some of the samples (below Core 205-1253A-25R; 513 mbsf) more closely approximate liquid compositions and, thus, better reflect the original mantle geochemical characteristics. In addition, we observed melt inclusions at the center of phenocrysts, and these inclusions may help to constrain the primary chemical composition of the magma. But first of all, it is important to distinguish between geochemical features related to magmatic processes and those induced by fluid-rock interaction. Most of the subunit boundaries, established on macroscopic and microscopic observations, are also highlighted in the geochemistry by concentration changes. This is true for the following subunit transitions: 4A-1 to 4A-2, 4B-2 to 4B-3, and 4B-6 to 4B-7; however, for the remaining three boundaries, additional data are needed. Boundaries characterized by significant changes of major element content such as TiO_2, Na_2O, or Fe_2O_3 and changes of concentrations for both an immobile trace element such as Zr and mobile elements like Sr or Ba should be considered as magmatic. In contrast, the boundary between Subunits 4B-6 and 4B-7 may be a zone of fluid-rock interaction, reflected in a systematic increase in all mobile element concentrations relative to immobile ones.

The effects of fractional crystallization and removal of minerals such as plagioclase, clinopyroxene, olivine, and ilmenite/opaque minerals on the geochemical composition of the melt must be evaluated. This could be assessed at first glance in Figure **F42.** For example, the covariation of TiO_2 and V throughout Subunits 4A and 4B indicates the control of ilmenite and/or titanomagnetite on the distribution of TiO_2 and V content. This is confirmed in Figure **F42,** which shows a positive linear variation of V content as a function of TiO_2. Both subunits present similar trends, but the gabbro sill is shifted to higher TiO_2 contents and lies along a trend with lower V concentration. Therefore, the two units were not generated at the same time and probably not from the same mantle source, as a common linear trend would have been expected in case of a single melting event of a mantle source.

Decreasing MgO and Cr contents for increasing Fe_2O_3 content at the same depth as shown in Figure **F41** suggest that clinopyroxene fractionation occurred and modified the chemical composition of the melt previous to emplacement. Mg# is calculated according to the following equation:

$$Mg\# = Mg^{2+}/(Mg^{2+}+Fe^{2+}),$$

where $FeO = 0.8998 \times Fe_2O_3$. Figure **F43** presents the variation of CaO/Al_2O_3 as a function of Mg# to assess the effect of clinopyroxene ($Ca[Mg,Fe]Si_2O_6$), olivine ($[Fe,Mg]_2SiO_4$), and plagioclase ($[Ca,Na]Al_{1-2}Si_{3-2}O_8$) fractionation on the melt composition. Subunits 4A and 4B are separated into two groups: a group with CaO/Al_2O_3 ratio ~0.9 for variable Mg# values (0.28–0.4) and a second one with CaO/Al_2O_3 ratios ~0.7 for similar Mg#. The first group may have undergone a significant amount of olivine crystallization and removal at an early stage of melt formation. This is shown in the Ni vs. CaO/Al_2O_3 diagram, as Ni content decreases with decreasing CaO/Al_2O_3 values (Fig. **F44**). In contrast, the low CaO/Al_2O_3 value of the second group might be related to early clinopyroxene crystallization and removal. This is consistent with a negative linear correlation between Cr and Zr contents of Subunits 4A and 4B (Fig. **F45**). Plagioclase fractionation seems to take place during melt crystallization and differentiation for the gabbro sill as emphasized by a slight

F42. V content as a function of TiO_2, p. 115.

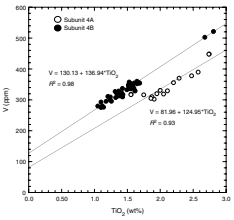

F43. CaO/Al_2O_3 ratio as a function of Mg#, p. 116.

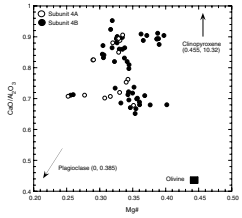

F44. Ni content as a function of CaO/Al_2O_3 ratio, p. 117.

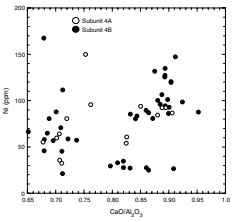

F45. Cr content as a function of Zr content, p. 118.

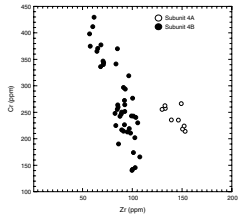

CaO/Al_2O_3 decrease for decreasing Mg# values. Possible plagioclase control on Sr content is highlighted in Figure F46, where we observe a positive linear correlation between Na_2O and Sr. As Sr is a compatible element in plagioclase, the fractionation of this mineral would lower the Sr and Na_2O content of the melt.

Overall, the chemical composition of melt derived from the mantle has been progressively changed by mineral fractionation and removal before the emplacement of the gabbro sill and the gabbro of Subunit 4B. From trace element systematics, Subunits 4A and 4B were not generated by the same melting episode. Regarding the mantle source, we do not have at the present the key analytical data (such as Nb, Th, and rare earth elements) to answer this question. It is unclear whether the mantle source is the Galapagos hotspot (an enriched mantle source), the East Pacific Rise (a depleted mantle source), or a combination of the two.

STRUCTURAL GEOLOGY

Sediments

Sediments recovered at Site 1253 show a variable degree of drilling disturbance; however, some sections both above and between the igneous units such as Cores 205-1253A-4R and 11R are indurated enough to allow observation of the original geometry of sedimentary layers and deformation structures.

The sediments are characterized by tilted bedding with 30° average dips (Figs. F47, F48). This is consistent with results from Leg 170 at Sites 1039 and 1040 (Kimura, Silver, Blum, et al., 1997), where continuous coring of the sedimentary section showed that this tilting starts at ~352 mbsf at Hole 1039B (Section 170-1039B-38X-6). At Hole 1040C the bedding in the lower part of the underthrust section, starting from 640 mbsf (Core 170-1040C-51R), shows a transition from horizontal to 20° average dips (Kimura, Silver, Blum, et al., 1997). At Site 1253, paleomagnetic reorientations indicate westward dip directions clustered at 221° (Fig. F49), also consistent with results from Sites 1039 and 1040.

Small normal faults perpendicular to bedding and with millimeter-scale offset are common throughout the recovered sediments (Fig. F50A). Structures recording fluid-related processes are also commonly observed, including incipient stylolites, fluid escape structures, and fluidized sediment injections (3 to 10 cm long). These have orientations both parallel and horizontal to bedding. Reverse faults with slickenlines are present, but less common, and their orientation is compatible with subhorizontal to shallowly dipping shortening. These steeply dipping structures may be reactivated normal faults formed during compaction, or they may be reverse faults formed as such. If they are not reactivated, their orientation may be used to infer stress orientation at the time of formation. Figure F51 shows a stereographic plot of a conjugate system of these reverse faults in interval 205-1253A-2R-3, 128–135 cm (Fig. F51B), in which the principal stress orientation reconstruction indicates a north-south (183°), horizontal orientation for σ. This stress field is oriented at ~30° to the convergence vector (DeMets et al., 1990).

The close spatial association of reworked pelagic sediment in the lower part of Subunit U3C (Kimura, Silver, Blum, et al., 1997), westward-tilted bedding, and the gabbro sill (Subunit 4A) suggest that the lowermost part of the sedimentary section may have been deformed

F46. Sr content as a function of Na_2O concentration, p. 119.

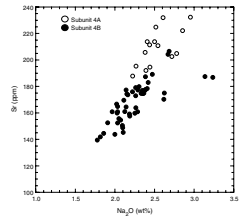

F47. Bedding dip and microfaults, p. 120.

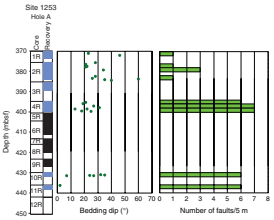

F48. Tilted primary laminations in nannofossil chalk, p. 121.

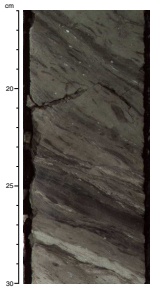

F49. Stereographic plot showing major circles and pole contouring, p. 122.

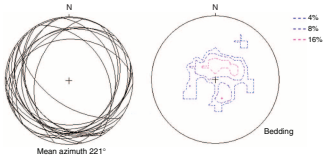

F50. Millimeter-scale normal faults and reversed faults, p. 123.

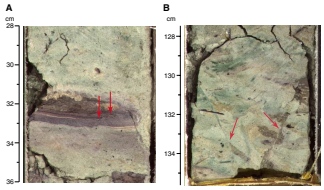

during the emplacement of sills by reactivation of inherited structures. Bedding perpendicular to vertical flattening and horizontal extension indicate progressive subvertical compression and may be related primarily to compaction processes. At Site 1253, the sediments do not show a clear signal that the subhorizontal shortening is related to incipient subduction.

Igneous Units

The igneous units were carefully analyzed for fractures because of their relevance to identifying intervals for the CORK-II experiment and to provide data directly comparable with the FMS data. The only geometrically reliable sediment/igneous contact was recovered in interval 205-1253A-27R-1, 1–6 cm, and it dips 72°. This piece was recovered at the top of the core and may not have been recovered in place. The only other contacts recovered are in core pieces too small to have preserved the true orientation. Internal magmatic contacts were common, especially in the upper part of the deeper igneous unit (Fig. **F52**). These magmatic contacts have been recognized mainly on the basis of mesoscopic observations of grain size and may represent either chilled margins or cumulate textures (see **"Petrology,"** p. 26). Reoriented magmatic contacts dip ~15°–20° to the northeast, mostly opposite to that of the sedimentary bedding (Fig. **F53A**).

The igneous units are commonly cut by veins (Fig. **F52**), either filled with glassy to mineral-rich groundmass (here called magmatic veins) or postemplacement alteration minerals (zeolite, clay, or calcite). The paleomagnetic reorientation of these two vein types reveals that they have the same general trend (Fig. **F53B, F53C**), poles oriented 60° to the north-northwest and 75° to the east-northeast. The good geometric agreement between the two vein systems suggests that the mineralized veins are a further evolution of the magmatic veins as products of alteration. Dilational joints are also frequent (Fig. **F52**); these are usually filled with a film of green minerals (zeolite?) and are rarely present as open fractures. Reoriented joint orientations for all joints (Fig. **F53D**) are similar to those determined in intervals where rocks show high magnetic intensity to allow confident reorientation (Fig. **F53E**). The joints show no strong preferential orientation.

The presence of joints can significantly contribute to the bulk porosity and permeability of the igneous units; their intensity downsection (Fig. **F52**), shows that the number of fractures increases with depth. Furthermore, joint distributions suggest that they are homogeneously distributed from Cores 205-1253A-30R through 36R, whereas in Cores 40R through 43R, comparable to the above interval in terms of recovery, fracture intensity is not constant. Other brittle deformation features include shear zones, represented by en echelon Riedel shears, usually showing reverse displacement. These structures are common in the lower part of the deeper igneous unit (Core 205-1253A-36R and below). In one case, measured conjugate fractures in interval 205-1253A-40R-1, 98–112 cm (Fig. **F54**), allow reconstruction of the principal stress orientation, with σ_1 oriented 246°/60°, at an angle of 40° to 50° to the convergence vector (Fig. **F55**). After reorientation, the plotting of the brittle shear zone's boundaries (Fig. **F56**) shows no clear indications of preferred orientation.

F51. Stereographic plot of reversed faults, p. 124.

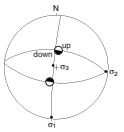

F52. Joints, magmatic and mineralized veins, and contact distribution, p. 125.

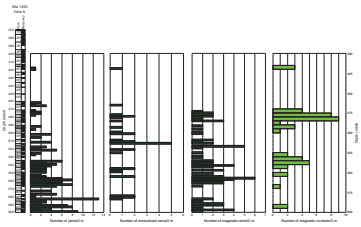

F53. Magmatic contacts, magmatic and mineralized veins, and joints, p. 126.

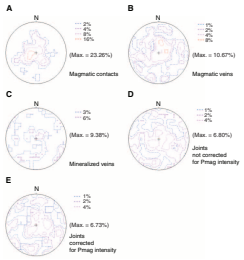

F54. Conjugate brittle shear zones, p. 127.

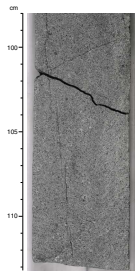

F55. Stereographic plot of a conjugate set of reversed faults, p. 128.

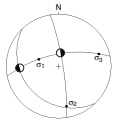

PHYSICAL PROPERTIES

At Site 1253, laboratory measurements were made to provide a downhole profile of physical properties at a reference site seaward of the subduction trench, as well as within igneous units not penetrated during ODP Leg 170. All cores were initially passed through the MST before being split. Gamma ray attenuation (GRA) bulk density, noncontact electrical resistivity (NCR), and volumetric magnetic susceptibility measurements were taken at 2-cm intervals, with measurements averaged from three separate 1-s data acquisitions for all cores. *P*-wave velocity logger measurements were not taken because of the small and variable diameter of RCB cores, which generally leads to poor coupling between the core liner and recovered core. NGR emissions were counted every 10 cm for 20-s intervals above 519.20 mbsf (Core 205-1253A-27R), after which the count time was increased to 60 s to improve data quality within the igneous units. Voids and cracks in hard rock and drilling disturbance in sediment were noted in all cores and degraded the volumetric magnetic susceptibility and GRA bulk density MST measurements. The NCR tool is still in a testing phase (see **"Physical Properties,"** p. 19, in the "Explanatory Notes" chapter). Data collected with the instrument exhibited significant scatter, and measured resistivity values were consistently and unreasonably low for both sediments and hard rock compared with measurements from Leg 170, suggesting a problem with the instrument or its calibration. These data will not be discussed further.

Moisture and density (MAD) samples were selected from undisturbed core at regularly spaced intervals of two per section in sediments (75-cm resolution) between 370–400 and 430–454 mbsf. In igneous rock, pieces were selected from intact core at a frequency of one per section and soaked in seawater for 24 hr prior to sampling for MAD and measurement of *P*-wave velocity and thermal conductivity, to ensure that the samples were fully saturated. Thermal conductivity was measured using the half-space needle probe for soft and indurated sediments and hard rock. After soaking, thermal conductivity was measured on hard rock pieces, which were subsequently sampled for MAD and used for *P*-wave velocity measurement. Measurements of dry volume and wet and dry mass were uploaded to the ODP Janus database and were used to calculate water content, bulk density, grain density, porosity, void ratio, and dry bulk density. *P*-wave velocities were measured at a frequency of one per section on core pieces in the x-direction (cross-core) using the *P*-wave velocity sensor system. In sediments, *P*-wave measurements were taken immediately adjacent to MAD samples. In igneous rock, measurements were made on the same intact piece that was sampled for MAD and thermal conductivity, usually immediately adjacent to the MAD sample location.

Raw and calculated physical property data are available from the Janus database for all MST, MAD, velocity, thermal conductivity, and *P*-wave velocity measurements.

Density and Porosity

Sediment porosities determined using the MAD method generally range from 66% to 77%; bulk densities range from 1.39 to 1.77 g/cm³ and show no trend with depth between 370 and 394 mbsf (Fig. **F57A, F57B**). Porosity values appear to show greater scatter, including some

F56. Stereographic plot of brittle shear zone boundaries, p. 129.

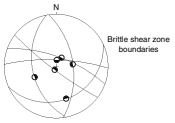

F57. Porosity and bulk density, p. 130.

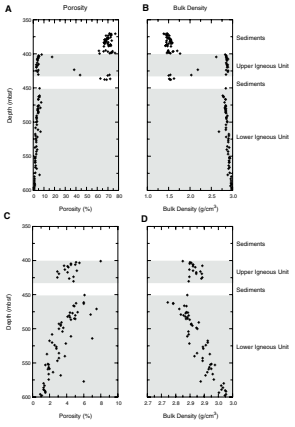

lower values (range from ~62% to 74%) immediately above the upper igneous unit between 394 and 396 mbsf and within sediments between the two igneous units (432–451 mbsf). Data coverage in these intervals is limited by poor recovery and also reflect that obviously baked sediments were not sampled for MAD because of their importance for other analyses. More data would be needed to verify whether these subtle differences in porosity reflect systematic changes in sediment properties. Porosity within the igneous units is significantly lower than that of sediments, ranging from 2% to 8%, and bulk densities are 2.77–2.97 g/cm³. Porosity within the upper igneous unit decreases from 8% near its upper boundary to ~2%–4% at its base (Fig. F57C). Bulk density within the upper igneous unit does not vary systematically with depth and ranges from 2.83 to 2.88 g/cm³. Within the lower igneous unit, porosity decreases systematically with depth, from ~6%–8% near its upper boundary to 1% at its base (Fig. F57C). This decrease in porosity coincides with a systematic increase in bulk density with depth from 2.77 g/cm³ at 451 mbsf to 2.97 g/cm³ at 598 mbsf (Fig. F57D).

GRA densities range from ~1.2 to 1.7 g/cm³ in sediments and from ~2.3 to 2.8 g/cm³ in igneous units (Fig. F58). The GRA densities show considerable scatter, mainly because of varying RCB core diameter and voids and fractures in the cores. In general, there is less scatter in the data from the igneous units because voids were easier to identify for these cores, in which the liner was split before runs, than for sediment samples. The calculated values of GRA densities assume a core diameter of 6.6 cm, whereas RCB cores have a smaller diameter. Therefore, GRA densities were corrected assuming a constant core diameter of 5.6 cm by multiplying the reported bulk densities by a factor of 6.6/5.6. Corrected GRA densities within the upper and lower igneous units follow the same trends as densities and porosities determined using the MAD measurements (Fig. F58).

Grain densities within the sediments, determined from dry mass and volume measurements, range from 2.45 to 2.75 g/cm³ and exhibit significant scatter both above the upper igneous unit and in the zone between the two igneous units (Fig. F59). Grain densities immediately above the upper igneous unit (394–396 mbsf) are 2.75–2.8 g/cm³, corresponding to a zone of slightly lower porosity. Grain densities within the sediments between the two igneous units are also slightly higher than those in the uppermost sediments (370–394 mbsf), ranging from 2.59 to 2.78 g/cm³. These high grain densities may represent recrystallization as a result of intrusion of the upper igneous unit, although denser sampling would be needed to verify this trend. Grain densities within the igneous units exhibit less scatter and are uniformly higher than in the sediments, ranging from 2.85 to 3.0 g/cm³ in the upper igneous unit and 2.88–3.01 g/cm³ in the lower unit (Fig. F59). Grain densities are uniform throughout the upper igneous unit, whereas in the lower unit there is a systematic increase in grain density with depth from 2.88–2.96 g/cm³ near its top to 2.98–3.01 g/cm³ at its base. This trend, combined with decreasing porosity with depth in this interval, results in a trend of increasing bulk density within the lower igneous unit.

Thermal Conductivity

On the first three cores (370–385 mbsf), thermal conductivity was determined using the full-space needle probe method. Erroneous values of thermal conductivity were measured when the liner was not completely

F58. Corrected GRA bulk density, p. 131.

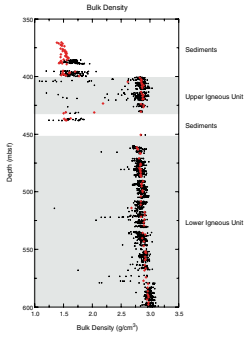

F59. Grain density, p. 132.

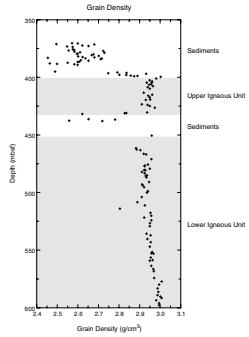

filled with sediments and the needle did not fully penetrate in the sediments or if the insertion of the needle produced cracks in the sediments that could not be seen through the core liner. Moreover, with increasing depth it became increasingly difficult to insert the needle into the stiff sediments. The half-space method was used for all cores below 385 mbsf to ensure consistency with half-space measurements made in the igneous units. The half-space method was also used to remeasure all points in Cores 205-1253A-1R through 3R for this reason.

Comparison between full-space and half-space measurements shows that the half-space method systematically yields higher thermal conductivity values than the full-space method. The deviations range from 0.1 to 0.2 W/(m·K). This could be explained by air in the liner or by cracks induced by penetration of the needle, both of which would produce a lower conductivity reading than that of the undisturbed sediment. In Cores 205-1253A-1R and 2R, thermal conductivities are ~0.9–1.0 W/(m·K) (Fig. F60). Core 205-1253A-3R was too disturbed to measure with the half-space method, so the full-space method value is shown in the plot at 385 mbsf. The thermal conductivity of 0.87 W/(m·K) measured in this core would probably be ~0.1–0.2 W/(m·K) higher if determined by the half-space method.

The data clearly show a distinction between the sedimentary unit and the igneous units (Fig. F60). The sediments close to the contact with the upper igneous unit at ~400 mbsf have higher conductivity than those above this zone (values up to 1.45 W/[m·K]). Within the upper igneous unit (401–432 mbsf), thermal conductivities range from 1.68 to 1.95 W/(m·K). Because the sediments between the two igneous units (432–451 mbsf) were too disturbed and the core pieces too small, no measurements were made in this section.

Within the lower igneous unit (451–600 mbsf), a slight trend of increasing thermal conductivity with depth is observed but starts with a lower value than within the upper igneous unit. Thermal conductivities increase from 1.71–1.87 W/(m·K), near the top of this unit, to 1.83–1.93 W/(m·K) at its base. This trend correlates with the observed increases in density and *P*-wave velocity and the decrease in porosity with depth as determined by MST and MAD measurements. Because the conductivity of the grains is higher than that of the pore fluid, a decrease in porosity leads to an increase in thermal conductivity.

F60. Thermal conductivity, p. 133.

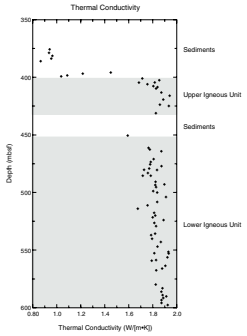

Acoustic Velocity

P-wave velocities in the uppermost sediments, from 370 to 394 mbsf, range from 1549 to 1577 m/s under laboratory temperatures and pressures (Fig. F61A). A small number (five) of velocities measured within sediments immediately above the upper igneous unit (394–397 mbsf) and between the two igneous units (432–451 mbsf) range from 1603 to 1914 m/s. These higher velocities correspond to zones of slightly lower porosity and higher grain density. Velocities are relatively uniform throughout the upper igneous unit, ranging from 4728 to 5345 m/s. Within the lower igneous unit, velocities increase with depth from 4552–5207 m/s near its top to 5438–5677 m/s at its base (Fig. F61A, F61B). There is a strong correlation between the decrease in porosity and the increase in velocity within this unit (Fig. F61C).

F61. *P*-wave velocity and porosity, p. 134.

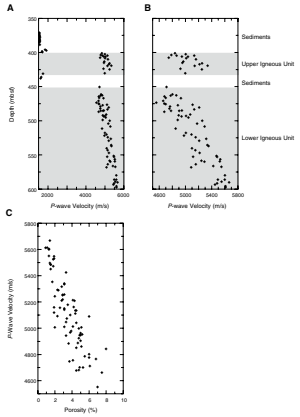

Natural Gamma Radiation

NGR results are presented in counts per second (cps) (Fig. F62). The background, produced by Compton scattering, photoelectric absorption, and pair production, was measured at the beginning and during MST runs for each core section (12.95 cps) and subtracted from the measured gamma ray values to obtain corrected counts. In addition, the NGR data were filtered after acquisition to improve data quality by discarding measurements obtained from hard rock fragments smaller than the instrument aperture of 12 cm. The filtering was conducted visually, using digital core images and manually filtering the data to exclude any NGR measurement taken from a core piece with <6 cm of unfractured material in either direction from the measurement point. The Janus database was not edited and contains all measurements.

The filtered NGR data show a clear distinction between the upper igneous unit (401–432 mbsf) and upper and lower parts of the lower igneous unit (451–600 mbsf) (Fig. F62). The upper unit is characterized by generally higher NGR emissions (7 cps) than the lower unit (1–3 cps). Within the lower unit, NGR values are systematically lower from 451 to 512 mbsf (averaging 1–2 cps, with local excursions to 5–6 cps) than from 512 to 600 mbsf (averaging 3–4 cps, with excursions to >10 cps). Increased NGR emissions typically reflect higher potassium, uranium, or thorium concentrations, suggesting that the upper and lower igneous units are chemically distinct, as are the upper 61 m and lower 88 m of the lower igneous unit.

F62. Corrected MST NGR measurements, p. 135.

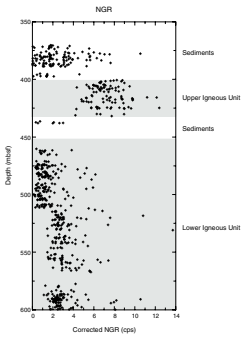

Magnetic Susceptibility

Volumetric magnetic susceptibility measured with the MST shows a clear difference between sediments and the igneous units (Fig. F63). Within the igneous units, values are widely scattered, due at least in part to the variable diameter of RCB cores. There are no unequivocal trends in magnetic susceptibility within the sediments or the igneous units. Below 510 mbsf, magnetic susceptibility is generally slightly higher than above this depth, although the scatter throughout the igneous units is significant. This change in susceptibility occurs at the same depth as a clear shift in NGR. A second shift from high values of magnetic susceptibility to generally lower values occurs at 567 mbsf. This shift does not correspond to changes in any other measured physical properties.

F63. Volumetric magnetic susceptibility, p. 136.

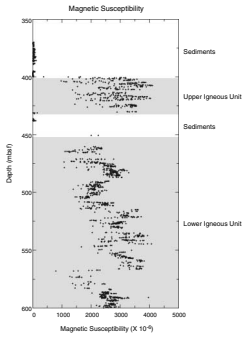

Summary and Discussion

Variations in physical properties correlate with major lithologic changes between sediments and igneous units. A limited number of measurements indicate decreased porosity and increased grain density and *P*-wave velocity within sediments immediately above and between the igneous units; these differences may reflect alteration (recrystallization) and porosity reduction caused by emplacement of the igneous units.

Perhaps the most striking trends in the physical property data are (1) the systematic increase in velocity, bulk density, and grain density and decrease in porosity within the lower igneous unit and (2) the clear shift in NGR emissions at 512 mbsf within the lower igneous unit. The cause of the trends in porosity, density, grain density, and velocity with depth in the lower igneous unit is unclear. The differences in NGR emis-

sions suggest chemical differences between and within the igneous units, which may reflect varying degrees of alteration within igneous units that were initially chemically similar. The fact that the trends in porosity, density, and velocity are not correlated with the NGR trend suggests that the processes that control porosity, density, and *P*-wave velocity are separate from the chemical or lithologic processes that affect the NGR emissions.

PALEOMAGNETISM

Paleomagnetic and rock magnetic measurements at Site 1253 were aimed at estimating magnetostratigraphy of sediments, age, and internal structure of the igneous units. After measuring the NRM, all sections of the archive half of the core were demagnetized using alternating-field (AF) magnetization up to 40 mT in increments of 5 mT at 5-cm intervals. Additionally, the maximum demagnetization level was changed to 50 mT in two intervals: 400.50–480.71 (Sections 205-1253A-5R-1 through 17R-4) and 542.79–543.49 mbsf (Section 205-1253A-31R-4) in order to remove magnetic overprints.

One to three oriented discrete samples were routinely collected from each section of the working half of the core primarily for analysis for shore-based anisotropy of magnetic susceptibility and rock magnetic study. All discrete samples were used to constrain interpretations of the magnetic record of the archive long core by providing additional measurements of polarity and basic magnetic characterization. The discrete samples were demagnetized up to 80 mT in 5-mT increments to permit principal component analysis. The rock magnetic investigations on the ship consist of progressive acquisitions of isothermal remanent magnetization (IRM) and stepwise thermal demagnetization on discrete samples. Magnetic stability analyses following the Lowrie-Fuller test (Lowrie and Fuller, 1971) were also conducted to investigate the magnetic domain state of the discrete samples.

Paleomagnetism

Sediments

The majority of NRM inclinations for archive sections show steep angles of ~30°–60°N. Continuously high NRM intensities are also observed, whereas rapid changes in magnetic susceptibility are measured by MST core logger (see **"Physical Properties,"** p. 37). In most of the sections, these high magnetic intensities were easily demagnetized in the earliest AF demagnetization steps at ~10 mT. This suggests that the steep NRM inclinations and constantly high magnetic intensities have been caused by a strong drilling-induced magnetic overprint. The drilling-induced magnetization generally shows steep angles of magnetic inclination and relatively high magnetic intensity that are thought to be a weak IRM (Musgrave et al., 1993). Changes in magnetic inclination and intensity observed after the AF demagnetization suggest the magnetic overprints were successfully removed in weak AF demagnetization levels. Changes in magnetic inclinations observed from pelagic sediments provide information about magnetic polarity changes and are used for the interpretation of sedimentary age after correlation with the standard magnetic polarity timescale of Berggren et al. (1995a, 1995b)

and with previous paleomagnetic results at Site 1039 (Kimura, Silver, Blum, et al., 1997).

Inclination changes of archive halves in the sedimentary sections after AF demagnetization of 40 mT are relatively unclear, although most inclinations are indicating normal polarity (Fig. F64). Comparison between the observed inclinations from the archive sections and discrete samples indicate that postdepositional remanent magnetization (pDRM) of mostly hemipelagic sediments above the gabbro represent normal polarity. However, a few intervals and discrete samples also indicate at least two reversed polarities are possibly identified at ~375–376 (Core 205-1253A-2R) and ~388–390 mbsf (Sections 205-1253A-3R-2 through 3R-3). The paleomagnetic study at Hole 1039B interpreted two positive inclinations below 370 mbsf as magnetic Subchron C5Bn.2n (15.034–15.155 Ma) and Subchron C5Cn.1n (16.014–16.239 Ma), respectively. Based on these previous identifications, a positive polarity at ~370–374 mbsf (Sections 205-1253A-1R-1 through 2R-1) may be interpreted as Subchron C5Bn.2n. Then, a polarity boundary at ~388 mbsf (Section 205-1253A-3R-3) might be identified as the appearance of Subchron C5Cn (16.726 Ma).

Magnetic inclination of sediments from 430 to ~450 mbsf show negative polarity. Only two discrete samples indicate positive polarity (Fig. F64); however, identification of magnetic chrons (or subchrons) was unsuccessful because of poor resolution of the paleomagnetic data.

F64. Paleomagnetic results, Hole 1253A, p. 137.

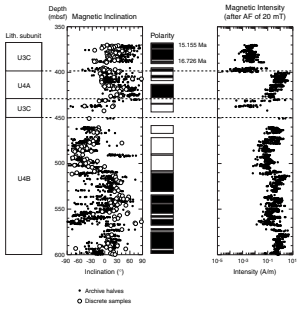

Gabbro

Demagnetization of the gabbro intrusions, conducted only within intact portions of core, revealed that these intrusions have high variations of magnetic inclinations with high magnetic intensity (Figs. F64, F65). After AF demagnetization to 40 mT, some changes in magnetic inclinations were observed; however, the high NRM intensity in most of the gabbro is easily demagnetized at weak AF demagnetization levels (Fig. F65). The ratio of magnetic intensity after the AF demagnetization (20 mT) to NRM intensity also suggests unstable magnetization of the gabbro. The gabbros' magnetic coercivity is very weak, whereas they show high NRM intensity. Three peaks in the intensity ratio, indicating relatively high coercivity magnetization, corresponds with high magnetic intensities after AF demagnetization. Probably, this unstable remanence of magnetization strongly depends on the grain size of magnetic minerals after AF demagnetization. Rock magnetic tests carried on discrete samples revealed most samples contain multidomain (MD) magnetite in which the grain sizes are large enough (>100 µm) to cause unstable magnetic behavior during the demagnetization (see below). Fortunately, some intervals of the intrusions have relatively stable magnetization behavior during demagnetization that coincides with four zones of high magnetic intensity (Fig. F65). The top of the first high intensity interval is observed at ~400 mbsf (Section 205-1253A-4R-CC) in the uppermost gabbro intrusion; the intensity decreases with depth in the intrusion. The lower igneous unit has three zones of high magnetic intensity at ~462 mbsf (Core 205-1253A-14R) to 478.4 mbsf (Section 17R-2, 130 cm), 513.20 mbsf (Section 25R-1, 20 cm) to ~523 mbsf (Section 27R-3), and ~572 mbsf (Section 38R-1) to ~593 mbsf (Section 4R-3).

Although most of the igneous section exhibits unstable magnetizations, magnetic inclinations between the archive sections and discrete samples show similar trends that indicate the gabbros may retain initial magnetizations that represent different age polarities (Fig. F64). Identi-

F65. NRM after 20-mT AF demagnetization, p. 138.

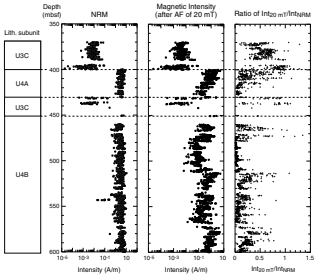

fied normal chrons (or subchrons) are shown in Table T7. Because discrete samples show negative inclination, positive inclinations of the archive-half core section at 491.38–492.80 mbsf (Section 205-1253A-20R-2) are not identified as normal polarity. The top of the high-intensity zone at 513.65 mbsf (Section 205-1253A-25R-1) nearly coincides with the start of a long normal polarity at 513.20 mbsf (Section 25R-1, 20 cm). Both polarity and magnetic intensity changes may indicate age boundaries within the igneous units. The polarity boundaries and the changes in the magnetic intensity ratio were compared with lithostratigraphic observations and identification of mineralogy in these units (see "Petrology," p. 26).

T7. Magnetic chrons in upper and lower igneous units, p. 176.

Rock Magnetism

Rock magnetic tests were conducted to investigate stability of magnetization and to identify magnetic minerals in the sediments and magmatic rocks. All samples for the tests were collected from minicore and cube samples taken from working-half core sections.

Saturation Isothermal Remanent Magnetization and Lowrie's Tests of Hemipelagic Sediments

For investigation of saturation isothermal remanent magnetization (SIRM), seven small samples (1 cm^3) were collected from cube samples and their IRM was measured after acquisition of an isothermal magnetization applied from 20 to 1200 mT. After 24 steps of IRM measurement, thermal demagnetization of multicomponent IRM (Lowrie, 1990) was used as the primary means of identifying magnetic minerals. For these experiments, orthogonal isothermal magnetizations of 100, 300, and 1200 mT were applied on +x-, +y-, and +z-axes of the sample, respectively. The samples were then demagnetized using 16 thermal steps from 50° to 650°C (Fig. F66). The IRM intensity curves for most of the samples smoothly increase up to 300 mT then saturate at ~600 mT. Thermal demagnetization curves indicate there are at least three unblocking temperatures (T_{ub}). The magnetic intensities suddenly decrease at 170°C and decay rapidly up to ~320°C. These two T_{ub} indicate goethite ($T_{ub} \approx 150$°C) and pyrrhotite or greigite ($T_{ub} \approx 320$°C) and are present in the hemipelagic sediments. The rapid decrease of magnetic intensity on the +x-axis up to 320°C suggests that pyrrhotite (or greigite) dominates rather than goethite. Therefore, gentle intensity curves from 300 to 600 mT on the SIRM are believed to reflect the presence of pyrrhotite. A third T_{ub} is identified at ~550°C, and all intensity components smoothly decay from 320°C to 550°C and indicate that the pDRM carrier might be magnetite (T_{ub} = 575°C), and its magnetization is very stable.

F66. SIRM and Lowrie's tests, p. 139.

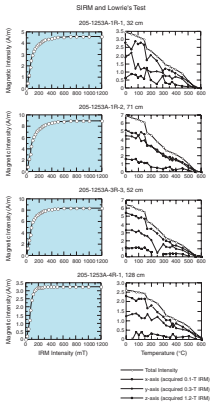

Lowrie-Fuller Tests for Hemipelagic Sediments and Igneous Rocks

The Lowrie-Fuller test (Lowrie and Fuller, 1971) was performed on seven hemipelagic sediments and seven gabbro samples. To interpret these data in terms of magnetic domain state, the relative shapes of the anhysteretic remanent magnetization (ARM) and the SIRM demagnetization curves were combined on a plot (Fig. F67A). The samples were progressively demagnetized up to 80 mT in increments of 5 mT after ac-

F67. Magnetic domain state above 400 mbsf, p. 140.

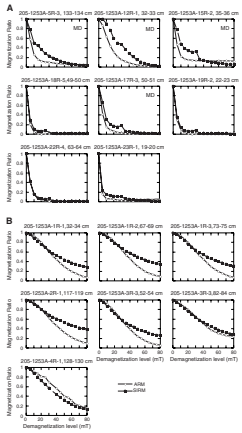

quisition of the ARM, represented as a weak-field thermal remanent magnetization (TRM), and produced by demagnetizing the samples in a 150-mT AF in the presence of a 0.05-mT direct-current field. The samples then acquired a laboratory SIRM in a 1-T magnetic field that represents TRM. After the acquisition, the samples were progressively demagnetized up to 80 mT in 5-mT increments. It should be emphasized that any interpretation relies on the assumption that the samples contain a simple magnetite or titanomagnetite mineralogy. Given this assumption, the ARM demagnetization curve decreases rapidly relative to SIRM for a few samples of the gabbro samples, suggesting the presence of MD grains. For most of the samples, the two curves are similar and clear constraints on magnetic domain state are not possible at this time.

In the hemipelagic sediments, the resistance of the ARM to early steps of AF demagnetization relative to SIRM suggests the presence of single- to pseudosingle-domain grains (Fig. F67B).

Demagnetization Analyses of Discrete Samples

For detailed analyses of the paleomagnetic and rock magnetic investigations, all discrete samples were demagnetized up to 80 mT in increments of 5 mT. In the hemipelagic sediments, demagnetization and magnetic component curves for both the inclination and the declination for most samples smoothly decrease toward the origin of the Zijderveld diagram (e.g., Sample 205-1253A-2R-2, 12–14 cm) (Fig. F68). However, a few samples show odd behavior during AF demagnetization (e.g., Sample 205-1253A-2R-6, 91–93 cm). The demagnetization curves are similar to the curve of magnetic iron sulfides, such as greigite, in which magnetization trends generally toward the opposite direction to the AF and causes an increase in the magnetic intensity during high AF demagnetization. However, decay of the magnetic intensity up to 80 mT emphasizes there are not serious effects of magnetic noise from the iron sulfides on the demagnetization of the samples. These curves may also reflect artificial disturbances of sediments during drilling so that these results should be excluded from the paleomagnetic study. Pervasive and severe drilling-induced disturbance on the sediments was observed as scattered plots of demagnetization steps on the Zijderveld diagram (e.g., Sample 205-1253A-2R-1, 15–17 cm) (Fig. F68).

In igneous samples, demagnetization curves of samples taken from working-half sections show relatively high magnetic intensity. These intensities resist weak AF demagnetization levels (Fig. F65) but smoothly decrease with increasing demagnetization level (e.g., Samples 205-1253A-5R-3, 133–144 cm, and 12R-1, 32–33 cm) (Fig. F68). Magnetic overprints in these samples are successfully removed at 20 mT. Additionally, the rock magnetic tests revealed their magnetic domain state to be MD (Fig. F67). Other discrete samples show a rapid decrease in magnetization in early AF demagnetization steps (e.g., Sample 205-1253A-22R-4, 63–64 cm) (Fig. F68). Although the magnetic behavior should be tested using other rock magnetic methods, this rapid decrease in magnetization of the igneous units (Fig. F65) indicates that much coarser magnetic grains are dominant in rocks than intrusions showing stable and high-coercivity magnetization.

Paleolatitude Analysis

The magnetic inclinations observed from the discrete samples are also used for estimations of paleolatitudes for the hemipelagic sedi-

F68. Zijderveld diagrams, p. 142.

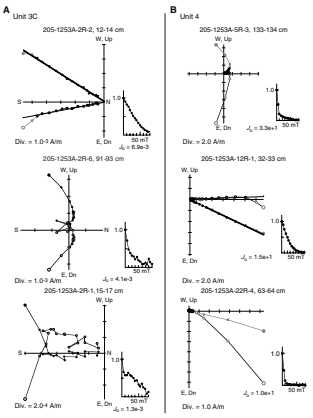

ments and the igneous units. For this analysis, only inclinations of samples that had maximum angular deviation values <4° were used. Additionally, the calculations used only positive inclinations interpreted as normal magnetized samples in the Northern Hemisphere. The paleolatitude for each unit was calculated from the geocentric dipole relationship:

$$\tan(I) = 2 \tan(\text{latitude}),$$

where I is the average of the inclination groups. An angle deviation of the paleolatitude was calculated by Fisher's deviation method (Fisher, 1953). The averaged inclinations of each lithologic unit are shown in Figure F69. Although these results show high standard deviations, the estimated paleolatitude of hemipelagic sediment above the gabbro sill is 8.6°N (upper confidence limit = +11.6° and lower confidence limit = –5.6°) and that of the upper gabbro and lower igneous unit are estimated to be 13.4°N (+24.6° and –1.0°) and 11.0°N (+14.3° and –7.8°), respectively. These values are close to the current latitude at this site, ~9°N.

F69. Average inclinations, p. 143.

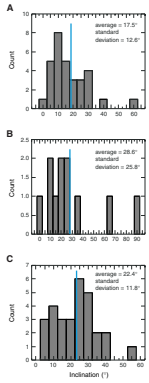

INORGANIC GEOCHEMISTRY

Long-term objectives and postcruise science for Leg 205 include documenting the chemistry of pore fluids and associated sediments at Site 1253 in order to (1) determine the distribution of key tracer elements and isotope ratios between pore fluids and the various sediment types, (2) quantify the fluxes of those key elements and isotopes into the subduction zone, (3) utilize these data as a starting point for establishing geochemical and material mass balances (including sediment underplating) through the subduction zone, and (4) better constrain the fluid flow system in the upper oceanic section inferred from Leg 170 results (Kimura, Silver, Blum, et al., 1997).

Shortly after coring, pore waters were squeezed from whole rounds (14–20 cm long) and analyzed for salinity, pH, alkalinity, Cl, SO_4, Ca, Mg, K, Sr, Ba, Mn, Li, B, Si, and NH_4 concentrations. Sodium was determined from the above data by charge balance calculations.

In conjunction with sediment lithology and bulk chemistry, pore water chemistry can often provide a very sensitive picture of in situ diagenetic reactions, the nature of diffusion of chemical species within the sediment column, and advective fluid flow. This is possible because the low concentrations of many elements in the pore fluids mean that changes too small to affect the sediment chemistry can produce significant changes in the fluid composition. This section first documents variations in pore water chemistry then discusses their implications for diagenesis. It concludes by examining the evidence from shipboard data for the character of the advective fluid with approximately seawater composition, derived from depth, presumably the upper oceanic basement.

Methods

Calcium and magnesium concentrations were determined by routine titrimetric methods, as well as by ICP-AES. Silica concentrations were determined both by ICP-AES and spectrophotometry. Comparison of the accuracy and precision of the analytical methods for determining

Ca, Mg, and Si concentrations are reported in "Inorganic Geochemistry," p. 24, in the "Explanatory Notes" chapter. Sediment concentrations of Rb, Cs, Ni, and Ce could not be determined by the shipboard ICP-AES. Pore water Rb concentrations were below the ICP-AES detection limit in all samples. One pore water Rb sample, analyzed at 1:5 dilution, just reached the 50-ppm detection limit of the ICP-AES. The reasons for this high level are not understood. Subsequent samples were not analyzed for Rb.

Pore Water Results

Chloride and Salinity

Chloride concentrations were approximately equal to that of seawater, except for a slightly lower concentration (1.5% seawater dilution) encountered just above the gabbroic sill at 399 mbsf. The Cl concentration was slightly higher (0.6% above seawater concentration) just below the sill at 432 mbsf. Note that the Cl concentration profile above the sill is similar to the corresponding Cl concentration profile observed at Site 1039 (Fig. F70). The salinity is approximately that of seawater throughout the sediment cored at Site 1253 (Table T8).

Sodium and Potassium

Sodium concentrations and the Na/Cl ratios in Figure F70 are slightly higher than those in seawater and increase toward and below the sill, even though Na concentrations in the sediment are fairly constant with depth. The tephras identified just above and below the sill are an exception to this pattern because of their different original composition. Potassium concentrations decrease sharply immediately above the gabbro sill, which is accompanied by a very sharp decrease in Si concentrations. Note that K concentrations approach seawater value below the sill, forming a trend subparallel to that observed at Site 1039 but at greater depth (Fig. F70).

Sulfate, Alkalinity, and Ammonium

The SO_4 profile at Site 1253 is almost identical to the corresponding profile observed at Site 1039 (Fig. F71). Sulfate concentrations are slightly less than that of seawater in the basal sediment section, in contrast to values <27 mM measured higher in the section (between 330 and 370 mbsf) during Leg 170 (Kimura, Silver, Blum, et al., 1997). The high SO_4 concentrations approaching seawater value indicate that the pore waters are not completely reduced.

Alkalinity is slightly lower than seawater concentration within the sediments above the lower igneous unit and remains fairly constant with depth (2.00 to 2.06 mM). The NH_4 concentrations above the gabbro sill decrease with depth, varying between 82.75 and 49 µM. Below the sill, NH_4 concentrations are lower and also decrease with depth from 58 µM at 432.1 mbsf to 47 µM at 437.0 mbsf (Fig. F71B).

Calcium, Magnesium, Strontium, and Barium

Calcium, Mg, Mg/Ca, and Sr decrease with depth toward seawater values with similar gradients to those observed at Site 1039 (Fig. F72), although they are shifted to deeper levels. Immediately below the gab-

F70. Cl, Na, Na/Cl, and K profiles, p. 144.

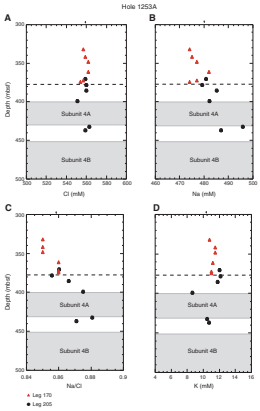

T8. Pore water major constituents, p. 177.

F71. SO_4, NH_4, Fe, and Mn profiles, p. 145.

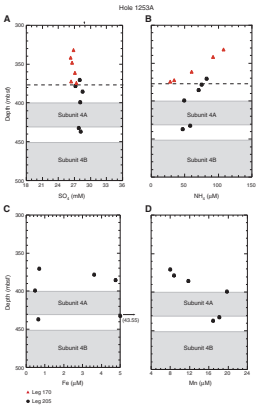

F72. Ca, Mg, Mg/Ca, and Sr profiles, p. 146.

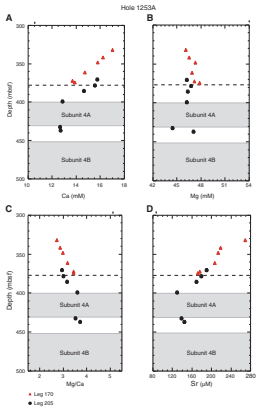

bro sill, Ca and Sr concentrations remain nearly constant rather than continuing to decrease. The Mg profile in pore waters taken from the basal sediments is similar to that observed at Site 1039 (Fig. F72B), although Mg concentrations are locally lower below the sill than above it. Barium concentrations decrease with depth above the sill; however, they are anomalously high considering the seawater-like sulfate concentrations within the sediment above and below the gabbro sill (Fig. F73A). Typically, at these sulfate concentrations, $BaSO_4$ solubility would predict Ba concentrations in the 100- to 200-nM range; however, Ba concentrations are as high as 5 µM. In addition, where pore water Ba concentrations are highest, sediment Ba concentrations are the lowest. The interstitial water (IW) sample immediately above the sill has a high Ba concentration (4.84 µM, relative to 1.04 µM at shallower levels). Below the sill, Ba concentrations decrease with depth.

F73. Ba, H_4SiO_4, Li, and B profiles, p. 147.

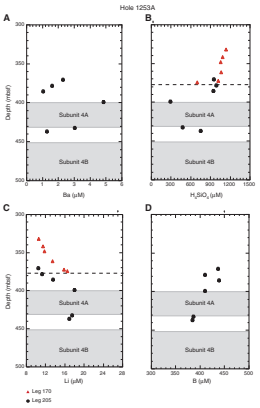

T9. Pore water minor constituents, p. 178.

Silica

Silica concentrations in the pore waters are similar to those observed at Site 1039 and decrease with depth, despite the fact that diatoms are abundant in the basal sediment section (Fig. F73B; Table T9). There is a very sharp decrease in Si concentration in the sample above the sill (changing from 964 to 297 µM over 14 m), most probably reflecting the diagenesis of amorphous Si to opal-CT and/or quartz as indicated by the chert layers described in "Lithostratigraphy," p. 19. The sample just below the gabbro sill also has a lower silica concentration but higher than just above the sill.

Iron and Manganese

Iron and manganese concentrations are relatively low (Fig. F71C, F71D; Table T9). Concentrations generally increase with depth in the basal sediment section, most likely from dissolution of Fe-Mn oxyhydroxide hydrothermal particles, which slightly color these sediments. Iron concentrations, however, sharply decrease at the upper sill contact and between the sill and Subunit 4B. Iron concentrations reach a maximum dissolved value of 43.55 µM just below the sill, and Mn reaches a maximum value of 23.27 µM immediately above it.

Lithium and Boron

The Li profile at Site 1253 (Fig. F73C; Table T9) shows increasing concentrations with depth. The gradient is similar to that from Site 1039 but shifted downward by 40 m, which may reflect the deeper level of the gabbro sill at this site. Below the sill, Li concentrations are comparable to those just above it. Although B was expected to behave similarly to Li, values appear to decrease slightly.

Discussion

The lithologic variations observed in the cores (see "Lithostratigraphy," p. 19) control the in situ reactions responsible for the gradients and offsets in the pore fluid profiles for many, although not all, elements. Several features in the pore water chemistry suggest a role for ash alteration and associated authigenic mineral formation, primarily zeolites, just above and below the sill. Higher Na and much lower K and Si are observed just above the sill. This is consistent with the uptake of

these elements by the authigenic formation of zeolites and quartz, which are also observed lithologically. Chloride concentrations are slightly lower (1.5%) relative to seawater, which may reflect opal-A or clay dehydration reactions immediately above the sill. The implied liberation of Na, Ca, and Sr to the fluids suggests ash alteration and carbonate recrystallization. Just below the sill, the low Mg concentrations in the fluid and the constant Li gradient are consistent with the authigenic formation of more Mg-rich clay minerals associated with ash alteration. Also noted in the section is a systematic decrease in NH_4, which may reflect decreasing organic matter content downsection.

The clear overall gradients with depth noted for Ca, Sr, SO_4, Si, and Li are also striking. The gradients parallel those measured during and after Leg 170 (Kimura, Silver, Blum, et al., 1997) but are shifted deeper by ~40 m, thus maintaining the same depth relationship to the top of the sill. The gradients trend toward values typical of modern seawater, and element systematics are similar to those associated with the $^{87}Sr/^{86}Sr$ variations observed in Leg 170 samples and discussed in **"Margin Hydrology,"** p. 11, in the "Leg 205 Summary" chapter. These gradients supported in the basal sediment pore waters suggest communication with an advective flow system of approximately seawater composition at greater depth, perhaps in the upper basement. Such a flow regime would mine heat from the plate and thus may be responsible for the extremely low geothermal gradient at this site.

ORGANIC GEOCHEMISTRY

Gas Results

Volatile Hydrocarbons

Hydrocarbon gases in the cores from Hole 1253A were analyzed by the headspace technique (see **"Organic Geochemistry,"** p. 26, in the "Explanatory Notes" chapter). This was done as part of the shipboard safety and pollution prevention monitoring program. The results are summarized in Table **T10.** Hydrocarbon concentrations do not exceed the background values of ~3 parts per million by volume (ppmv) throughout all of the sedimentary sequences. This is in agreement with the measurements of the cores from Site 1039 during Leg 170 (Kimura, Silver, Blum, et al., 1997). As an example, the methane concentration depth profiles from Sites 1039 (Leg 170) and 1253 (Leg 205) are shown in Figure **F74.** Correspondingly, sulfate concentrations are high and close to the seawater value in the respective sediment strata (Table **T8;** Fig. **F71**). Hence, the strong reducing conditions needed for bacterial methane production are not achieved in the sediments of the incoming oceanic plate at Sites 1039 and 1253.

Sediment and Igneous Rock Results

Inorganic Carbon, Organic Carbon, and Total Sulfur

The depth distributions of inorganic carbon (represented as calcium carbonate), organic carbon, nitrogen, and sulfur in the solid phase from Hole 1253A are reported in Table **T11.** The combined data from Sites 1039 and 1253 are plotted for $CaCO_3$, total organic carbon (TOC), and total sulfur (TS) vs. depth in Figure **F75.**

T10. Headspace gas composition, p. 179.

F74. Headspace gas analyses, p. 148.

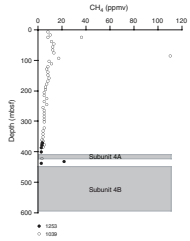

T11. $CaCO_3$, TC, TOC, total nitrogen, and TS, p. 180.

F75. TOC, $CaCO_3$, and S profiles, p. 149.

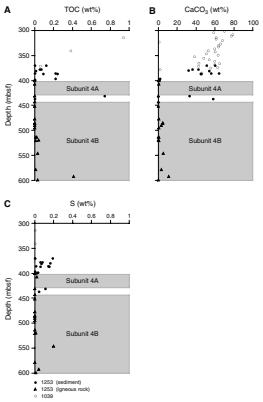

The determination of the TOC content is largely biased because of the different amounts of total carbon (TC) and accuracies of the carbon-nitrogen-sulfur (CNS) technique and the carbonate titration. At high $CaCO_3$ contents (>10 wt%) and low TOC concentrations (close to the detection limit of the CNS element analyzer) (see **"Organic Geochemistry,"** p. 26, in the "Explanatory Notes" chapter), the TOC values only reflect the noise in the TC measurements of the CNS technique. Hence, small differences in TC with respect to $CaCO_3$ values easily lead to even "negative" TOC concentrations. Thus, the TOC values measured at this site and its derived information (TOC/total nitrogen ratio) are considered unreliable. From these findings it can only be estimated that the TOC content of the sediments is very low—about or below the detection limit of the method (i.e., 0.3 wt%, a typical value for pelagic, carbonate-rich sediments). This is consistent with results in Unit U3 of Leg 170, Site 1039 (Kimura, Silver, Blum, et al., 1997). As expected, no significant organic matter could be observed in the igneous rock (Fig. **F75;** Table **T11**).

The carbonate content follows the general trend of Site 1039 and further decreases to ~45 wt% at 385 mbsf. Immediately above the sill (400 mbsf), $CaCO_3$ is almost absent (<2 wt%), corresponding to a more lithified, clay-dominated layer where Si increases and K and $Si(OH)_4$ show changes in the pore water (see **"Inorganic Geochemistry,"** p. 45). The sediment samples analyzed between the two igneous units (431–442 mbsf) are again enriched in $CaCO_3$ (40–60 wt%) (Fig. **F75**). The two igneous rock sections show no observable calcareous alteration with contact of the overlying and enclosed sediment layers (Table **T11**). Measurements of the alteration material in veins and voids yields carbonate contents up to 10 wt%. These values (and the other concentrations reported in Table **T11**) represent minimum concentrations because they are diluted by the surrounding igneous material.

TS concentrations below 370 mbsf at Site 1253 are up to 0.2 wt% and decrease to zero directly above the sill. The sediment layer between the sill and the lower igneous section shows values up to 0.1 wt%, whereas the igneous rock does not show significant amounts of sulfur, except for one vein filling with 0.2 wt% (Section 205-1253A-32R-3 [Piece 3A]) (Table **T11**). The sulfur minerals are most likely pyrite and chalcopyrite, which were macroscopically observed in Section 205-1253A-15R-3 (Piece 7B) (not analyzed aboard ship).

MICROBIOLOGY

Microbiological sampling of Site 1253 covered the carbonate sediment intervals (370.0–400.5 and ~430–442.0 mbsf) and the more altered lower igneous section, Subunit 4B (544.4–598.7 mbsf). For sediments, 5-cm-long whole rounds were removed from Cores 205-1253A-2R, 3R, 4R, 10R, and 11R adjacent to IW whole rounds and processed in the microbiology laboratory. Samples from the lower Subunit 4B in the vicinity of filled veins or fractures were obtained from Cores 205-1253A-32R through 34R, 36R through 39R, and 41R through 43R. One piece of igneous rock was taken from each core and transferred to the anaerobic chamber in the microbiology laboratory to break off a ~40-cm^3 whole round, using sterile techniques at all times. Digital photographs were taken prior to and after the initial breaking of the core (Figs. **F76, F77**). The unused portion was returned to the core liner, and

F76. Rock image used before breaking, p. 150.

F77. Image of sample after breaking, p. 151.

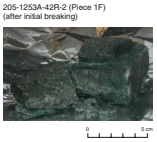

the sample was subdivided for multiple analyses (see "Microbiology," p. 28, in the "Explanatory Notes" chapter).

Contamination Tests

Perfluorocarbon Tracer

The perfluorocarbon tracer (PFT) was run continuously during coring, with a target concentration of 1 ppm in the drilling fluid, as developed by Smith et al. (2000). The Hewlett-Packard 8059 gas chromatograph designated for PFT quantification was calibrated for the range of 4.4×10^{-15} to 4.4×10^{-7} g PFT. The 10^{-9} dilution calibration standard sets the detection limit for PFT at 0.045 µL. Catwalk sampling for PFT levels allowed rapid encapsulation of sediment plugs, and PFT measurement proceeded as detailed in "Microbiology," p. 28, in the "Explanatory Notes" chapter. Analyses showed arrival of PFT along the length of the cores, with variable amounts of intrusion, as anticipated with RCB coring methods. Fluid intrusion was not consistent down the cored section. Drilling fluid intrusion of 0.05–0.62 µL PFT/g sediment was observed at the innermost part of the core for more lithified intervals (Cores 205-1253A-2R through 4R), whereas less indurated samples, Cores 10R and 11R, showed intrusion at the innermost core of 2.6 and 105 µL PFT/g of sediment, respectively (Table T12).

T12. Seawater contamination in sediment cores, p. 181.

The PFT contamination results for the sediment sections highlight three major issues necessary for microbiological investigations of such deep-sea sediments. First, cell counting of background drilling fluid samples is necessary to constrain the impact, in terms of estimated cell numbers, because of fluid intrusion in the range of 0.05 to 105 µL PFT/g of sediment calculated from PFT data. Second, for tracer sampling in all future assays, intact whole-round samples must be used and sampled in the interior. Third, some contamination penetrates even the interior samples with RCB coring of nonindurated sediments.

PFT delivery was confirmed in all of the igneous Subunit 4B cores. Swabs of the inner core liner during catwalk sampling showed PFT concentrations significantly above the detection limit of 0.045 µL. The swabs are used to determine the concentration of PFT on the outside of the gabbro core.

Given these detection limits, the results of PFT samples taken from the inside of the gabbro core indicate a fair amount of drilling fluid intrusion, ranging from 0.61 to 510.37 µL PFT/g of rock (Table T13). These calculations are corrected for background PFT contamination occurring on the catwalk where initial cutting of the core liner and sampling took place, as well as the background in the anaerobic chamber where the core was cut and subsampled. In most cases, the background on the catwalk was either below or slightly above the detection limit of 0.045 µL. The background in the anaerobic chamber ranged from low to fairly high PFT concentrations and did not increase in any systematic way. In Core 205-1253A-38R, the background PFT concentration in the chamber and on the catwalk was higher than the inner core concentration, indicating significant volatilization of the PFT during sample distribution.

T13. Seawater contamination in gabbro cores, p. 182.

The PFT results indicate a fair amount of contamination in all samples. However, there are several limitations in using these results quantitatively for the igneous samples. The time between cutting the core liner for sampling, crushing the sample, and distributing the subsamples (including the sample for PFT analysis) was ~1 hr. The PFT volatil-

izes at room temperature, so it is difficult to determine if the tracer penetrated the sample with the drilling fluid or during the 1-hr sampling procedure. Also the exteriors of the samples were rinsed with a sterile salts solution (see "Microbiology," p. 28, in the "Explanatory Notes" chapter) before crushing, but they were not flamed or sterilized to more effectively rid the sample of excess tracer. In addition, the outer portion of the core was not removed, as the gabbro was fresh and difficult to break. Thus, the samples used to measure drilling fluid intrusion into the center of the core may contain a large portion of PFT transferred from the outside of the core during handling. Nevertheless, the samples (including the outer portions of the core) used for measuring the tracer concentration were from the same mixture used for inoculating media and for genetic analyses, therefore, providing a qualitative assessment of drilling contamination. Additionally, sampling of veins and fractures is required to determine the impact that microorganisms have in the weathering of the rock; these veins may act as weak boundaries that easily break and as a conduit for the flow of drilling fluids containing PFT or volatilized PFT in the ambient air. Because of the numerous unknowns involved prior to analyzing the tracer, the calculated contamination in the gabbro will be used in a qualitative sense rather than a quantitative one.

Particulate Tracer

Heat-sealed Whirl-Pak bags of fluorescent microspheres were deployed in every other core catcher during sediment coring and in every core catcher for igneous cores. Adjacent to microbiological sampling sites, toothpick samples of sediments at the core interior and exterior were taken and suspended in 0.5 mL of synthetic seawater solution. The small sample volume and prolonged exposure of the microspheres to natural and artificial light precluded rigorous microsphere counting at this site. To minimize this problem at future sites and to preserve microsphere fluorescence, particulate tracer Whirl-Paks will be kept refrigerated for as long as possible prior to deployment and core samples for microsphere counts will be kept refrigerated at all times except during microscope observation. The original protocol for microsphere sampling (Smith et al., 2000) was modified during recent legs to increase the sensitivity of counting assays after analyses at the site. The updated method will be employed at future sites. Sediment plugs of 3 cm^3 will be placed in 25 mL of saturated salt solution in a 50-mL Falcon centrifuge tube, mixed, and centrifuged to settle the large grain sizes only. The supernatant will be filtered onto a black polycarbonate filter, and the microspheres will be counted.

Fluorescent beads were successfully deployed in all igneous cores except for Core 205-1253A-33R. A sterile minimal salts solution used for rinsing the gabbro core was collected and used as a proxy for outer core contamination. The crushed sample, primarily the interior of the core with small amounts of the outer core, was also mixed with the minimal salts solution to make a slurry for microsphere counts, representing intrusion of the drilling fluids into the core. For bead counting, the filters were viewed under a 100× objective with the area for one field of view = ~3.14×10^4 μm^2. Beads were detected on the outside of all of the cores where samples were taken except for Core 205-1253A-43R (Table T14). For the interior of most cores, significantly fewer microspheres were observed or there was a complete absence of microspheres.

T14. Potential contamination using fluorescent beads, p. 183.

Because the gabbro was so fresh and difficult to break, the outer edge of the core could not be excluded from the samples. Thus, some amount of contamination was expected and the results are to be used qualitatively rather than quantitatively. However, of the techniques used here, microsphere tracers may more accurately indicate contamination by microorganisms from the drilling fluid. This is because PFT is soluble at room temperature, can travel through very small pore spaces (smaller than bacteria), and is found in the laboratory air and on the hands of anyone who has handled a core liner. The presence of beads is a strong indication that contamination by microbe-sized particles from the drilling fluid has occurred. Nevertheless, the absence of microspheres alone cannot confirm that a sample is uncontaminated.

Sediment Sampling and Distribution

Five sediment cores (Cores 205-1253A-2R, 3R, 4R, 10R, and 11R) were sampled for microbial community assessment. For each core, a ~5-cm^3 whole round was obtained adjacent to the IW whole round to relate microbiological and interstitial water chemistry results. From the centermost part of the cleaned whole round, two ~5-cm^3 sediment plugs were taken with sterile, cut-off syringes, one for postcruise DNA evaluation and one for postcruise ATP quantification. Both sets of plugs were frozen at –80°C. Formalin-fixed 0.5-cm^3 sediment samples from the same sites were refrigerated for postcruise cell counting.

Gabbro Sampling and Distribution

After sampling a ~40-cm^3 whole round from the core in an aerobic glove box, the sample was crushed using sterile techniques into small fragments. Some fragments were set aside for postcruise analyses involving fluorescent in situ hybridization, microscopy, or chemical mapping using the microprobe. The rest of the fragments were subsequently crushed with a sterile mortar and pestle. Half of the fine-grained sample was stored for genetic analyses or for PFT analyses. The sterile, anoxic minimal salts solution was added to the other half of the crushed sample and used to inoculate enrichment media or for microsphere tracer analyses.

Cultivations

Cultivations were conducted with slurries prepared from the crushed gabbro and sterile, anoxic marine salts solution (see **"Microbiology,"** p. 28, in the "Explanatory Notes" chapter). The enrichment media were inoculated with ~0.5 mL of slurry or with the drilling fluids for a control and were incubated at 8°C. The media used were selective for primarily anaerobic chemolithotrophic and heterotrophic microorganisms such as methanogens, sulfate reducers, sulfur oxidizers, iron(II) oxidizers, and iron(III) reducers. Further subculturing and molecular analyses will be performed postcruise.

Deoxyribonucleic Acid Extractions and Polymerase Chain Reaction

DNA was extracted using the freeze-thaw protocol outlined in **"Microbiology,"** p. 28, in the "Explanatory Notes" chapter. The DNA ob-

tained is a mixture from all of the microorganisms present in the sample, including that from any contamination introduced during the drilling process. Agarose gel electrophoresis of total community DNA, before performing polymerase chain reaction (PCR), did not show any banding in the gels. This result may mean that there was no DNA in the sample or, more likely, that the amount of DNA was so small that it could not be observed.

DNA was amplified with PCR using Taq polymerase and universal 16S ribosomal ribonucleic acid primers. PCR was performed several times using differing concentrations of template DNA and primers. Agarose gel electrophoresis was also used to quantify the PCR products. All PCR results came back negative (no DNA present). One possible explanation for this is an absence of total community DNA. Another explanation is that the primers, polymerase, and/or nucleotides degraded during shipping because a positive control did not work on several occasions. One more possibility is that there is some substance (for example, a high metal concentration) in the sample that is inhibiting the PCR. Initial DNA extractions and samples will be shipped to shore for purification and further genetic analyses.

DOWNHOLE MEASUREMENTS

At Site 1253, the DVTPP was deployed twice in order to determine the in situ temperature and pressure of the formation. The first measurement was performed directly beneath the casing of the reentry cone at a depth of 60 mbsf; the second was at a depth of 150 mbsf. Prior to these measurements, the bottom water temperature was determined by attaching a high-resolution miniaturized temperature data logger (MTL) to the video system used for reentering the borehole. A conductivity/temperature/depth (CTD) profile recorded offshore Nicaragua in September 2002 during the German *Meteor* cruise is presented here as an independent reference. It is used to calibrate the DVTPP tool to this well-constrained bottom water temperature. The MTL was also used during wireline logging to record a high-resolution temperature profile within the pipe and the borehole.

High-Resolution Temperature Measurements with the Miniaturized Temperature Data Logger

Determination of Bottom Water Temperature

For the determination of the downhole temperature gradient, it is necessary to know the exact bottom water temperature to calibrate the tools to a stable reference temperature. For high-resolution temperature measurements, we used an MTL (Pfender and Villinger, 2002) (see also "Downhole Tools," p. 32, in the "Explanatory Notes" chapter).

By mounting an MTL on the video system while reentering the borehole, we measured a high-resolution temperature profile of the water column down to 4333 mbrf. Figure F78 shows a part of the record that includes a temperature inversion with the lowest temperature of 1.837°C (1450 hr UTC). The plot indicates a temperature of 1.985°C close to the seafloor at a depth of 4333 mbrf.

In Figure F79, we present data from a CTD performed in September 2002 offshore Nicaragua to compare the temperature profiles. The inversion recorded by the MTL is also seen in the CTD data at a depth of

F78. Temperature record of an MTL, p. 152.

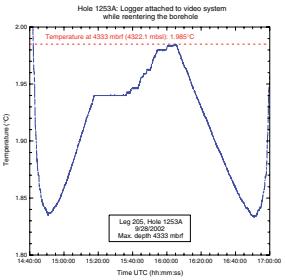

F79. CTD profile from 2500 to 5318 mbsl, p. 153.

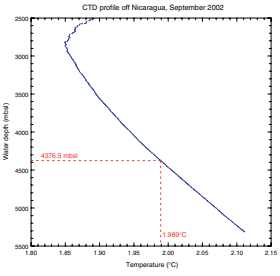

2817 mbsl and a temperature of 1.849°C. At 4322 mbsl (4333 mbrf), the temperature is 1.983°C, which corresponds very well to the value determined by the logger during the video run at the same depth. At 4376 mbsl, the CTD temperature reading is 1.989°C, which we assume is the bottom water temperature for Site 1253. This bottom water temperature deviates from that determined during Leg 170. At Site 1039, the temperature was 1.81°C, as measured by two different tools (water sampling temperature probe and the Adara temperature tool). The cause of this difference is not clear.

Downhole Temperatures from the Miniaturized Temperature Data Logger during Logging Runs

Additional MTL temperature measurements were performed during wireline logging to detect possible hydrologically active horizons. The MTL was mounted in the TAP tool close to the sensor tip of the TAP temperature sensor attached to the bottom of the triple combo tool string (Fig. F80). In a first attempt at logging early on 8 October, a bridge at a depth of 528 mbsf could not be passed and the run was stopped because of tool problems. After replacing the broken tool, the second logging run took place on the afternoon of 8 October and covered the depth interval from 413 to 530 mbsf.

Figure F81A and F81B illustrates the temperature and pressure profiles of both runs, beginning with the mudline stop and ending with the pull-out from the borehole.

Run 1

In the first run, the 5-min-long stop (0632–0637 hr UTC) at the mudline (4387.1 mbrf) was clearly marked by a constant pressure of 44.3 MPa. Detailed investigation of the pressure shows periodic variations of ±0.1 MPa, corresponding to a vertical movement of ~10-m amplitude, which is interpreted as being caused by the ship's heave. As the tool was lowered into the borehole, the pressure increased up to 48.5 MPa at 4800 mbrf (end of 10¾-in casing), where the tool was held for 10 min. The pressure showed smaller variations here, up to ±0.07 MPa, corresponding to ~7 m of vertical movement. At the end of this period, the wireline heave compensator was switched on. The record then shows the tool being lowered through the open hole and reaching a maximum pressure of 50 MPa at 530 mbsf.

The temperature at the mudline varies from 2.05° to 2.52°C for the MTL; the TAP tool temperatures show similar variation but are offset by +0.88°C. This joint change in both records indicates first a fast increase then a slower decrease in temperatures while the tool was held at the mudline, which might be caused by previous pumping and excessive tool movement. Because the MTL has also been used to determine the bottom water temperature and is calibrated to a high-precision thermometer, it is regarded as the more reliable tool. It is also obvious that the scatter of the MTL data (±1 mK) is lower than that of the TAP tool (±30 mK). Nevertheless, both instruments show the same trend and have the same offset over time. As the tool was lowered through the borehole to the end of the casing at 4800 mbrf, the temperature increased to 5.715°C. During the stop there, the temperature slowly increased to 5.735°C at the end of the stop. The trend is not obvious with the TAP tool because its scatter is higher than this increase.

Further lowering the tool resulted in a further increase in measured temperatures followed by a decrease when the tool actually reached the

F80. The MTL mounted in the TAP tool, p. 154.

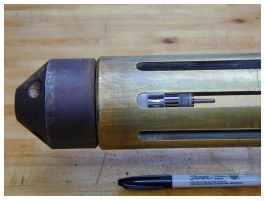

F81. Temperatures and pressures during wireline logging, p. 155.

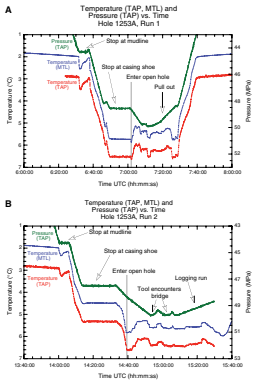

open hole. The temperature recorded with time in the hole was mainly determined by raising and lowering the tool during the attempts to pass the bridge at 530 mbsf. Unable to pass the bridge, the tool was pulled out of the hole.

Run 2

Pressure and temperatures recorded during run 2 in general show the same features as run 1. At the mudline stop, a constant pressure corresponding to the seafloor depth of 4387 mbrf was seen. The observed temperatures were the same as in the first attempt while the tool was lowered to the seafloor, but the increase during the mudline stop was not as prominent. As the tool was lowered down in the borehole, pressure and temperatures both increased in the same manner as in the previous run. During the stop close to the casing shoe, the pressure at 4700 mbrf remained constant at 47.5 MPa and temperature increased from 4.482° to 4.492°C. As the tool was lowered, temperature increased and suddenly dropped as the tool entered the open hole. In the open hole, the attempts to pass the bridge were marked by the two peaks in the pressure at ~1457 and 1505 hr UTC. The peaks marked the vertical position of the tool pulled up; the low parts in between marked the deepest position of the tool at ~4917 mbrf. Temperatures mirrored this vertical movement and increased with increasing depth. Around 1510 hr UTC, the logging run started from 4917 mbrf (530 mbsf) upward. Again, the zone of the temperature disturbance in the borehole was crossed at the end of the record.

Temperature Disturbance at the End of the Casing

The temperature vs. borehole depth plot can be seen in Figure **F82A** and **F82B.** Only temperatures that were collected while the tool was lowered down through the borehole are used. In contrast to lowering the tools where the sensors measure undisturbed temperature fields, the measurements taken while the tool was pulled up take place in a turbulent temperature field and might slightly be shifted against the undisturbed values and are for that reason neglected.

A significant feature in the profiles is the strong increase of temperatures around the end of the casing at 413 mbsf. This structure is almost symmetrical around the end of the 10¾-in casing and extends ~40 m above and below the casing shoe. The amount of incoming heat to produce the observed 0.8°C temperature increase is too large to be caused by incoming warm fluids. Instead, it is probably due to cement curing, which is an exothermic reaction. Cementing the borehole was done ~36 hr prior to logging.

The temperature gradient in the casing (from seafloor to 50 m above the casing shoe) is ~0.006 K/m and still lower than the expected gradient of 0.0098 K/m. The temperature profile in the open hole is shown in Figure **F82B.** The large negative gradient up to 450–460 mbsf probably characterizes the influence of the cement curing described above. Below 460 mbsf, the gradient is much smaller and becomes positive at 525 mbsf. Increased borehole temperatures between runs 1 and 2 indicate that the borehole had not yet completely equilibrated to the formation temperatures.

F82. Temperatures in the borehole and the open hole, p. 156.

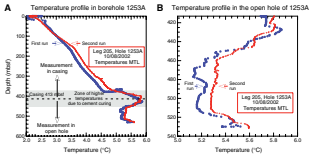

Davis-Villinger Temperature-Pressure Probe

The in situ measurements of temperature and pressure took place on 23 September between 60 and 150 mbsf. During the deployment, the

tool was held for 10 min at the mudline and another 10 min within 1 or 2 m of the bottom of the hole. After penetrating the sediments, the tool was left for 30 min in the formation to record the decay of in situ temperature and pressure to allow extrapolation to undisturbed values.

The ship's heave was compensated by the shipboard active heave compensator, which was activated each time after the mudline stop. Figure F83 shows a general overview of temperature and pressure data collected during both DVTPP deployments.

The temperature channel of the DVTPP showed a noise level that was considerably higher than expected from the manufacturer's specifications. After the thermistor was replaced with a fixed resistor in the laboratory for test purposes, it became obvious that the noise was created by the probe electronics. After we had discussions with RBR Ltd., the manufacturer of the probe's logger, we came to the conclusion that oscillations in the amplifier circuit probably caused the noise. Unfortunately, repair at sea was not possible.

F83. DVTPP measurements, Hole 1253A, p. 157.

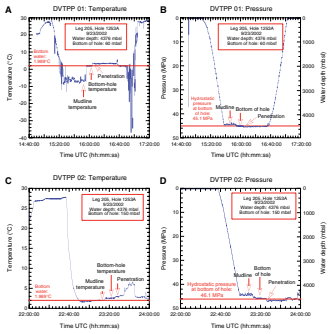

F84. Close-up profiles of temperature and pressure records, p. 158.

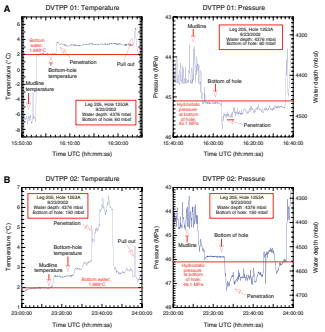

Davis-Villinger Temperature-Pressure Probe at 60 mbsf

Temperature

The stops at the mudline (1545–1555 hr UTC), the bottom of the hole (1555–1605 hr UTC), and the penetration into the sediment (1605 hr UTC) can be clearly seen in Figures F83A and F84A. Large negative excursions were observed while the tool was lowered and raised in the drill pipe. Following the first deployment, we detected an intermittent contact between a cable and the tool's housing, which caused the spikes in temperature during movement of the tool. After the repair, temperature spikes were not observed in subsequent deployments.

Because of the electrical problem, the bottom water temperature is offset by 9°C and is not of any use. The active heave compensator was switched on shortly before reaching the bottom of the hole. Its effect can be clearly seen when comparing the relative temperature changes at the mudline and at the bottom of the hole, where the scatter is strongly reduced. With tool movement minimized by active heave, the intermittent electrical problem was eliminated and valid temperatures were measured. Temperatures at the bottom of the hole are 2.04° ± 0.02°C. The frictional heating caused by the penetration of the tool tip in the sediment is clearly marked but lacks a clear decay (Fig. F83A). Only the first 5 min can be seen as a decay; the rest of the record is strongly spiked. The spikes in the temperature record while the probe is resting in the formation indicate movement of the probe, which produces further spikes of frictional heating with a following decay. Pressure data also show vertical movement, although the heave compensation is active. One reason for the different behavior of temperatures and pressures at the bottom of the hole and in the formation is that the effect of any movement is enhanced in the formation, causing frictional heating and pressure pulses.

It is possible to estimate the expected temperature at 60 mbsf using the temperature gradient of 0.0173 K/m, as calculated from Site 1039 data, and the bottom water temperature of 1.989°C, determined during Leg 205 with independent methods. This calculation yields 3.026°C, which is in good agreement with a visual extrapolation of the early and mostly undisturbed temperature decay.

Pressure

The observed pressure increases from ~0.1 MPa at sea level to ~45 MPa at the bottom of the borehole (Figs. F83B, F84A). The record at the mudline can be clearly distinguished from the stop at the bottom of the borehole and the penetration. During the mudline stop, the heave compensator was not yet activated and high variability of the measured pressure is observed. Large pressure changes during the stop at the mudline are most probably caused by vertical heave-induced movement of the tool, which acts as a moving piston inside the drill pipe. After the heave compensation is activated, the bottom-hole record does not show significant heave-induced distortion. The penetration record does, however, show disturbance. The penetration itself is clearly marked, but the pressure decay trend is quite noisy and indicates vertical movement of the tool, which becomes more obvious in the formation in contrast to the open hole. The decay of measured pressure at the bottom of the hole points to a formation pressure of ~45.2 MPa. Assuming a constant seawater salinity, temperature, and, therefore, density of 1030 kg/m^3, calculations yield a hydrostatic pressure of 44.8 MPa at 60 mbsf. Accounting for the increasing density of water with pressure, the result is 45.1 MPa, which is very close to the estimated formation pressure.

Davis-Villinger Temperature-Pressure Probe at 150 mbsf

Temperature

After thoroughly checking the electrical contacts of the DVTPP after the first deployment and correcting a possible intermittent contact, the second deployment retrieved data of only slightly better quality (Figs. F83C, F83D, F84B). The numerous negative spikes observed during the first run disappeared, and a reasonable bottom water temperature of 1.99° ± 0.02°C was recorded at the mudline (2305–2315 hr UTC). The bottom-hole temperature at 150 mbsf was ~2.58°C. The frictional decay following the penetration into the sediments at 2325 hr UTC cannot be processed because it is highly disturbed and does not show any sign of a interpretable decay. The expected temperature at 150 mbsf, calculated in the same way as that for 60 mbsf, would give a value of 4.102°C, which could be possible but is not obvious from the measured temperature data.

Pressure

For the pressure measurement, we see the same characteristic features as were observed during the first DVTPP run (Figs. F83D, F84B). High pressure variations at the mudline, which suggest vertical motion, were observed when heave compensation was not switched on (~2300 hr UTC). However, the suggested vertical motion of up to 80 m is unreasonable. After the heave compensation was switched on before reaching the bottom of the hole, a stable pressure of 45.9 MPa was recorded. The calculated pressure at this depth, taking into account the increasing density of seawater with pressure, is 46.1 MPa and corresponds well to the observation. The disturbed pressure decay after penetration at 2325 hr UTC cannot be processed because of tool movement.

DOWNHOLE LOGGING

Hole 1253A was logged with two tool strings, the triple combo and the FMS-sonic string. Previous logging-while-drilling measurements taken during Leg 170 at Site 1039 did not include the sonic or FMS tool strings and reached to only 407 mbsf (Shipboard Scientific Party, 1997). As expected, logging at Site 1253 was technically challenging. The first logging attempt failed to pass beneath 150 mbsf. After the entire sediment section and part of the upper sill was cased (necessary for eventual CORK-II installation), a second logging attempt was made but was stopped at 564 mbsf when the tool string lost communication as a result of a broken Hostile Environment Litho-Density Sonde (HLDS). The subsequent triple combo run and two FMS-sonic runs were successful.

Logging Operations

Downhole logging was performed in Hole 1253A after it had been drilled to a depth of 600 mbsf with a 9⅞-in RCB drill bit. The hole was opened to a depth of 423 mbsf using a 14¾-in bit, and a 10¾-in casing was installed beneath the sedimentary section into the upper sill to a depth of 413 mbsf. The casing was then cemented in place (see **"Operations,"** p. 11). The weather was good, with a maximum heave of 1.1 m, and the wireline heave compensator was used throughout the logging operations.

Downhole logging operations began with the deployment of the triple combo tool string (Table **T15;** Fig. **F85**). The tool string initially reached a depth of 530 mbsf. However, communication to the tool's power was lost after several attempts to pass the bridge. The triple combo tool string was pulled out of the hole, and it was found that the HLDS was leaking oil. The HLDS was replaced with another density tool (Hostile Environment Litho-Density Tool [HLDT]), and the tool string was run back into the hole. The tools encountered the bridge at the same depth of 530 mbsf, and upward logging was started from that depth.

For the second logging run in Hole 1253A, the FMS-sonic string was deployed. During the first pass, the tools reached the same bridge depth as in the triple combo run (530 mbsf). During the second pass of the FMS-sonic tool string, it penetrated through the 530-mbsf bridge and reached another bridge at 564 mbsf. Upward logging began from 564 mbsf.

Log Quality

Data from the logging runs were transmitted to the LDEO Borehole Research Group (BRG) for depth shifting, environmental correction, and evaluation of the acoustic data. To aid comparison with core observations, all plots and text in this report will use the drillers depth of 4387 m (water depth). However, all data on the "Log and Core Data" CD-ROM assumed a 4390 m seafloor depth, which was determined by LDEO-BRG based on the step in gamma ray values at the sediment/water interface. The FMS-sonic pass 2 was depth matched to the triple combo run using the gamma ray (environmentally corrected gamma ray and Hostile Environment Natural Gamma Ray Sonde [HNGS]) logs and checked with the caliper logs. The gamma ray log from the FMS-sonic pass 1 was depth matched to that from the FMS-sonic pass 2. The

T15. Logging operations, Hole 1253A, p. 184.

F85. Logging summary diagram, p. 159.

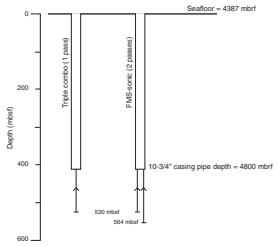

HNGS and Scintillation Gamma Ray Tool (SGT) data were corrected for hole size during the recording. The Accelerator Porosity Sonde and HLDT were corrected for standoff and hole diameter, respectively, during the recording.

Enlarged hole size degrades the quality of density measurements if the density pad does not contact the formation. The measurement of neutron porosity is also degraded because of attenuation by the borehole fluids. Gamma ray counts and resistivity may be underestimated in enlarged intervals. Hole diameter was recorded by the hydraulic caliper on the HLDT and by the caliper on the FMS string. The second caliper on the FMS string did not record the diameter correctly. Because of the mechanical problem with caliper 2 in the FMS-sonic tool string, a second pass of the tool string was made. It had a 90° rotation from the orientation of the first pass, thus providing a more complete picture of the borehole shape (Fig. **F86**).

The caliper data indicate that the hole diameter in the intervals between 417–431 mbsf and 461–541 mbsf was relatively uniform, ranging mostly between 10 to 12 in except for isolated rougher sections (Figs. **F86, F87**). An interval of increased diameter is observed above 424 mbsf within the upper igneous unit, corresponding to the 14¾-in hole that was drilled prior to the casing installation. Intervals of very large hole diameter are observed from 433 to 463 mbsf, and the caliper reached maximum extension between 435 and 461 mbsf. These intervals roughly correspond to the sedimentary section observed in cores. Thin intervals of increased hole diameter are present within the section where igneous rock was recovered.

The density correction (DRHO) curve (Fig. **F88**) is calculated from the difference between the short- and long-spaced density measurements and provides a further indication of the quality of the bulk density data. DRHO values in excess of 0.1 g/cm³ indicate unreliable density data. Intervals of unreliable density data occur between 440 and 458 mbsf, corresponding to high caliper readings and probable poor contact with the sedimentary formation (Fig. **F88**). In addition, poor data quality is indicated below 513 mbsf by DRHO values of 0.30–0.35 g/cm³. Thinner (1 to 2 m) spikes of unacceptably high DRHO values occur throughout the logging run. Despite high caliper values in the interval between 433 and 443 mbsf, low DRHO values suggest that density values may be reliable in this interval.

The caliper from the HLDT indicates a thin enlarged hole section between 433 and 434 mbsf. In contrast, caliper data from the FMS-sonic runs do not indicate an enlarged borehole at this depth (Figs. **F86, F87**). The caliper data from the two runs indicate that the caliper from run 1 is slightly greater than that from run 2 through sections of the lower igneous unit. Azimuth data from the runs suggest that the FMS tool rotated throughout the runs, indicating that there is not likely to be a consistent ellipticity to the borehole.

The logging data show a good correlation with the physical property measurements from cores, particularly for bulk density. The contacts between the sediment and gabbro zones are distinct with sharp increases in density, velocity, and resistivity and a sharp decrease in porosity. The two passes of the FMS images are generally in agreement except at depths where the hole conditions are bad.

Hole inclination can also affect log quality, especially during the FMS-sonic run, as the FMS pad can lose contact because of tool weight if the inclination is >10°. Measured inclinations range from 0.5° to 1.6°.

F86. Caliper and azimuth data, p. 160.

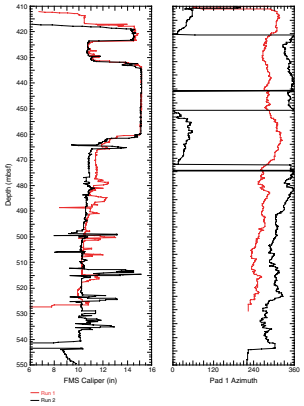

F87. Gamma ray log, Hole 1253A, p. 161.

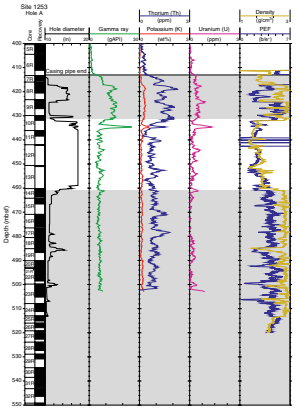

F88. Density and porosity logs, Hole 1253A, p. 162.

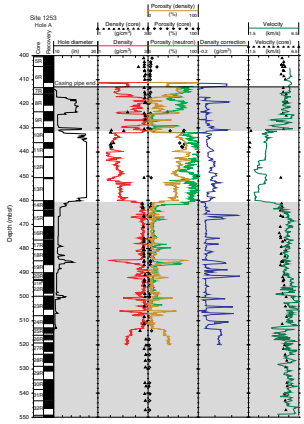

Results

Plots of logging results are presented in Figures F87, F88, F89, and F90, and the complete logging data are available (see the "Related Leg Data" and the "Log and Core Data" CD-ROM). As explained above, the depths calculated in the complete, depth-shifted logging data will be 3 m below the drillers depth that we use in this report.

Recovered cores from the logged section of Hole 1253A indicated two intervals of igneous rocks separated by nannofossil chalk. The Hole 1253A logs can be clearly separated into three large intervals on the basis of obvious changes in hole diameter, velocity, resistivity, bulk density, and porosity. These intervals generally correspond to the major lithology changes identified in the recovered cores. Between the bottom of the casing (413 mbsf) and 431 mbsf, porosities are low and densities, resistivities, and *P*-wave velocities are high. This interval corresponds to the upper igneous unit. Between 431 and 461 mbsf, high porosities and low bulk densities, resistivities, and *P*-wave velocities identify sediments. This interval also has an enlarged diameter. A return to high bulk densities, resistivities, and *P*-wave velocities at 461 mbsf indicates the top of the lower igneous unit. The boundaries identified in the logs vary from those shown by the core descriptions, probably because of uncertainty in depths of recovered core pieces in Cores 205-1253A-10R and 13R, which had low recovery. The NGR is not distinctly different between the lower igneous and the sedimentary rocks in Hole 1253A. In contrast, there does appear to be a difference in natural gamma values between the upper igneous unit and the sediments and lower igneous units.

In addition to identification of the major intervals, the logging data identify a change in the character of the resistivity and *P*-wave velocity logs that occurs at ~491 to 493 mbsf. High-resistivity intervals are present between 493–497 and 503–507 mbsf. A significant interval of decreased resistivity and sonic velocity is present between 513 and 517 mbsf. Unfortunately, porosity information is not available for these depths and the bulk density data may be unreliable, as discussed above. FMS images indicate a change in character at a depth of ~508 mbsf. Above that depth, conductive features are generally discontinuous and are generally randomly oriented. Below that depth, more closely spaced, thin, near-horizontal to slightly dipping conductive features are present in several intervals that are separated by intervals of poor images and irregular borehole size.

Ideally, fractured igneous rock can be distinguished from sediment layers by comparing the sonic velocity log to the bulk density log. Because acoustic waves transmit through the solid portion of fractured rock, intervals of decreased bulk density but no corresponding velocity decrease may indicate a fractured interval. In contrast, sediment interlayers should cause a velocity decrease. However, the vertical resolution of the sonic tool is 107 cm, so small sediment interlayers may not be clearly distinguishable in this log. Based on the bulk density and sonic logs, potential fractured intervals are observed at 466–468, 484–486, 490–493, and 506–508 mbsf.

Gamma Radiation

Among the two gamma ray tools run in Hole 1253A, the HNGS on the triple combo string can be considered to more accurately measure true formation natural gamma ray values than the SGT on the FMS-

F89. Resistivity logs, Hole 1253A, p. 163.

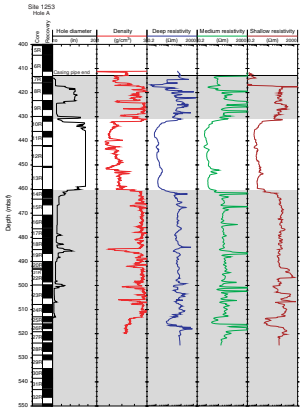

F90. Acoustic logs, Hole 1253A, p. 164.

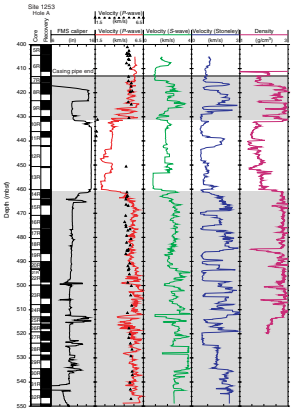

sonic string, which is not corrected for borehole diameter effects. The SGT log is used for depth comparisons with the triple combo run. In addition, the SGT data from the second FMS-sonic run provide information at greater depths than reached by the triple combo tool string.

Gamma ray data (Fig. F87) show elevated values from 413 to 432 mbsf, corresponding to the upper igneous section. In this section, thorium values range between 0.8 and 2.3 ppm compared to 0.2–1.8 ppm in the lower part of the borehole, corresponding to the sediments and the lower igneous unit. Within the lower igneous unit, narrow thorium spikes (~2 ppm) are observed at 469–473 and 477–481 mbsf. Uranium and potassium also show elevated values in the upper igneous section. A thin spike in the gamma ray values occurs at 434 mbsf, reaching the highest value (25 gAPI) of the run. Maximum values in uranium (1.3 ppm) and potassium (0.56 wt%) are also associated with this high gamma ray spike. This spike is also observed in the gamma ray data from both of the FMS-sonic runs.

Below 435 mbsf to the deepest measurement, the gamma ray curve shows little variation, despite the lithologic change between sediments and igneous rocks apparent in the recovered cores. The NGR values from the MST run on recovered cores indicates a shift to slightly higher values at ~513 mbsf. This depth is below that logged by the HNGS on the triple combo string but can be compared to gamma ray data from the second FMS-sonic run that were recorded to 523 mbsf. Although some values above 10 gAPI were recorded in the interval between 508 and 518 mbsf, no consistent shift is distinguishable.

Bulk Density

Bulk density data were recorded in high-resolution mode, which increased the sampling rate to 2.54 cm from 15 cm in normal mode, and Schlumberger-enhanced processing was performed on the Schlumberger minimum configuration maxis system onboard (Fig. F88) the ship. Bulk density values are variable between the bottom of the casing and 425 mbsf and may be affected by the enlarged borehole. Between 425 and 432 mbsf, most bulk density values are between 2.8 and 2.9 g/cm^3, with some thin spikes of low values. Bulk density in the interval between 432 and 460 mbsf is between 1.3 and 2.0 g/cm^3, corresponding to the recovered sediments.

In the interval from 460 to 513 mbsf (the lower igneous unit), bulk density values generally vary between 2.7 and 2.9 g/cm^3, with spikes to lower values. Most but not all spikes are associated with zones of enlarged borehole diameter. Physical property measurements taken on recovered cores are consistent with the density logs in both the igneous and sediment intervals.

Porosity

Neutron porosity data (Fig. F88) also were recorded in high-resolution mode, which increased the sampling rate to 5.08 cm from 15 cm in normal mode, and an enhanced processing technique was used. Porosities for Hole 1253A were estimated from bulk density log data and compared to the neutron porosity data. The density log (ρ_b) was converted to porosity (ϕ) using the relationship

$$\phi = (\rho_s - \rho_b)/(\rho_s - \rho_w),$$

where water density, ρ_w, and grain density, ρ_s, were assumed to be 1.03 and 2.95 g/cm^3, respectively. This estimate for grain density was based on core moisture and density property measurements of dry mass and volume on the igneous cores (see "Physical Properties," p. 37).

Comparison of values indicates an inconsistent depth offset between peaks in neutron and density porosity, which is surprising because these sensors are on the same tool string. At 500.5 mbsf, peaks in neutron and density porosity coincide, whereas the peak in density porosity at 504 mbsf is below a neutron porosity peak at 503.5 mbsf, and a large density porosity peak at 485 mbsf is ~1 m above the corresponding peak in neutron porosity.

In general, values determined from neutron porosity exceed those calculated from the bulk density log. The largest discrepancy (40%) occurs in the upper igneous unit between 416 and 424 mbsf. The difference is also high in the sediments (20%–30% difference). In the lower igneous unit, values are much closer. Both neutron and calculated density porosity values are slightly higher than those determined from core moisture and density properties. The higher log values may reflect fracture porosity that is not reflected in the moisture and density property measurements, which are made on intact samples. The difference may also reflect chemically bound water that is not removed during the drying of the core samples.

Resistivity

Deep and medium induction resistivity data from Hole 1253A (Fig. F89) show lower values than the spherically focused resistivity log (SFLU) in the high-resistivity sections of the hole. This is atypical of most logging applications, because the SFLU has the shallowest penetration and is, therefore, most affected by the conductive borehole fluids. However, the deep and medium induction tools are not accurate in highly resistive (>100 Ωm) formations, as would be expected for igneous rock. Therefore, in the high-resistivity sections, the SFLU data should be considered to best reflect true formation resistivity.

The SFLU data show an interval of higher values (20–310 Ωm) between the top of the logged section and 432 mbsf. Low resistivities (0.6–5 Ωm) were recorded between 432 and 462 mbsf. The medium and deep induction data are slightly greater than the SFLU values. Between 462 and 493 mbsf, resistivity values are consistently high with minor variations. Below 493 mbsf, the curve shows greater variation, with intervals of elevated resistivity between 493–497 and 503–507 mbsf. No corresponding change is seen in the other logs within these intervals. An interval of low SFLU resistivity, with values of 5–15 Ωm, is present between 513 and 517 mbsf. This interval is also seen clearly in the deep and medium resistivity logs and is associated with decreased *P*-wave velocity.

Acoustic Velocity

The Dipole Sonic Imager was operated with the modes of *P* and *S* monopole (standard frequency), lower dipole (low frequency), upper dipole (standard frequency), and Stoneley (standard frequency) in both passes of the FMS-sonic tool string, except no upper dipole logs were taken for pass 1. Velocity data from the deeper second run are presented in Figure F90. Among these measurements, the compressional velocities (*P* and *S* mode) generally correlate well between the two passes. The

lower dipole shear velocities are generally good too; however, there are a few sections of low-quality values at some depths. In contrast, the upper dipole shear velocities are of poor quality, and Stoneley wave velocities are well determined only in the igneous rocks, not in the sediments. Postcruise analyses of full waveform data will allow a better assessment of data quality.

P-wave velocities from the top of the logged section to 423 mbsf are mostly between 5000 and 6000 m/s. Between 423 and 433 mbsf, *P*-wave values become more variable and generally decrease. Between 433 and 460 mbsf, velocities range between 2050 and 3400 m/s. Between 460 and 513 mbsf, most values are between 4500 and 6000 m/s. Between 513 and 518 mbsf, the *P*-wave velocities become more variable, with a number of values as low as 3800–4000 m/s.

Shear wave velocities follow similar trends to those of the *P*-wave velocity log. However, variation is large, ranging from 220 to 5400 m/s where igneous sections, especially the lower igneous unit, are larger than sediment sections. Unlike that for the *P*-wave velocities, the boundary between the upper igneous unit and sediment section is not apparent in the shear wave data.

Physical property measurements taken from cores are consistent with *P*-wave velocities between the top of the logged section and 423 mbsf. The few values of sediment velocity measured in cores between 433 and 453 mbsf (~1600–1900 m/s) are significantly lower than the logging velocities (~3200 m/s between 433 and 443 mbsf), despite good correlation between bulk density values from logging and core moisture and density properties.

A single core sample of igneous rock from Core 205-1254A-13R yields a velocity significantly higher than that observed for the same depth in the sonic log. This discrepancy suggests that the recovered interval may be from the bottom of the cored interval (460 mbsf) rather than from the top, as curated. Below 460 mbsf, *P*-wave velocities from igneous core samples are consistently and slightly lower than the velocities from the sonic log.

Formation MicroScanner Imaging

The FMS tool produces high-resolution images of the electrical resistivity characteristics of the borehole wall that can be used for detailed structural interpretations (Figs. **F91, F92, F93**). Because of the malfunction of caliper 2, detailed structural interpretation will require merging of the two FMS runs where they overlap. Shipboard processing provided preliminary FMS images. In Figure **F91,** static normalized FMS images are shown together with caliper, velocity, and density curves. Resistivity contrasts between the igneous rock and soft sediments are clearly defined and are consistent with density and velocity data. Because hole conditions were good in most of the igneous intervals, textural and structural variations between the upper and lower sections and within the lower igneous unit itself are resolvable.

The upper igneous unit between 419 and 426 mbsf exhibits a blocky texture with a spacing of ~0.5 m between conductive features. Between 426 and 432 mbsf, the formation appears more massive with thin, conductive features at a 0.5- to 2-m spacing (Fig. **F93A**). In this interval, it is difficult to trace the conductive features across the four FMS pads.

At the top of the lower igneous unit (463 to 467 mbsf), curved conductive features (fractures or irregularities in the borehole wall) are common. Between 467 and 493 mbsf, the formation appears more mas-

F91. FMS profile for the second logging pass, p. 165.

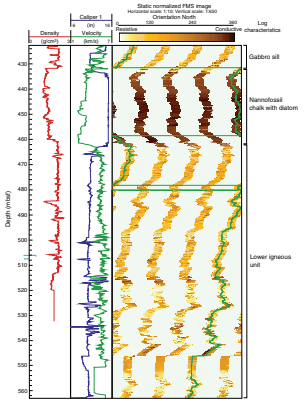

F92. FMS images of gabbro and the lower igneous unit, p. 166.

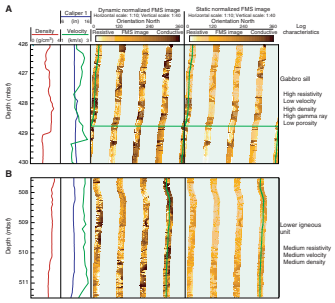

F93. FMS images of the upper and lower OsmoSamplers, p. 167.

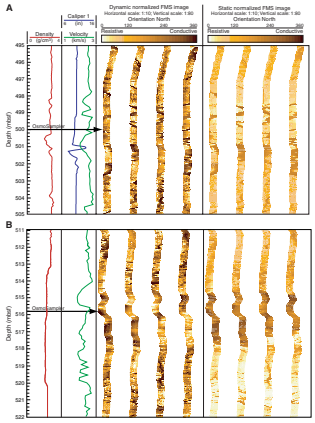

sive to blocky, with 0.5- to 1-m spacing between thin conductive features. At ~472 to 478 mbsf, these conductive features can be clearly traced across the four pads, whereas in other intervals, the conductive features appear discontinuous. Between 487 and 493 mbsf, irregular to curved vertical conductive features are present, representing possible fractures or irregularities in the borehole wall. From 493 to 498 mbsf, conductive features are rare, becoming more common again between 498 and 508 mbsf.

At 508 mbsf, the character of the FMS image changes to more closely spaced conductive features (<0.5 m spacing). In rare cases, such as from 513 to 514 mbsf, these conductive features can be traced across the four pads and suggest a low dip angle (Fig. **F93B**). Image quality between 514.5 and 518 mbsf is poor because of a borehole enlargement. Relatively low (3800–4000 m/s) *P*-wave velocities and low (5–15 Ωm) SFLU resistivities occur at similar depths

Below 518 mbsf, the layered character returns but the absolute value of resistivity increases, as indicated by the static image (Fig. **F93B**). This high resistivity below 518 mbsf is confirmed by the SFLU measurements in this interval. Image quality is poor from 525 to 527, 534 to 539, and 542 to 555 mbsf. From 539 to 541 and 555 to 563 mbsf, the image is characterized by more closely spaced (<0.5 m) thin, nearly horizontal conductive features. These conductive features appear to dip to the southwest. Although no SFLU data exist for these intervals, the static FMS images indicate that both intervals have high resistivity. Therefore, it appears unlikely that these are sediment layers.

Images from the intervals into which the upper and lower OsmoSamplers were stationed are shown in Figure **F93.** Dipping conductive features are visible in the section screened for the upper OsmoSampler. The lower OsmoSampler is located in an area with a layered character beneath a zone of poor images because of an irregular borehole shape.

Magnetic Field Measurements

Downhole magnetic field measurements were made with a three-axis fluxgate magnetometer of the General Purpose Inclinometer Tool (GPIT) that is used to orient the FMS images. The tool utilizes a three-axis inclinometer and a three-axis magnetometer to determine magnetic field strength and inclination of the x-, y-, and z-directions and make calculations of the tool deviation, tool azimuth, and relative bearing.

Magnetic field strength recorded by the GPIT is shown with paleomagnetic intensity results (Fig. **F94**). Even though core measurements (see **"Paleomagnetism,"** p. 41) are scattered, the general trend of the curve is in good correlation with logging measurements. Sharp intensity changes at the depths of 412, 419, 435, 463, and 515 mbsf may be linked to lithologic changes. Additional detailed analyses are required to verify and quantify these initial, tentative observations.

F94. Magnetic field strength and magnetic intensity, p. 168.

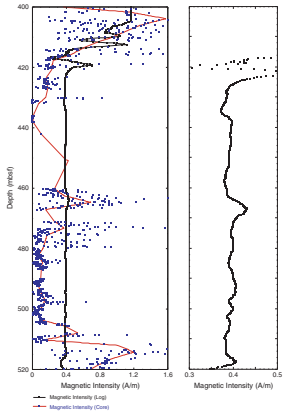

REFERENCES

Berggren, W.A., Hilgen, F.J., Langereis, C.G., Kent, D.V., Obradovich, J.D., Raffi, I., Raymo, M.E., and Shackleton, N.J., 1995a. Late Neogene chronology: new perspectives in high-resolution stratigraphy. *Geol. Soc. Am. Bull.,* 107:1272–1287.

Berggren, W.A., Kent, D.V., Swisher, C.G., III, and Aubry, M.P., 1995b. A revised Cenozoic geochronology and chronostratigraphy. *In* Berggren, W.A., Kent, D.V., Aubry, M.-P., and Hardenbol, J. (Eds.), *Geochronology, Time Scales and Global Stratigraphic Correlation*. Spec. Publ.—SEPM, 54:129–212.

Chan, L.-H., and Kastner, M., 2000. Lithium isotopic compositions of pore fluids and sediments in the Costa Rica subduction zone: implications for fluid processes and sediment contribution to the arc volcanoes. *Earth Planet. Sci. Lett.,* 183:275–290.

DeMets, C., Gordon, R.G., Argus, D.F., and Stein, S., 1990. Current plate motions. *Geophys. J. Internat.* 101:425–478.

Ekdale, A.A., Bromley, R.G., and Pemberton, S.G. (Eds.), 1984. *Ichnology: The Use of Trace Fossils in Sedimentology and Stratigraphy.* SEPM Short Course, 15.

Fisher, R.A., 1953. Dispersion on a sphere. *Proc. R. Soc. London A,* 217:295–305.

Hein, J.R., Scholl, D.W., and Miller, J., 1978. Episodes of Aleutian Ridge explosive volcanism. *Science,* 199:137–141.

Kennett, J.P., McBirney, A.R., and Thunnell, R.C., 1977. Episodes of Cenozoic volcanism in the Circum-Pacific region. *J. Volcanol. Geotherm. Res.,* 2:145–163.

Kennett, J.P., and Thunnell, R.C., 1977. On explosive Cenozoic volcanism and climatic implications. *Science,* 196:1231–1234.

Kimura, G., Silver, E.A., Blum, P., et al., 1997. *Proc. ODP, Init. Repts.,* 170: College Station, TX (Ocean Drilling Program).

Lowrie, W., 1990. Identification of ferromagnetic minerals in a rock by coercivity and unblocking temperature properties. *Geophys. Res. Lett.,* 17:159–162.

Lowrie, W., and Fuller, M., 1971. On the alternating field demagnetization characteristics of multidomain thermoremanent magnetization in magnetite. *J. Geophys. Res.,* 76:6339–6349.

Musgrave, R.J., Delaney, M.L., Stax, R., and Tarduno, J.A., 1993. Magnetic diagenesis, organic input, interstitial water chemistry, and paleomagnetic record of the carbonate sequence on the Ontong Java Plateau. *In* Berger, W.H., Kroenke, L.W., Mayer, L.A., et al., *Proc. ODP, Sci. Results,* 130: College Station, TX (Ocean Drilling Program), 527–546.

Perkins, M.E., Brown, F.H., Nash, W.P., McIntosh, W., and Williams, S.K., 1998. Sequence, age, and source of silicic fallout tuffs in middle to late Miocene basins of the Northern Basin and Range Province. *Geol. Soc. Am. Bull.,* 110:344–360.

Pfender, M., and Villinger, H., 2002. Miniaturized data loggers for deep sea sediment temperature gradient measurements. *Mar. Geol.*, 186:557–570.

Rampino, M.R., and Ambrose, S.H., 2000. Volcanic winter in the Garden of Eden: the Toba supereruption and the late Pleistocene human population crash. *In* McCoy, F.W., and Heiken, G. (Eds.), *Volcanic Hazards and Disasters in Human Antiquity.* Spec. Pap.—Geol. Soc. Am., 345:71–82.

Shipboard Scientific Party, 1997. Site 1039. *In* Kimura, G., Silver, E., Blum, P., et al., *Proc. ODP, Init. Repts.,* 170: College Station, TX (Ocean Drilling Program), 45–93.

————, 2003. Leg 206 Preliminary Report. *ODP Prelim. Rpt.,* 106 [Online]. Available from World Wide Web: <http://www-odp.tamu.edu/publications/prelim/206_prel/206PREL.PDF>. [Cited 2003-03-19]

————, in press. Site 1256. *In* Wilson, D.S., Teagle, D.A.H., Acton, G.D., et al., *Proc. ODP, Init. Repts.,* 206 [CD-ROM]. Available from: Ocean Drilling Program, Texas A&M University, College Station TX 77845-9547, USA.

Sigurdsson, H., Kelley, S., Leckie, R.M., Carey, S., Bralower, T., and King, J., 2000. History of Circum-Caribbean explosive volcanism: $^{40}Ar/^{39}Ar$ dating of tephra layers. *In*

Leckie, R.M., Sigurdsson, H., Acton, G.D., and Draper, G. (Eds.), *Proc. ODP, Sci. Results,* 165: College Station, TX (Ocean Drilling Program), 299–314.

Silver, E.A., Kastner, M., Fisher, A.T., Morris, J.D., McIntosh, K.D., and Saffer, D.M., 2000. Fluid flow paths in the Middle America Trench and Costa Rica margin. *Geology,* 28:679–682.

Smith, D.C., Spivack, A.J., Fisk, M.R., Haveman, S.A., Staudigel, H., and ODP Leg 185 Shipboard Scientific Party, 2000. Methods for quantifying potential microbial contamination during deep ocean coring. *ODP Tech. Note,* 28 [Online]. Available from World Wide Web: <http://www-odp.tamu.edu/publications/tnotes/tn28/INDEX.HTM>. [Cited 2002-09-02]

Wilson, D.S., Teagle, D.A.H., Acton, G.D., et al., in press. *Proc. ODP, Init. Repts.,* 206 [CD-ROM]. Available from: Ocean Drilling Program, Texas A&M University, College Station TX 77845-9547, USA.

Figure F1. Location of Site 1253. Drill sites occupied during Legs 205 (yellow circles) and 170 (white circles) are shown. The segment of multichannel seismic profile BGR 99-44 (red line) across Sites 1253 and 1039 is shown in Figure F2, p. 68.

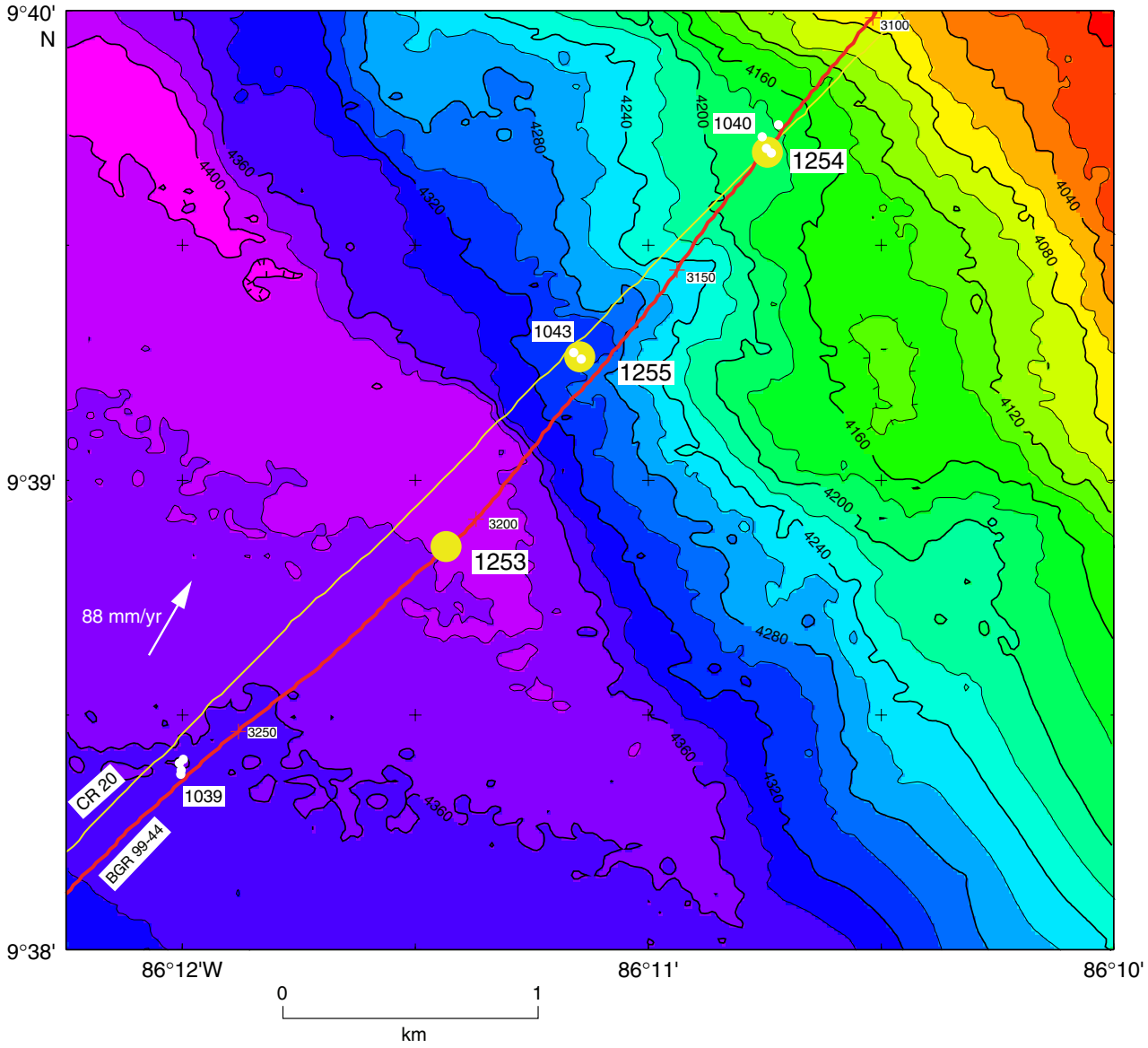

Figure F2. Portion of multichannel seismic profile BGR 99-44 across Sites 1253 and 1039. Location of seismic profile is shown in Figure F1, p. 67. Fig. F24, p. 66, in the "Leg 205 Summary" chapter, shows the BGR 99-44 seismic profile across all drill sites. Vertical exaggeration = 1.6.

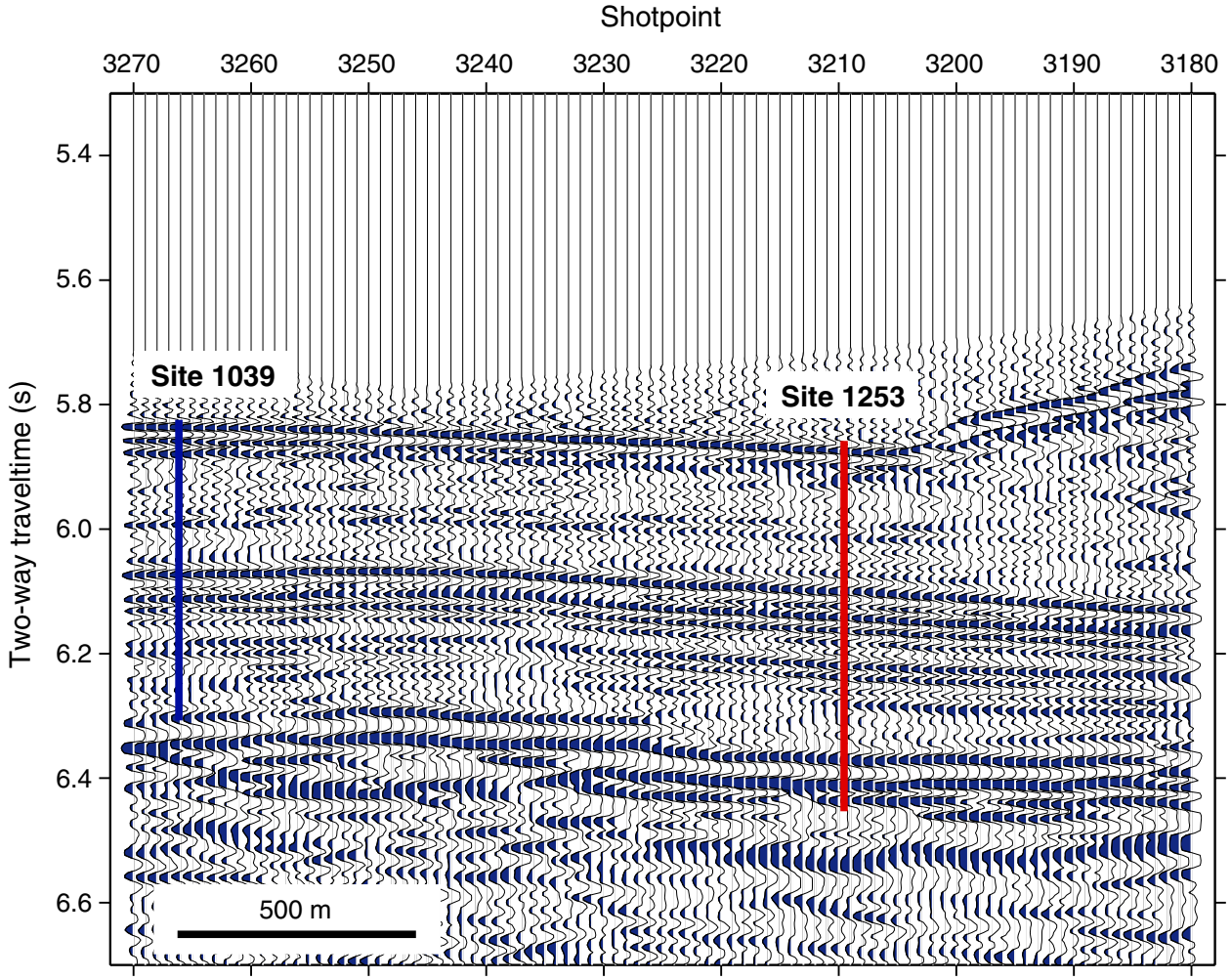

Figure F3. Hole 1253A borehole installation showing subseafloor depths for osmotic water samplers, screens, packers, and casing strings. This figure is not to scale.

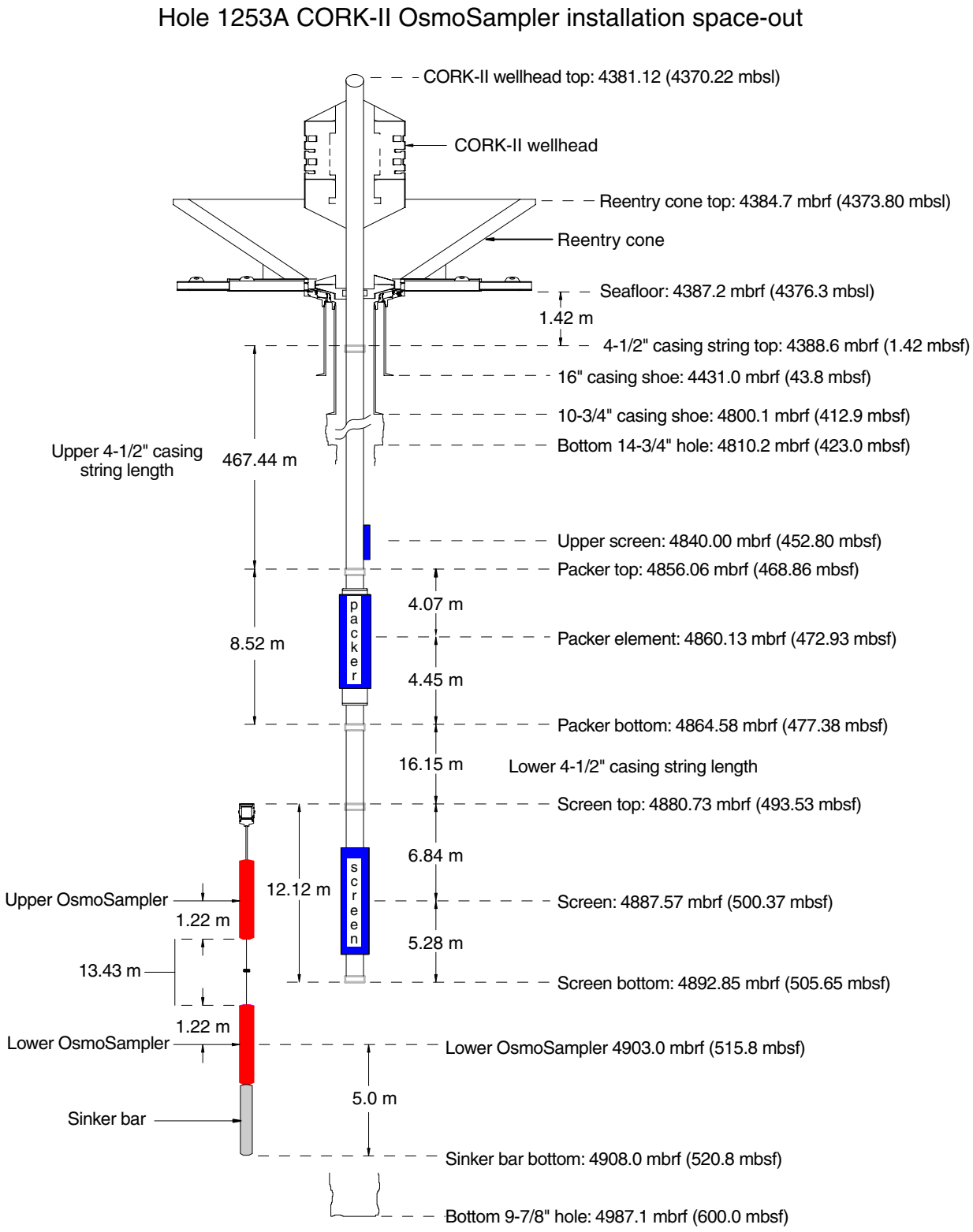

Figure F4. Composite diagram of pore fluid chemical data from Leg 205 and Leg 170, measured just above and below the gabbro sill (Subunit 4A). Dashed horizontal line = depth of the sill in Hole 1039C for comparison.

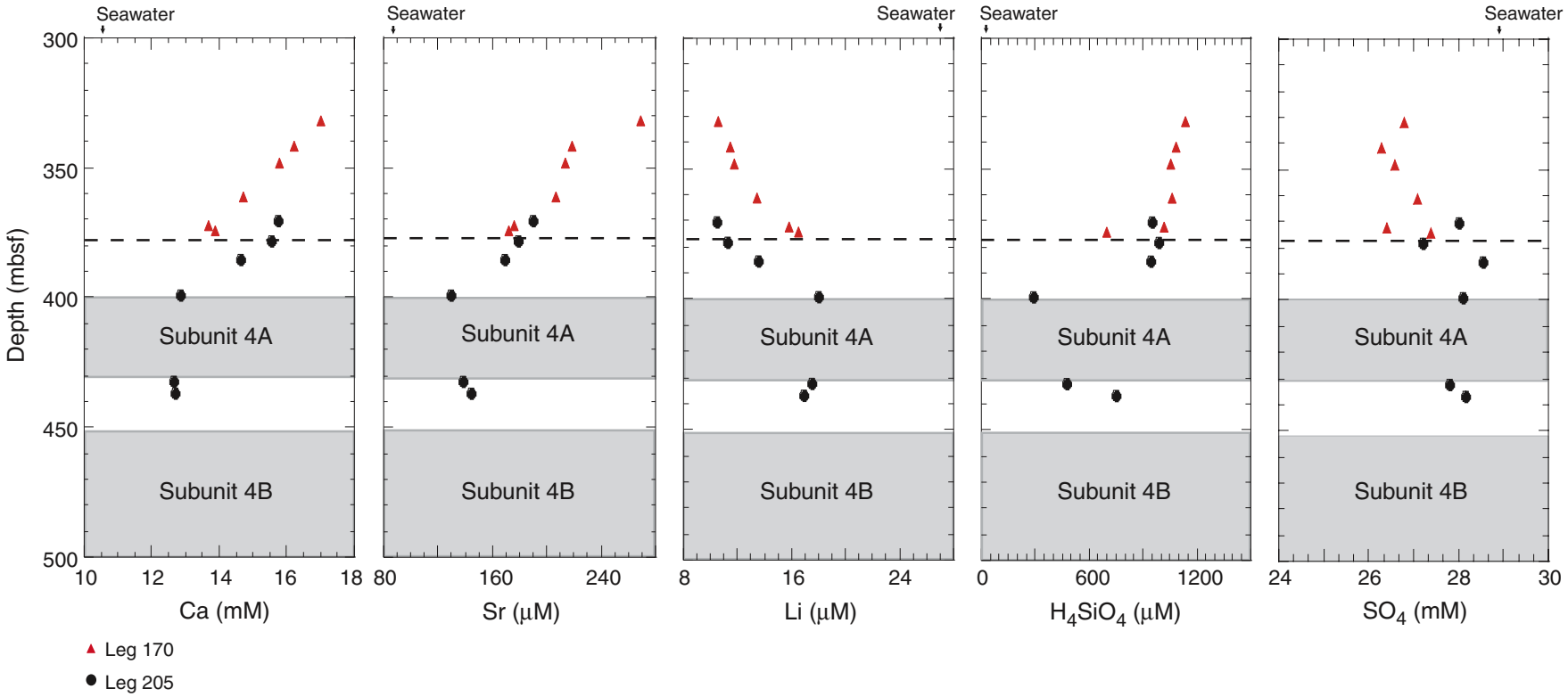

Figure F5. Composite diagram showing selected logging data annotated with physical property measurements on the cores, petrologic observations, and paleomagnetic and rock magnetism results. Petrologic and magnetic results are reported in the core reference frame, wherein Subunit 4B was curated at a depth of 450 mbsf. Logging data show that Subunit 4B begins at a depth of ~460 mbsf. Correlations between core and logging intervals are shown as solid lines to indicate major boundaries (bottom of Subunit 4A and top of Subunit 4B) or as dashed lines to indicate subunit boundaries identified petrologically. Labeled zones at the base of the petrologic section indicate the following observations: (1) location of the cryptocrystalline horizon of basaltic texture; (2) greater number of magmatic contacts; (3) more veins or voids filled with holo- and cryptocrystalline groundmass/altered glass, clay, and zeolites; (4) up to 5% degree of alteration within 1 m of Section 205-1253A-37R-1 and higher abundance of voids filled with clays and zeolites, ending in an homogeneous microcrystalline gabbro; (5) increasing number of centimeter-scale fractures and veins; and (6) very homogeneous microcrystalline to fine-grained gabbro with very weak magmatic contacts. Also indicated are the positions of the two OsmoSamplers (OS). (**Figure shown on next page.**)

Figure F5 (continued). (Caption shown on previous page.)

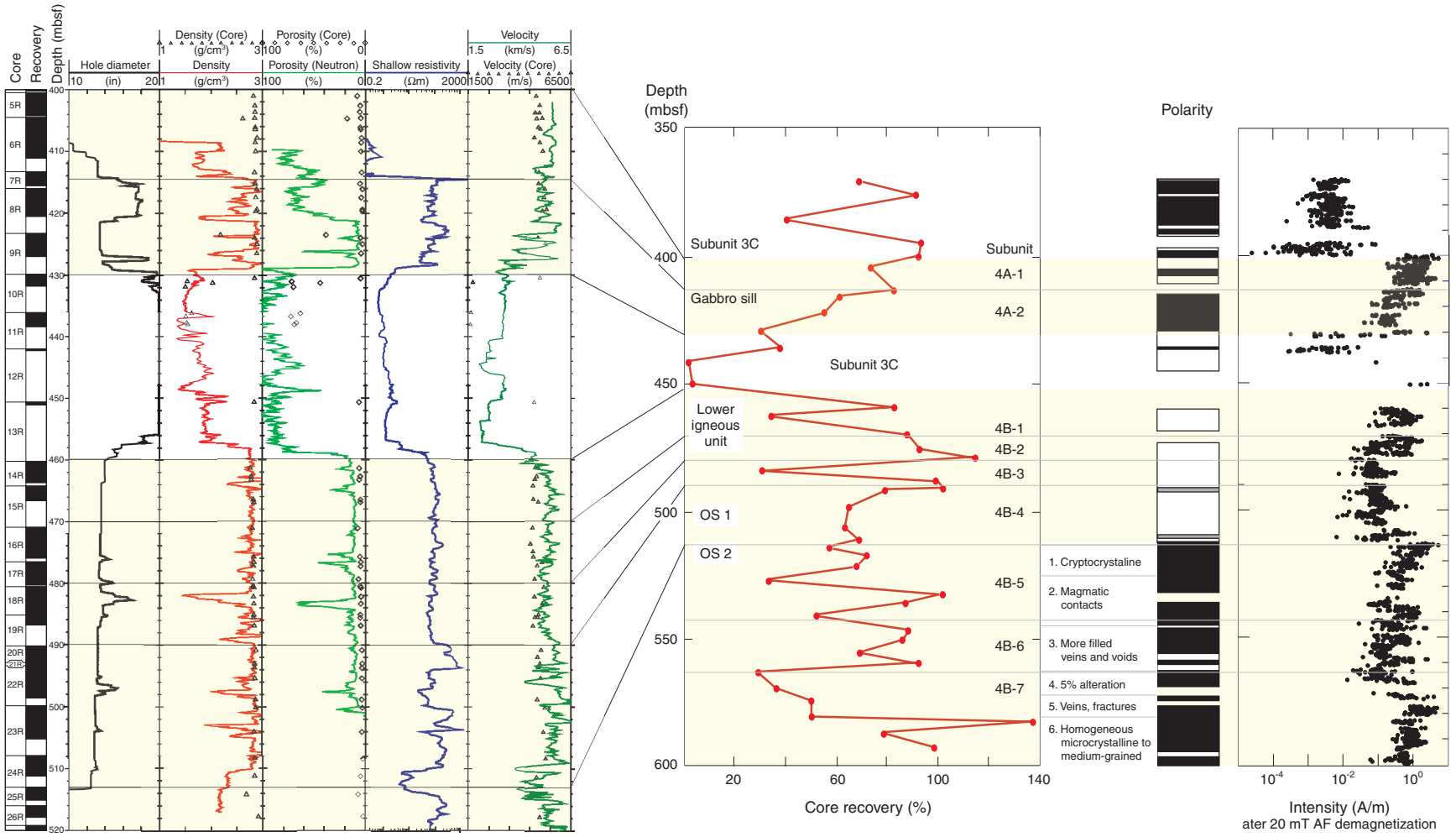

Figure F6. Composite diagram showing fracture distribution within the igneous units, core recovery and a summary of petrologic observations, and detailed FMS images for the depths at which OsmoSamplers (OS) 1 and 2 were installed.

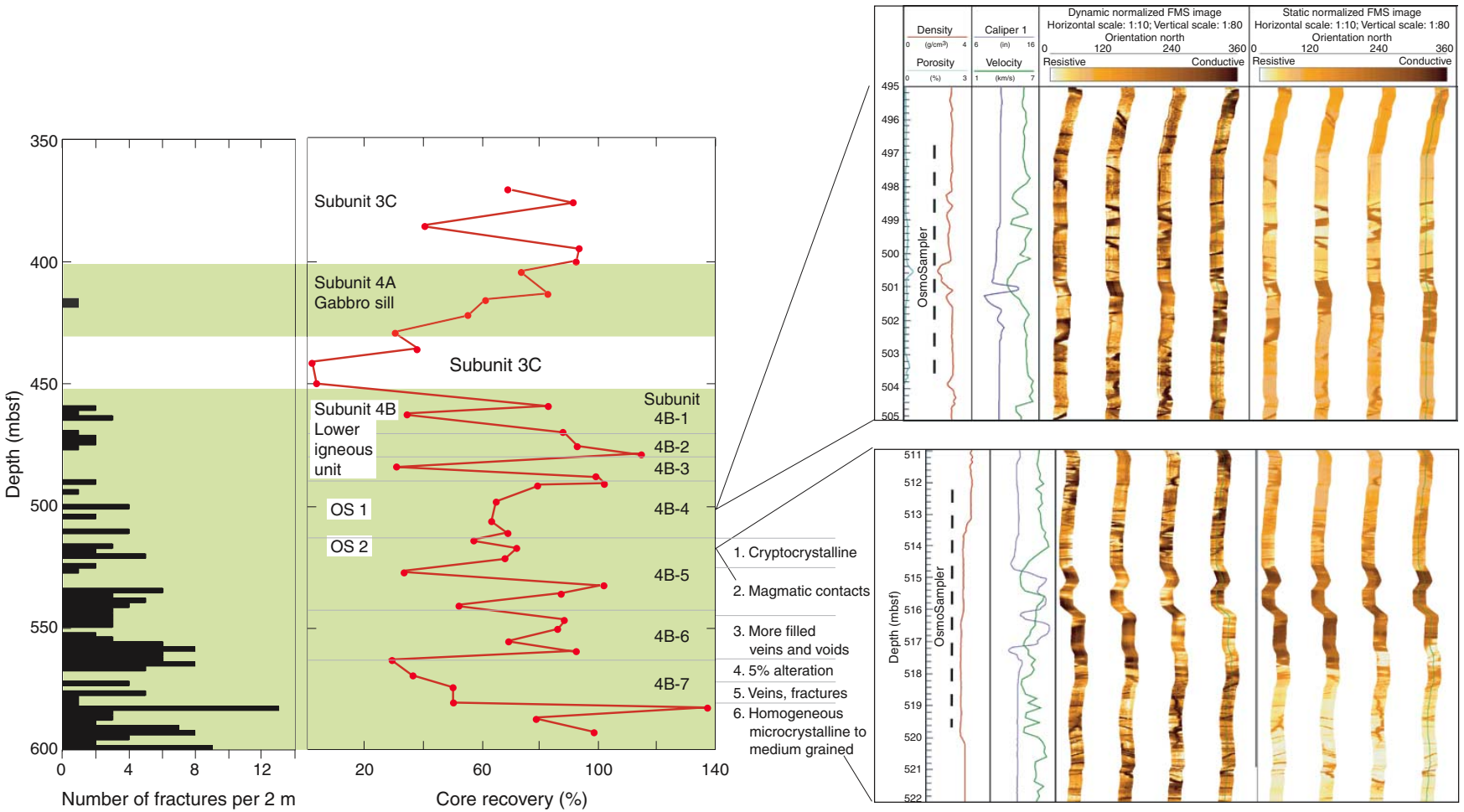

Figure F7. Composite stratigraphic log of the sedimentary section recovered at Sites 1039 and 1253, which shows the degree of recovery, the principal stratigraphic units consistent with those defined by the Leg 170 scientific party, and the variation in lightness and chromaticity measured by the archive multisensor track (AMST). Calcar. = calcareous.

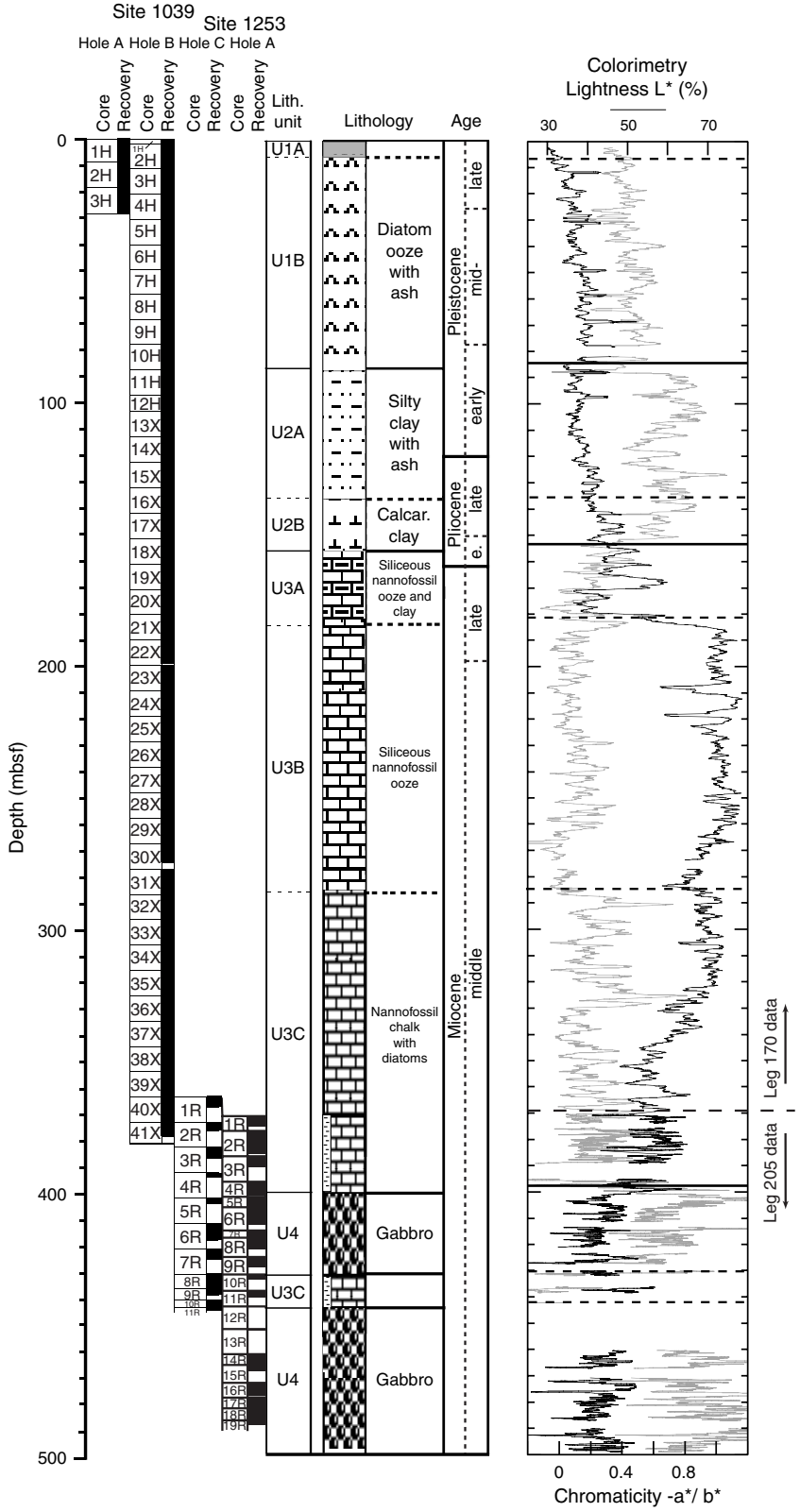

Figure F8. Close-up photograph of a typical section of the nannofossil chalk with diatoms that dominates lithostratigraphic Subunit U3C toward the base of the section (interval 205-1253A-2R-3, 67–80 cm). Note the pervasive bioturbation of *Planolites* and *Chondrites*.

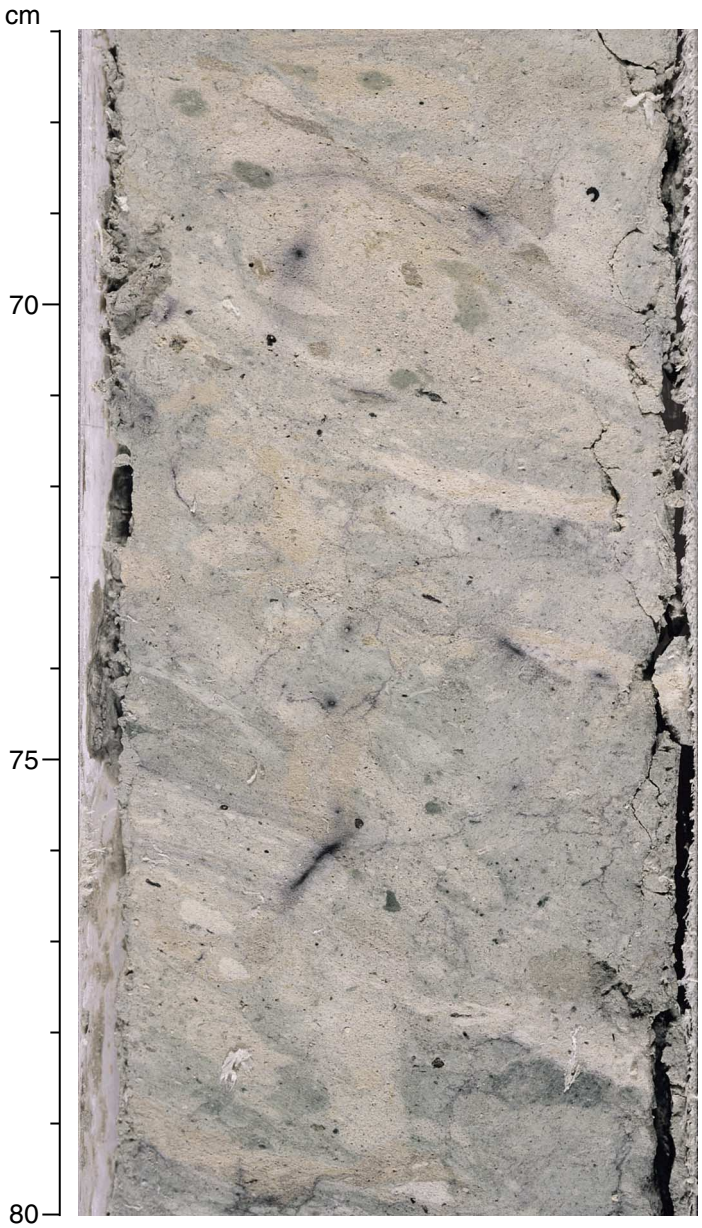

Figure F9. Photograph showing the darker-colored more laminated facies that directly overlies the gabbro sill of lithostratigraphic Subunit U4A (interval 205-1253A-4R-2, 70–78 cm). This section comprises calcite-rich claystone.

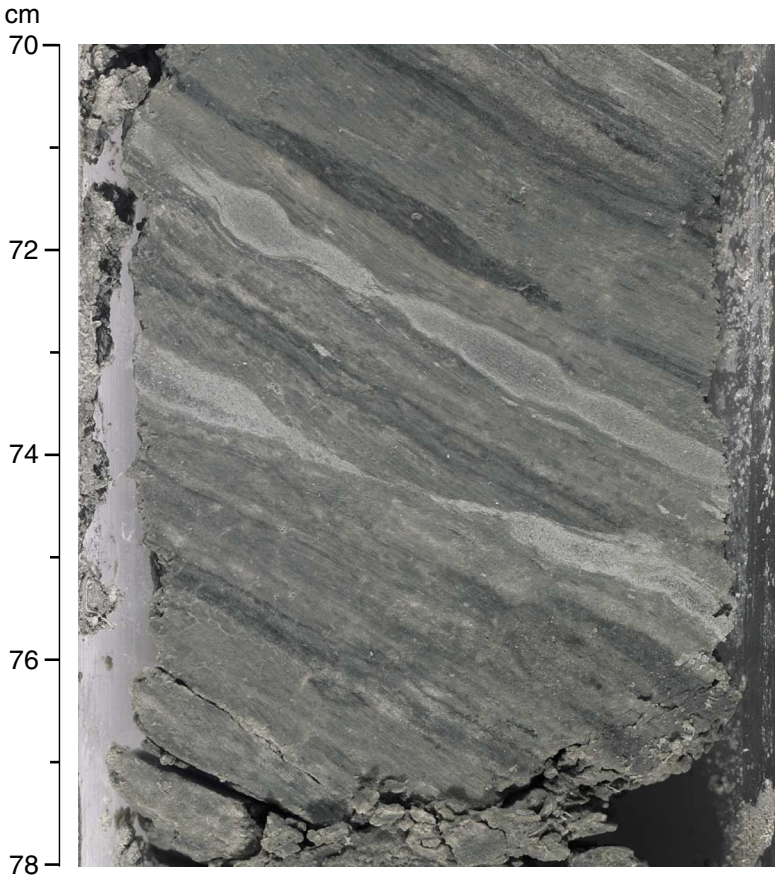

Figure F10. Close-up photograph showing a graded, redeposited layer of nannofossil chalk with clay and spicules interbedded within the dominant nannofossil chalk with foraminifers (interval 205-1253A-1R-1, 78–104 cm). Parallel lamination, darker color, and lack of bioturbation testify to the current controlled origin of this interval.

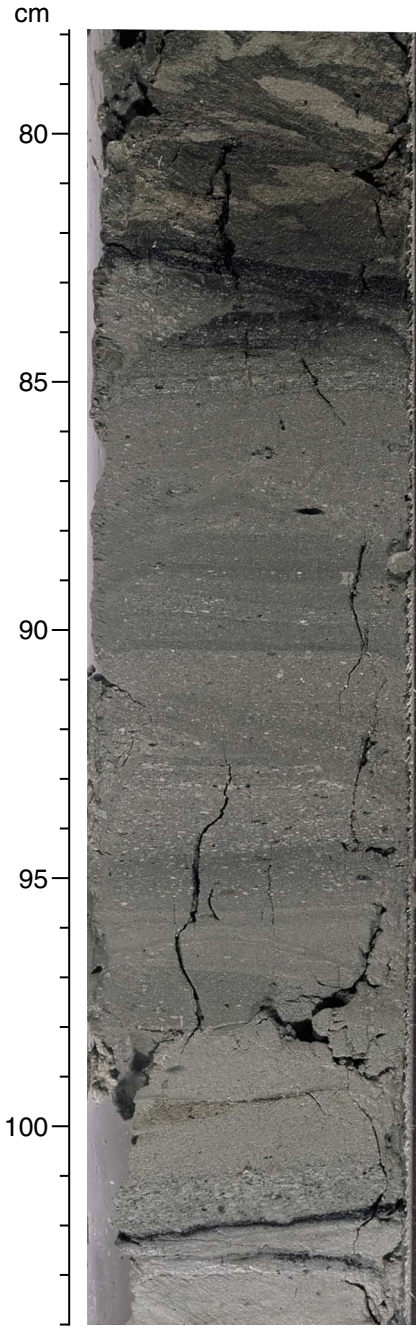

Figure F11. Photomicrographs of smear slides made from sediments recovered from Hole 1253A. **A.** Nannofossil chalk with foraminifers and spicules (Sample **205-1253A-1R-2, 65 cm**). **B.** Clay, nannofossil, and volcanic ash mixed sediment (Sample **205-1253A-2R-1, 76 cm**). **C.** Claystone with volcanic ash (Sample **205-1253A-4R-2, 113 cm**). **D.** Calcite-rich nannofossil chalk (Sample **205-1253A-10R-2, 101 cm**). **E.** Volcanic ash with clay (Sample **205-1253A-4R-3, 90 cm**). **F.** Claystone with zeolites (Sample **205-1253A-4R-3, 40 cm**).

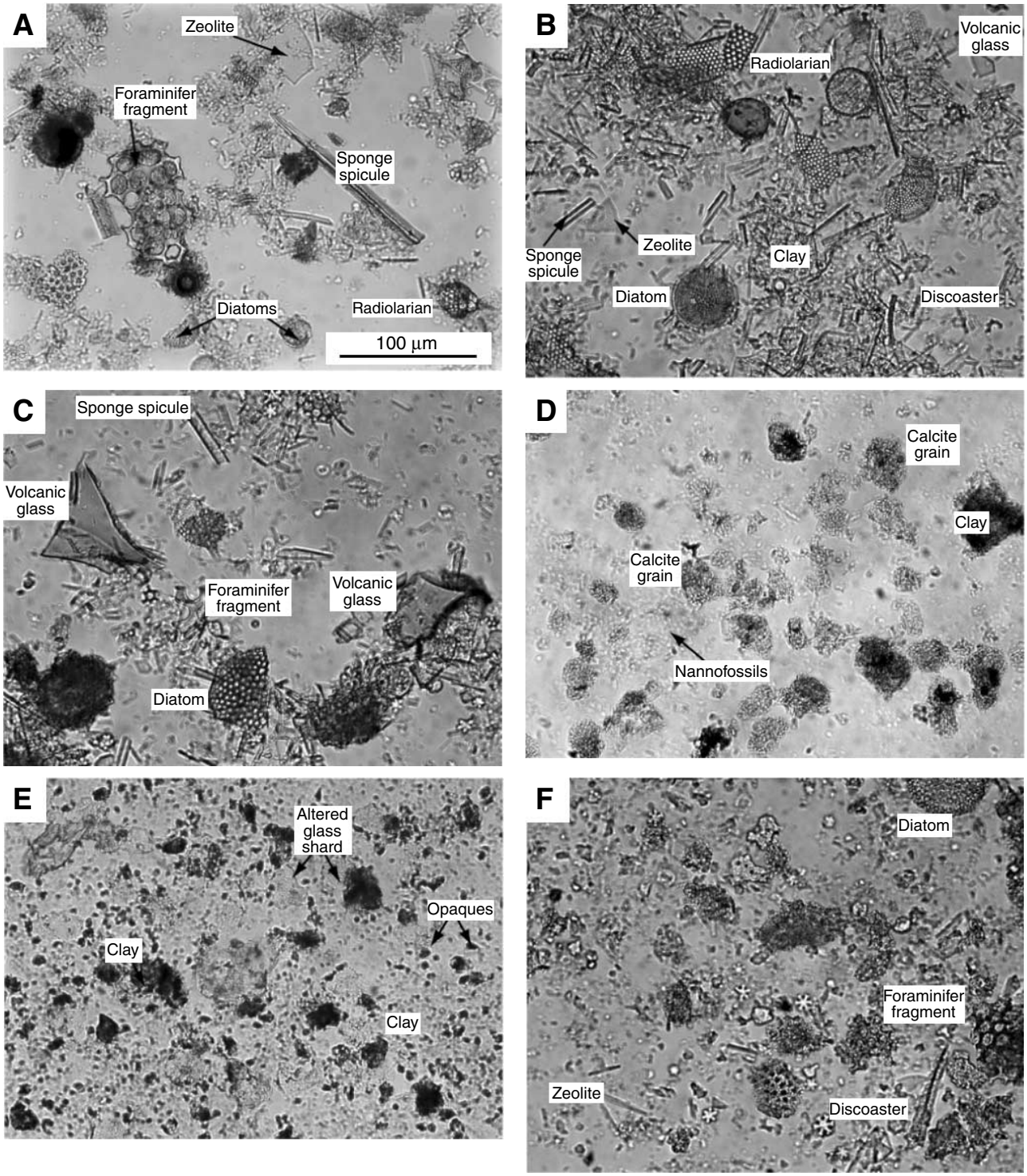

Figure F12. Diagram showing the variation in various sedimentary components with depth in the sequence at Sites 1039 and 1253 as identified in smear slide analyses during Legs 205 and 170. Plots show only where the component was considered to be abundant (>30%). Sandy beds are only present as minor lithologies and are restricted to lithostratigraphic Units U1 and U2. Diatoms are present throughout the core but are most common in lithostratigraphic Unit U1; conversely, nannofossil abundance is higher in lithostratigraphic Subunits U3A–U3C. Volcanic ash is present throughout the section.

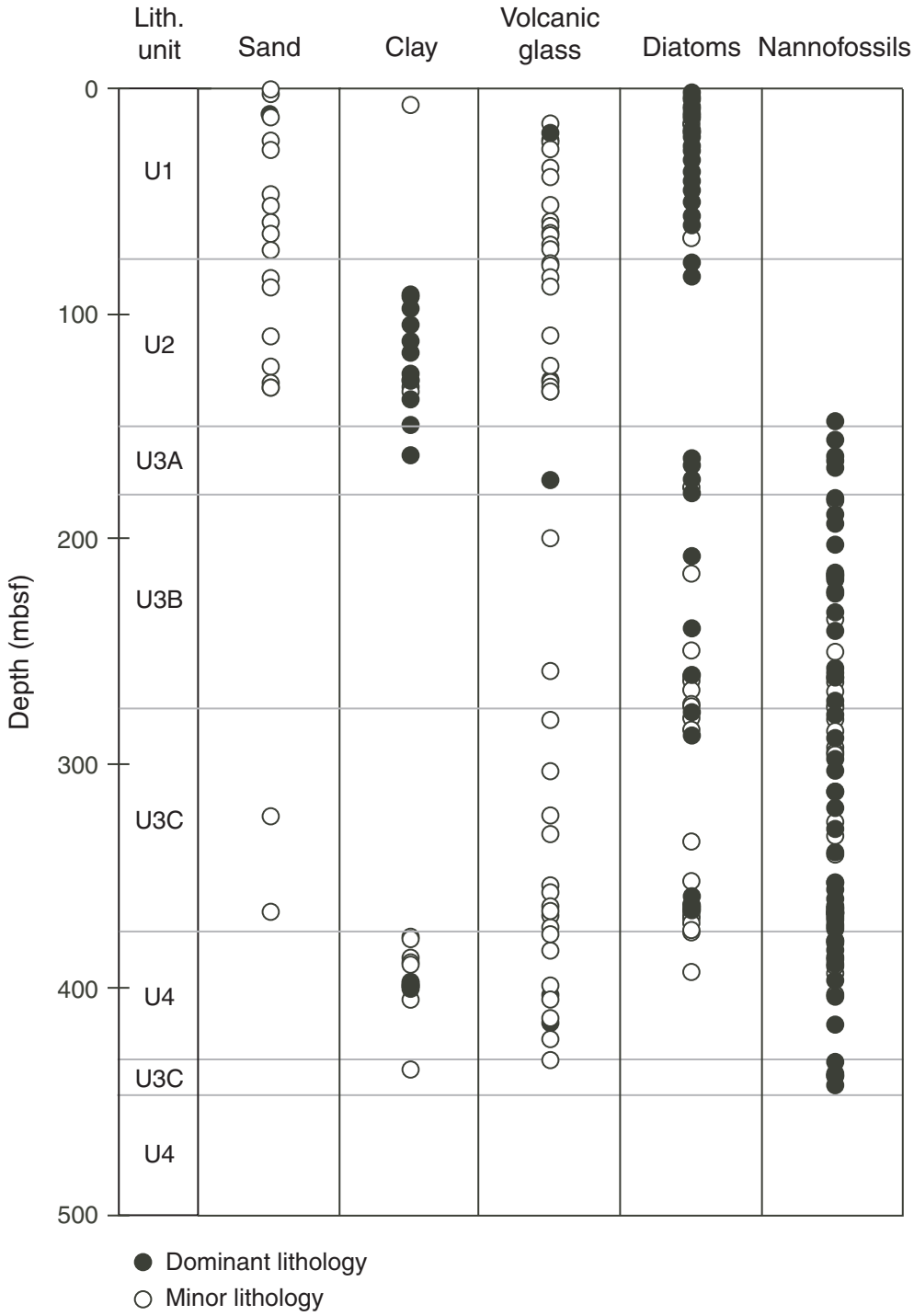

Figure F13. Close-up photograph showing a light-colored altered volcanic ash layer within the background sedimentation of claystone with zeolites (interval 205-1253A-4R-3, 82–94 cm). High degree of alteration and induration may reflect proximity to the gabbro sill of lithostratigraphic Subunit U4B, which lies slightly >2 m below the bed.

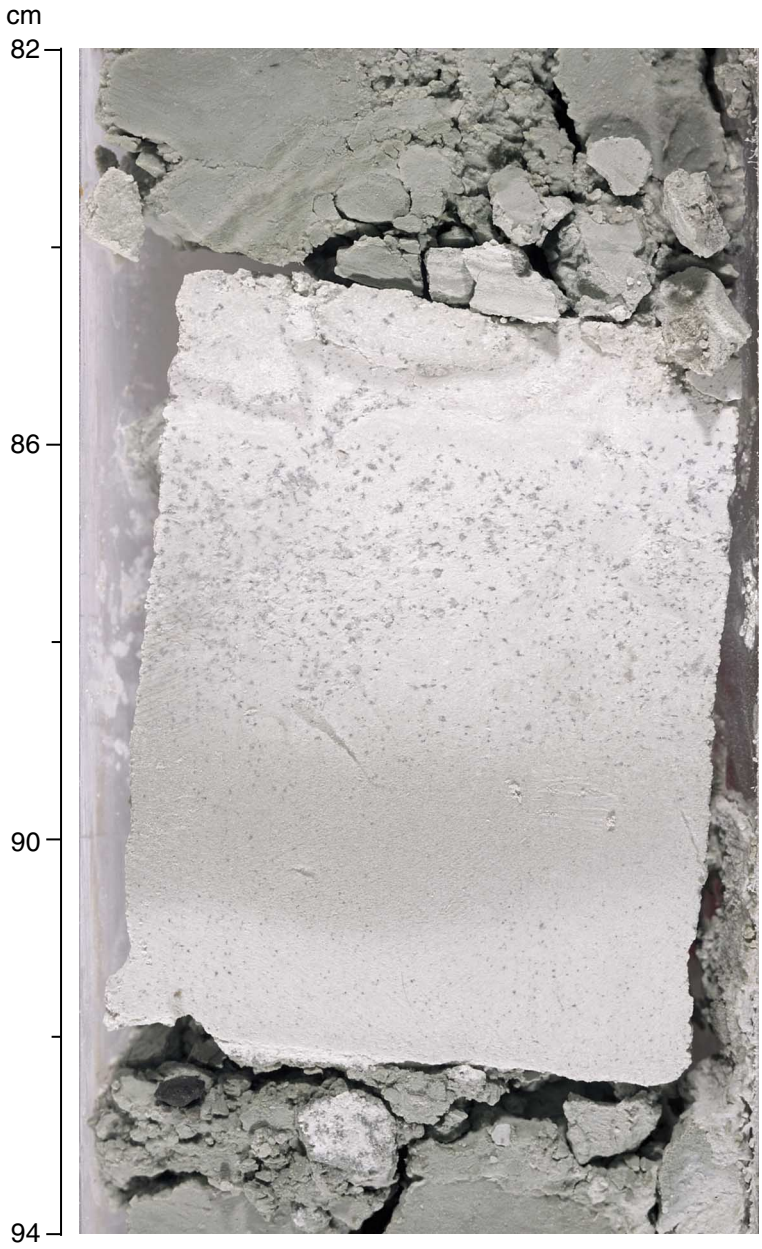

Figure F14. Close-up photograph showing *Zoophycos* ichnofossils disturbing a clay-rich interval within the dominant nannofossil chalk with diatoms (interval 205-1253A-2R-3, 92–107 cm). This trace fossil is indicative of deposition within abyssal water depth (>2000 m).

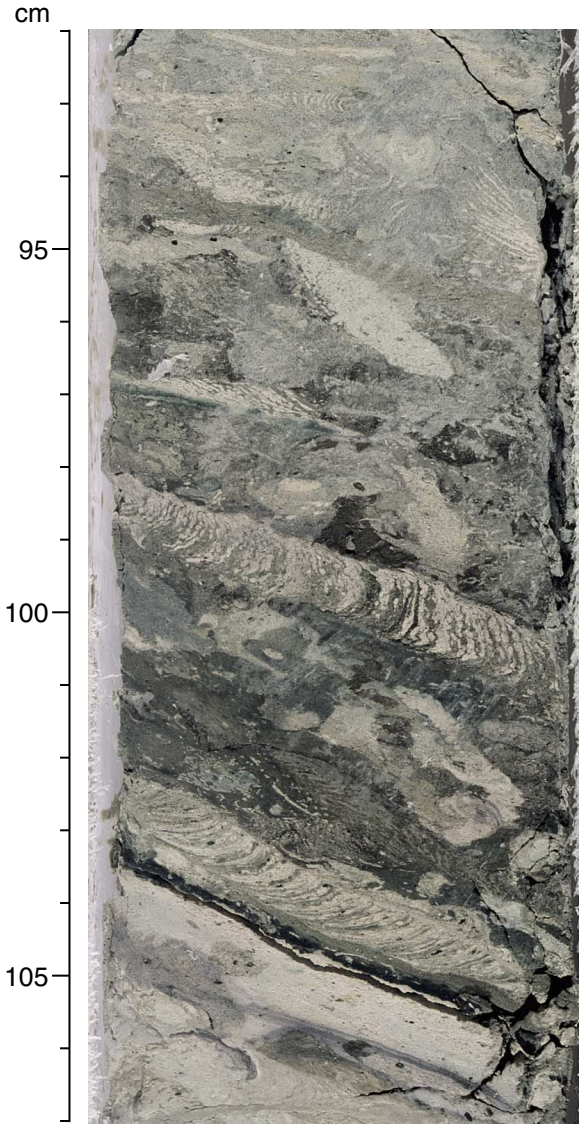

Figure F15. Depth profiles of (**A**) TiO_2, (**B**) Al_2O_3, (**C**) SiO_2, and (**D**) Ti/Al concentrations. Subunit 4A = gabbro sill, Subunit 4B = lower igneous section. Circles = basal sediments, red diamonds = volcanic ash samples, and triangles = baked sediments.

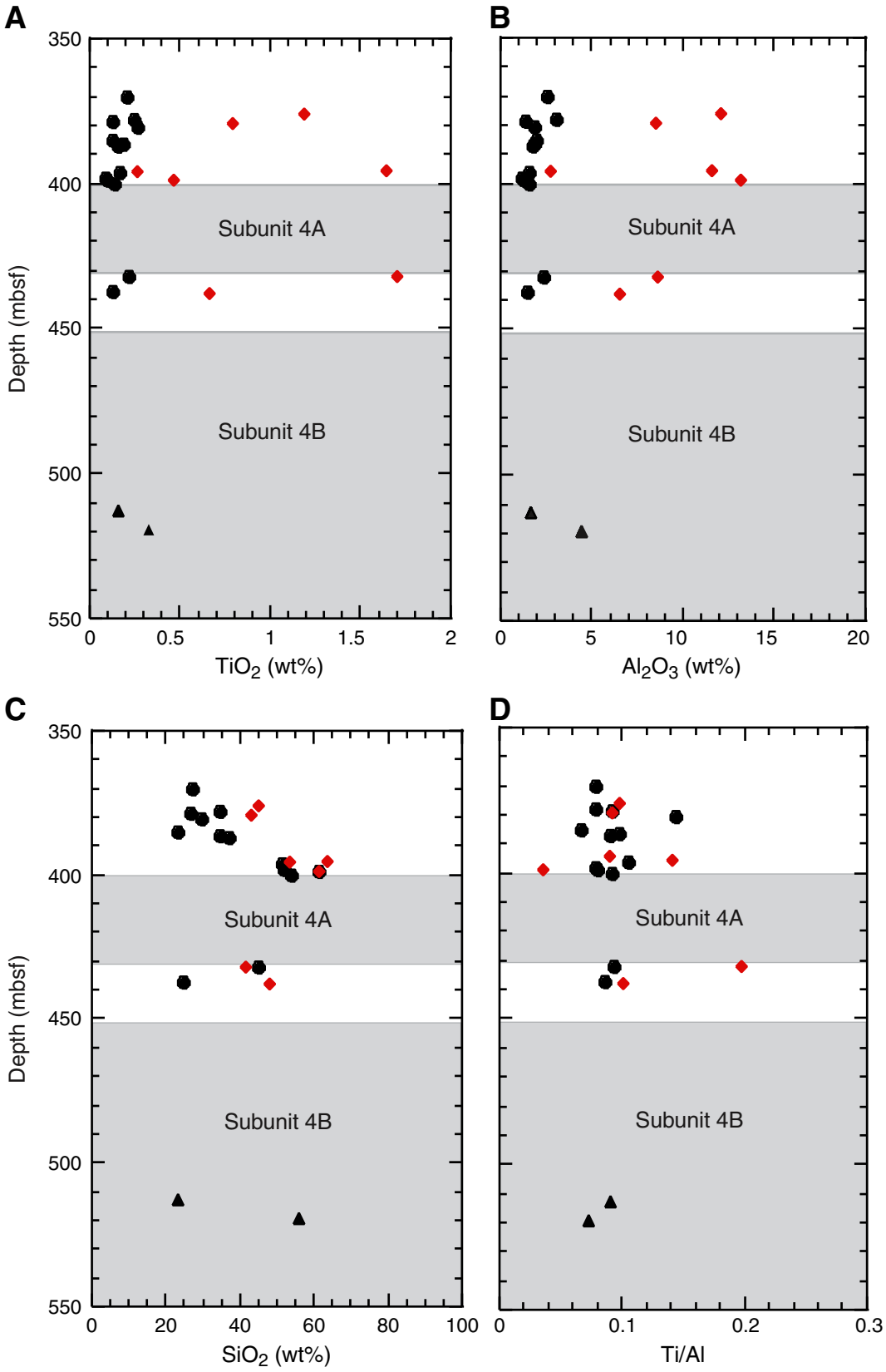

Figure F16. Depth profiles of (A) CaO, (B) MgO, (C) Sr, and (D) Ba concentrations. Circles = basal sediments, red diamonds = volcanic ash samples, and triangles = baked sediments.

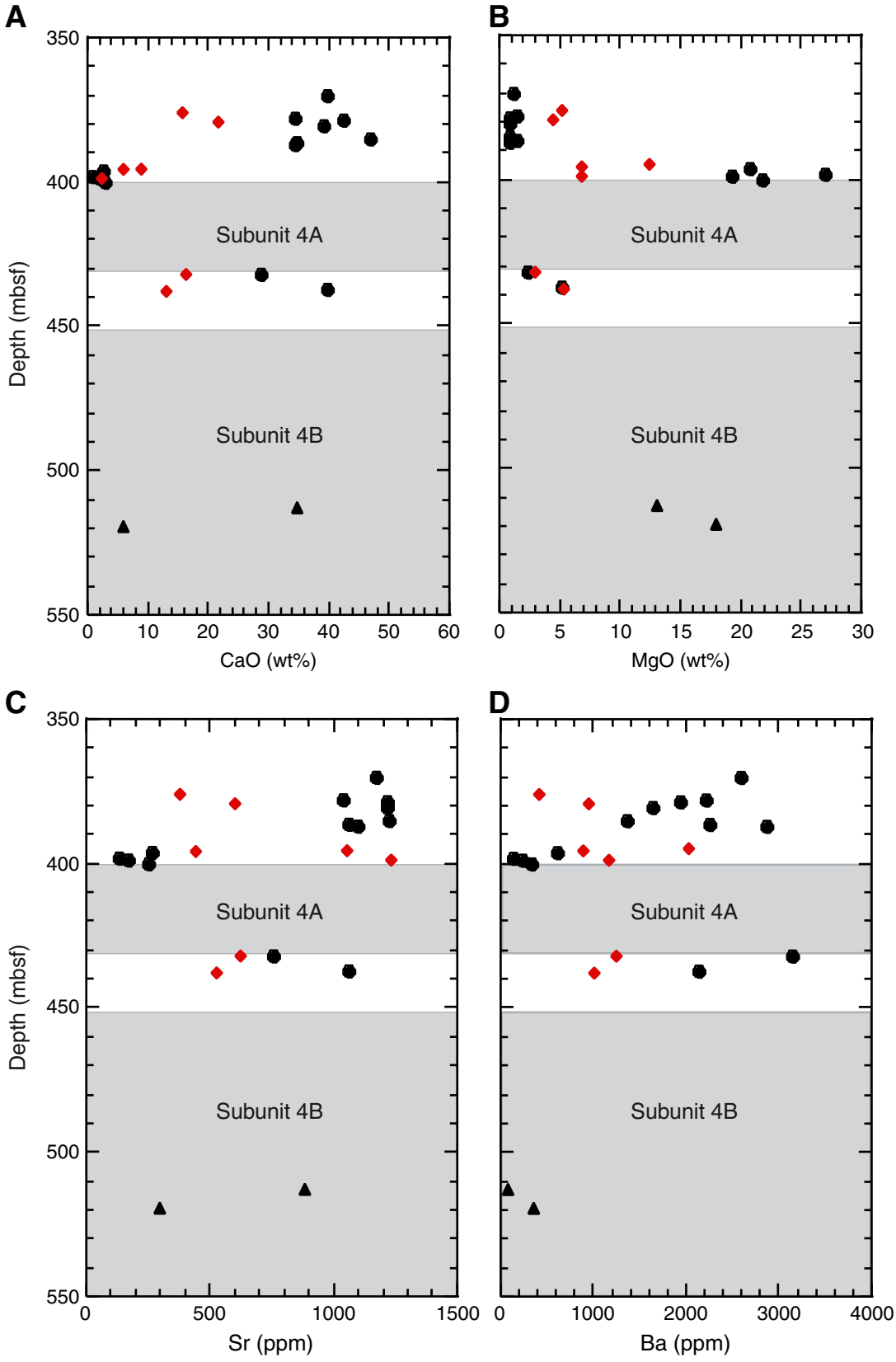

Figure F17. Depth profiles of (**A**) Na_2O and (**B**) K_2O concentrations. Circles = basal sediments, red diamonds = volcanic ash samples, and triangles = baked sediments.

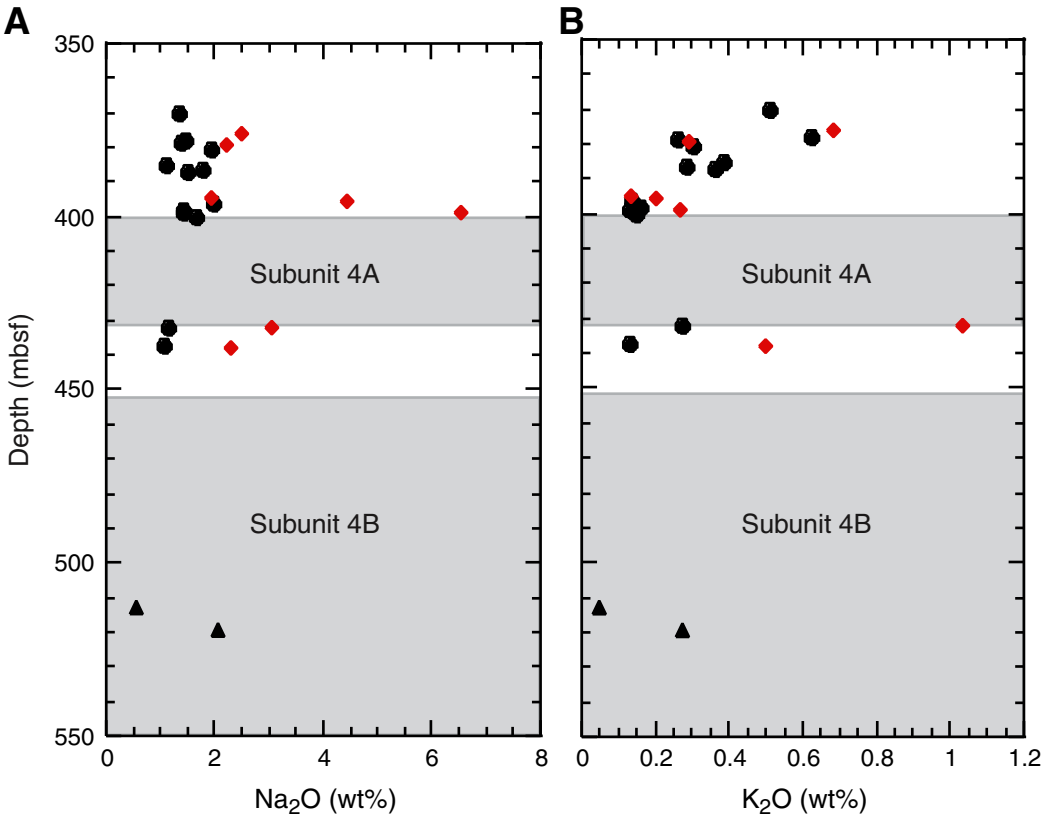

Figure F18. Photomicrograph of the white tephra layer (Sample 205-1253A-4R-3, 85–93 cm). Note the fresher vesicular glass shard surrounded by more altered glass shards that are largely transformed to palagonite.

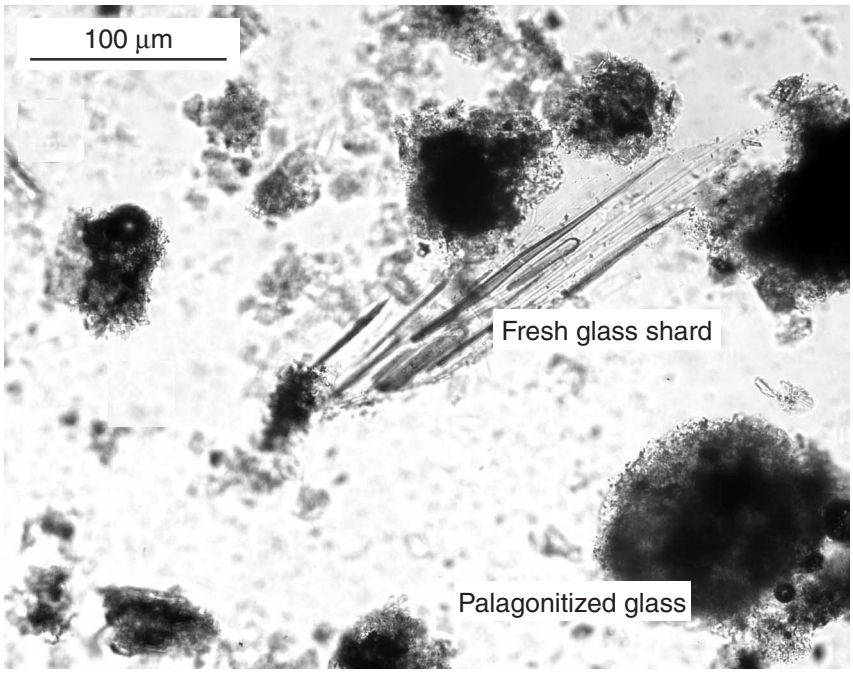

Figure F19. Close-up photograph of microcrystalline to fine-grained homogeneous holocrystalline gabbro (interval 205-1253A-8R-2 [Piece 2, 45–60 cm]).

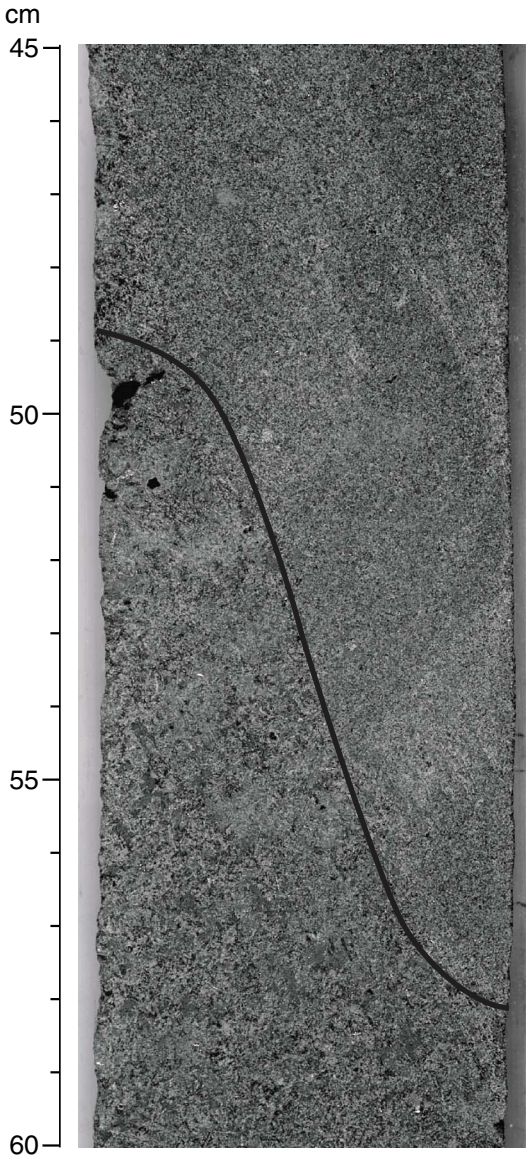

Figure F20. Structural, textural, and mineralogical features of Subunit 4A Cores 205-1253A-4R through 10R described in terms of veins, fractures, magmatic contacts, and voids and proportions of each mineral phenocryst. Core photographs illustrate representative features of Subunit 4A. Blue = medium grained, green = fine grained, yellow = microcrystalline, white = cryptocrystalline. A = aggregates, L = laths. Phenocryst percentage expresses mineral abundance over the full section length. Y = yes, evidence of voids. The number of plus or minus symbols rates the abundance of voids. Subunit 4A is further subdivided into Subunits 4A-1 and 4A-2 (see **"General Description,"** p. 26, in "Subunit U4A: Gabbro Sill" in "Petrology"). Magnetic polarity is also shown. **A.** Close-up photograph of veining within upper Subunit 4A-1 (interval 205-1253A-5R-4, 14–25 cm). **B.** Close-up photograph of the changes in grain size groundmass on a centimeter scale (interval 205-1253A-7R-1, 130–146 cm). 1, 6. Microcrystalline gabbro. 2. Cumulate fine- to medium-grained groundmass. 3. Microcrystalline groundmass. 4. Fine-grained groundmass with 10% pyroxene phenocrysts (1-mm size and subhedral). 5. Microcrystalline to fine-grained groundmass. **C.** Example of magmatic contact (interval 205-1253A-8R-1, 84–89 cm). (**Figure shown on next page.**)

Figure F20 (continued). (Caption shown on previous page.)

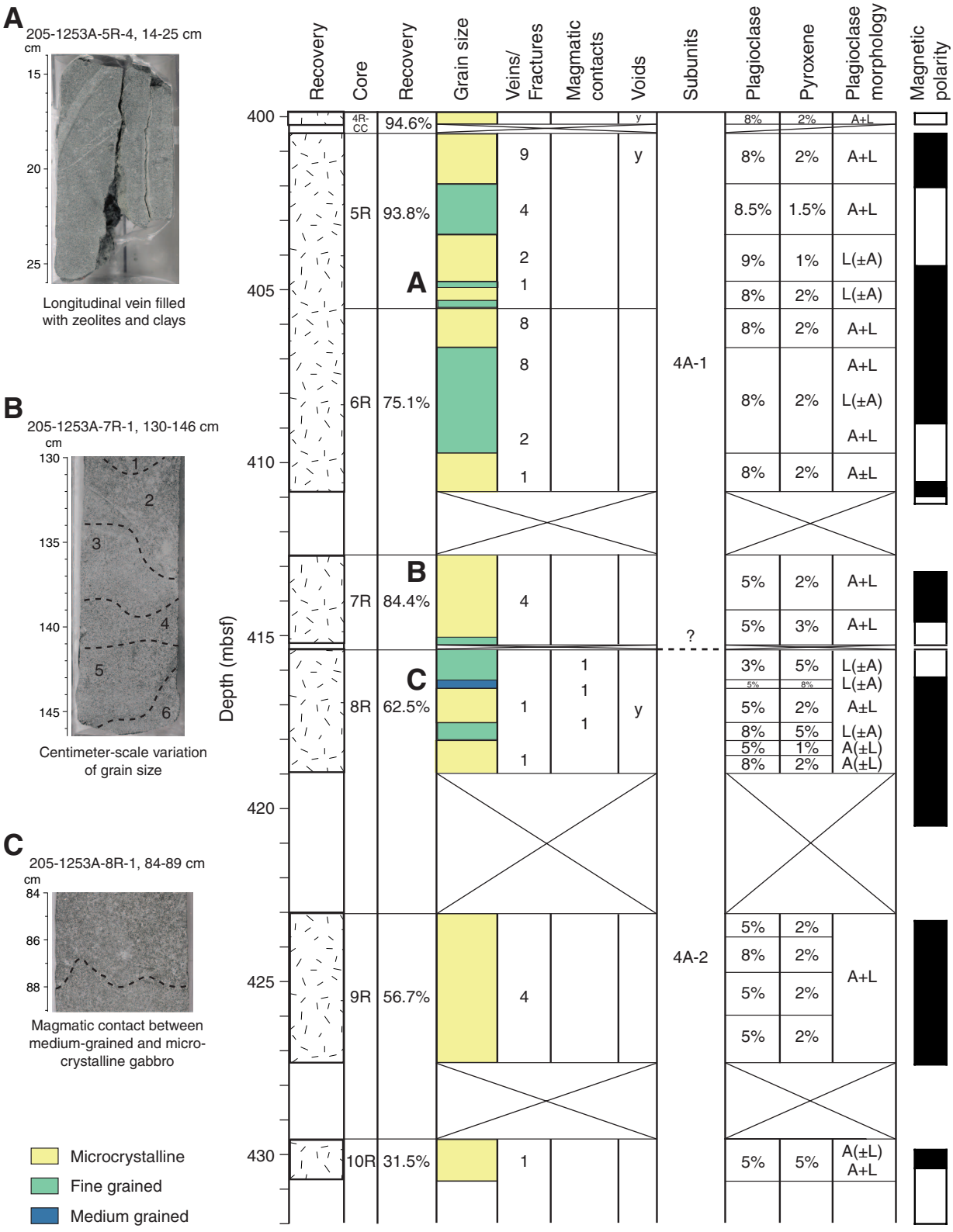

Figure F21. Photomicrograph of thin section in cross-polarized light illustrating the microcrystalline gabbro observed within Subunit 4A (Sample **205-1253A-8R-1, 24–27 cm;** thin section 13). Mag = magnetite, Pl = plagioclase, Ilm = ilmenite, Cpx = clinopyroxene.

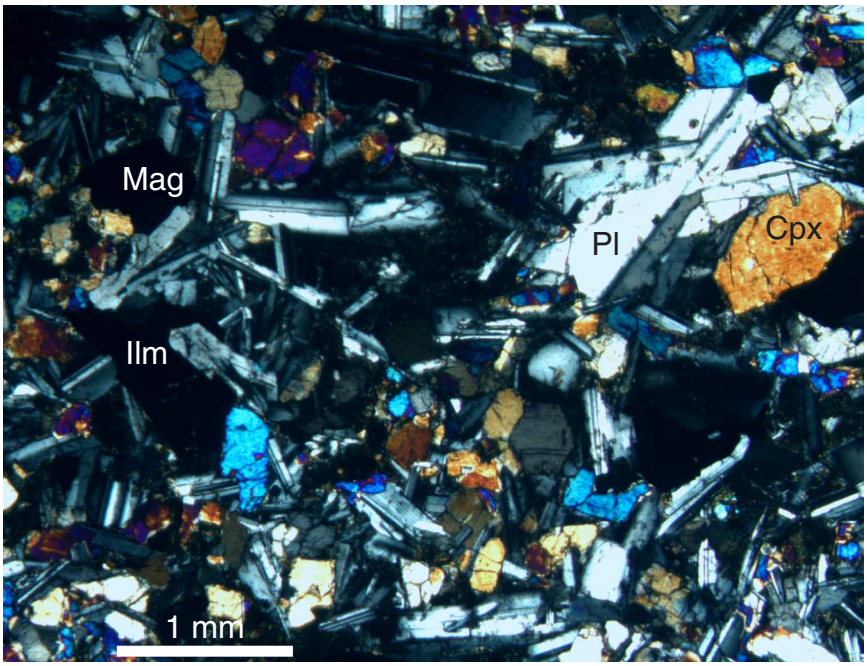

Figure F22. Photomicrographs of thin sections in cross-polarized light. Both figures show inclusions of glass, altered glass, and possibly clinopyroxene in plagioclase phenocrysts. Inclusions, with various morphologies, are mostly restricted to the phenocryst center. Rare inclusions are observed in clinopyroxene. Cpx = clinopyroxene, Pl = plagioclase. **A.** Sample **205-1253A-8R-1, 85–88 cm** (thin section 15). **B.** Sample **205-1253A-8R-2, 52–55 cm** (thin section 17).

A

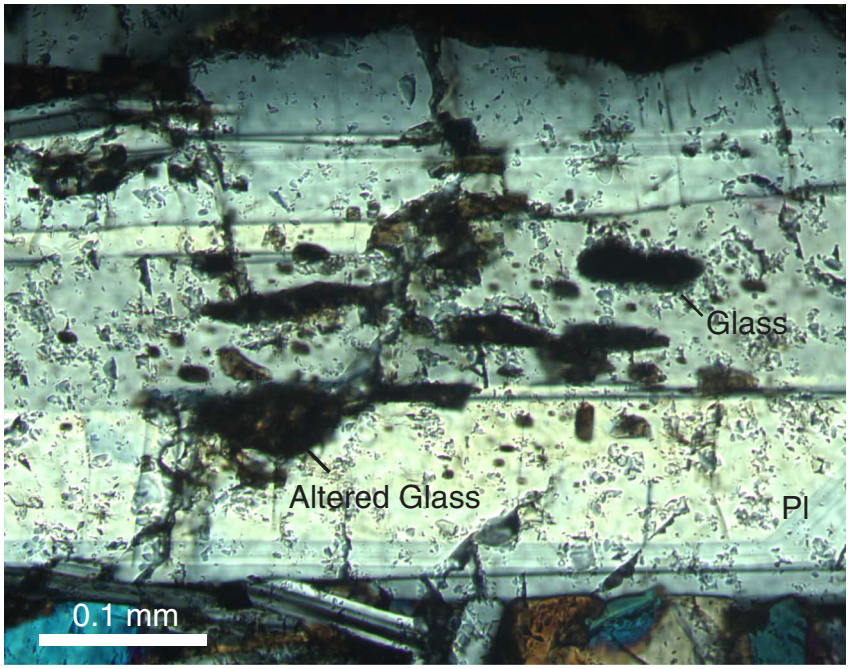

B

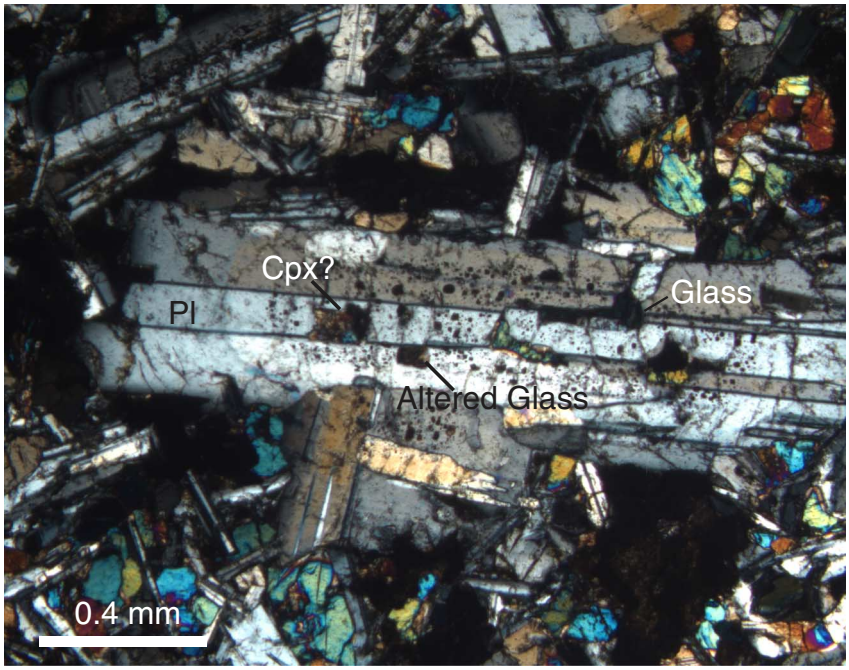

Figure F23. Close-up photograph of a vein of cryptocrystalline to holocrystalline groundmass within microcrystalline gabbro (interval 205-1253A-7R-2 [Piece 2, 91–96 cm]).

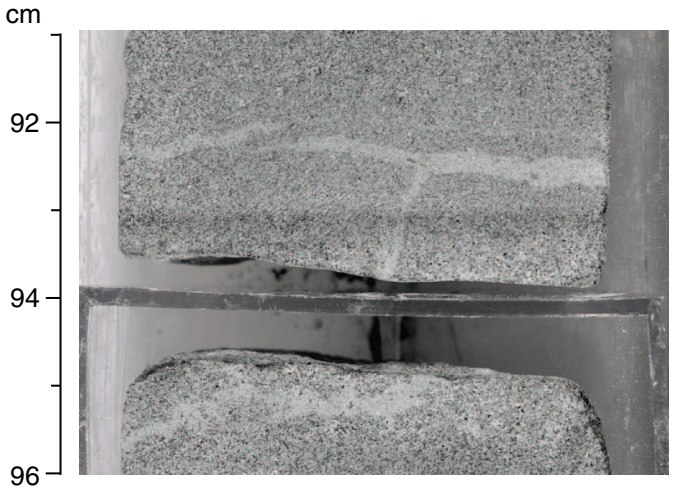

Figure F24. Alteration of primary minerals in Subunit 4A. Pl = Plagioclase, Ilm = ilmenite, Ol = olivine. **A.** Completely altered primary mineral, replaced by clay (Sample 205-1253A-7R-1, 130–133 cm; 414.6 mbsf). **B.** Olivine completely altered to clay (Sample 205-1253A-8R-1, 24–27 cm; 416.24 mbsf). **C.** Olivine mostly replaced by clay (Sample 205-1253A-8R-1, 24–27 cm; 416.24 mbsf). **D.** Altered plagioclase replaced by a mixture of clay and isotropic secondary products (Sample 205-1253A-8R-1, 24–27 cm; 416.24 mbsf).

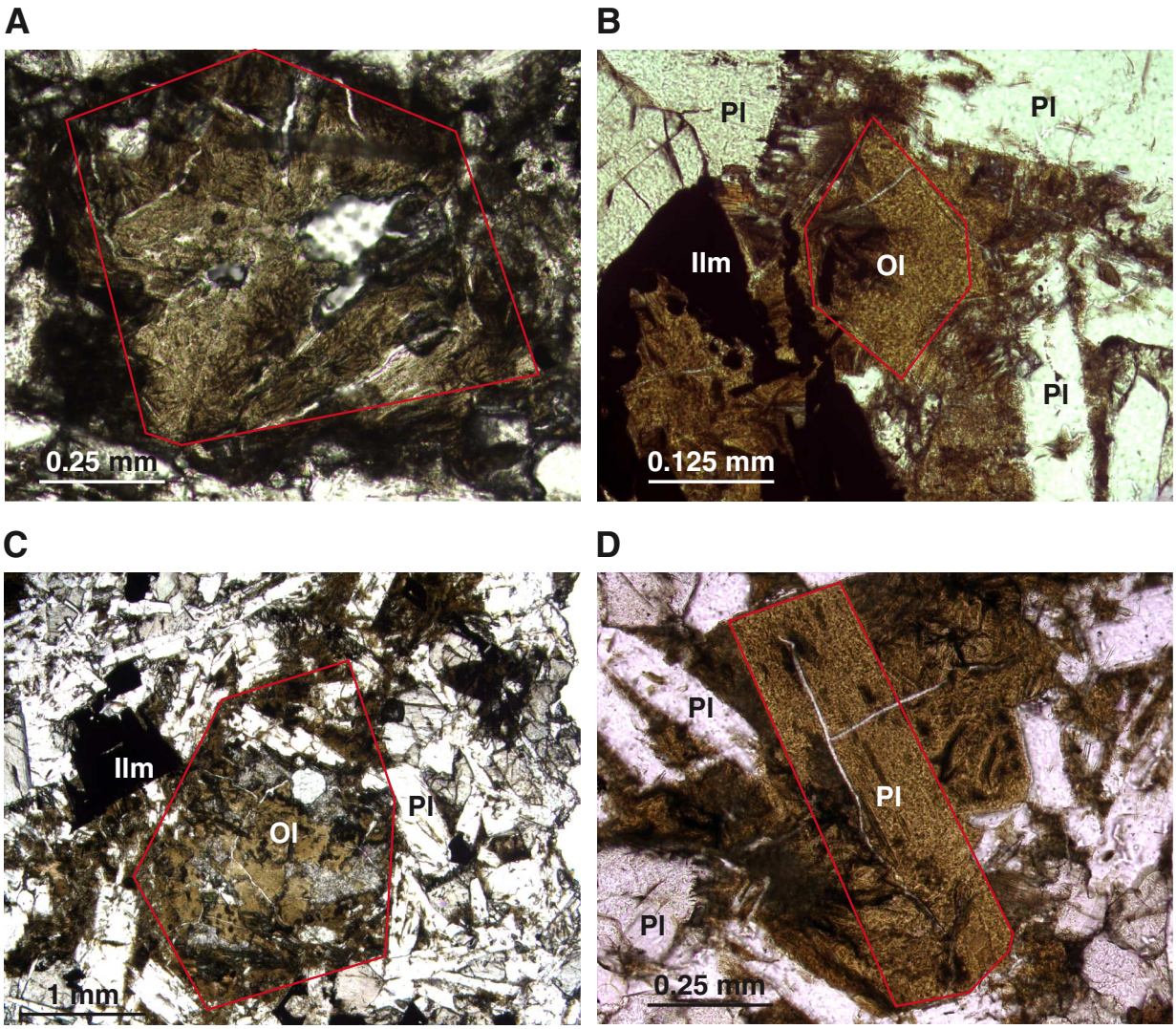

Figure F25. Structural, textural, and mineralogical features of Subunit 4B Cores 205-1253A-12R through 16R described in terms of veins, fractures, magmatic contacts, and voids and proportions of each mineral phenocryst. Additional pictures illustrate the typical features of Subunit 4B. Blue = medium grained, green = fine grained, yellow = microcrystalline, white = cryptocrystalline. A = aggregates, L = laths. Phenocryst percentage expresses mineral abundance over the full section length. Y = yes, evidence of voids. The number of plus or minus symbols rates the abundance of voids. Magnetic polarity and close-up photographs of the main core macroscopic features are also shown. 1, 6. Microcrystalline gabbro. 2. Cumulate fine- to medium-grained groundmass. 3. Microcrystalline groundmass. 4. Fine-grained groundmass with 10% pyroxene phenocrysts (1-mm size and subhedral). 5. Microcrystalline to fine-grained groundmass. See text for criteria used to further subdivide Subunit 4B. **A.** Interval 205-1253A-12R-1, 26–37 cm. **B.** Interval 205-1253A-16R-1, 109–116 cm. (**Figure shown on next page.**)

Figure F25 (continued). (Caption shown on previous page.)

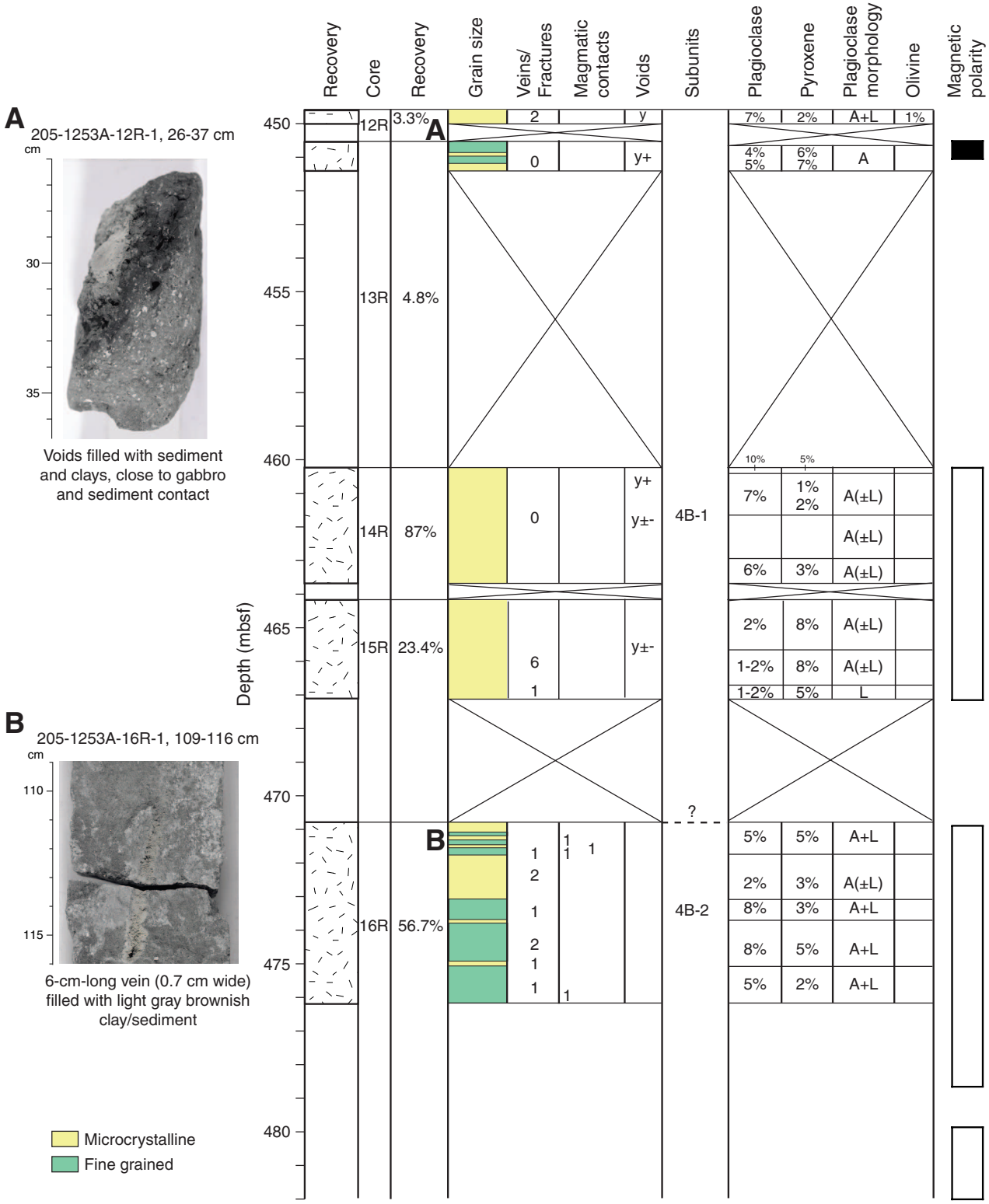

Figure F26. Structural, textural, and mineralogical features of Subunit 4B Cores 205-1253A-16R through 22R described in terms of veins, fractures, magmatic contacts, and voids and proportions of each mineral phenocryst. Additional pictures illustrate the typical features of Subunit 4B. Blue = medium grained, green = fine grained, yellow = microcrystalline, white = cryptocrystalline. A = aggregates, L = laths. Phenocryst percentage expresses mineral abundance over the full section length. Y = yes, evidence of voids. The number of plus or minus symbols rates the abundance of voids. Magnetic polarity and close-up photographs of the main core macroscopic features are also shown. See text for criteria used to further subdivide Subunit 4B. 1, 6. Microcrystalline gabbro. 2. Cumulate fine- to medium-grained groundmass. 3. Microcrystalline groundmass. 4. Fine-grained groundmass with 10% pyroxene phenocrysts (1-mm size and subhedral). 5. Microcrystalline to fine-grained groundmass. **A.** Interval 205-1253A-17R-2, 0–3 cm. **B.** Interval 205-1253A-17R-2, 100–129 cm. **C.** Interval 205-1253A-22R-1, 28–35 cm. (**Figure shown on next page.**)

Figure F26 (continued). (Caption shown on previous page.)

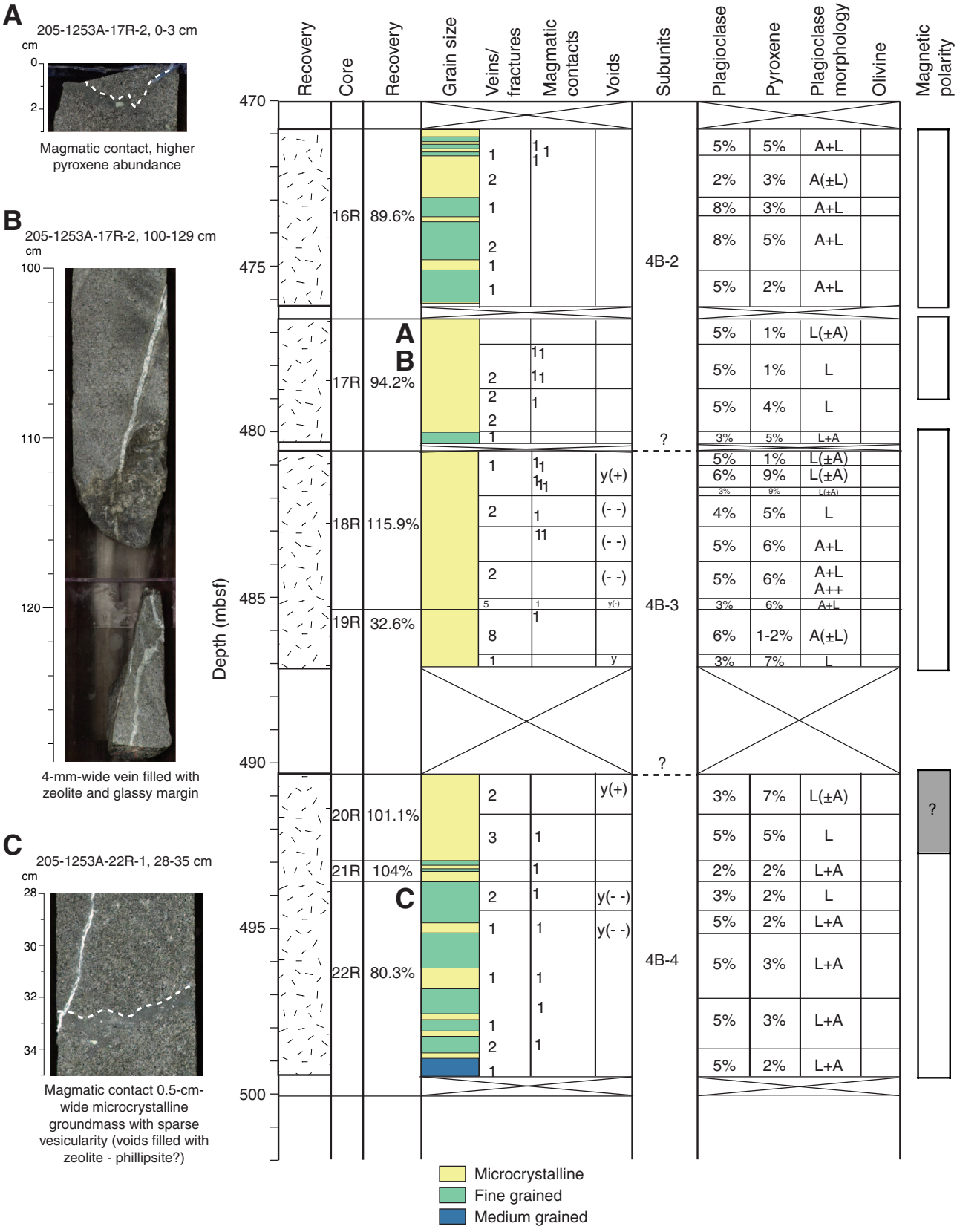

Figure F27. Structural, textural, and mineralogical features of Subunit 4B Cores 205-1253A-23R through 28R described in terms of veins, fractures, magmatic contacts, and voids and proportions of each mineral phenocryst. Additional pictures illustrate the typical features of Subunit 4B. Blue = medium grained, green = fine grained, yellow = microcrystalline, white = cryptocrystalline. A = aggregates, L = laths. Phenocryst percentage expresses mineral abundance over the full section length. Y = yes, evidence of voids. The number of plus or minus symbols rates the abundance of voids. Magnetic polarity and close-up photographs of the main core macroscopic features are also shown. See text for criteria used to further subdivide Subunit 4B. 1, 6. Microcrystalline gabbro. 2. Cumulate fine- to medium-grained groundmass. 3. Microcrystalline groundmass. 4. Fine-grained groundmass with 10% pyroxene phenocrysts (1-mm size and subhedral). 5. Microcrystalline to fine-grained groundmass. **A.** Interval 205-1253A-25R-1, 58–63 cm. **B.** Interval 205-1253A-25R-1, 110–126 cm. **C.** Interval 205-1253A-27R-1, 3–8 cm. (**Figure shown on next page.**)

Figure F27 (continued). (Caption shown on previous page.)

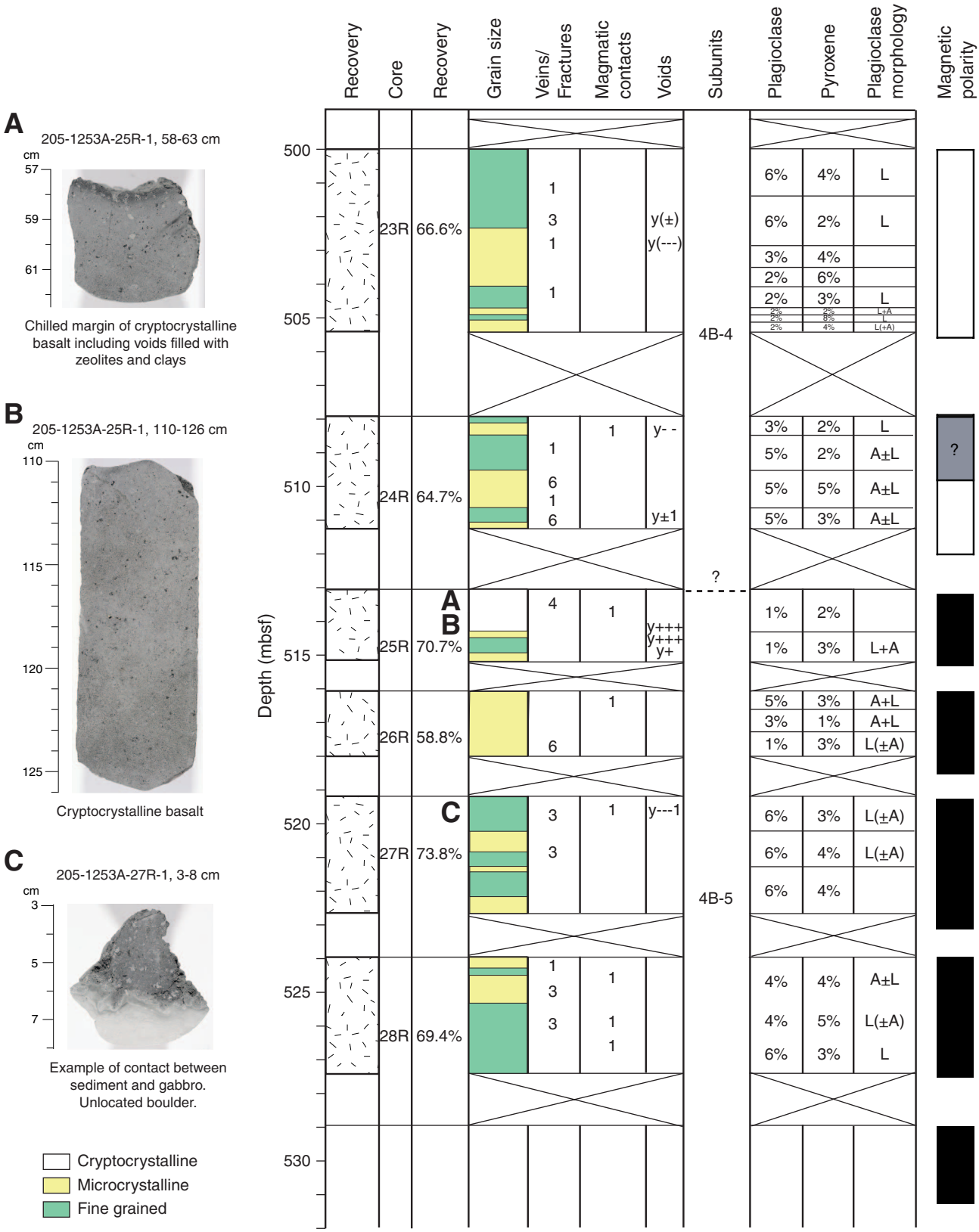

Figure F28. Photomicrographs in cross-polarized light taken with a blue filter at 5× magnification. Cpx = clinopyroxene, Pl = plagioclase. **A.** Cryptocrystalline groundmass observed at the top of Subunit 4B (Sample **205-1253A-13R-1, 35–37 cm**). **B, D.** Progressive increase of the groundmass grain size in Core 205-1253A-25R from cryptocrystalline basalt (Sample **205-1253A-25R-1, 33–35 cm**) in B through microcrystalline groundmass (Sample **205-1253A-25R-2, 101–103 cm**) in D. **C.** Sample **205-1253A-25R-2, 3–5 cm.**

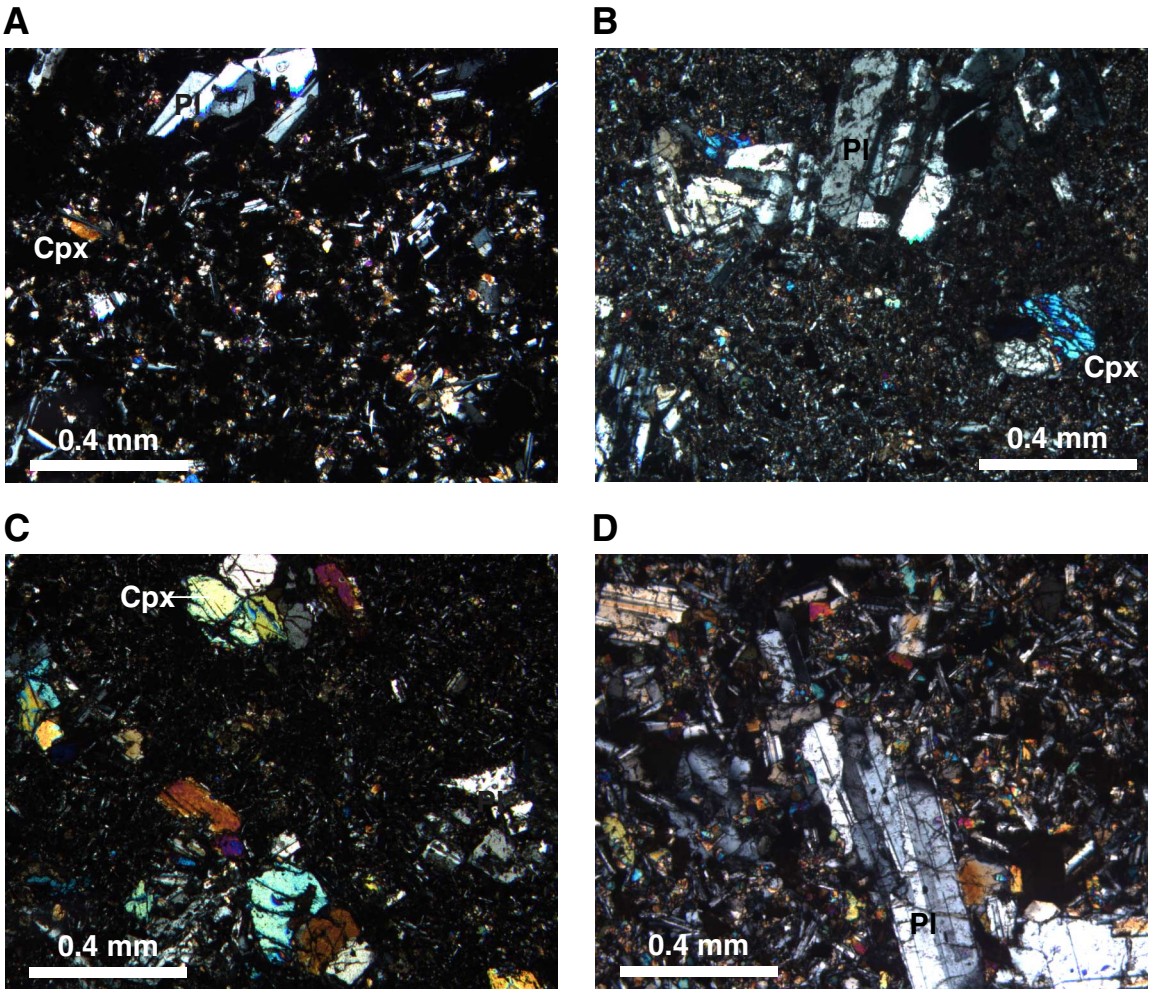

Figure F29. Structural, textural, and mineralogical features of Subunit 4B Cores 205-1253A-28R through 35R described in terms of veins, fractures, magmatic contacts, and voids and proportions of each mineral phenocryst. Additional pictures illustrate the typical features of Subunit 4B. Blue = medium grained, green = fine grained, yellow = microcrystalline, white = cryptocrystalline. A = aggregates, L = laths. Phenocryst percentage expresses mineral abundance over the full section length. Y = yes, evidence of voids. The number of plus or minus symbols rates the abundance of voids. Magnetic polarity and close-up photographs of the main core macroscopic features are also shown. See text for criteria used to further subdivide Subunit 4B. 1, 6. Microcrystalline gabbro. 2. Cumulate fine- to medium-grained groundmass. 3. Microcrystalline groundmass. 4. Fine-grained groundmass with 10% pyroxene phenocrysts (1-mm size and subhedral). 5. Microcrystalline to fine-grained groundmass. **A.** Interval 205-1253A-29R-2, 1–8 cm. **B.** Interval 205-1253A-34R-2, 120–126 cm. **C.** Interval 205-1253A-35R-1, 45–62 cm. (**Figure shown on next page.**)

Figure F29 (continued). (Caption shown on previous page.)

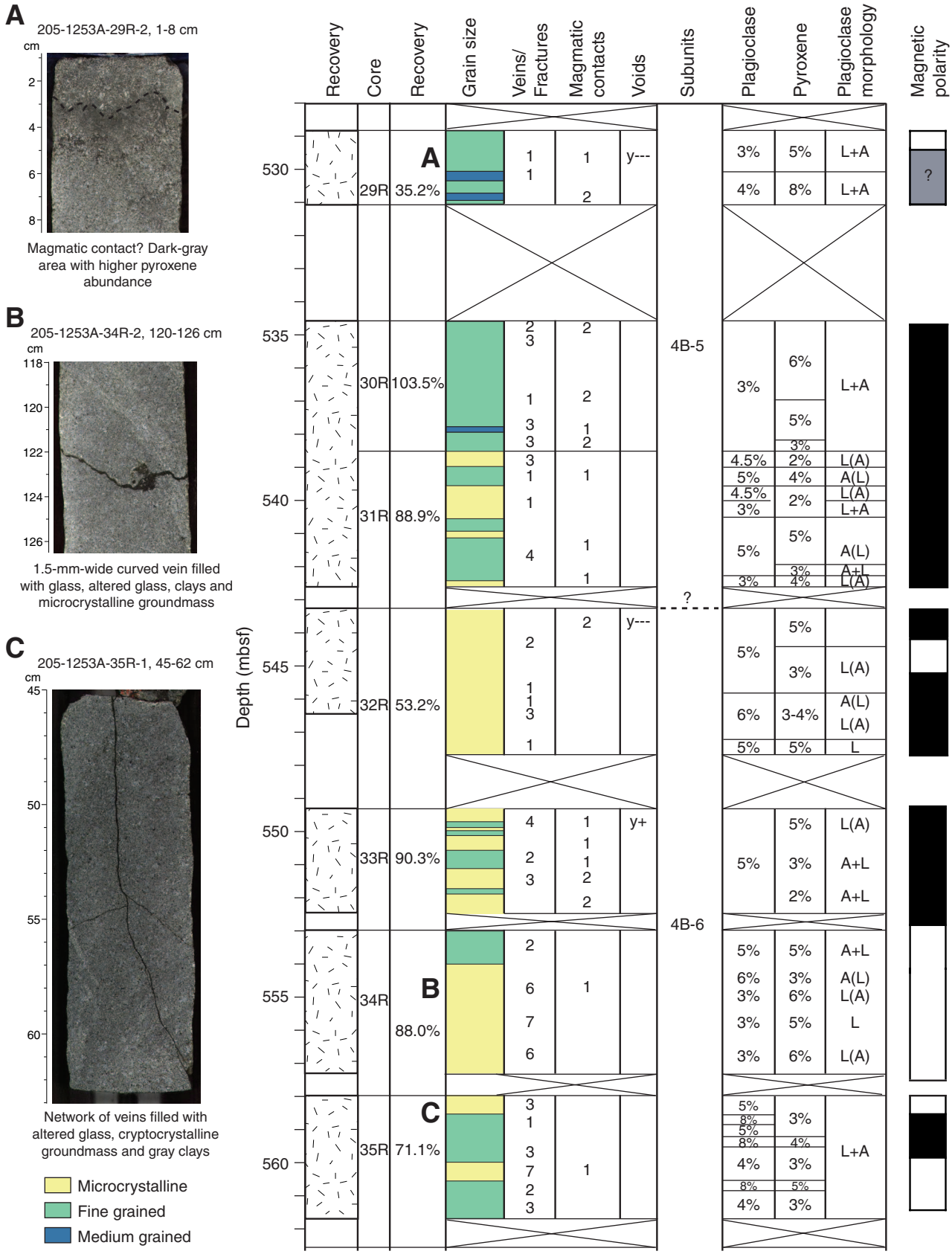

Figure F30. Structural, textural, and mineralogical features of Subunit 4B Cores 205-1253A-36R through 40R described in terms of veins, fractures, magmatic contacts, and voids and proportions of each mineral phenocryst. Additional pictures illustrate the typical features of Subunit 4B. Blue = medium grained, green = fine grained, yellow = microcrystalline, white = cryptocrystalline. A = aggregates, L = laths. Phenocryst percentage expresses mineral abundance over the full section length. Y = yes, evidence of voids. The number of plus or minus symbols rates the abundance of voids. Magnetic polarity and close-up photographs of the main core macroscopic features are also shown. See text for criteria used to further subdivide Subunit 4B. 1, 6. Microcrystalline gabbro. 2. Cumulate fine- to medium-grained groundmass. 3. microcrystalline groundmass. 4. Fine-grained groundmass with 10% pyroxene phenocrysts (1-mm size and subhedral). 5. Microcrystalline to fine-grained groundmass. **A.** Interval 205-1253A-37R-1, 54–63 cm. **B.** Interval 205-1253A-37R-1, 107–116 cm. **C.** Interval 205-1253A-40R-1, 94–114 cm. (**Figure shown on next page.**)

Figure F30 (continued). (Caption shown on previous page.)

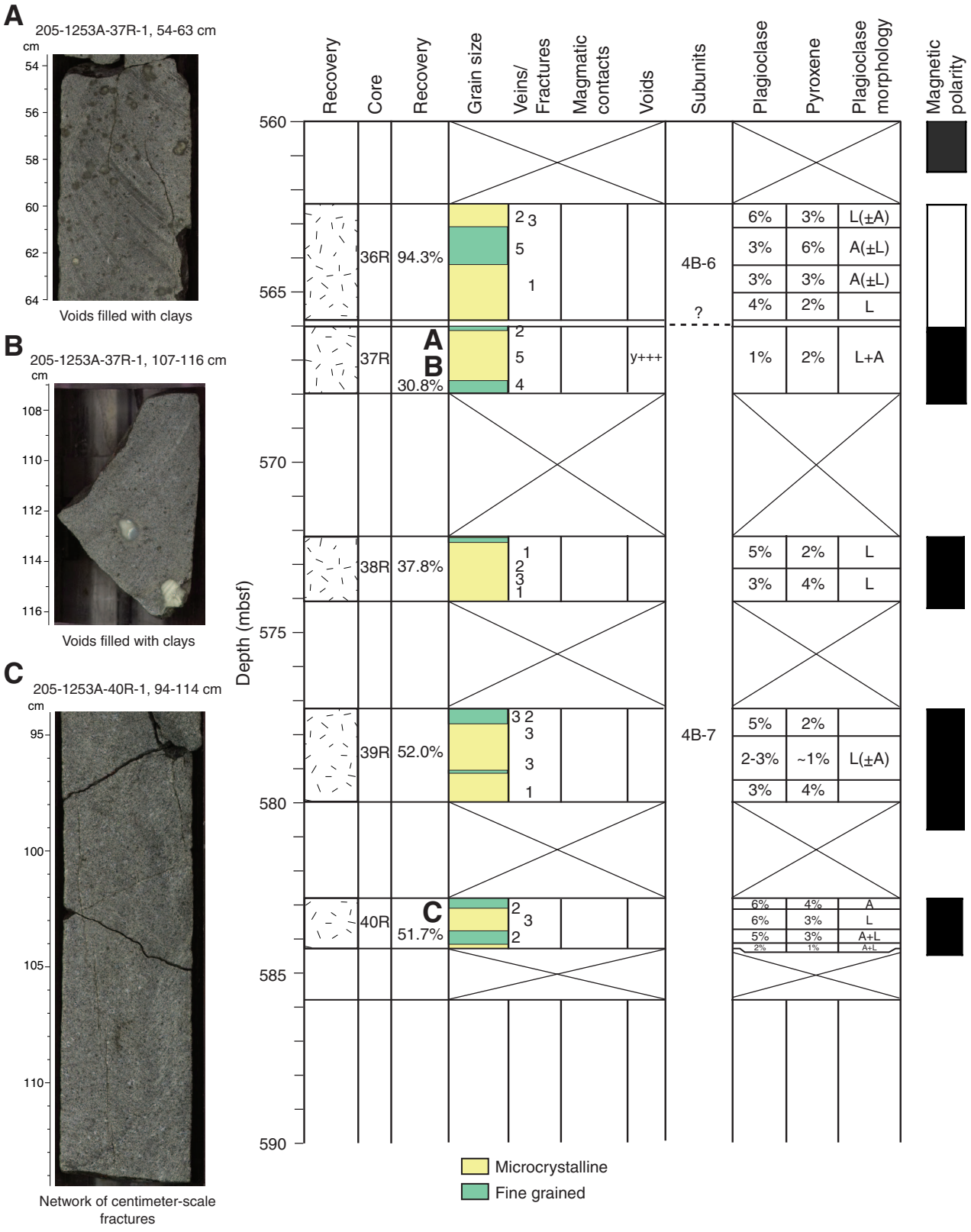

Figure F31. Structural, textural, and mineralogical features of Subunit 4B Cores 205-1253A-41R through 43R described in terms of veins, fractures, magmatic contacts, and voids and proportions of each mineral phenocryst. Additional pictures illustrate the typical features of Subunit 4B. Blue = medium grained, green = fine grained, yellow = microcrystalline, white = cryptocrystalline. A = aggregates, L = laths. Phenocryst percentage expresses mineral abundance over the full section length. Y = yes, evidence of voids. The number of plus or minus symbols rates the abundance of voids. Magnetic polarity and close-up photographs of the main core macroscopic features are also shown. See text for criteria used to further subdivide Subunit 4B. 1, 6. Microcrystalline gabbro. 2. Cumulate fine- to medium-grained groundmass. 3. Microcrystalline groundmass. 4. Fine-grained groundmass with 10% pyroxene phenocrysts (1-mm size and subhedral). 5. Microcrystalline to fine-grained groundmass. **A.** Interval 205-1253A-42R-2, 72–101 cm.

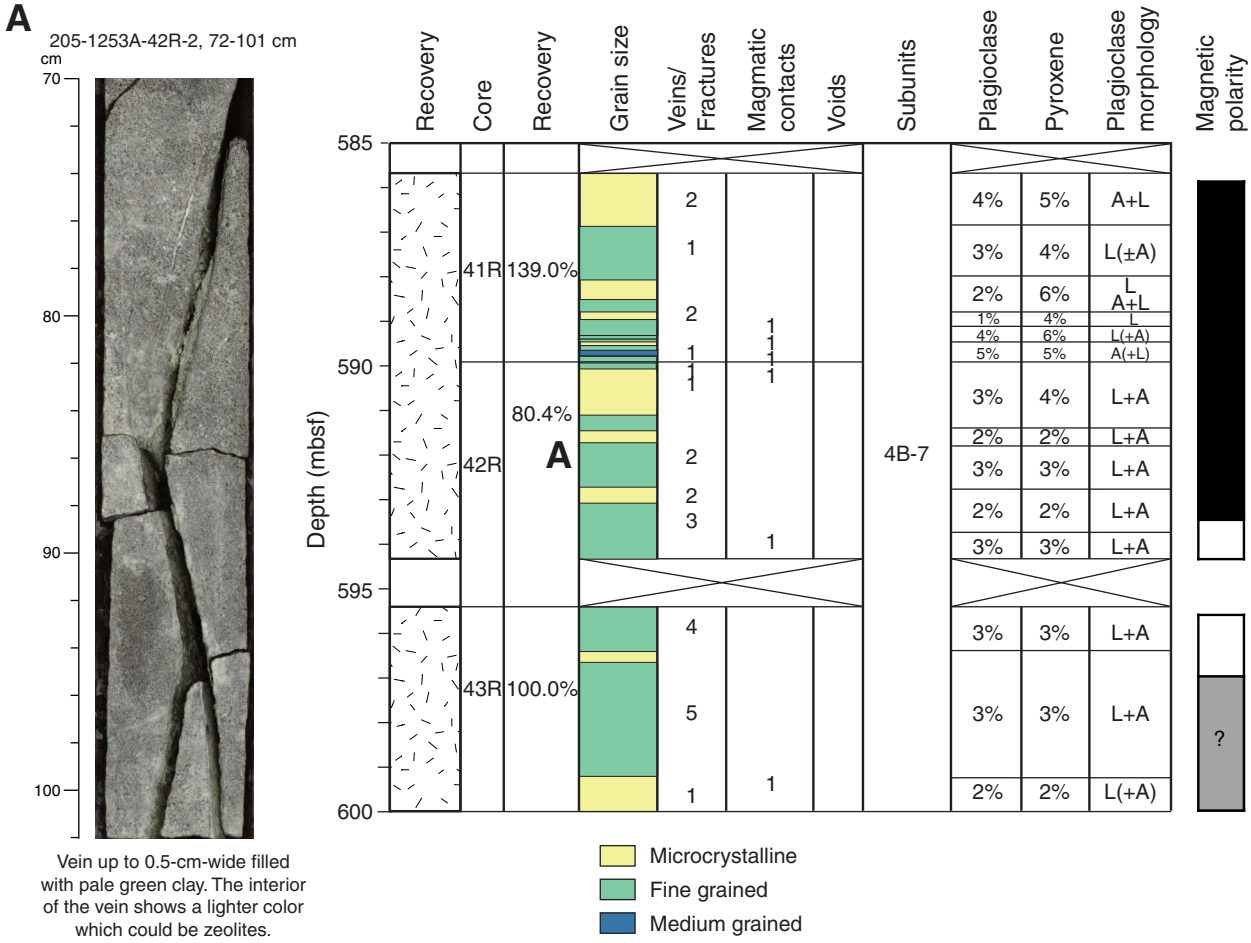

Figure F32. Core recovery plot of Hole 1253A from 370 to 600 mbsf. Indicated are the different units encountered during the drilling, the limit of each subdivision within Subunit 4A, the gabbro sill, and Subunit 4B. Different colored areas indicate the following observations. 1 = location of the cryptocrystalline basaltic texture, 2 = higher number of magmatic contacts, 3 = more veins or voids filled with holocrystalline and cryptocrystalline groundmass/altered glass, clay, and zeolites, 4 = up to 5% degree of alteration within 1 m of Section 205-1253A-37R-1 and higher abundance of voids filled with clays and zeolites ending in an homogeneous microcrystalline gabbro, 5 = increasing number of centimeter-scale fractures and veins, 6 = very homogeneous microcrystalline to fine-grained gabbro with very weak magmatic contacts. Also indicated are the positions of the two OsmoSamplers (OS).

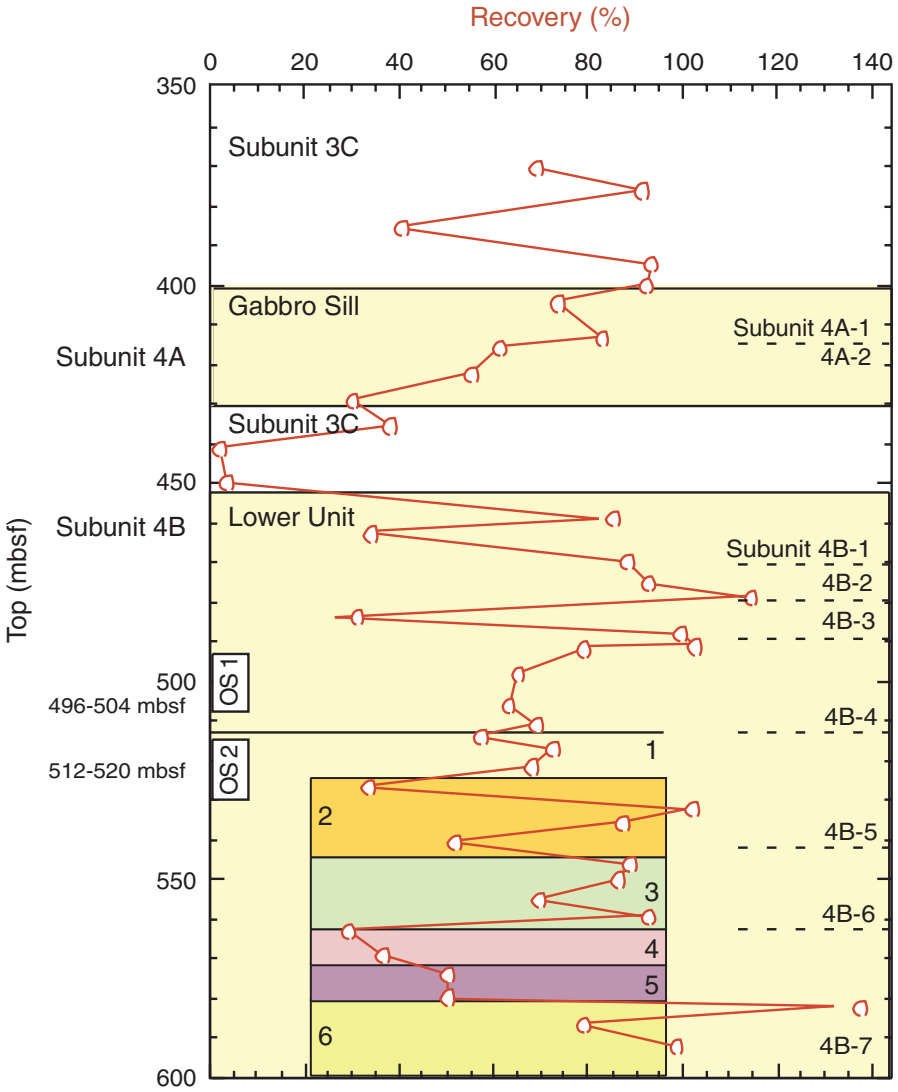

Figure F33. Six photomicrographs in cross-polarized light taken with a blue filter at 5× magnification. Cpx = clinopyroxene, Pl = plagioclase. Microcrystalline gabbro in (**A**) Sample **205-1253A-17R-2, 108–111 cm** (478.2 mbsf), (**B**) Sample **205-1253A-27R-2, 114–115 cm** (521.47 mbsf), and (**E**) Sample **205-1253A-32R-2, 19–20 cm** (544.51 mbsf). Fine-grained gabbro in (**C**) Sample **205-1253A-31R-4, 29–30 cm** (543.04 mbsf), and (**D**) Sample **205-1253A-31R-4, 29–30 cm** (543.04 mbsf). Medium-grained gabbro in (**F**) Sample **205-1253A-41R-4, 92–94 cm** (590.97 mbsf).

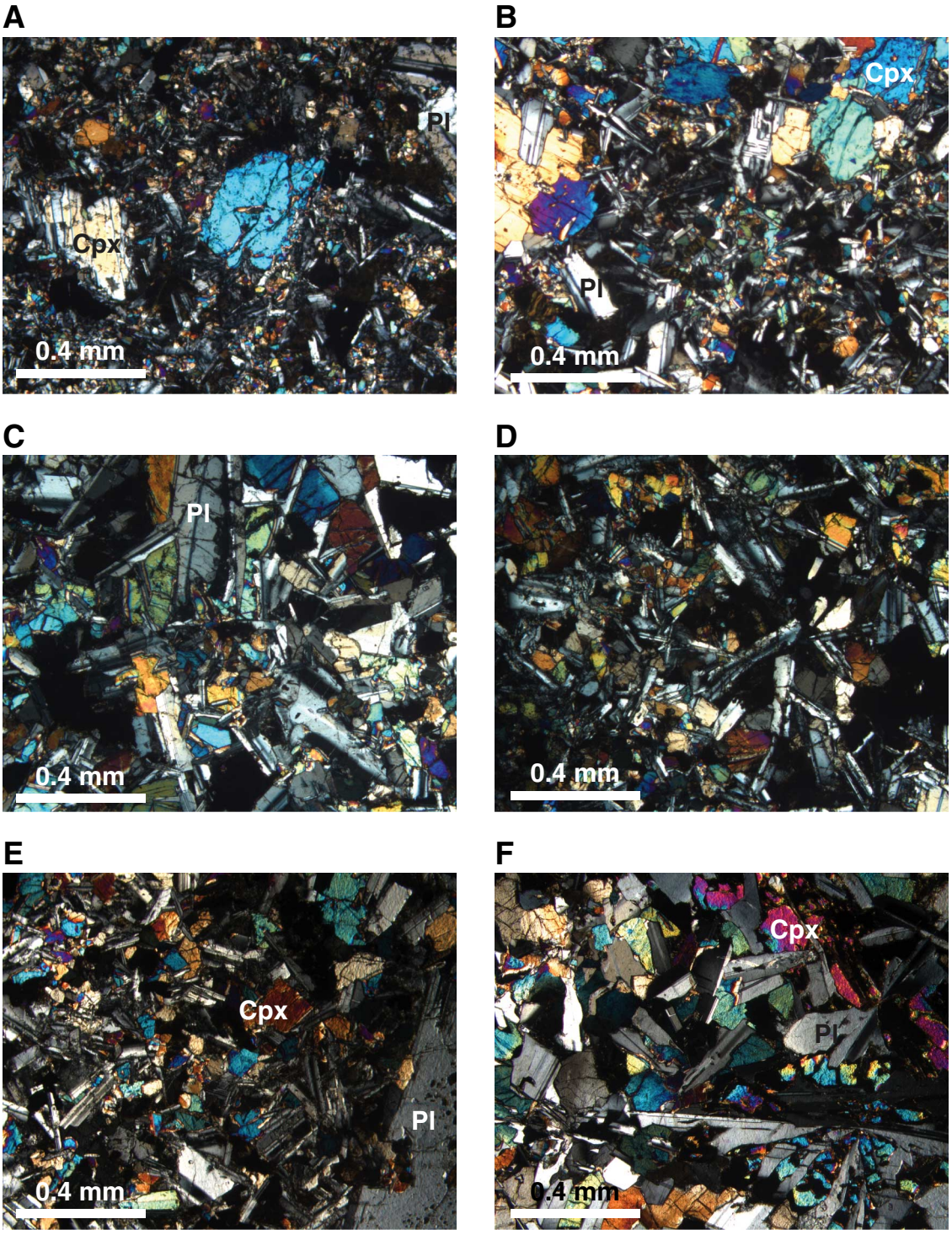

Figure F34. Photomicrographs in cross-polarized light taken with blue filter at 5× magnification. Pl = plagioclase. **A, B.** Growth zoning within plagioclase (Sample 205-1253A-27R-2 [Piece 5B, 114–116 cm]). **C.** Sample 205-1253A-34R-2 (Piece 5A, 97–99 cm).

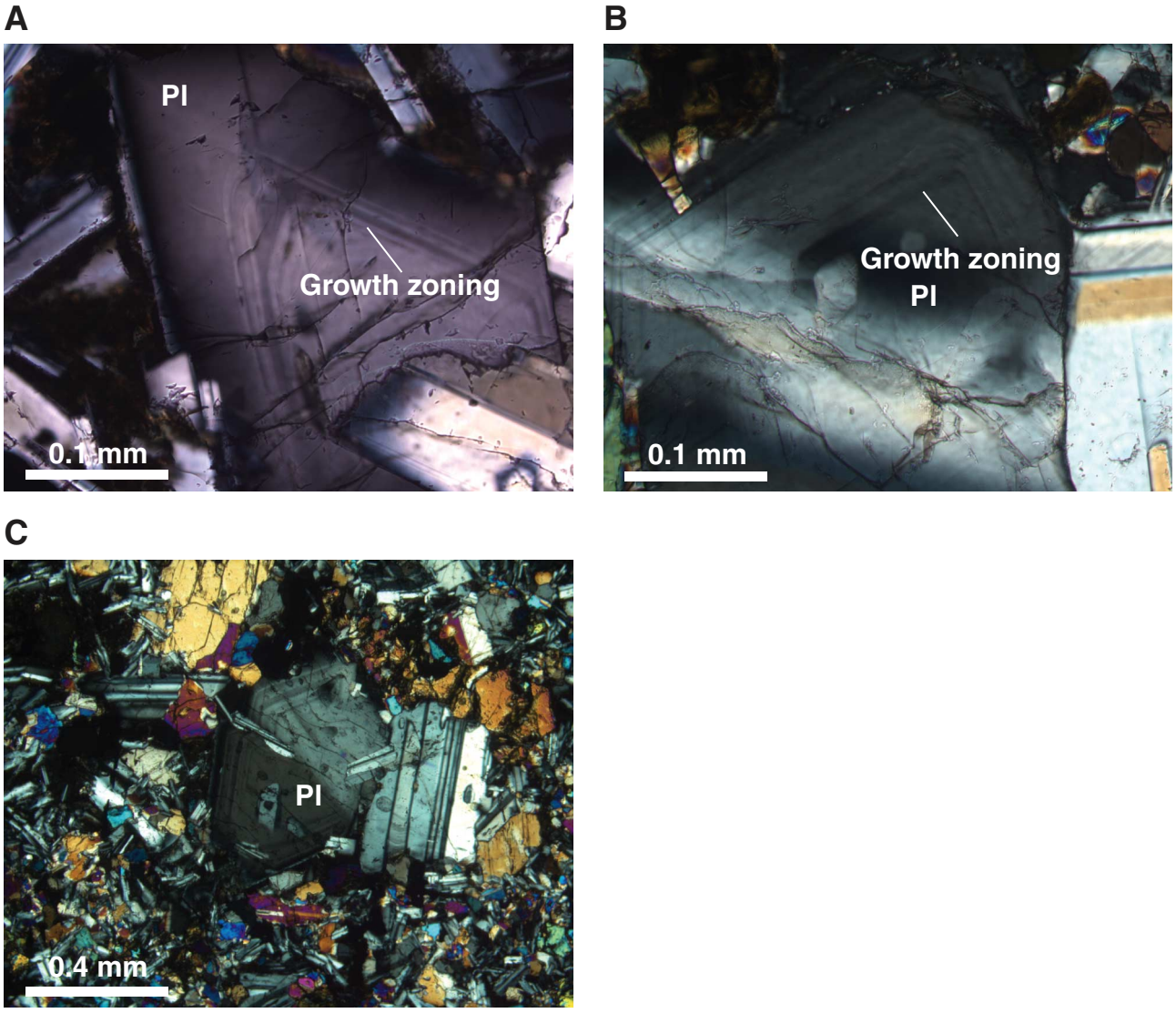

Figure F35. Photomicrographs in cross-polarized light taken with blue filter at 20× magnification. Inclusions of glass and altered glass could be observed at the center of plagioclase phenocryst or groundmass plagioclase. Note that the inclusions are located only within the center at the early stage of plagioclase crystallization before extensive magma differentiation as shown from growth zoning. These inclusions are up to 30 µm in size and do not present any specific morphology. Pl = plagioclase. **A.** Sample **205-1253A-34R-4 (Piece 2, 70–72 cm).** **B.** Sample **205-1253A-39R-2 (Piece 5, 82–84 cm).**

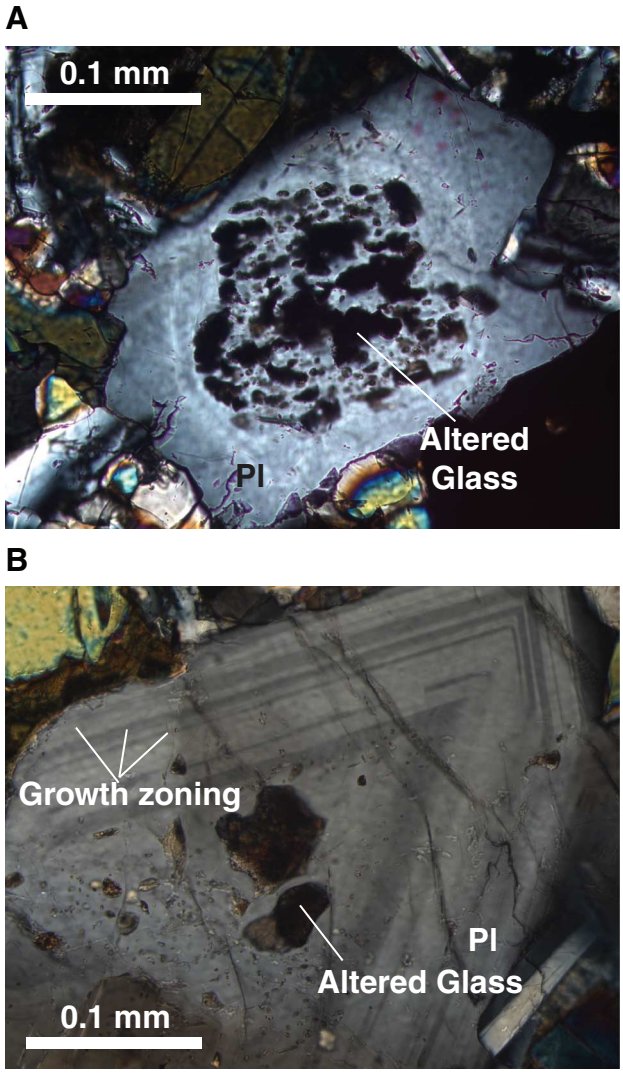

Figure F36. A. Sharp increase of groundmass size at the magmatic contact (Sample **205-1253A-31R-2, 106–108 cm;** 540.96 mbsf; cross-polarized light [XPL]). Intergrowth of plagioclase and clinopyroxene in (**B**) Sample **205-1253A-30R-3, 117–120 cm** (538.20 mbsf; XPL), (**C**) Sample **205-1253A-41R-4, 92–94 cm** (590.97 mbsf; plane-polarized light), and (**D**) Sample **205-1253A-31R-1, 50–52 cm** (539 mbsf; XPL). Pl = plagioclase, Cpx = clinopyroxene.

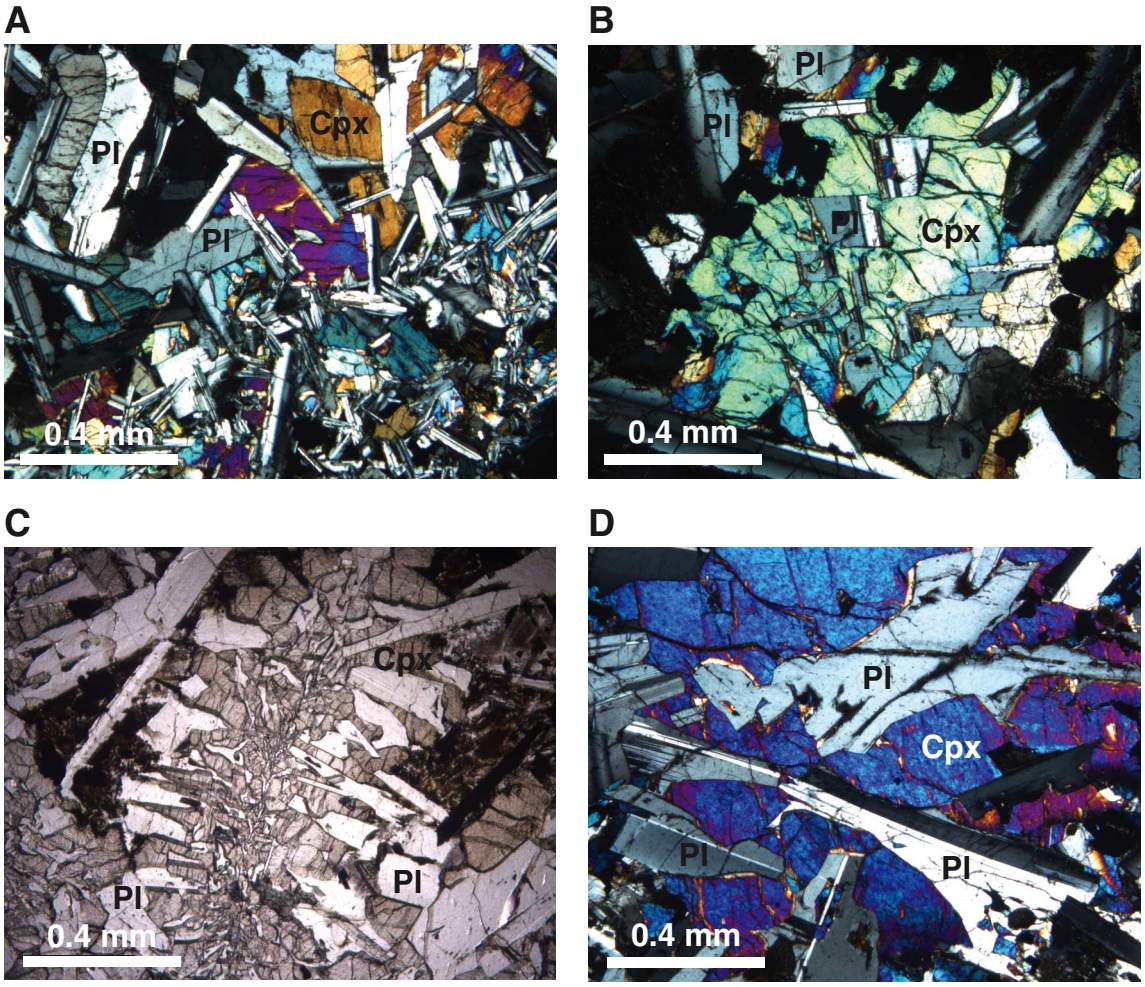

Figure F37. Photomicrographs of altered primary minerals (olivine) by clay (probably saponite). Pl = plagioclase, Ol = olivine, Ilm = ilmenite, Px = pyroxene. **A.** Weathering along a part of the rim (Sample 205-1253A-34R-2, 97–99 cm; 555 mbsf; cross-polarized light [XPL]). **B.** Alteration along intramineral fissures (Sample 205-1253A-34R-2, 97–99 cm; 555 mbsf; XPL). **C.** Nearly complete replacement of olivine by clay (Sample 205-1253A-34R-2, 97–99 cm; 555 mbsf; XPL). **D.** Totally replaced olivine by clay (Sample 205-1253A-32R-3, 32–34 cm; 546.07 mbsf; plane-polarized light).

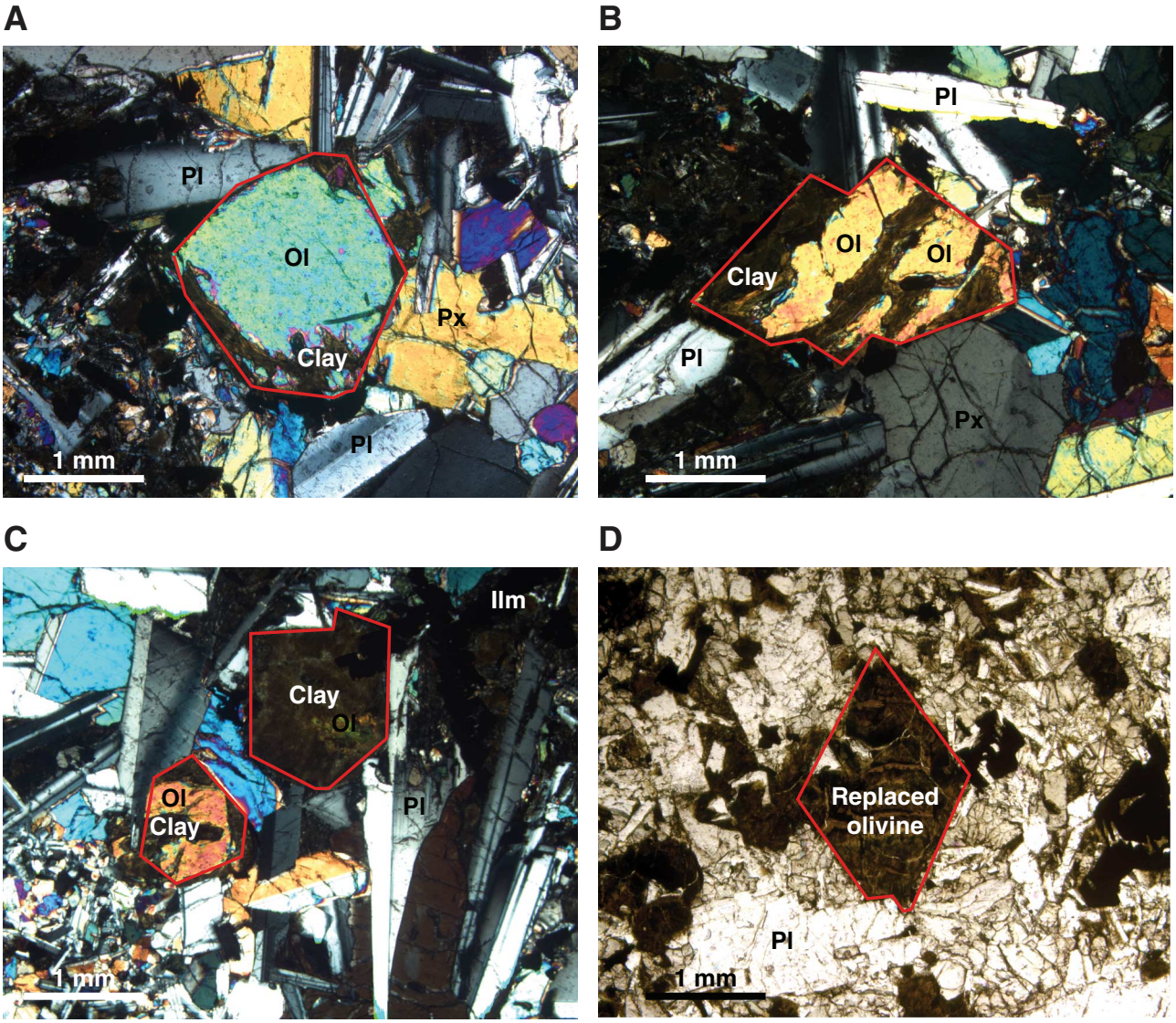

Figure F38. Representative XRD pattern of an air-dried sample with peaks for zeolite minerals mesolite and scolecite (Sample 205-1253A-22R-2, 55–57 cm; 494.63 mbsf). This sample was taken from a fracture. The baseline was defined from background counts.

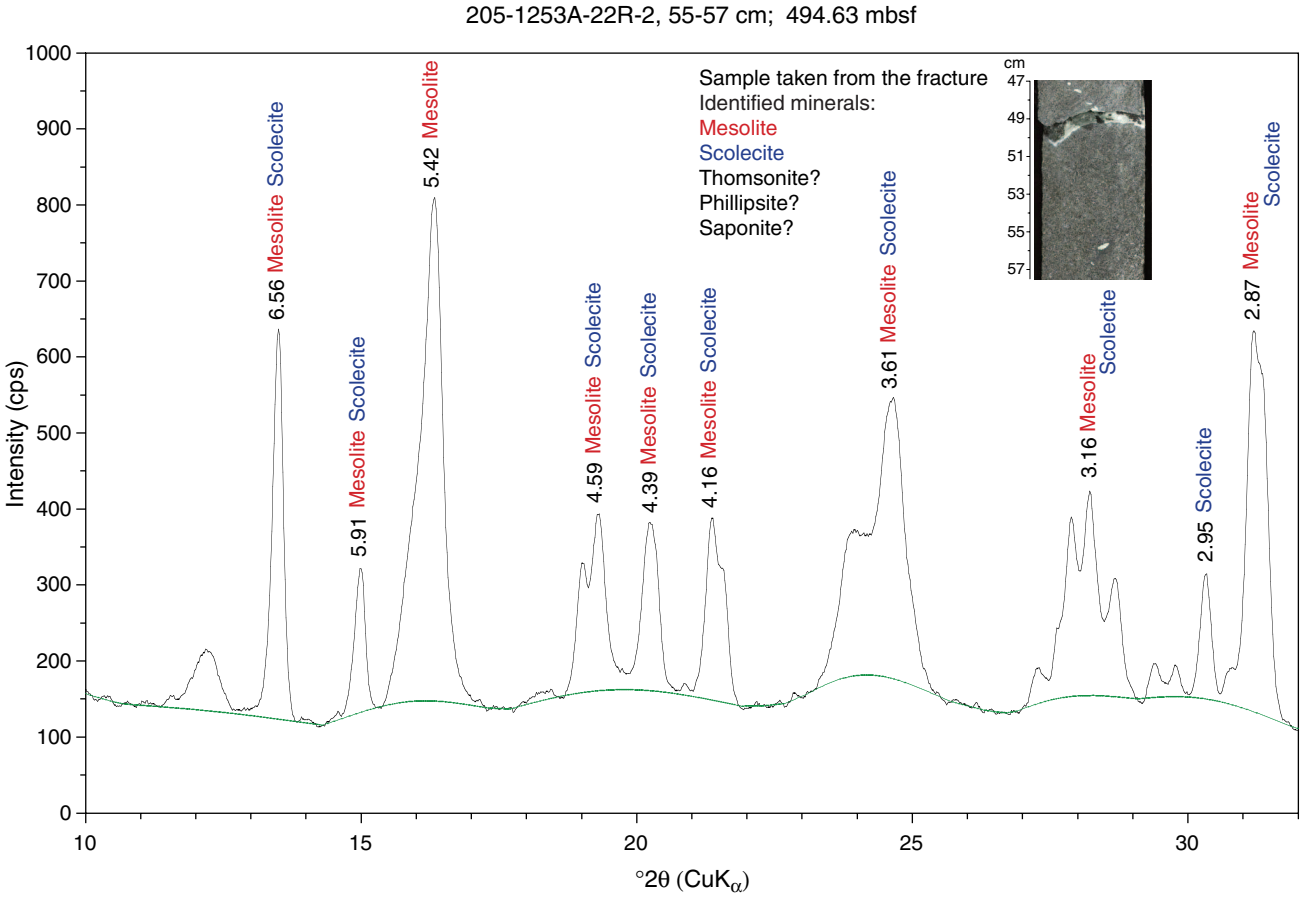

Figure F39. Representative XRD pattern of an air-dried sample with peaks for zeolite minerals phillipsite and stilbite (Sample 205-1253A-37R-1, 114–115 cm; 567.14 mbsf). This sample was separated from a void at 115 cm. The baseline was defined from background counts.

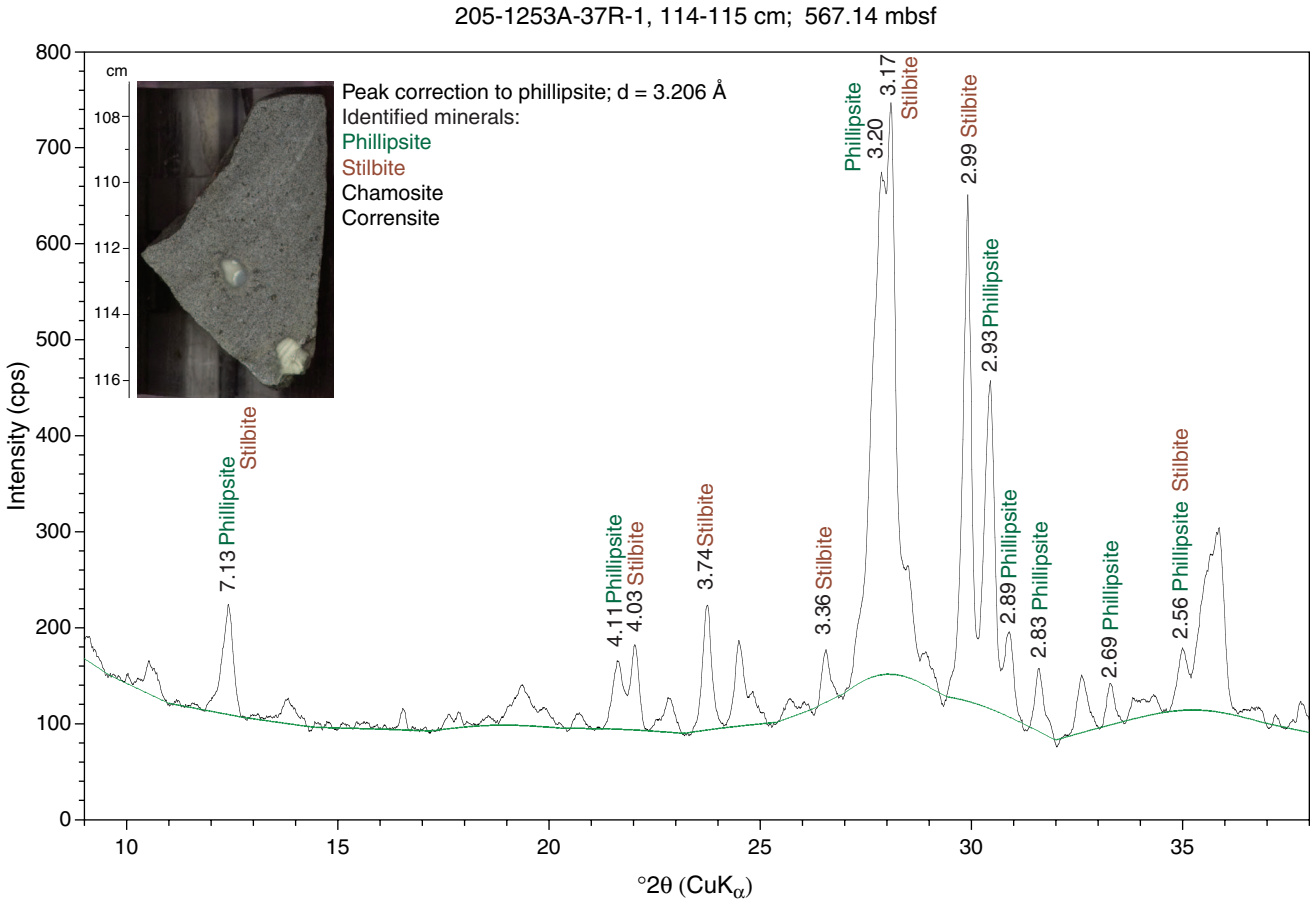

Figure F40. Photomicrographs of zeolites. Pl = plagioclase, Cpx = clinopyroxene. **A–C.** Stilbite is shown and is easily identified by the sheaflike aggregates and radiated masses (Sample 205-1253A-33R-1 [Piece 8B]; 550.52 mbsf; in cross-polarized light [XPL] in A and plane-polarized light [PPL] in B and C). **D.** Radiating fibrous aggregates of zeolites (Sample 205-1253A-20R-1 [Piece 1D]; 492.04 mbsf; PPL). **E, F.** Radiating and fibrous aggregates, probably mesolite or thomsonite (Sample 205-1253A-17R-2; 478.18 mbsf; PPL).

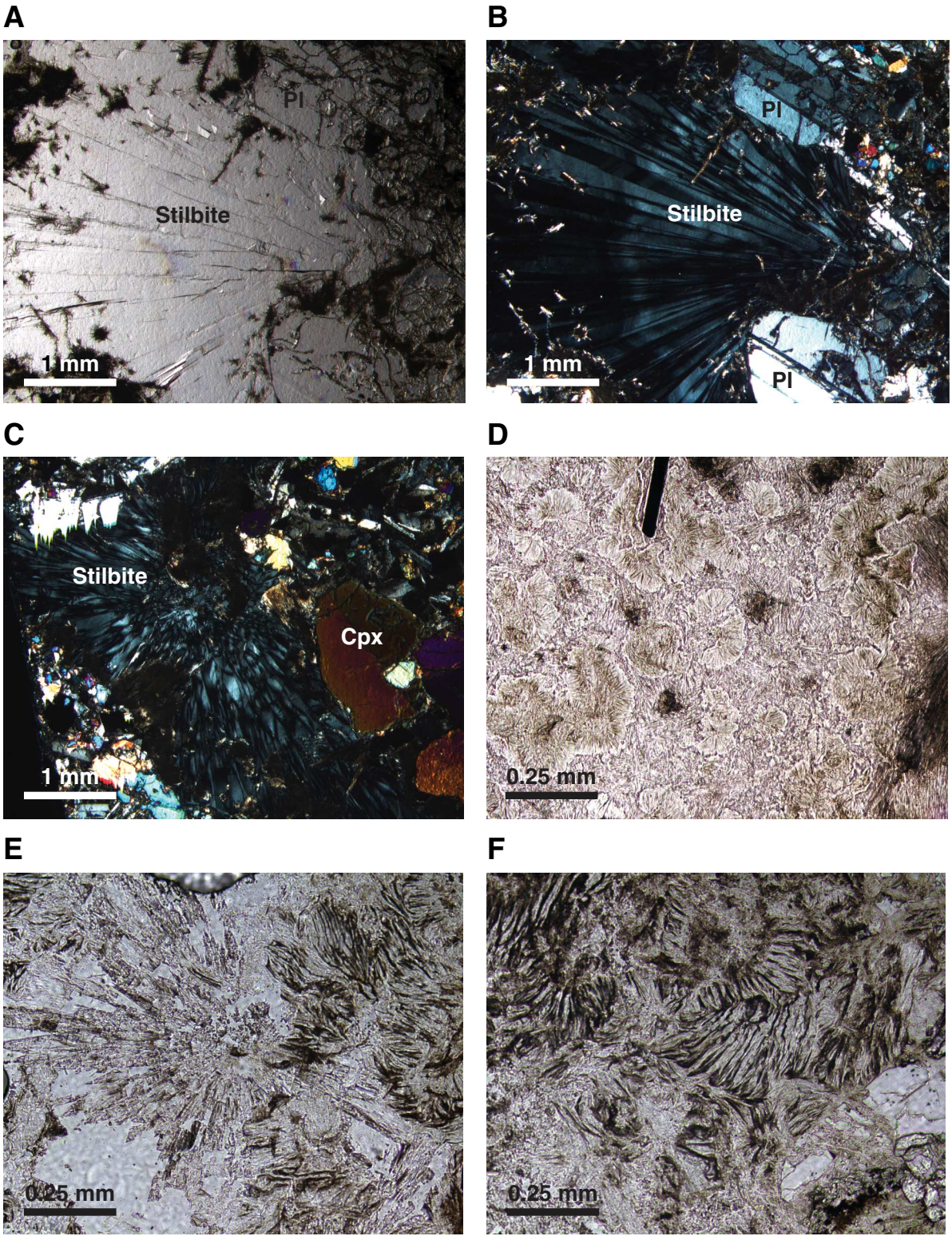

Figure F41. Concentration variations of major and trace elements as a function of depth. Subunit boundaries are also shown.

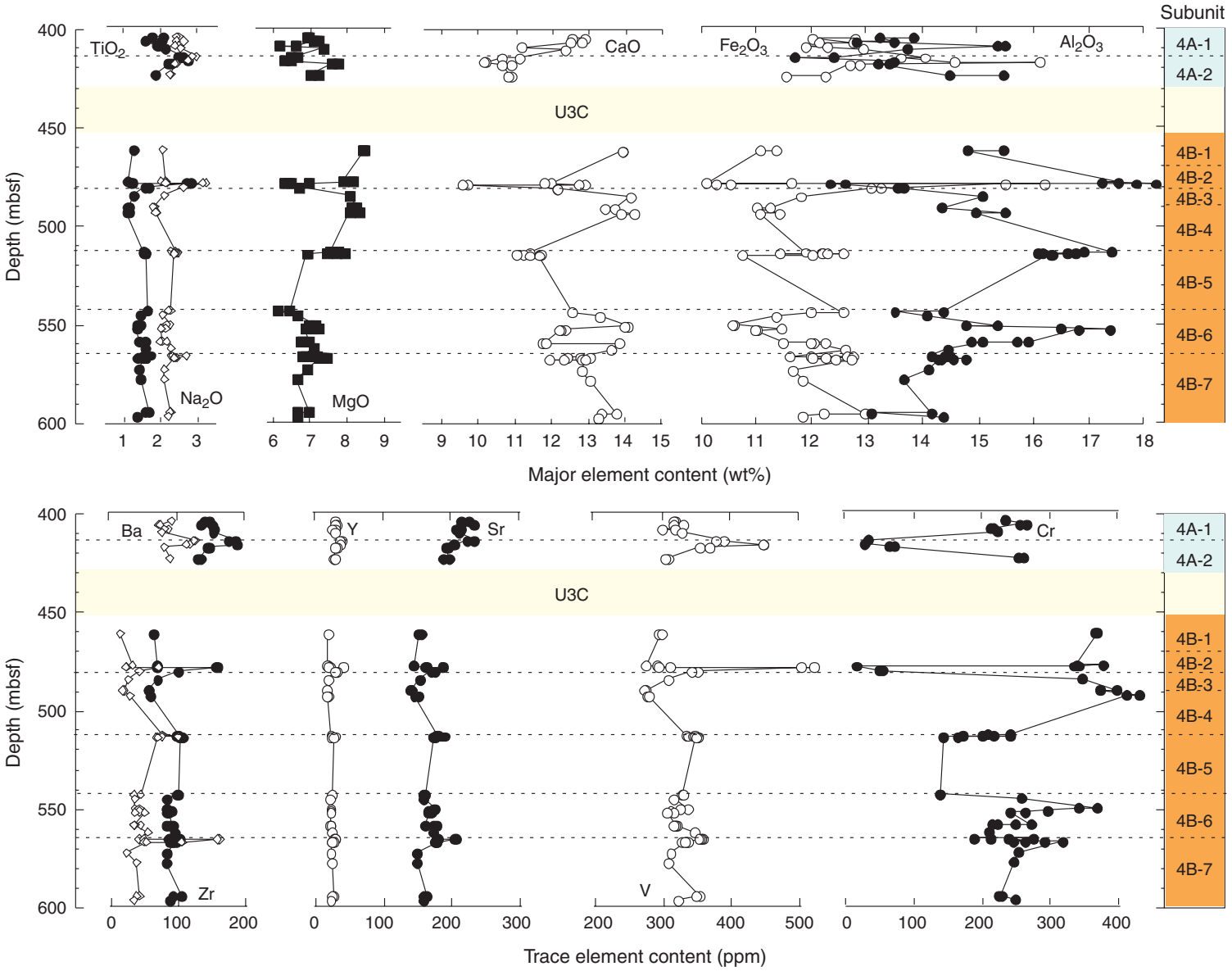

Figure F42. Variation of V content as a function of TiO_2 for the gabbro sill and the gabbro of Subunit 4B. Both subunits present a positive linear correlation (R^2 shown on figure) indicating the control of ilmenite and/or titanomagnetite on the distribution of V and Ti of the melts.

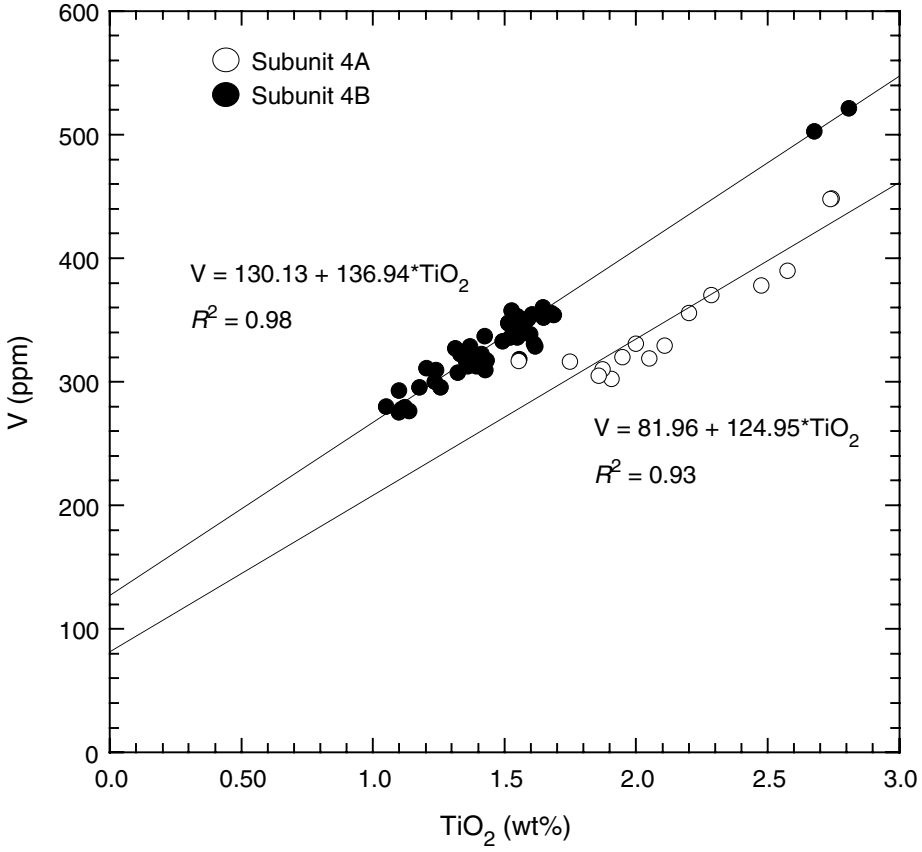

Figure F43. Variation of CaO/Al_2O_3 ratio as a function of Mg# (Mg# = Mg/[Mg+Fe^{2+}]). Compositions of plagioclase, clinopyroxene, and olivine are indicated.

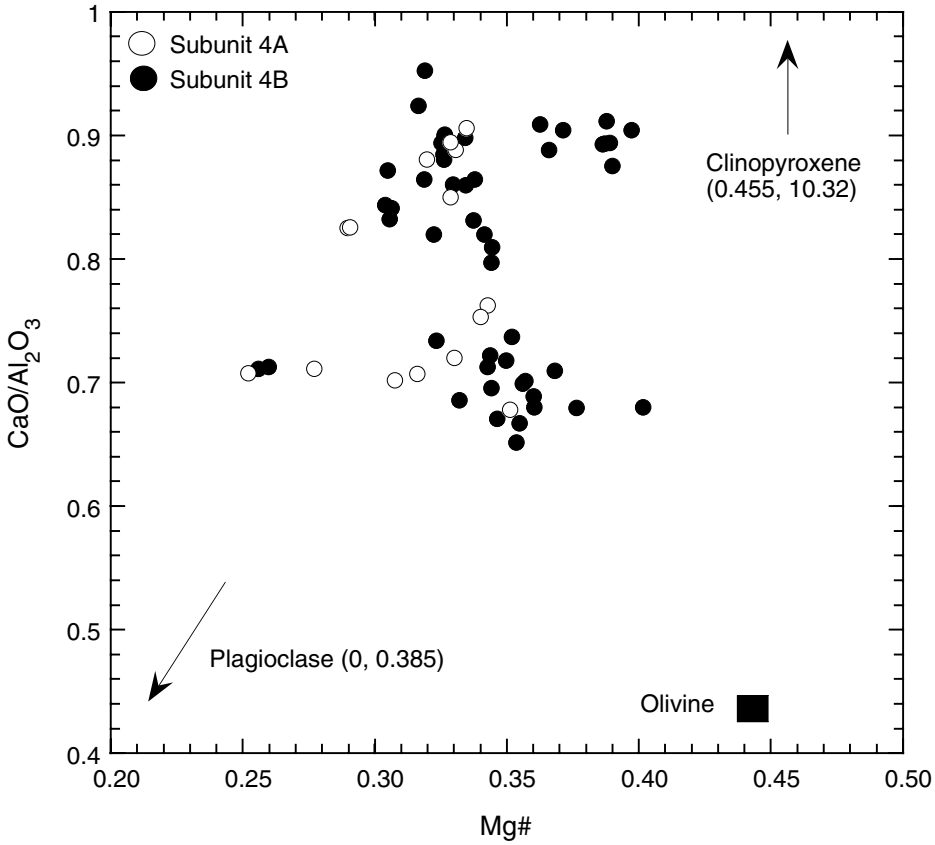

Figure F44. Variation of Ni content as a function of CaO/Al_2O_3 ratio.

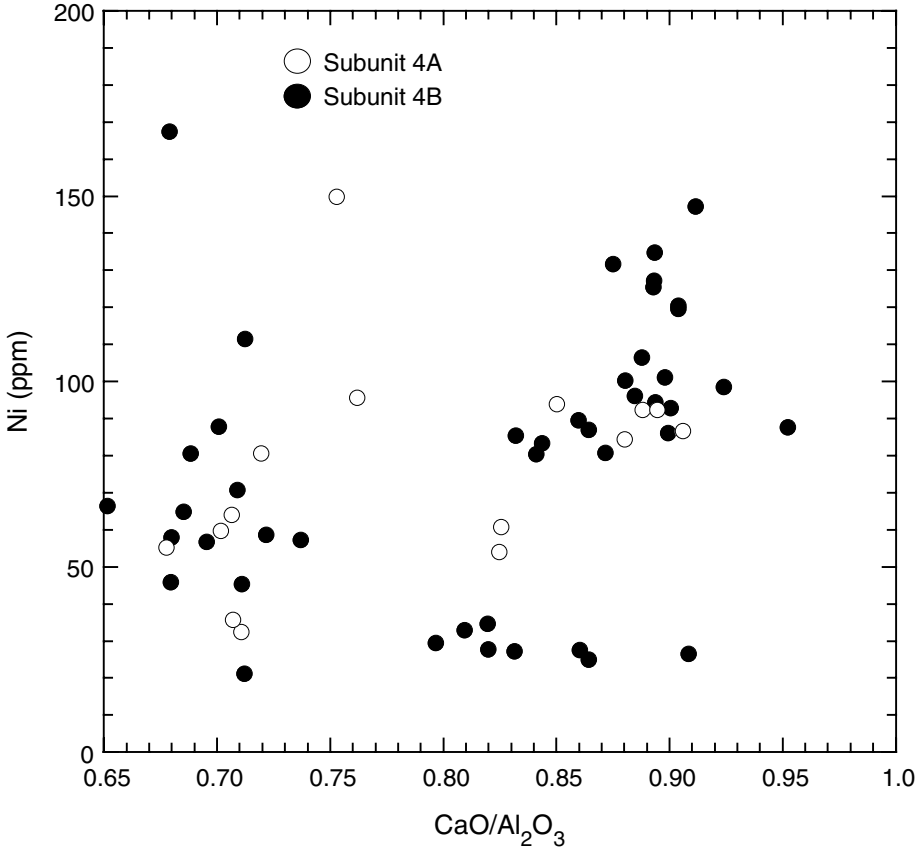

Figure F45. Variation of Cr content as a function of Zr content.

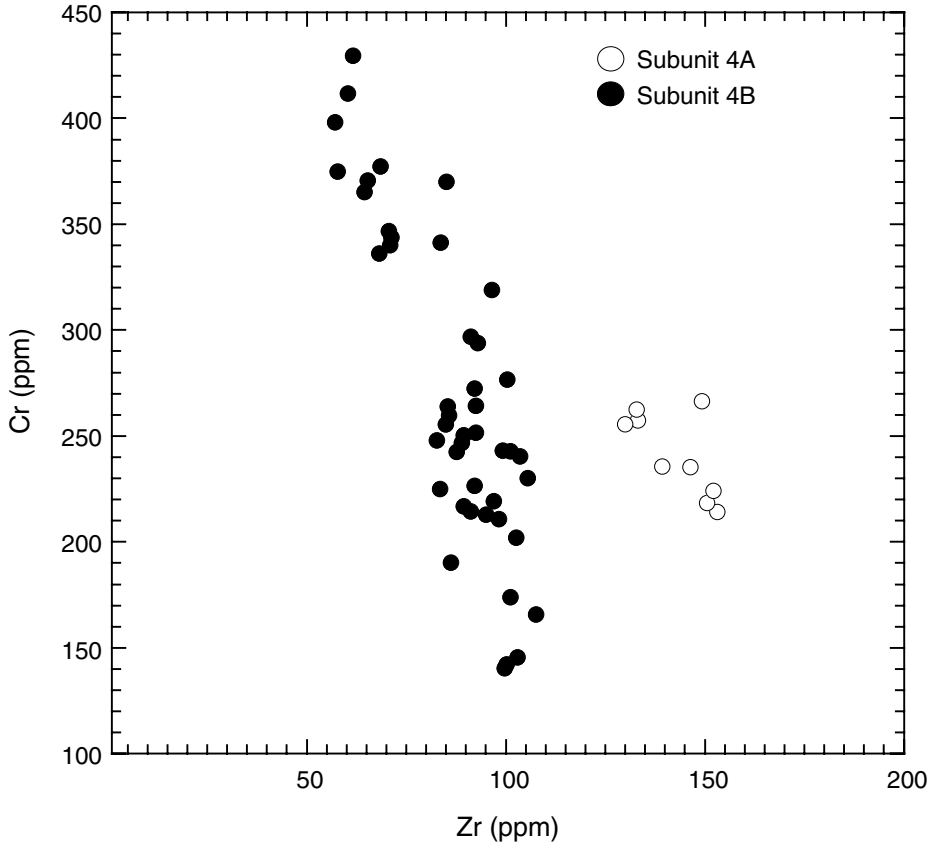

Figure F46. Variation of Sr content as a function of Na_2O concentration.

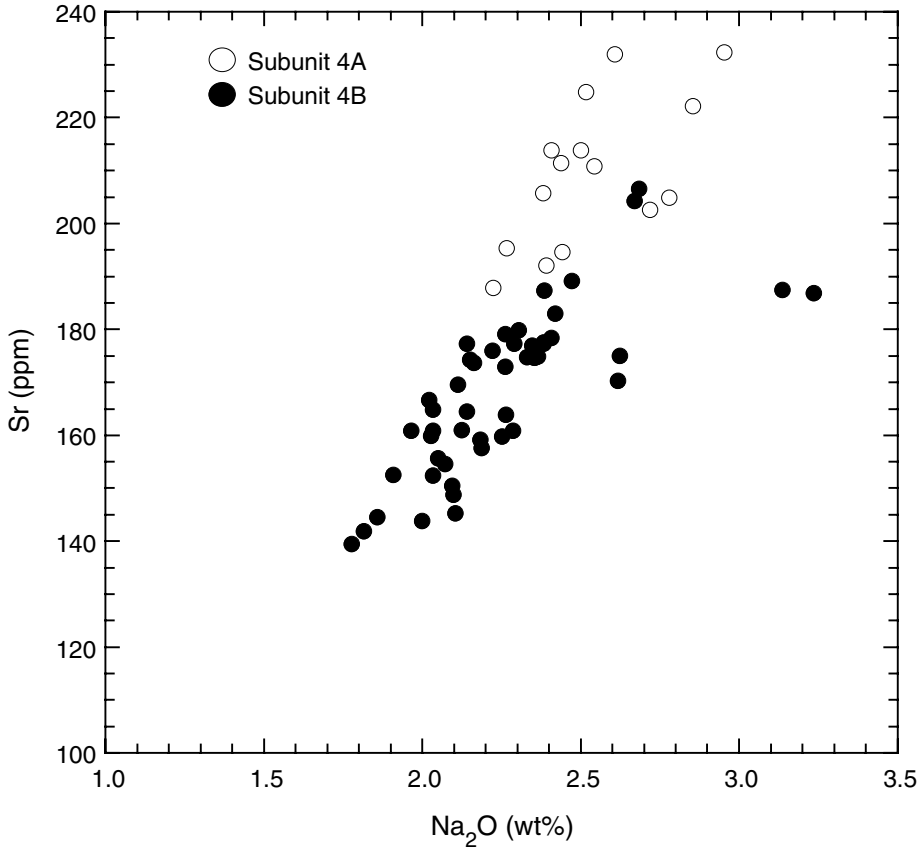

Figure F47. Sediment bedding dip and number of microfaults for every 5 m of recovered cores. Blue = sedimentary cores in the recovery column on the left, black = magmatic cores.

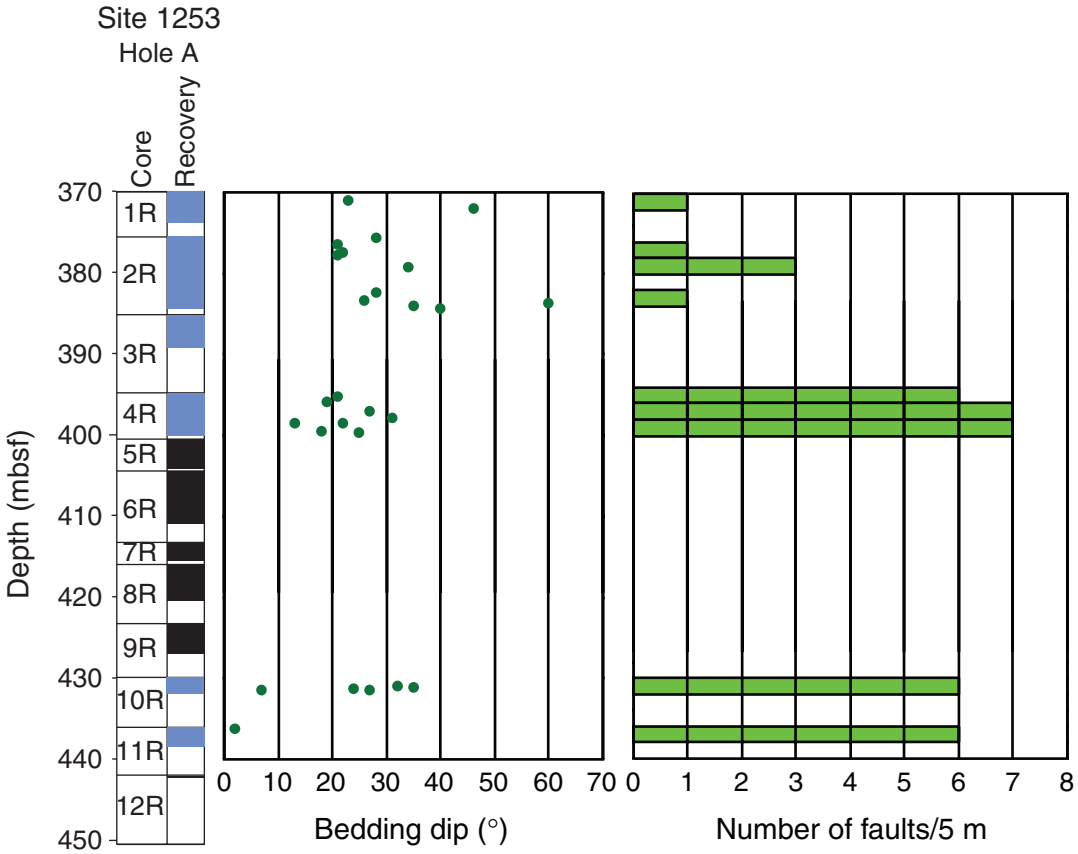

Figure F48. Close-up photograph (interval 205-1253A-4R-2, 16–30 cm) of tilted primary laminations in the nannofossil chalk of Unit U3.

Figure F49. Stereographic plot (equal area, lower hemisphere) showing bedding plane orientations and poles to bedding after paleomagnetic corrections.

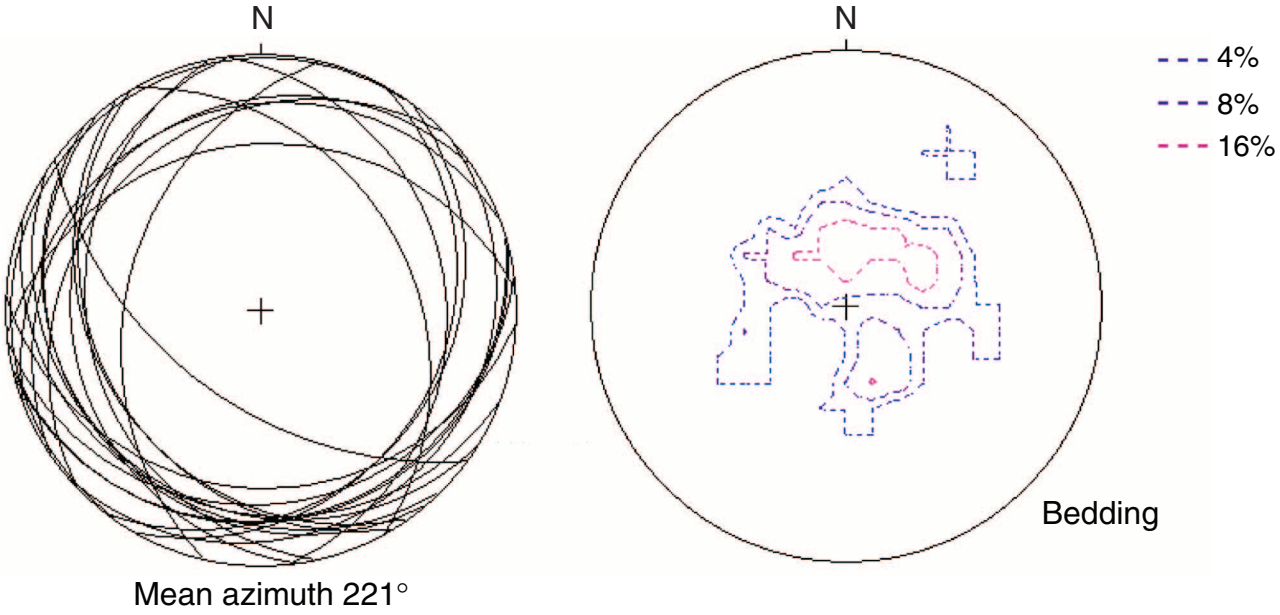

Figure F50. A. Close-up photograph of millimeter-scale normal faults (interval 205-1253A-1R-2, 28–36 cm). **B.** Close-up photograph of a conjugate set of reversed faults (interval 205-1253A-2R-3, 128–135 cm).

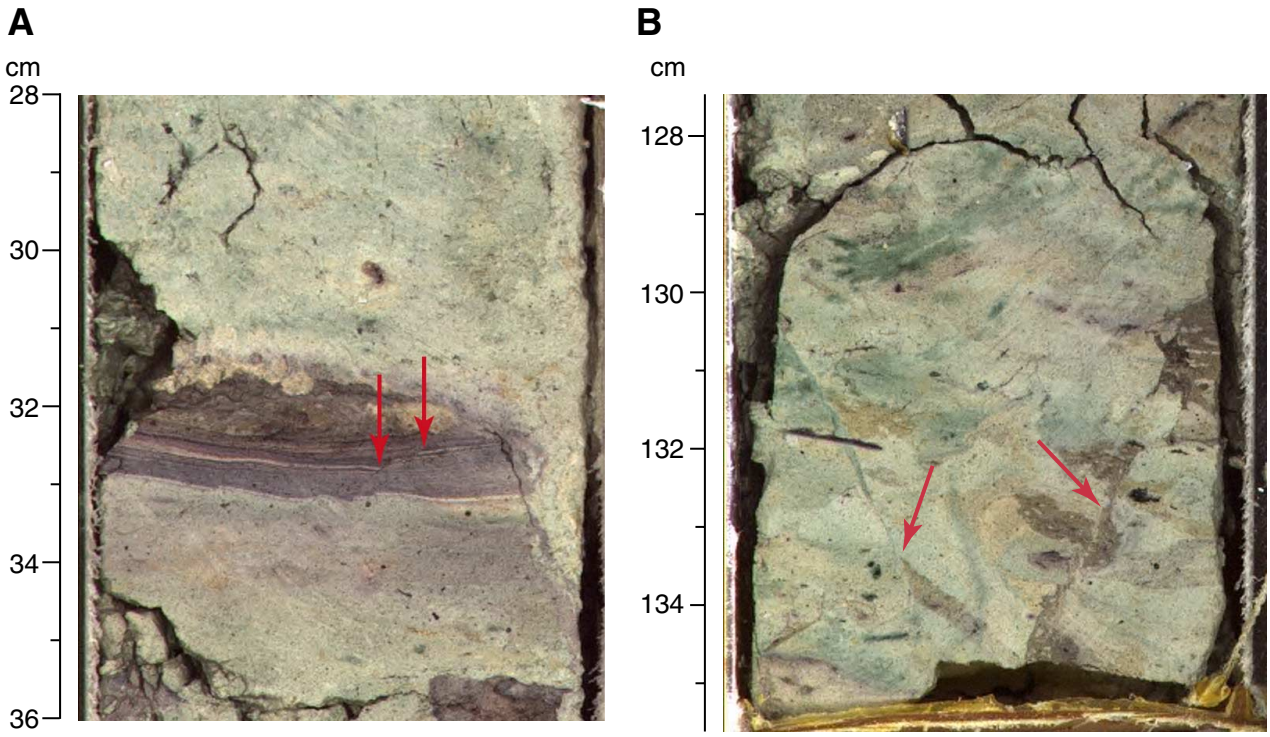

Figure F51. Stereographic plot (equal area, lower hemisphere) of the conjugate set of reversed faults. The black and white split symbols indicate the sense of movement along the plane (black = down; white = up).

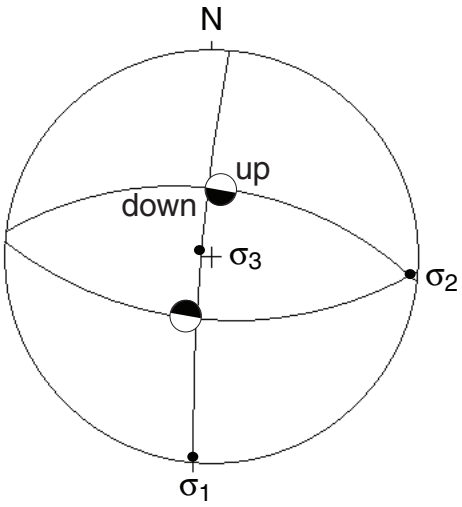

Figure F52. Joints, magmatic veins, mineralized veins, and magmatic contact distribution along the recovered length of pyroxene gabbro of Unit 4.

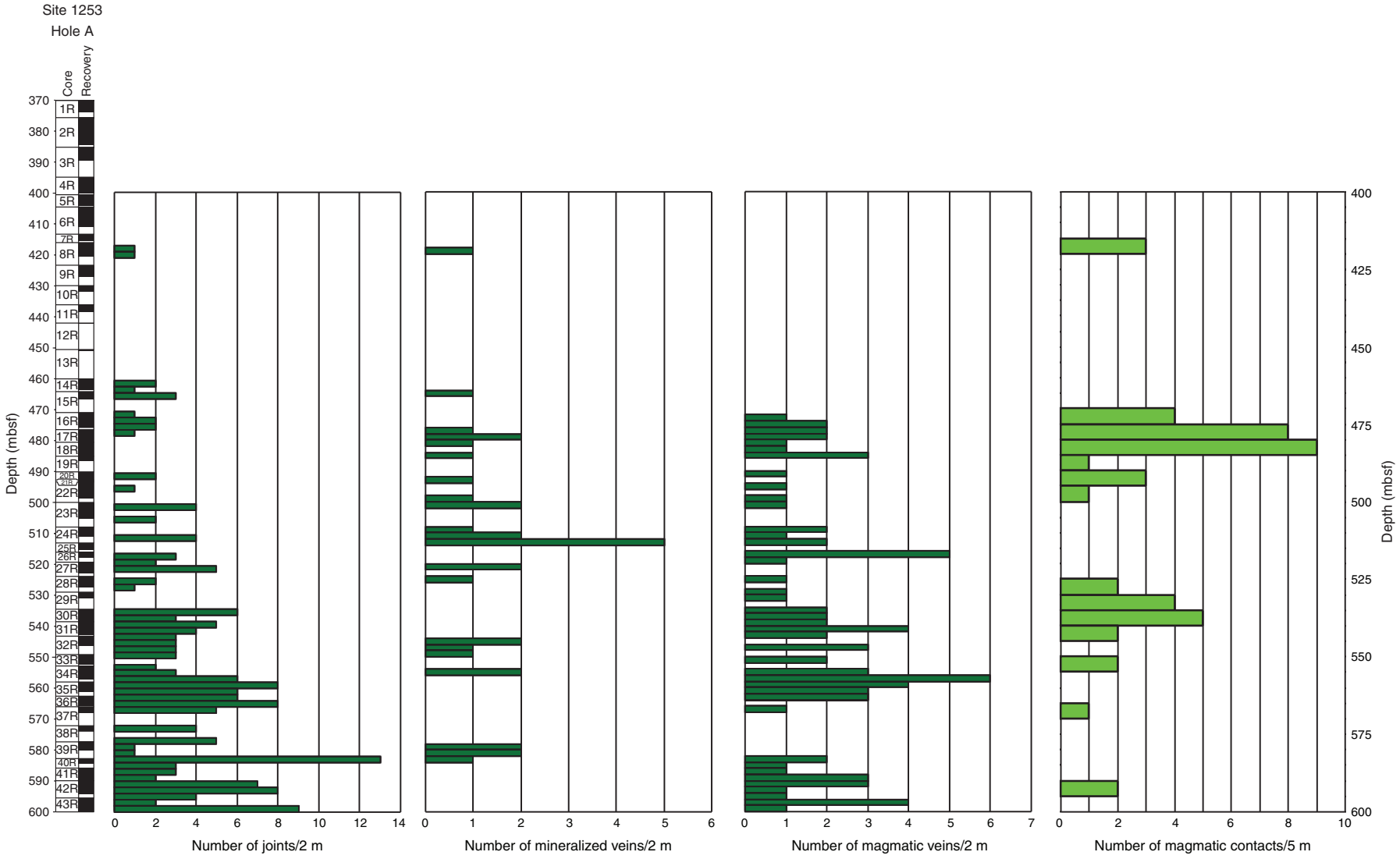

Figure F53. Contour plot (equal area, lower hemisphere) of poles to (**A**) magmatic contacts, (**B**) magmatic veins, (**C**) mineralized veins, and (**D**) joints after paleomagnetic (Pmag) reorientation and (**E**) joints filtered to remove low magnetic intensity intervals. Max. = maximum.

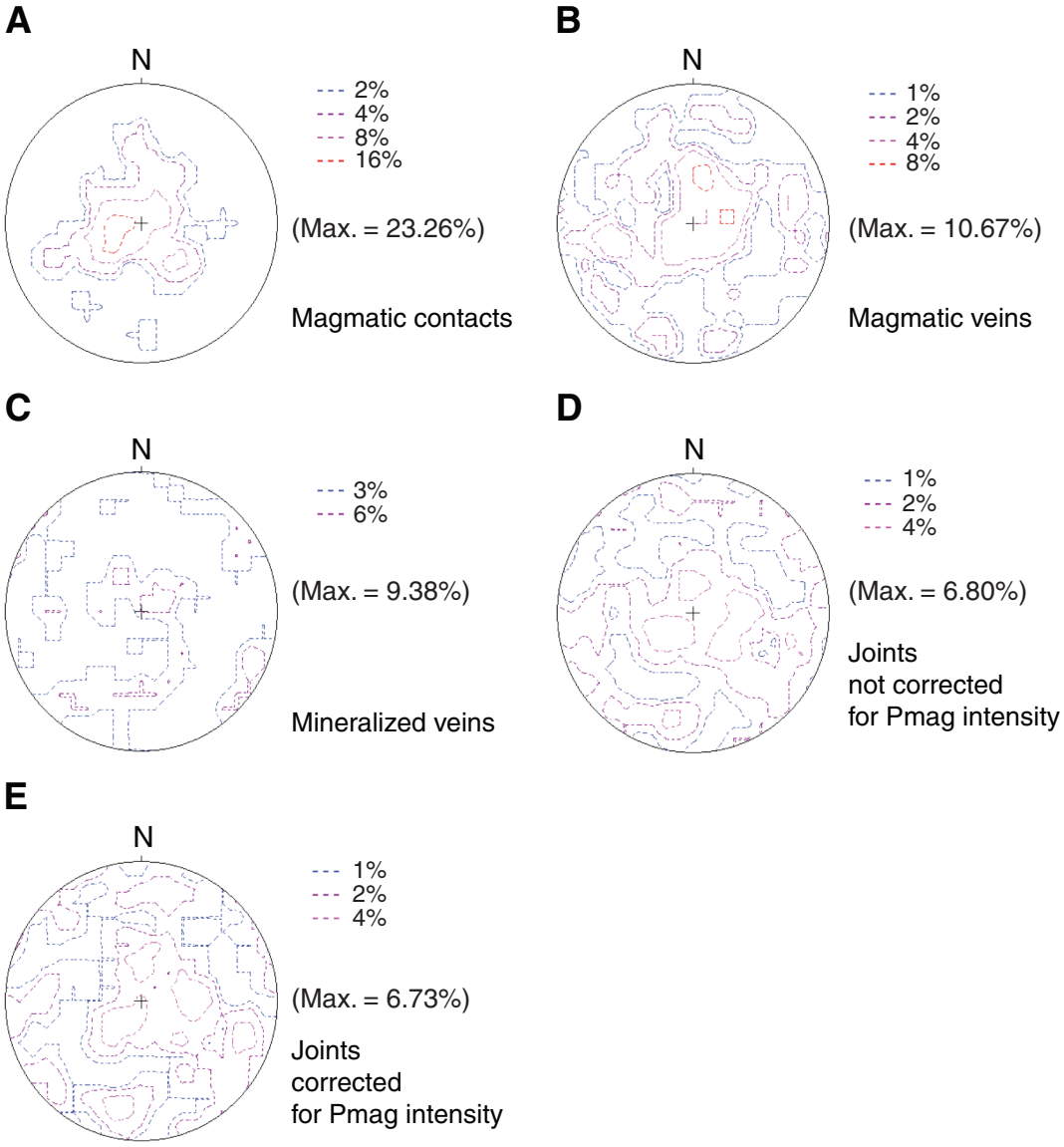

Figure F54. Close-up photograph of conjugate brittle shear zones (interval 205-1253A-40R-1, 98–113 cm).

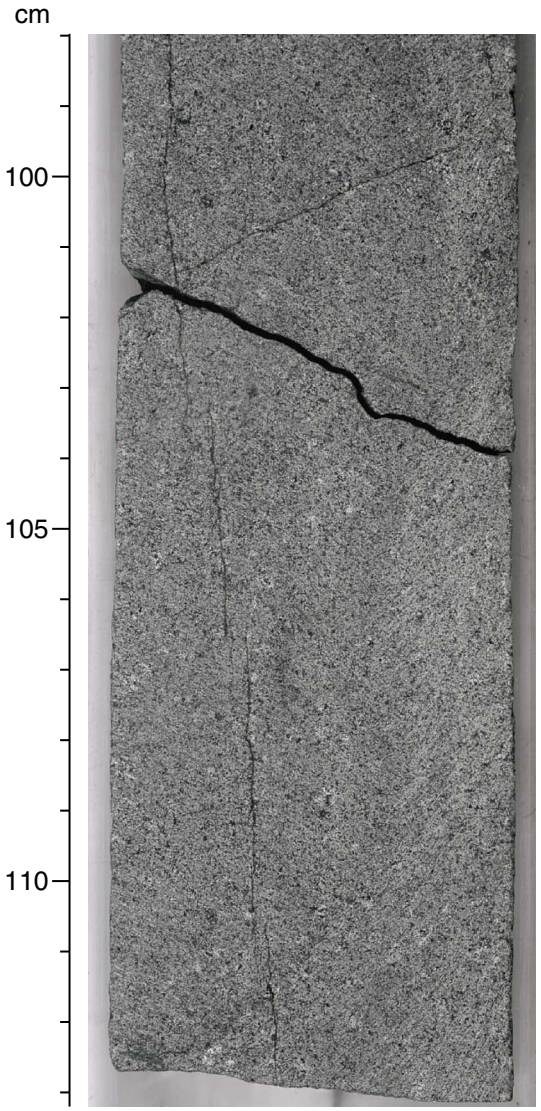

Figure F55. Stereographic plot (equal area, lower hemisphere) of the conjugate set of reverse faults shown in Figure **F54,** p. 127. The black and white split symbols indicate the sense of movement along the plane (black = down, white = up).

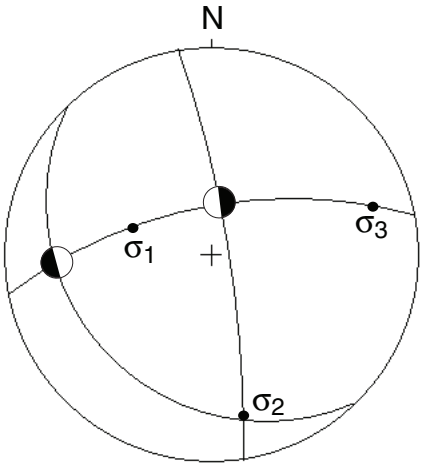

Figure F56. Stereographic plot (equal area, lower hemisphere) of the brittle shear zone boundaries as observed in Unit 4 pyroxene gabbro. The black and white split symbols indicate the sense of movement along the plane (black = down, white = up).

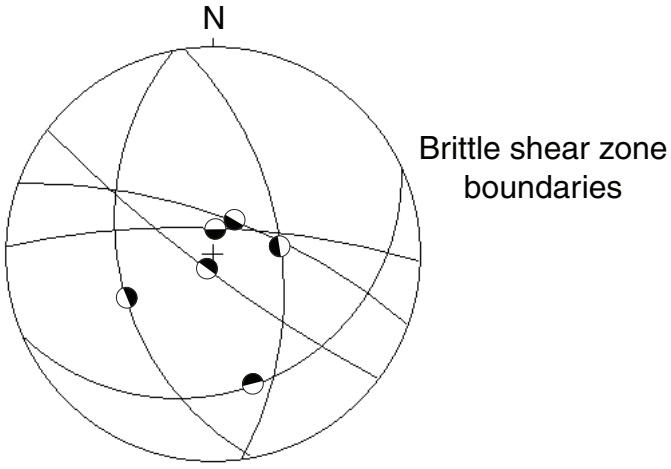

Figure F57. **A.** Porosity calculated from wet and dry mass and volume measurements. **B.** Bulk (wet) density. **C.** Close-up of porosity within igneous units. **D.** Close-up of bulk density. Gray shading denotes the upper and lower igneous units.

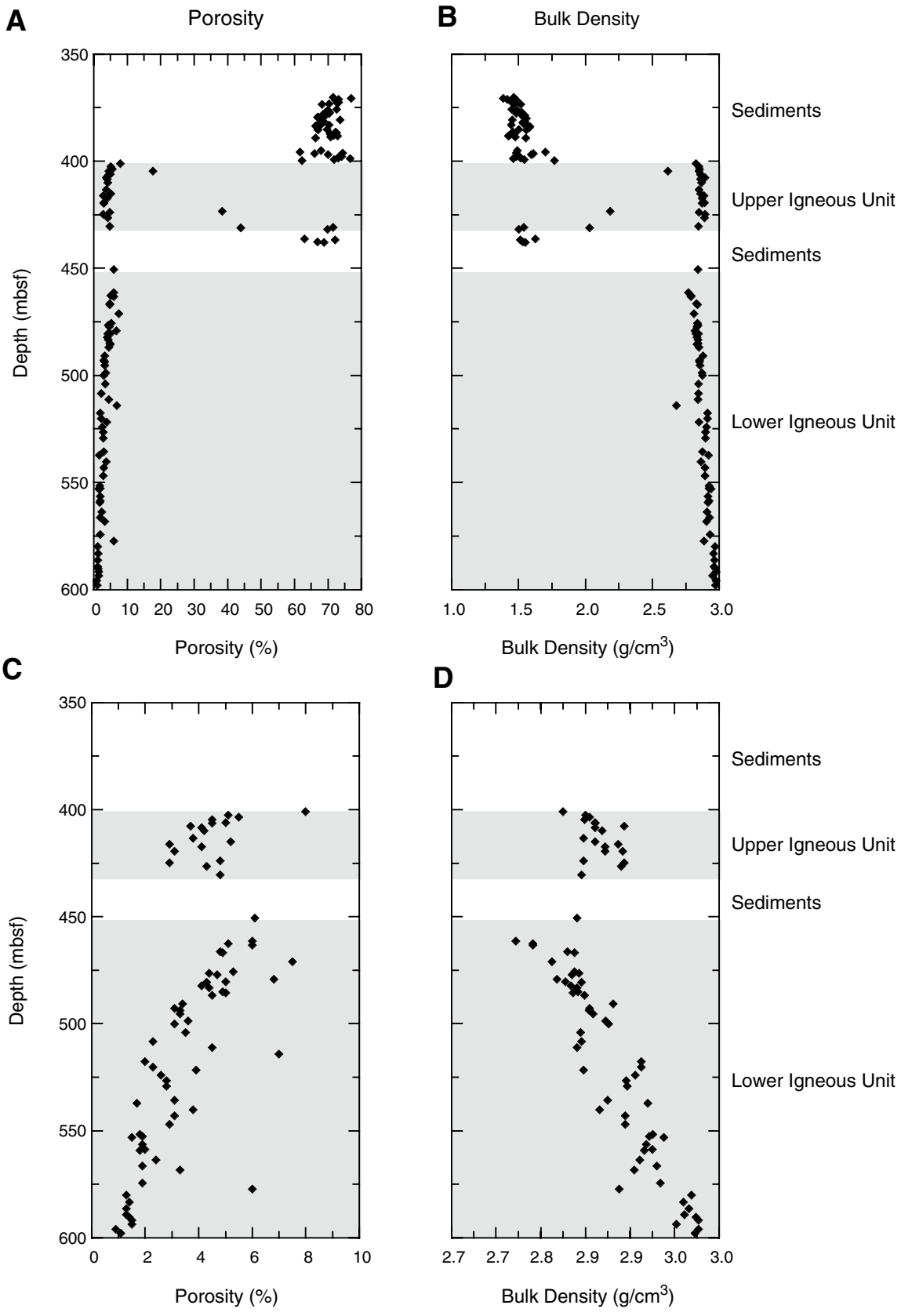

Figure F58. Corrected GRA and MAD bulk densities. Black symbols = corrected GRA bulk density, red symbols = moisture and density property bulk density.

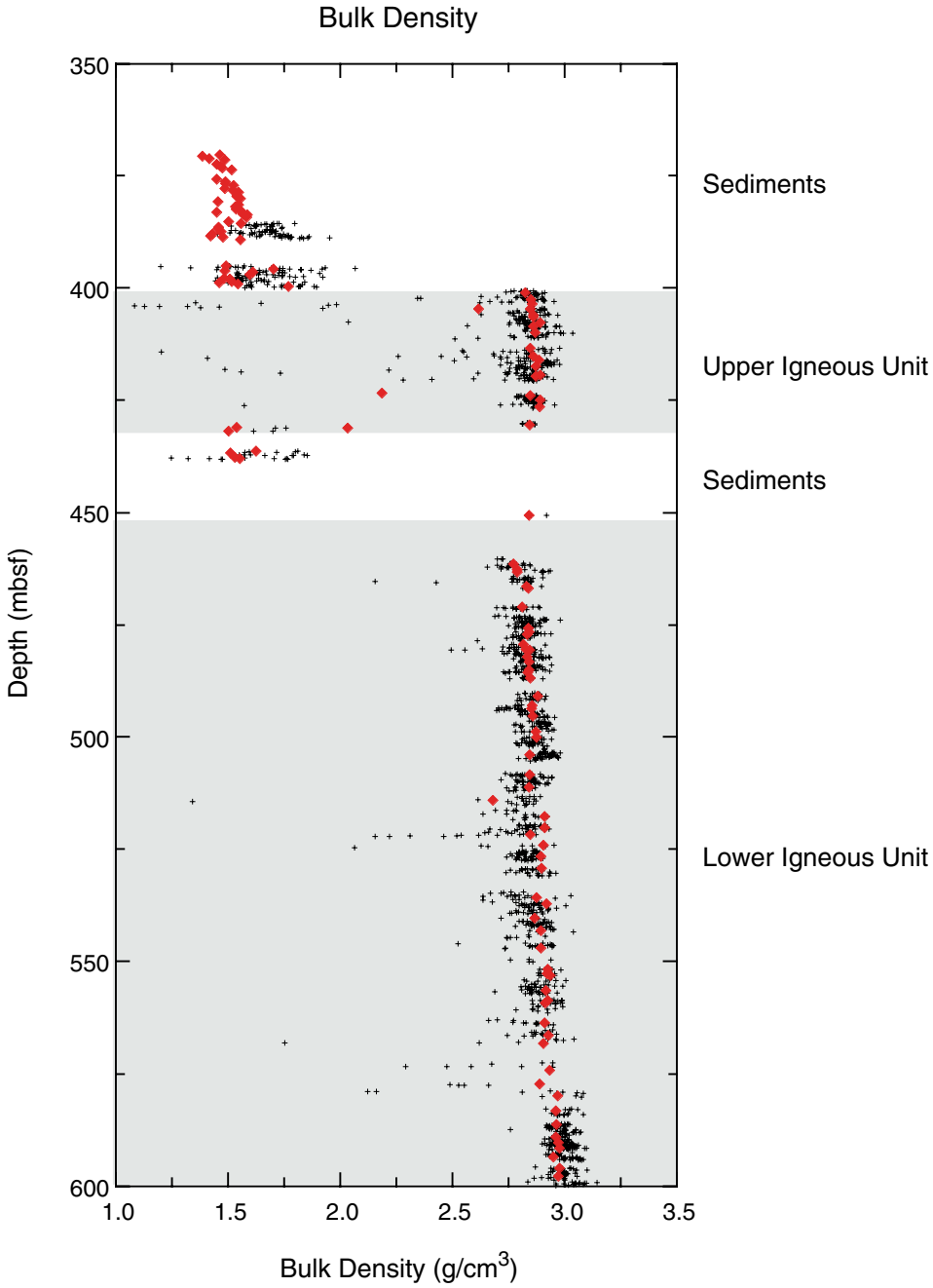

Figure F59. Grain density determined from dry mass and volume measurements.

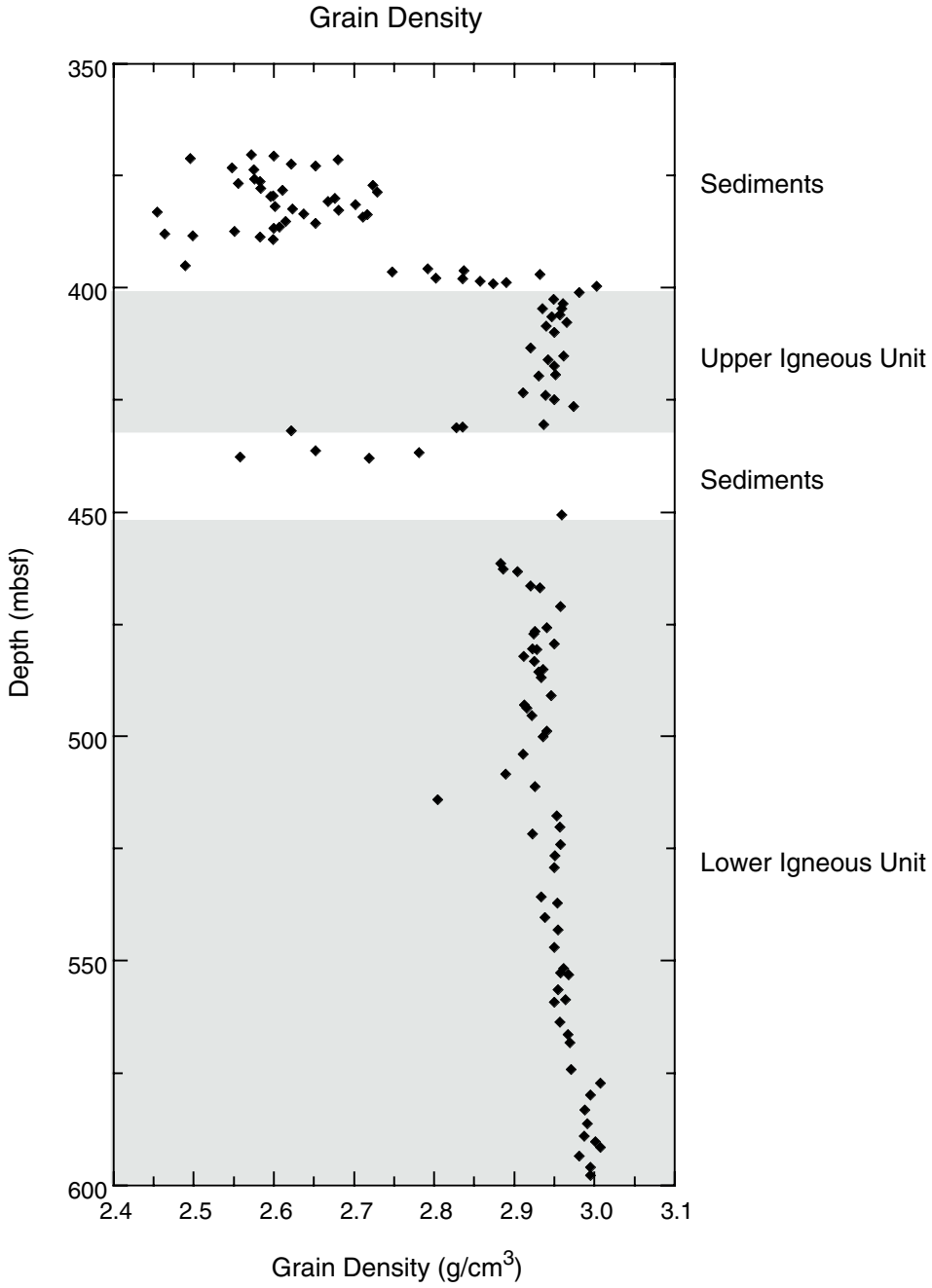

Figure F60. Thermal conductivity.

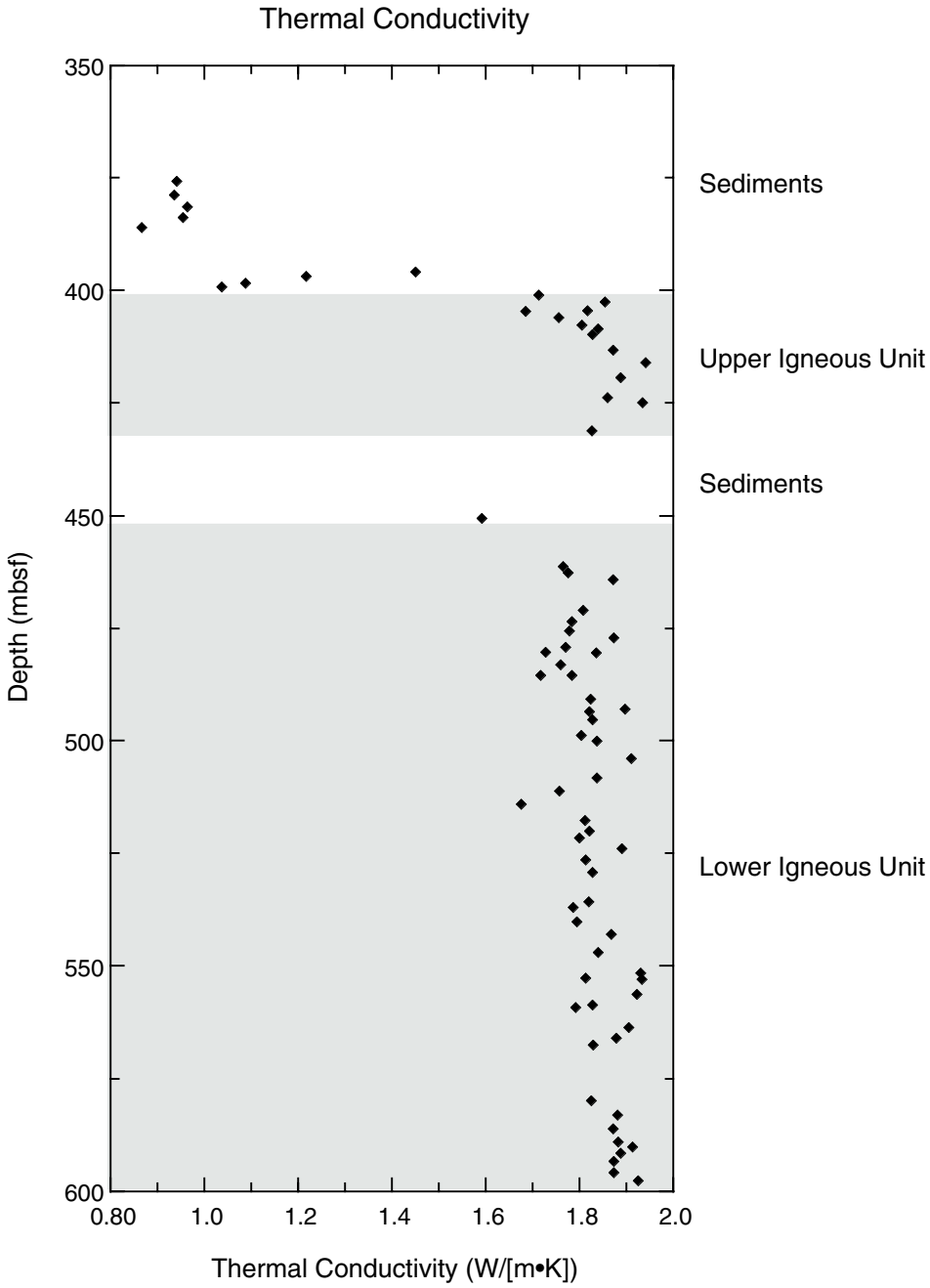

Figure F61. **A.** PWS *P*-wave velocity. **B.** Close-up of *P*-wave velocity in the igneous units. **C.** *P*-wave velocity as a function of porosity in samples from the igneous units.

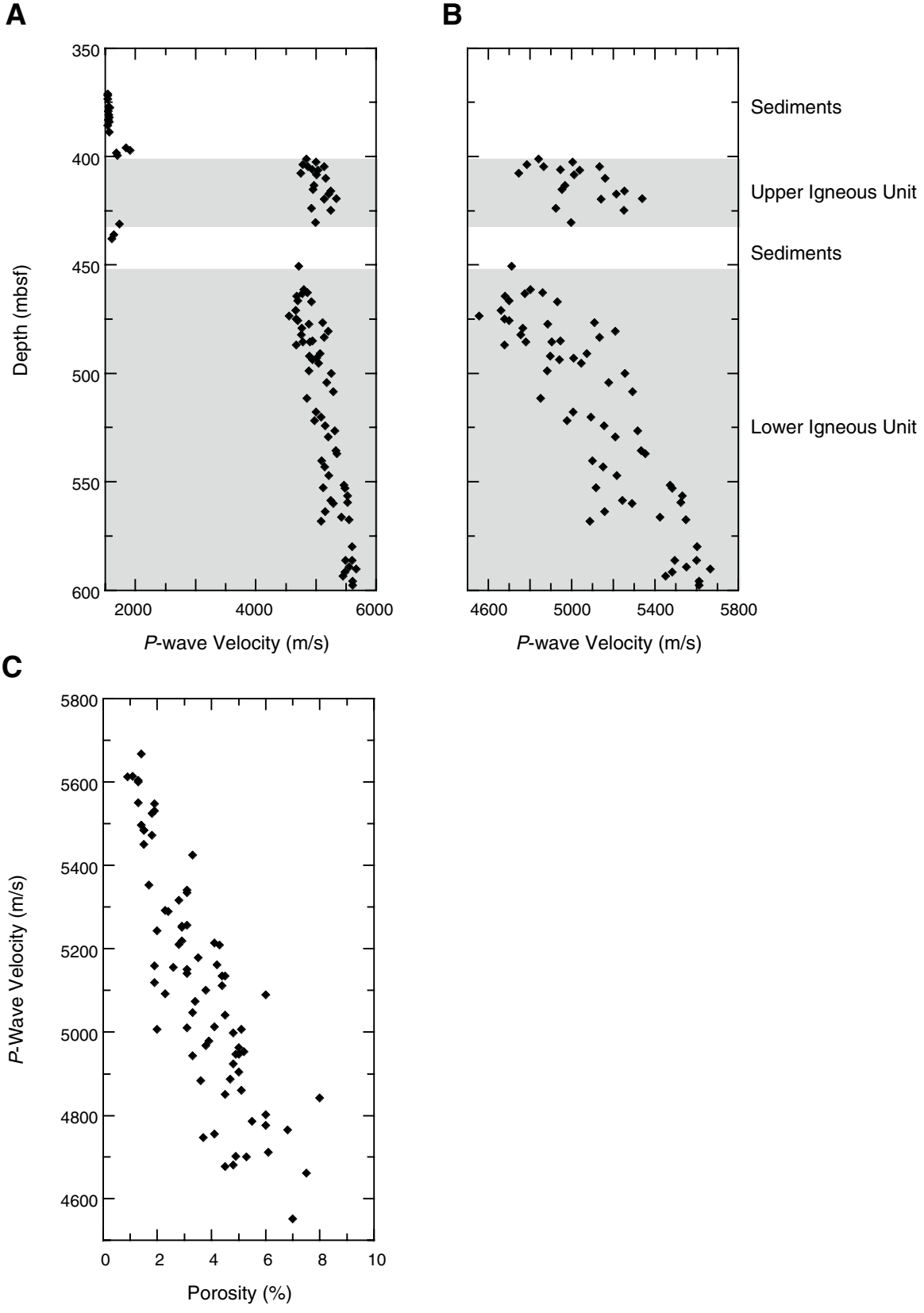

Figure F62. Filtered, corrected multisensor track natural gamma ray (NGR) measurements. cps = counts per second.

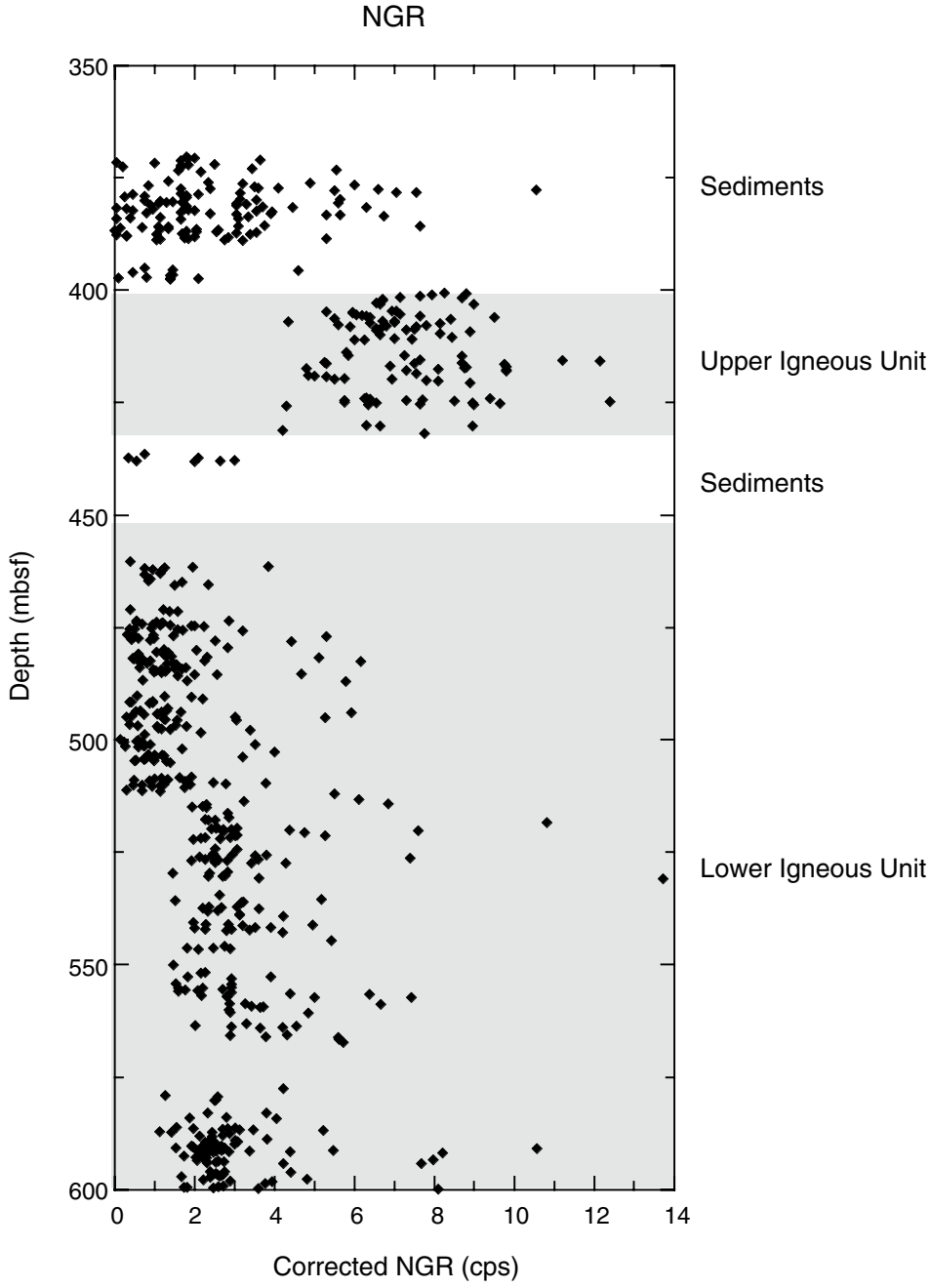

Figure F63. Multisensor track volumetric magnetic susceptibility (dimensionless).

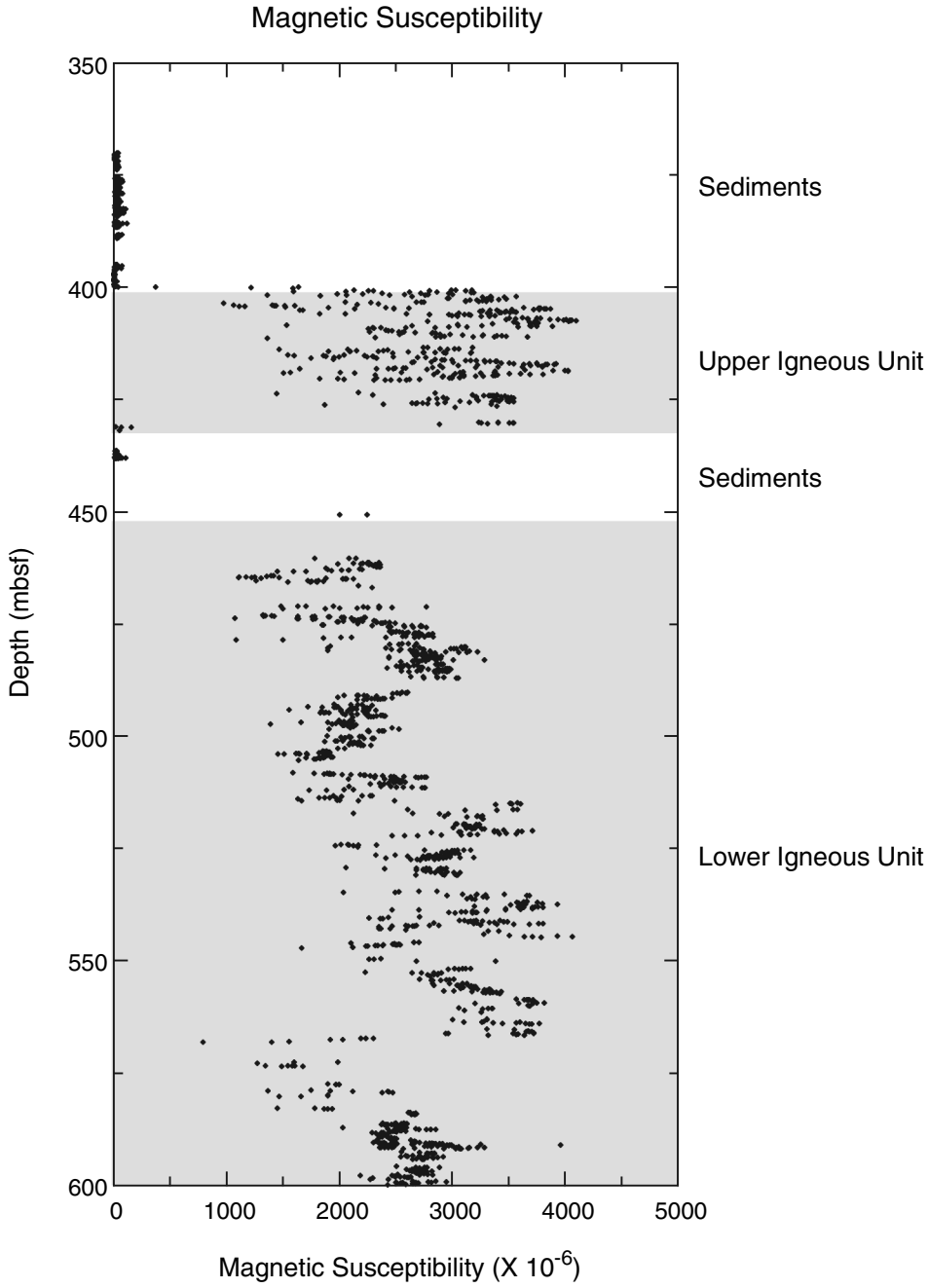

Figure F64. Paleomagnetic results at Hole 1253A. Black dots = magnetic inclinations of the archive sections after AF demagnetization to 40 mT, white circles = magnetic inclinations measured on discrete samples. The magnetic intensity after the 20 mT of the AF demagnetization shows several high intensity peaks in the gabbro intrusions. Age of clear magnetic polarities are estimated based on magnetostratigraphy from Site 1039.

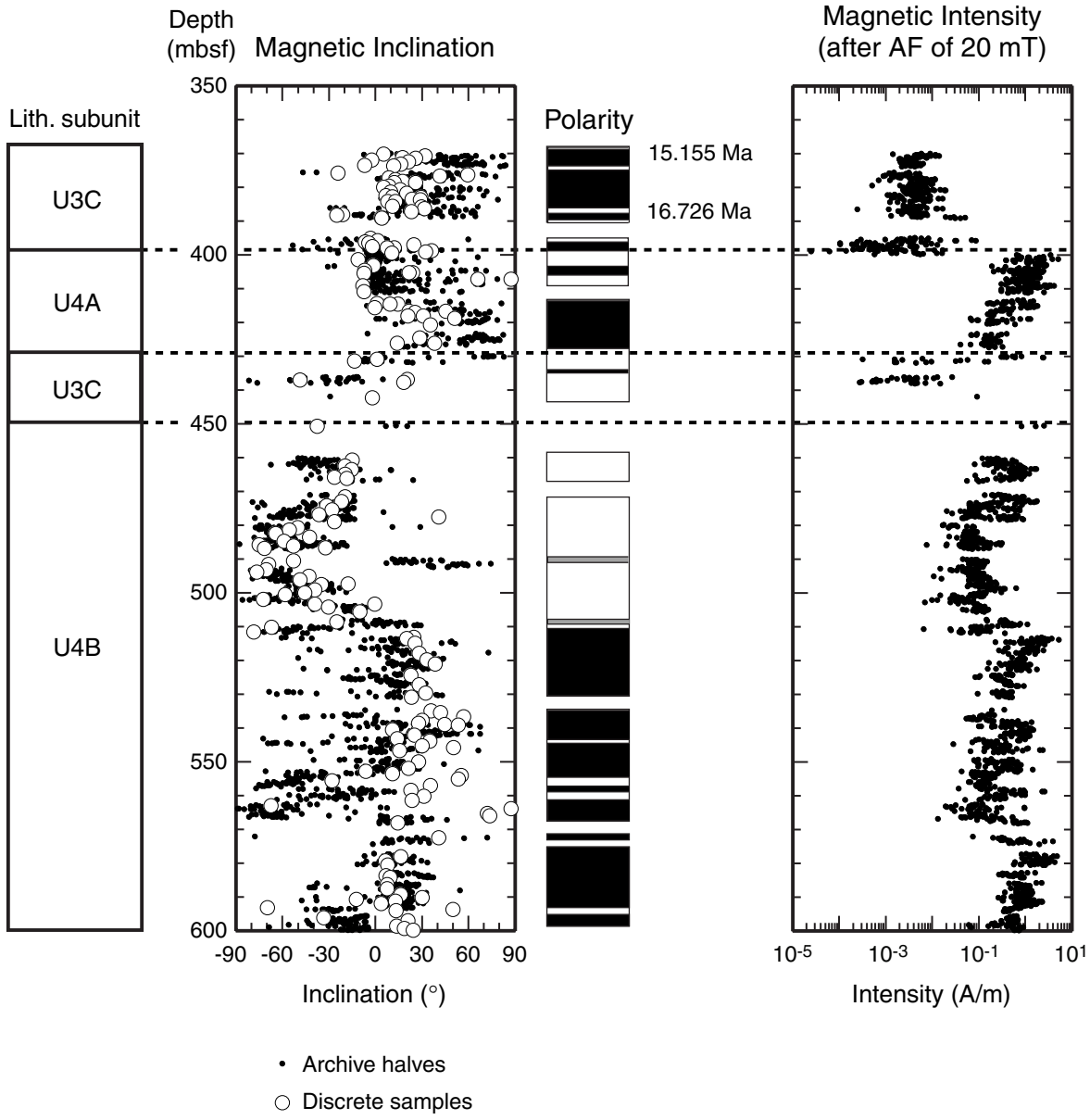

Figure F65. Natural remanent magnetization (NRM) intensity and the magnetic intensity after alternating-field (AF) demagnetization to 20 mT. The high ratio of the magnetic intensity between the demagnetization and the NRM intensity indicates stability of magnetization of the core. Int = intensity.

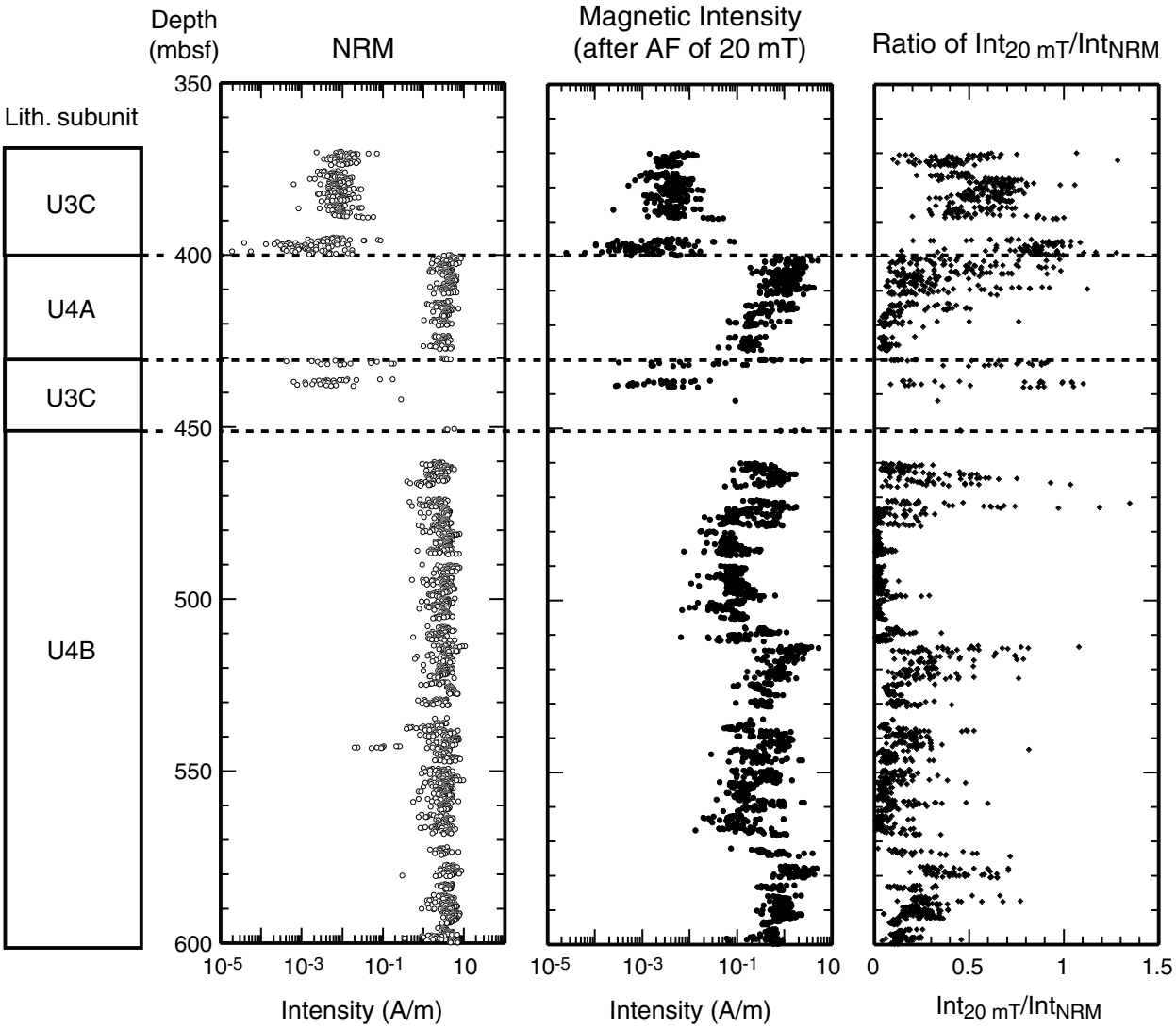

Figure F66. Results of saturation remanent magnetization (SIRM) and the Lowrie's tests conducted on sediment samples. IRM = isothermal remanent magnetization.

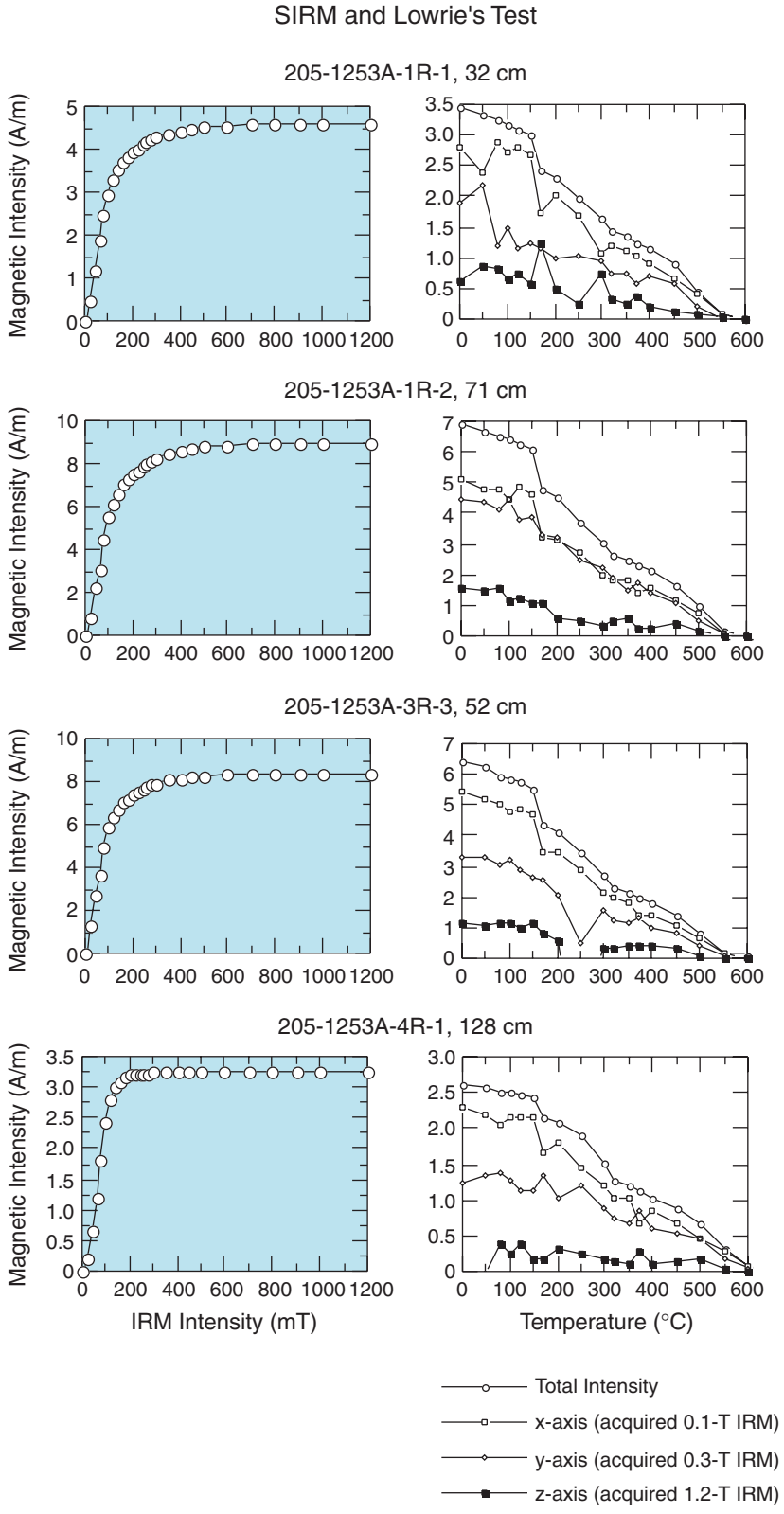

Figure F67. A. Magnetic domain state of the gabbro rocks. Some samples are identified as multidomain (MD); however, identification of domain state for other samples taken from weak magnetic intensity zones are unsuccessful because of similar anhysteretic remanent magnetization (ARM) and the saturation remanent magnetization (SIRM) curves. **B.** Magnetic domain state of the sediments above 400 mbsf. Resistance of the ARM relative to the SIRM suggests that single domain states may be dominant in the sediments. (**Figure shown on next page.**)

Figure F67 (continued). (Caption shown on previous page.)

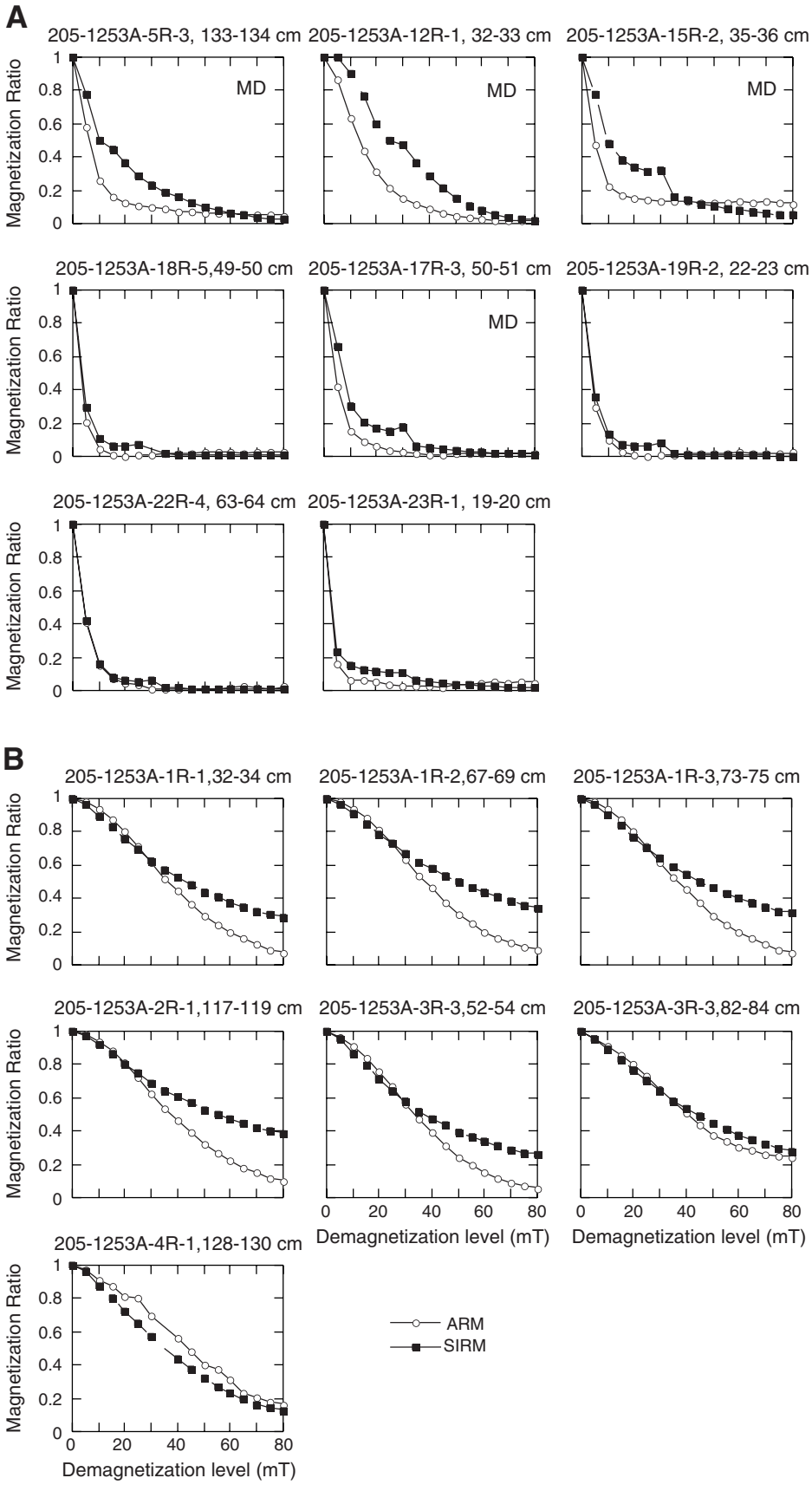

Figure F68. Zijderveld diagrams for discrete samples. Results of the (**A**) sediments and (**B**) gabbro rocks show stability of natural remanent magnetizations. Div. = divergency, J_0 = magnetic intensity of NRM.

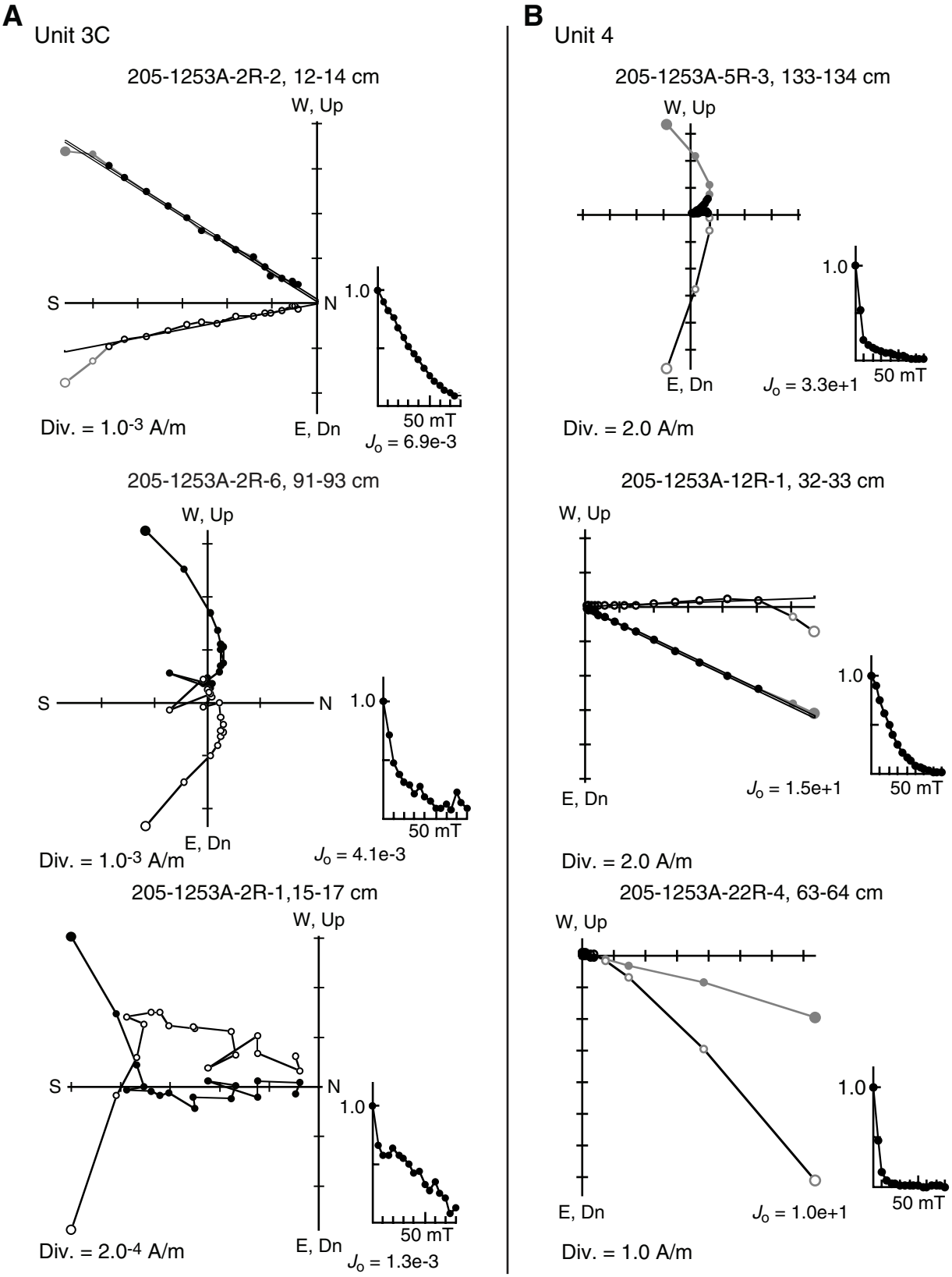

Figure F69. Average inclinations collected from (**A**) sediments, (**B**) upper gabbro intrusions, and (**C**) lower gabbro unit.

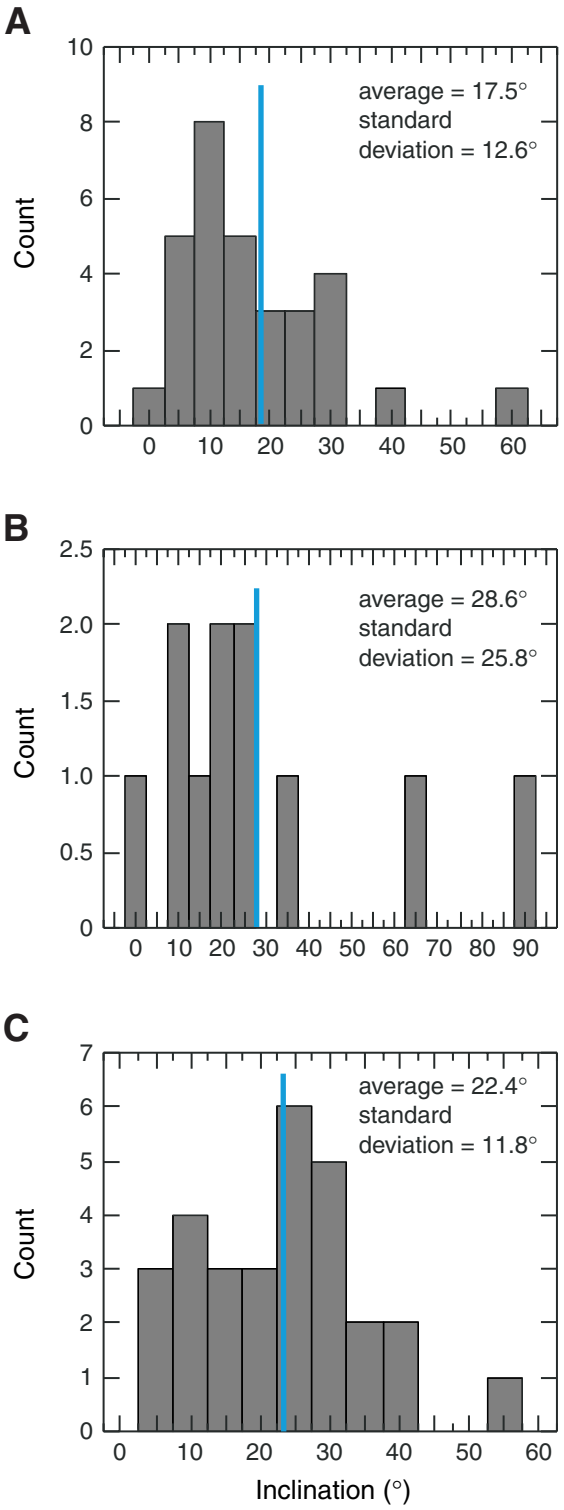

Figure F70. Depth profiles of (**A**) Cl, (**B**) Na, (**C**) Na/Cl, and (**D**) K. Arrows = seawater concentration. Dashed line = sill depth at Site 1039. Error bars are smaller than or comparable to symbol size (see "Inorganic Geochemistry," p. 24, in the "Explanatory Notes" chapter). Subunit 4A = gabbro sill, Subunit 4B = lower igneous section.

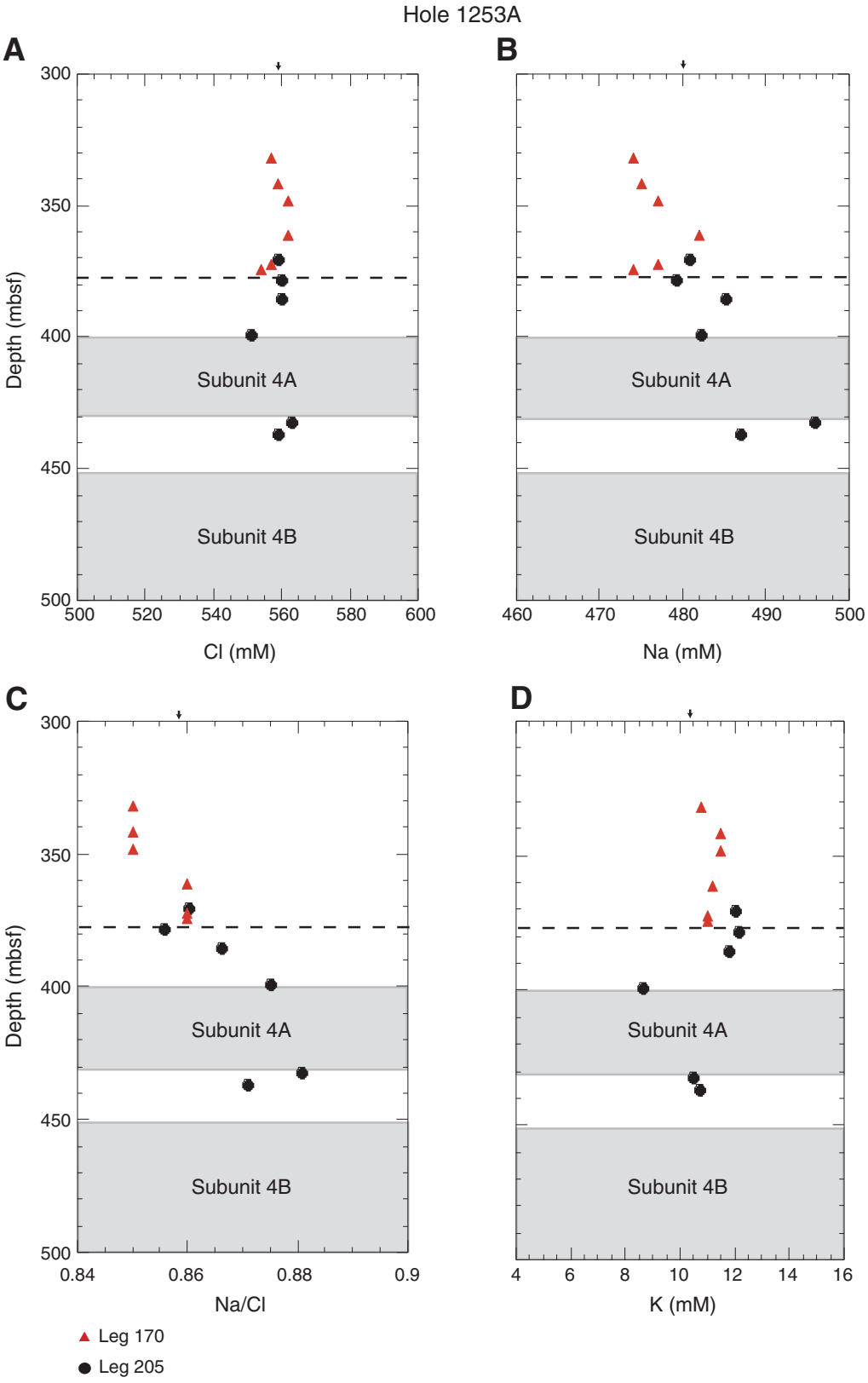

Figure F71. Depth profiles of (**A**) SO_4, (**B**) NH_4, (**C**) Fe, and (**D**) Mn. Arrow = seawater concentration. Dashed line = sill depth at Site 1039. Error bars are smaller than or comparable to symbol size (see "Inorganic Geochemistry," p. 24, in the "Explanatory Notes" chapter).

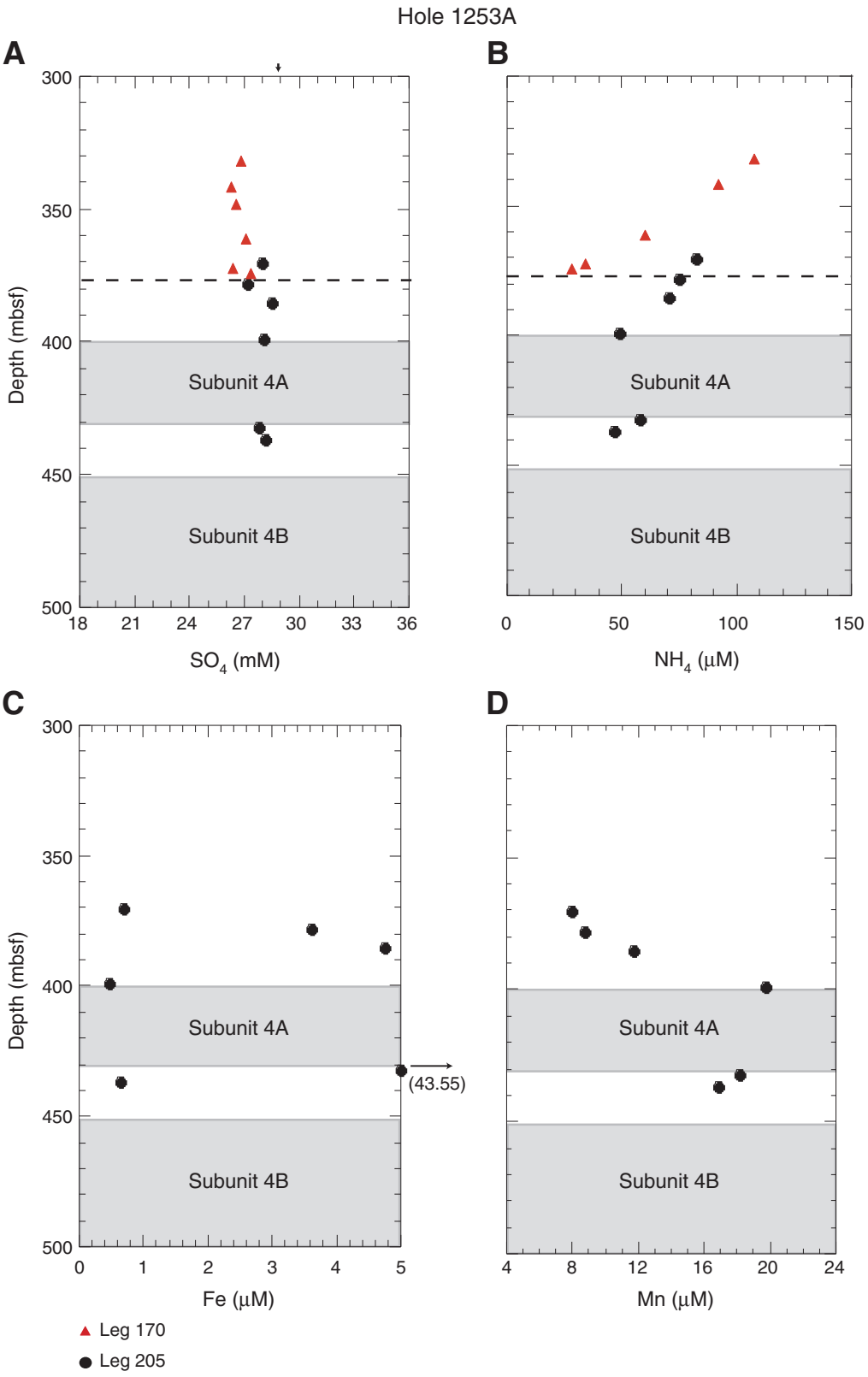

Figure F72. Depth profiles of (**A**) Ca, (**B**) Mg, (**C**) Mg/Ca, and (**D**) Sr. Arrows = seawater concentration. Dashed line = sill depth at Site 1039. Error bars are smaller than or comparable to symbol size (see "Inorganic Geochemistry," p. 24, in the "Explanatory Notes" chapter). Leg 170 Sr data provided by Scripps Institution of Oceanography.

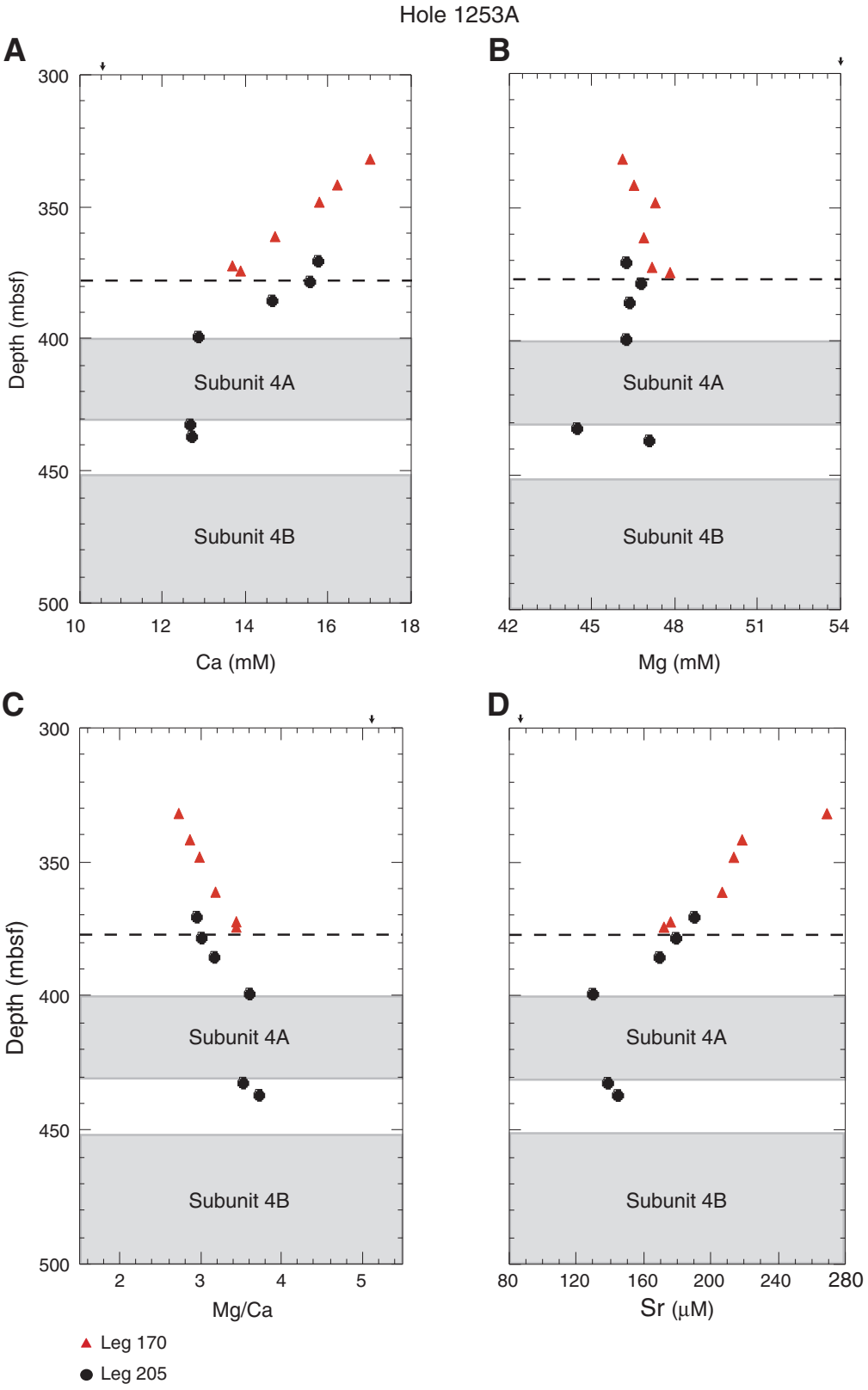

Figure F73. Depth profiles of (**A**) Ba, (**B**) H_4SiO_4, (**C**) Li, and (**D**) B. Arrows= seawater concentration. Dashed line = sill depth at Site 1039. Error bars are smaller than or comparable to symbol size (see **"Inorganic Geochemistry,"** p. 24, in the "Explanatory Notes" chapter). Leg 170 Li data are from Chan and Kastner (2000).

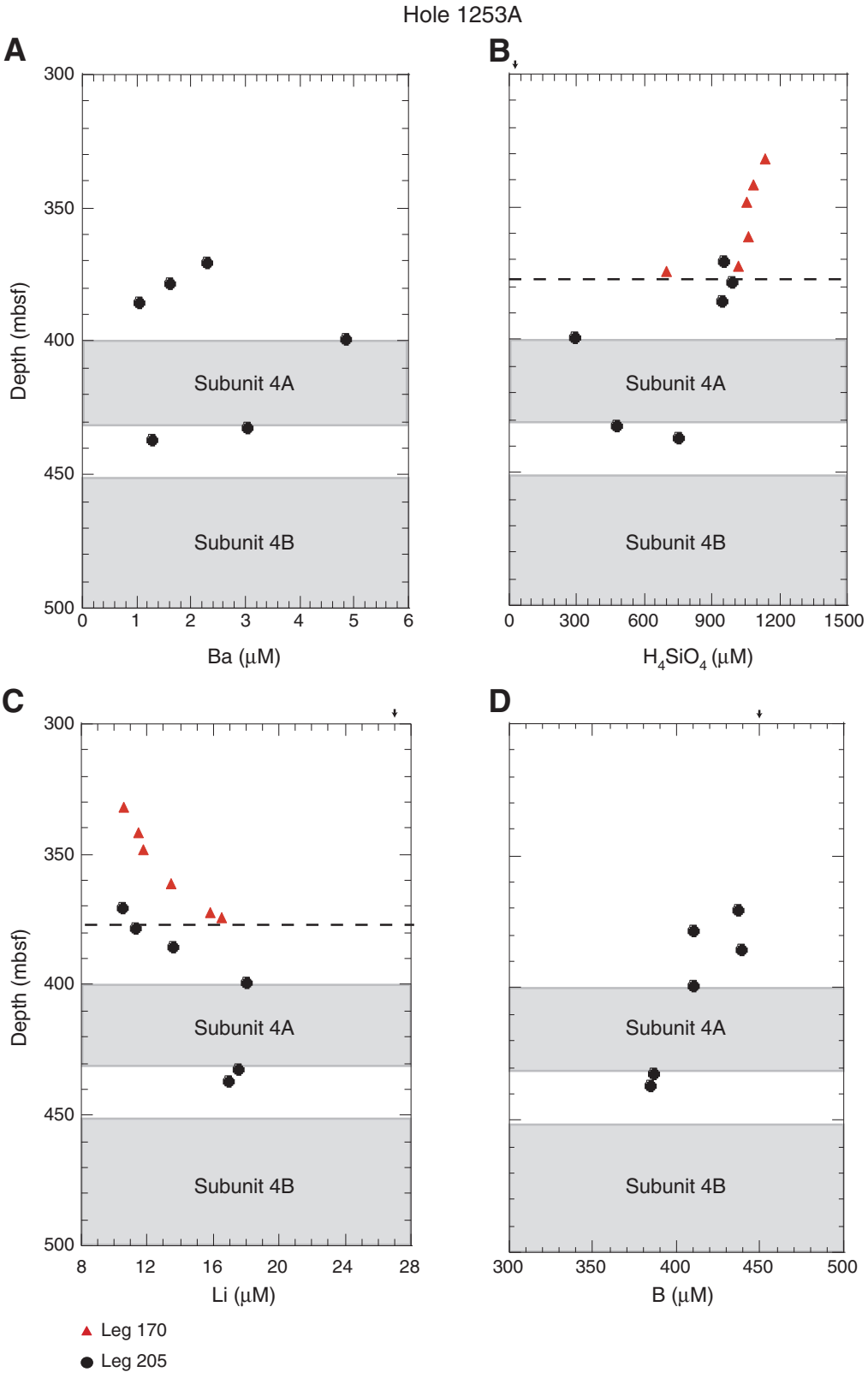

Figure F74. Results of headspace gas analyses for methane depth distribution at Sites 1253 (solid circles) and 1039 (open circles). Subunit 4A = gabbro sill, Subunit 4B = lower igneous section. Gray shaded areas = recovered igneous rock.

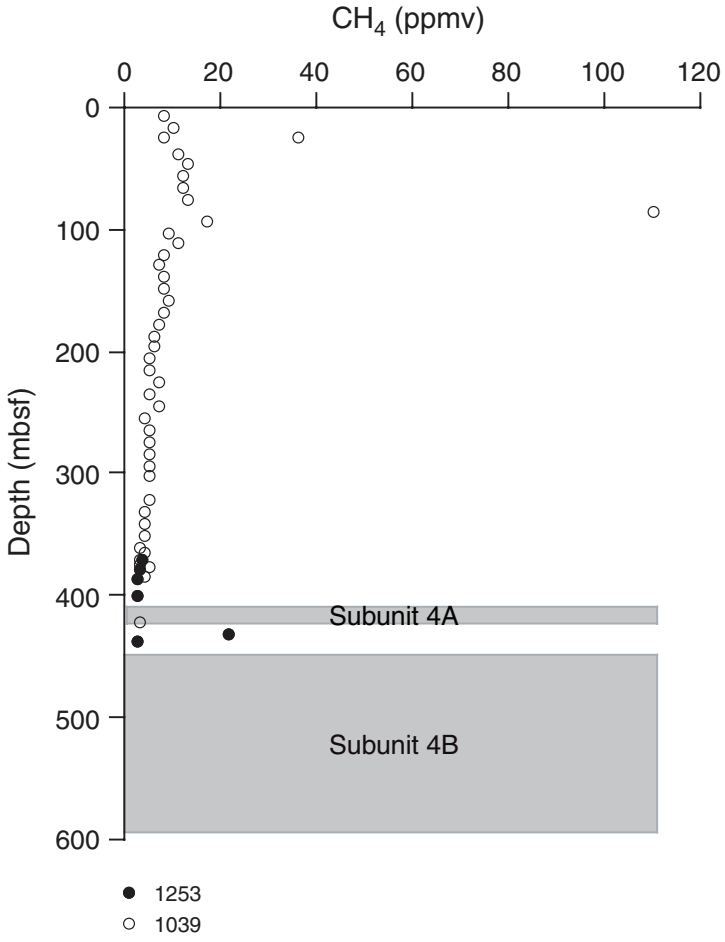

Figure F75. Depth profiles of (A) total organic carbon (TOC), (B) calcium carbonate, and (C) sulfur concentrations for Sites 1253 and 1039. Gray shaded areas = depth intervals of the igneous rock.

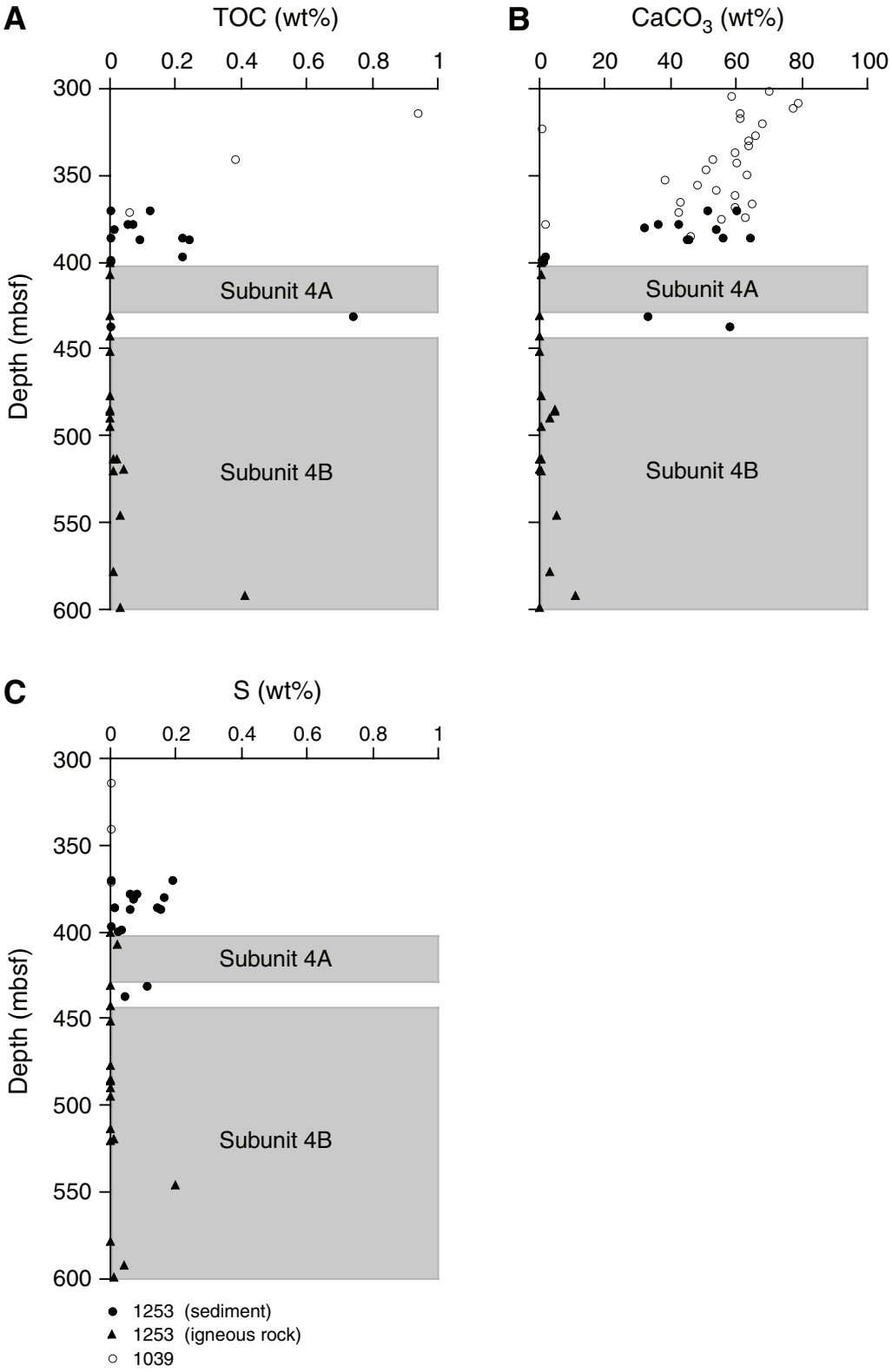

Figure F76. Image of the rock (Core 205-1253A-42R) used for sampling of Core 42R prior to the initial breaking.

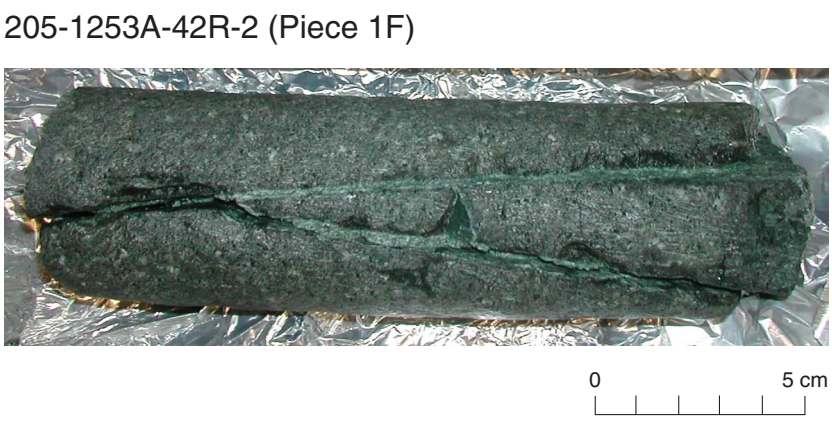

Figure F77. Image of sample from Core 205-1253A-42R, shown in Figure F76, p. 150, after the initial breaking, to be used for all analyses.

Figure F78. Temperature record of a miniaturized temperature data logger mounted on the video system while reentering the borehole. The different plateaus in the record mark times when the system was held at constant depth. At the maximum depth of 4333 mbrf at 1605 hr UTC, the temperature was 1.985°C.

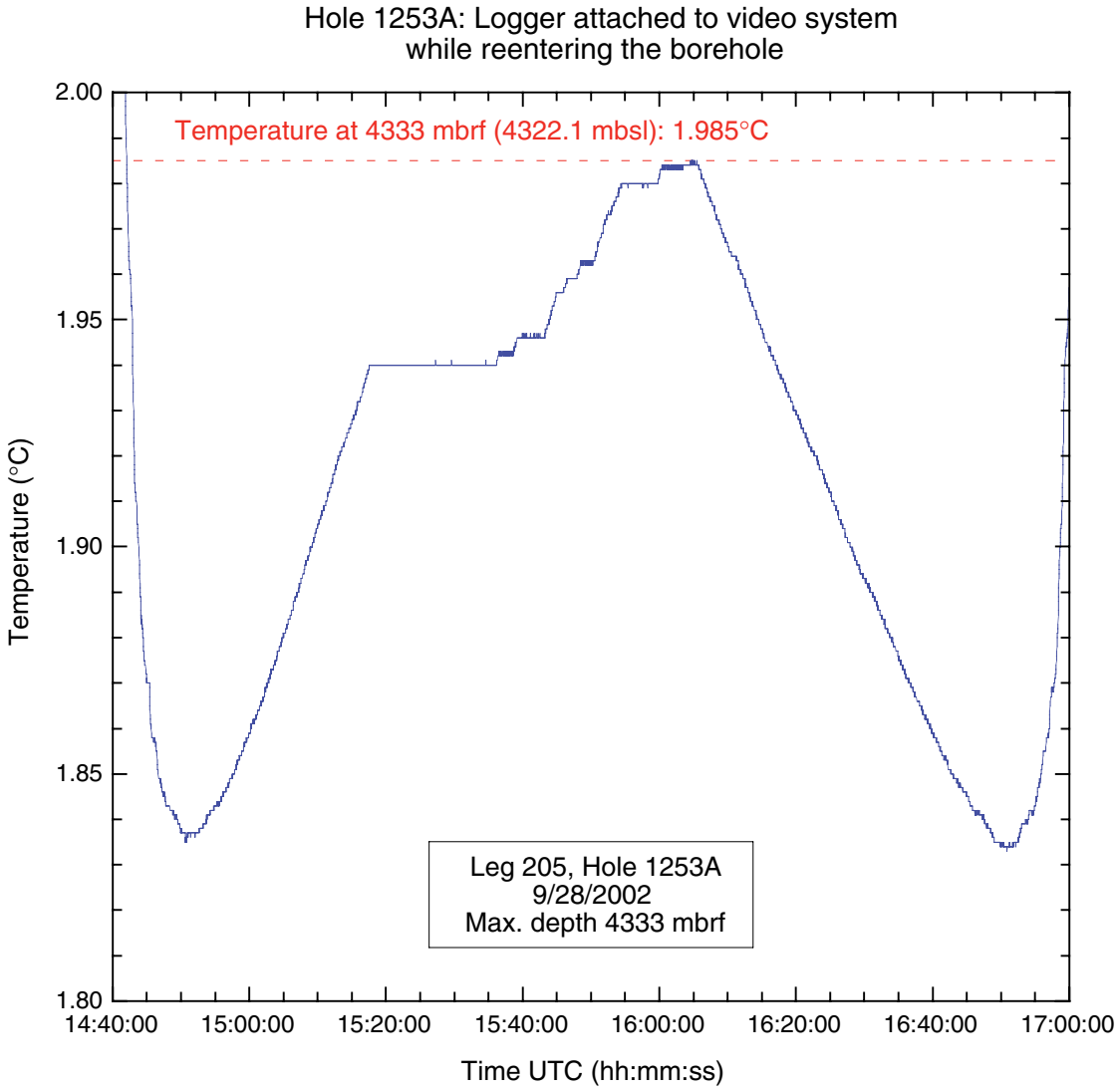

Figure F79. A conductivity/temperature/depth recorder (CTD) profile from 2500 to 5318 mbsl recorded offshore Nicaragua by the German *Meteor* in September 2002. A measured temperature of 1.989°C is observed at the water depth of Site 1253 (4376.5 mbsl). At the maximum depth of the miniaturized temperature data logger record shown in Figure **F78,** p. 152 (4322 mbsl), the temperature is 1.983°C.

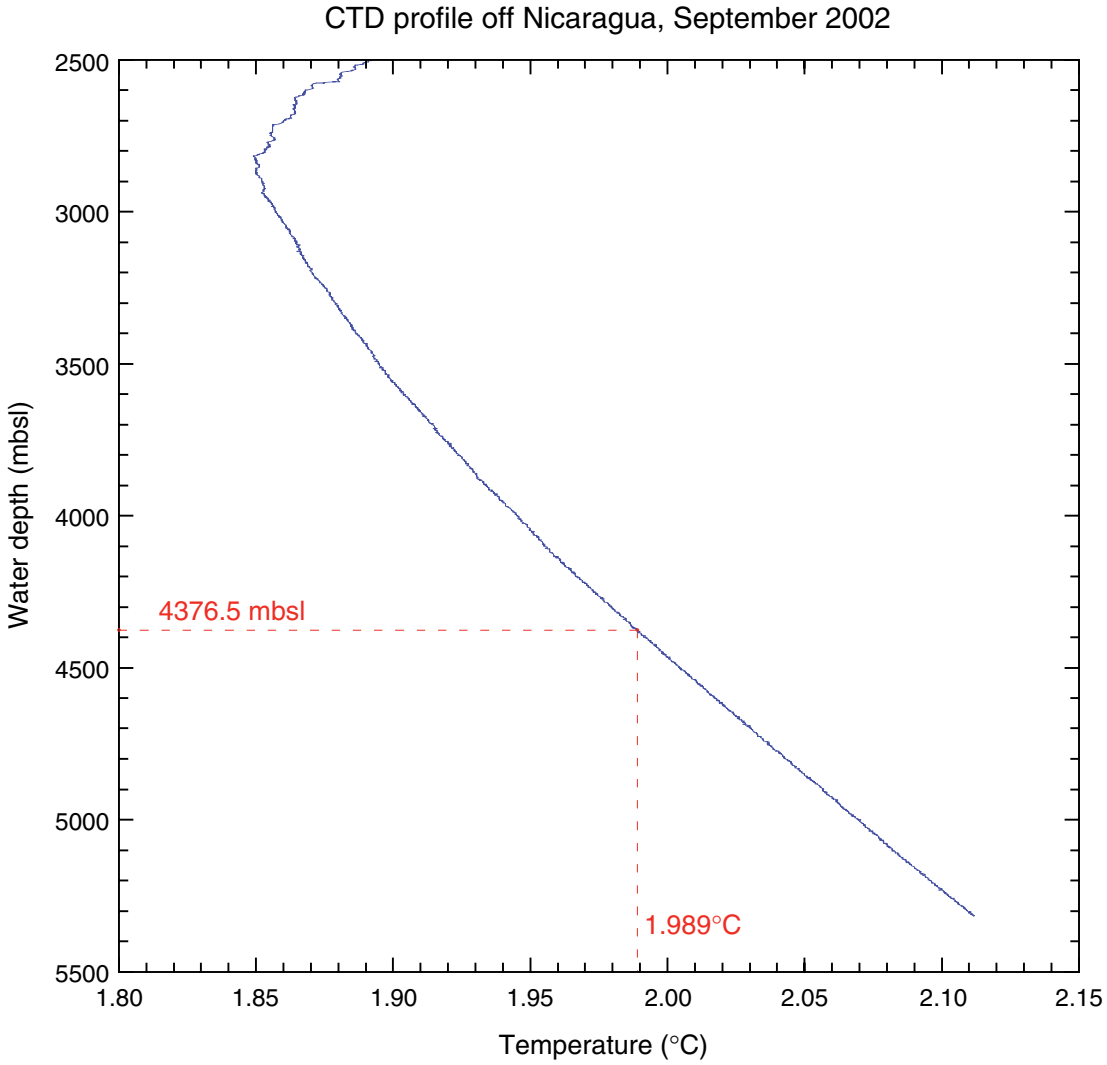

Figure F80. The miniaturized temperature data logger mounted in the Temperature/Acceleration/Pressure tool, which is located on the bottom of the triple combo tool string.

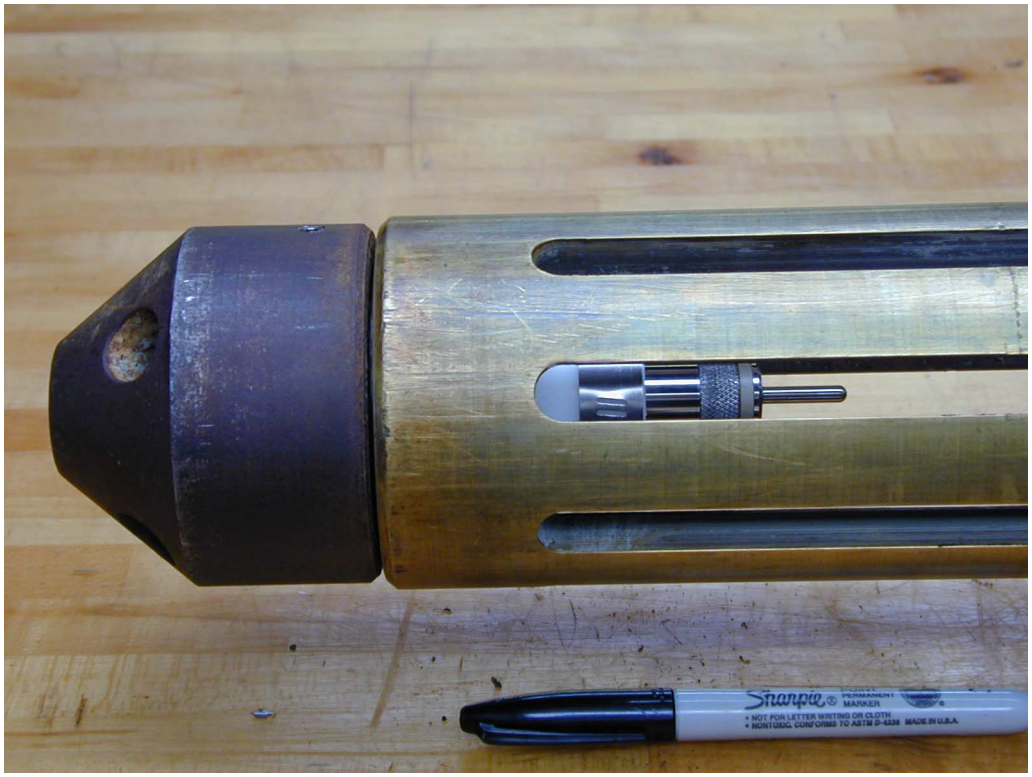

Figure F81. Temperatures (miniaturized temperature data logger [MTL] and Temperature/Acceleration/Pressure [TAP]) and pressures (TAP) observed during (**A**) run 1 and (**B**) run 2 of the wireline logging.

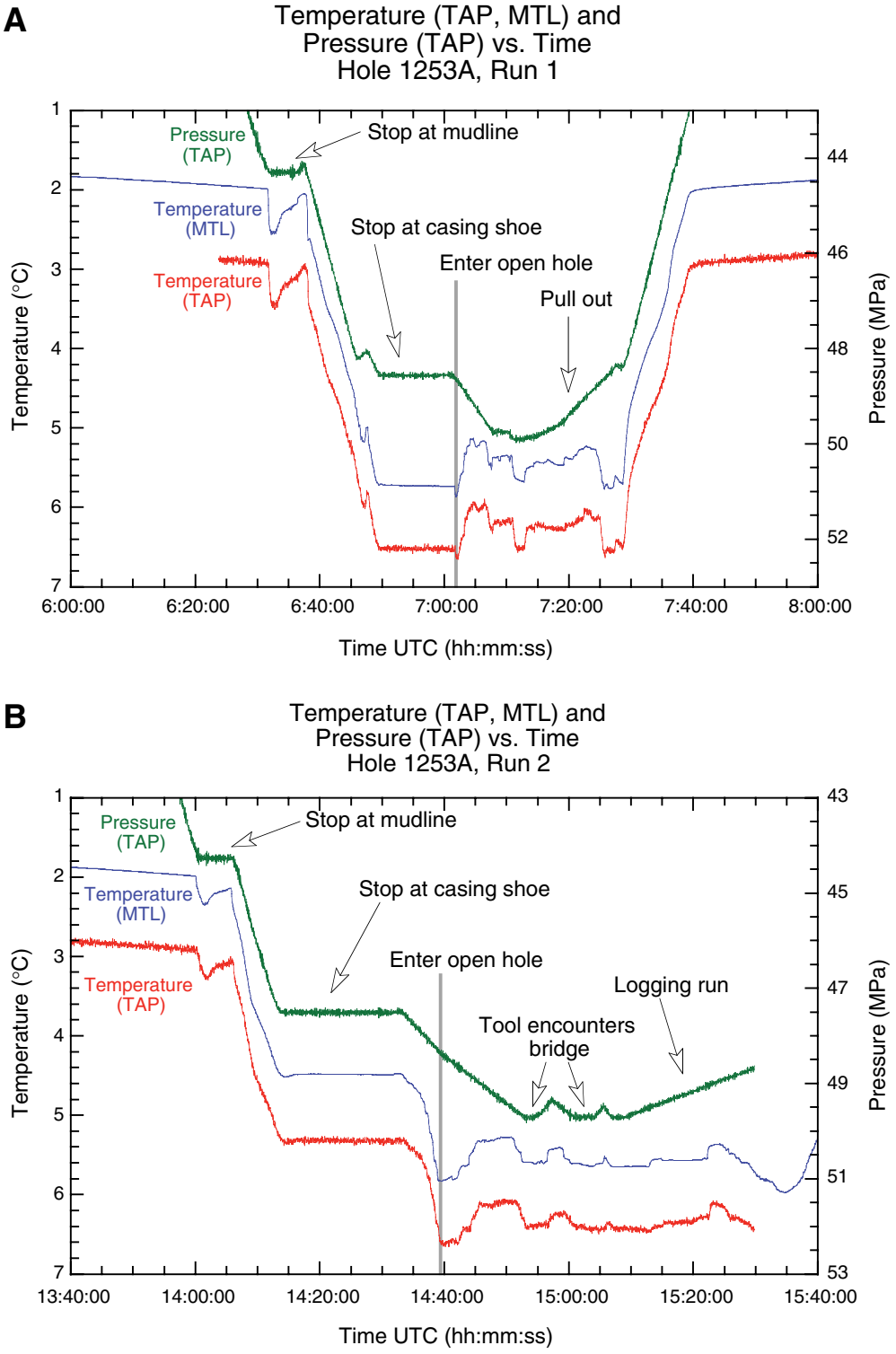

Figure F82. A. Temperatures recorded with the miniaturized temperature data logger (MTL) during lowering of the Temperature/Acceleration/Pressure tool down through the borehole. Both runs are shown and indicate a rather constant gradient in the casing, the presumed influence of the cement curing, and below the casing shoe, the temperature profiles in the open hole. **B.** Magnification of the open hole record. Increased temperatures of run 2 vs. run 1 indicate that the temperature had not yet reached equilibrium state.

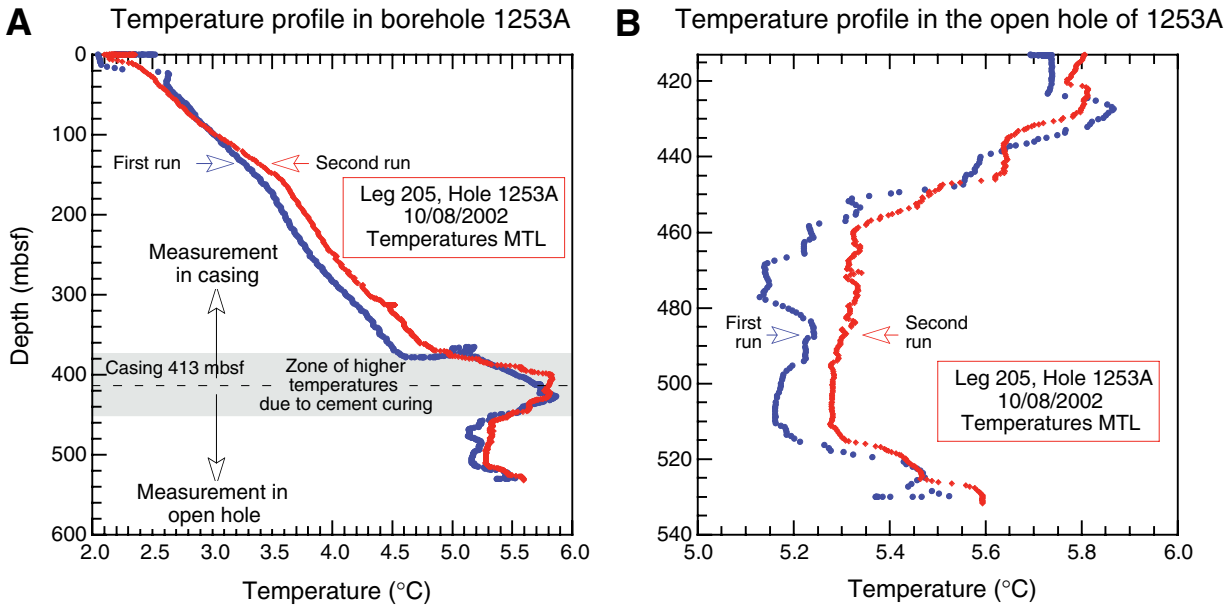

Figure F83. Overview of DVTPP measurements made in Hole 1253A. **A.** DVTPP 01: complete temperature record at 60 mbsf. **B.** DVTPP 01: complete pressure record at 60 mbsf. **C.** DVTPP 02: complete temperature record at 150 mbsf. **D.** DVTPP 02: complete pressure record at 150 mbsf.

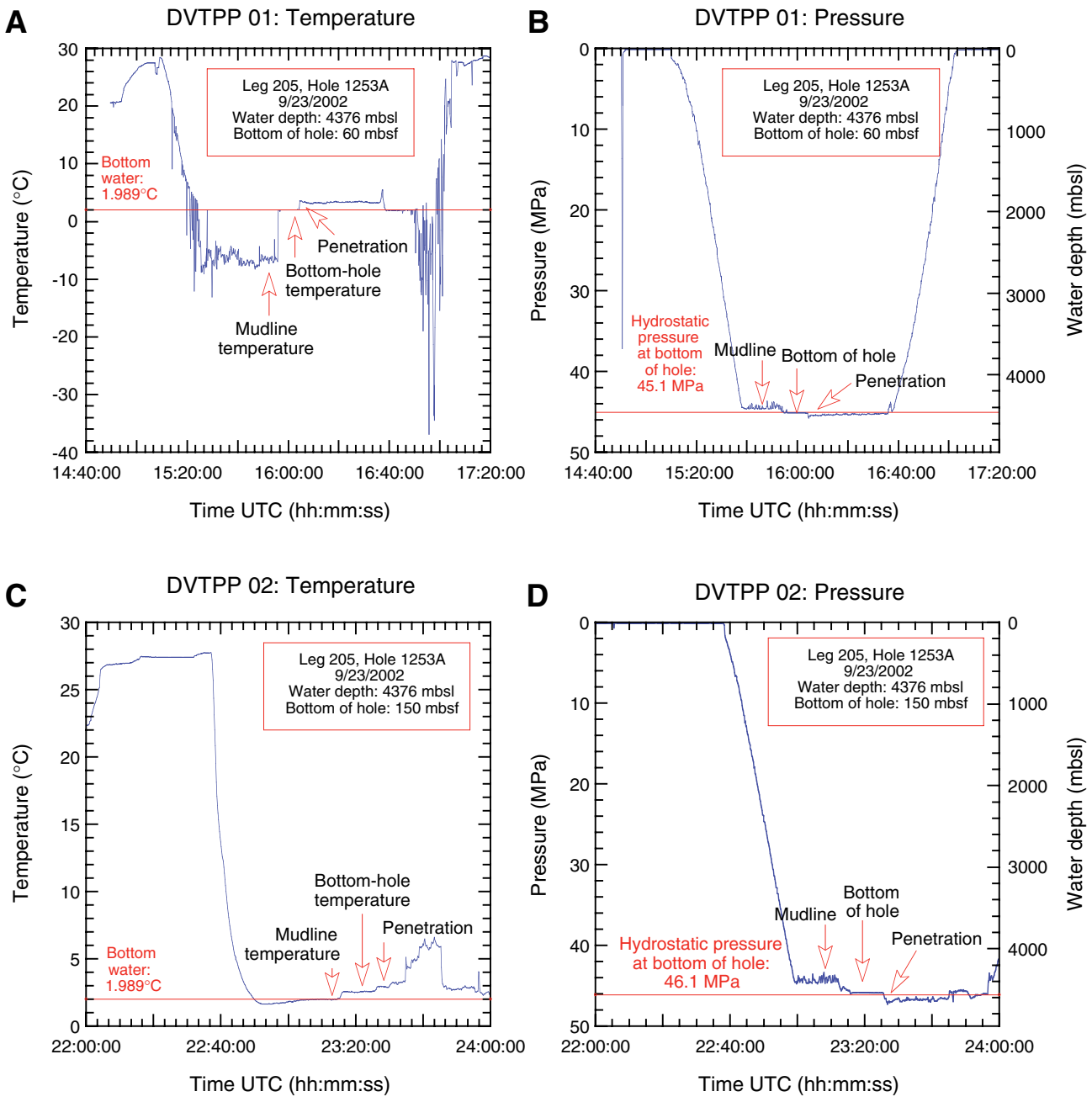

Figure F84. A. Close-up profile of temperature and pressure records at the mudline, bottom of the hole, and during penetration of the DVTPP 01 at 60 mbsf. **B.** Close-up profiles of temperature and pressure records at the mudline, bottom of the hole, and during penetration of the DVTPP 02 at 150 mbsf.

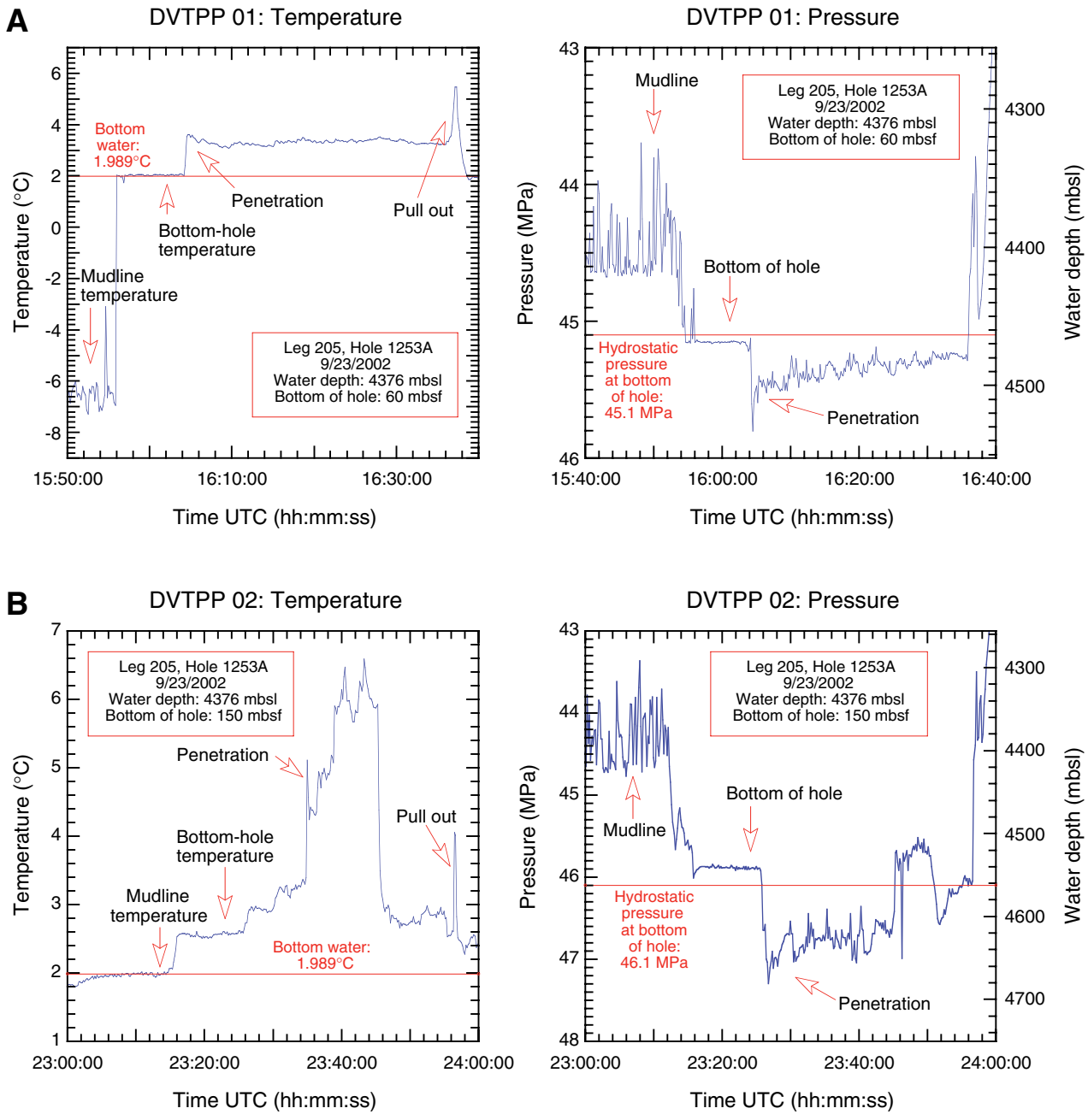

Figure F85. Logging summary diagram showing log, pipe, and seafloor depths. Although the logging data indicate a mudline of 4390 mbrf, all depths in this volume are referenced to the drillers mudline of 4387.1 mbrf.

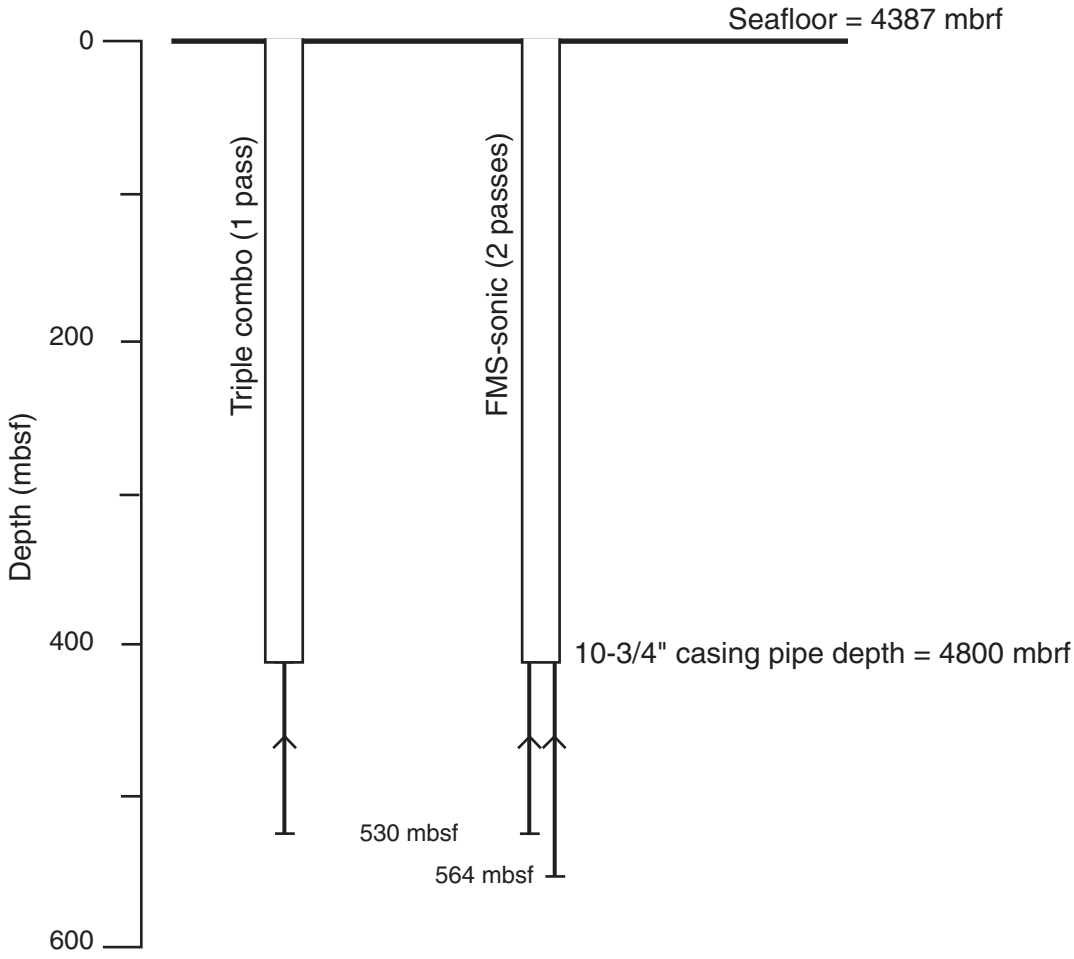

Figure F86. FMS caliper and pad 1 azimuth data from runs 1 and 2.

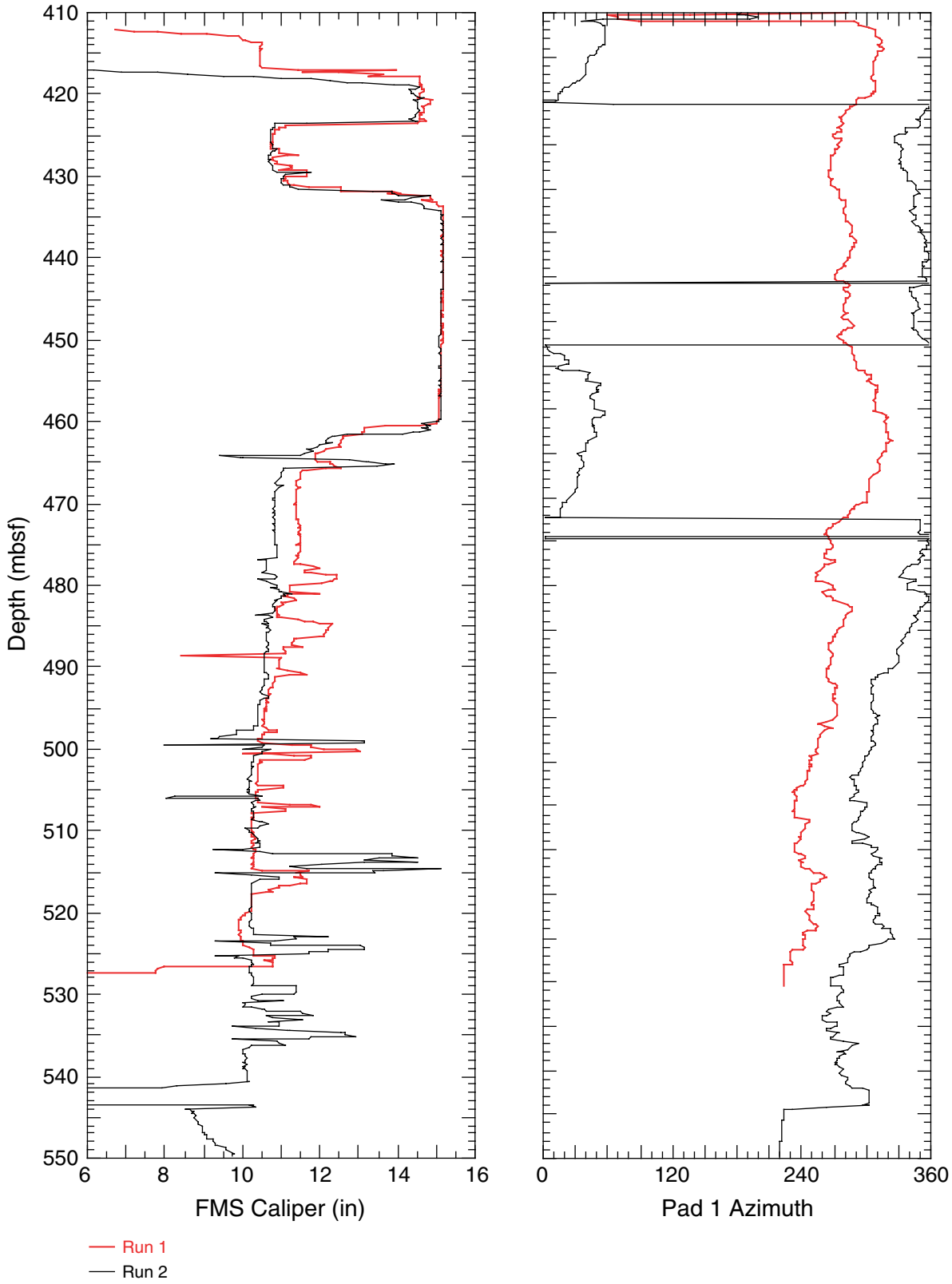

Figure F87. Gamma ray log data from Hole 1253A. PEF = photoelectric effect. Shaded intervals indicate igneous sections.

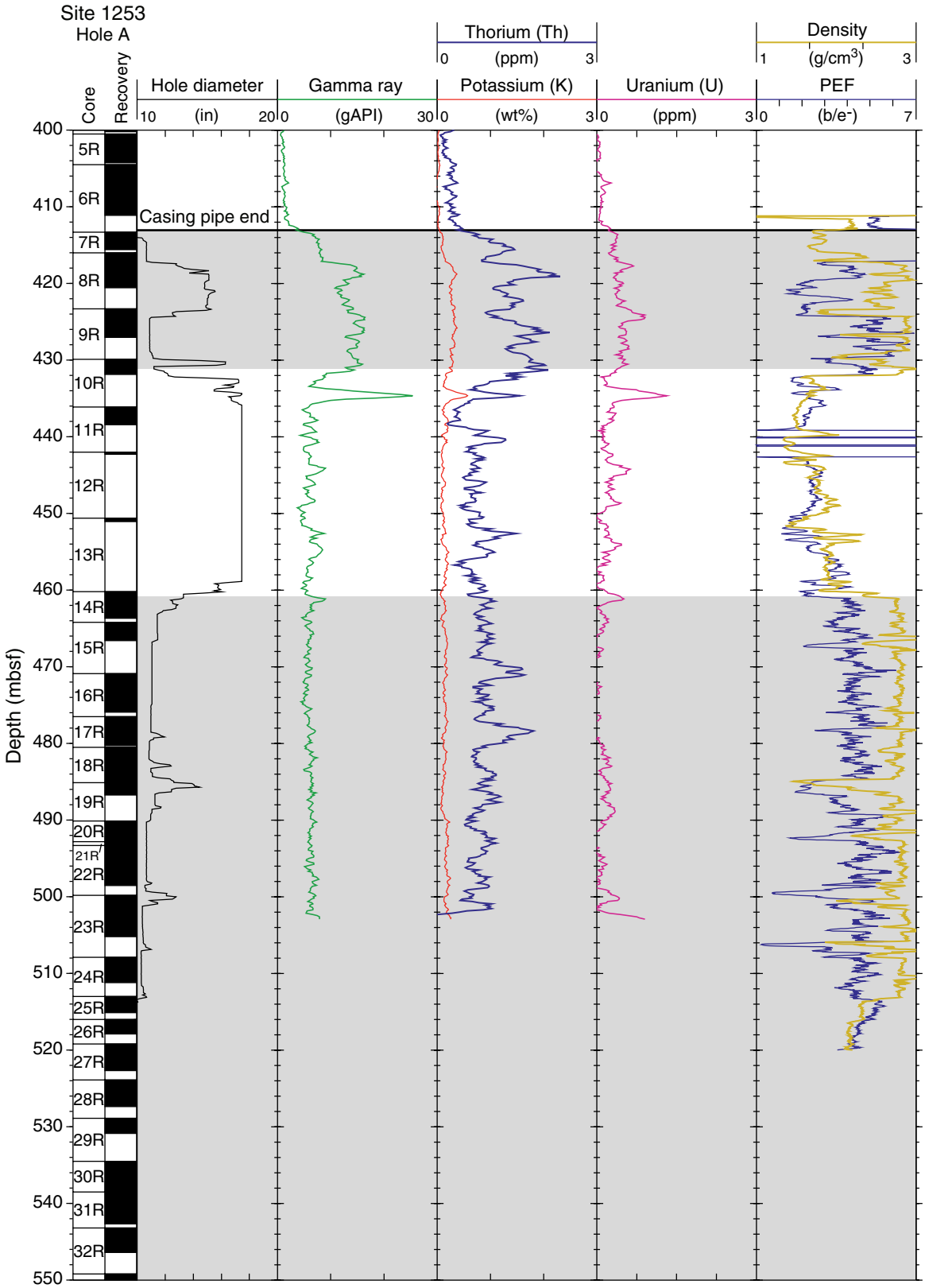

Figure F88. Density and porosity logs from Hole 1253A. Open triangles = bulk density and velocity, open diamonds = porosity. Shaded intervals indicate igneous sections.

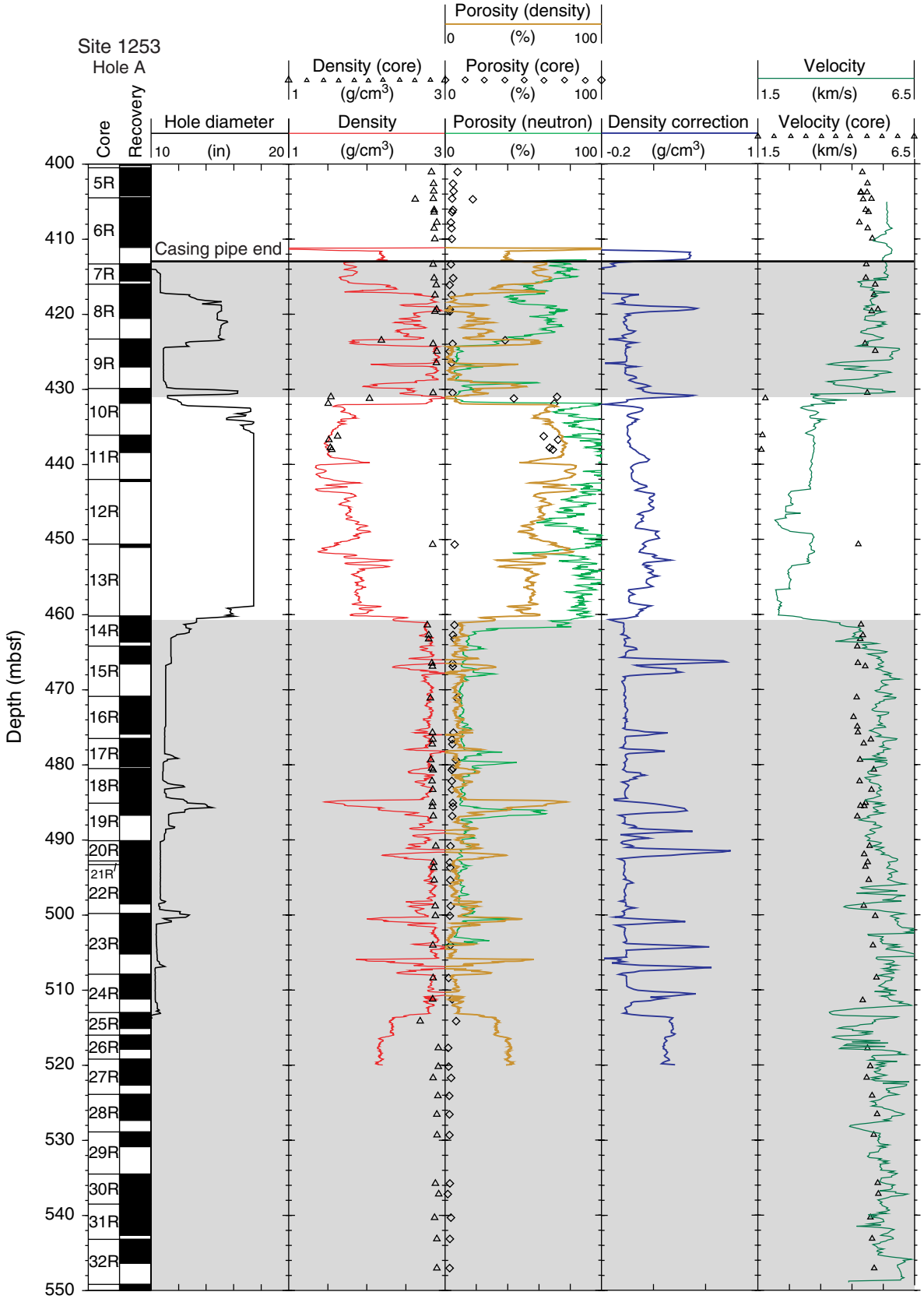

Figure F89. Resistivity logs from Hole 1253A. Shaded intervals indicate igneous sections.

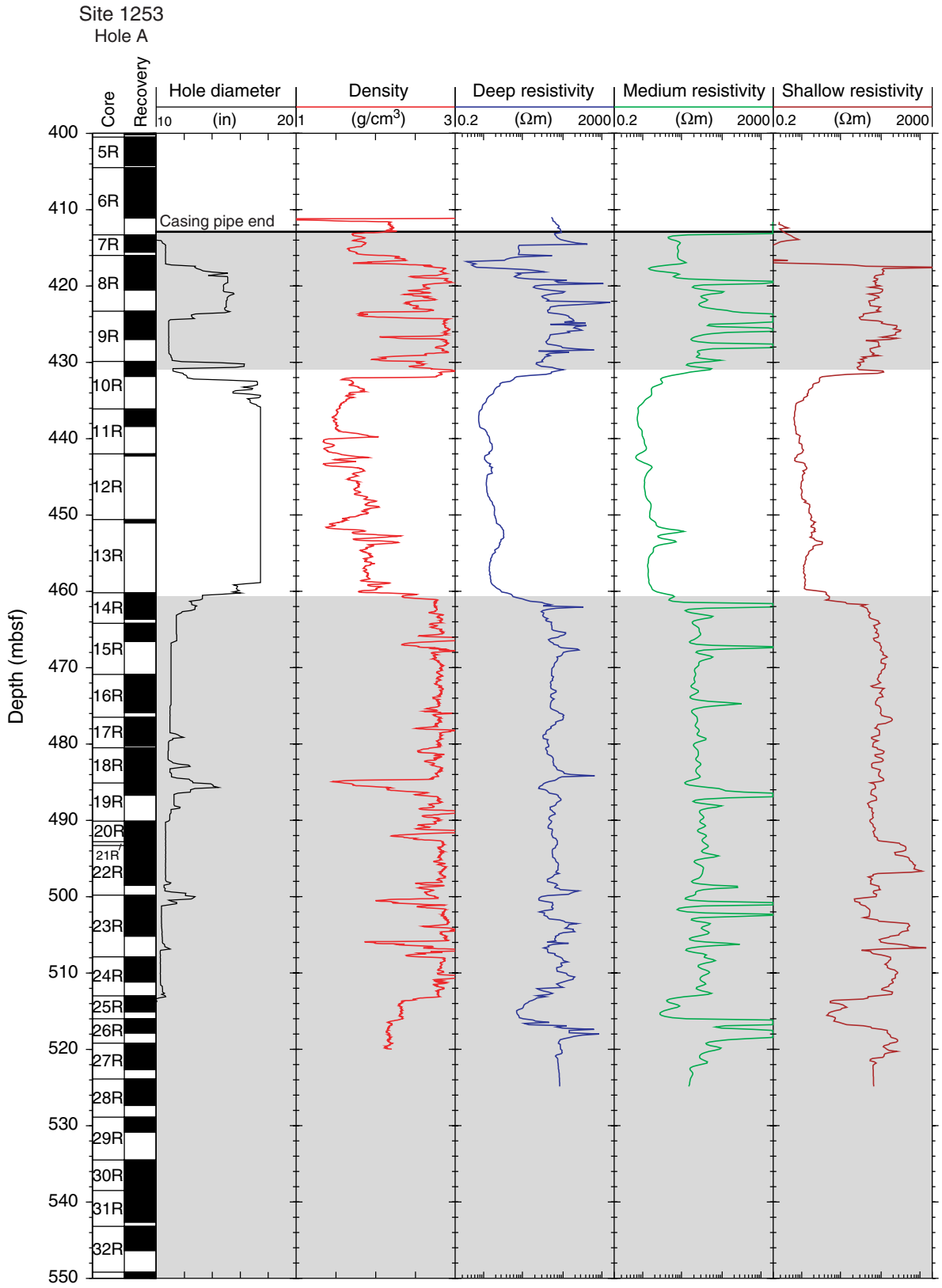

Figure F90. Acoustic logs from Hole 1253A. Open triangles = velocities measured on curves. Shaded intervals indicate igneous sections.

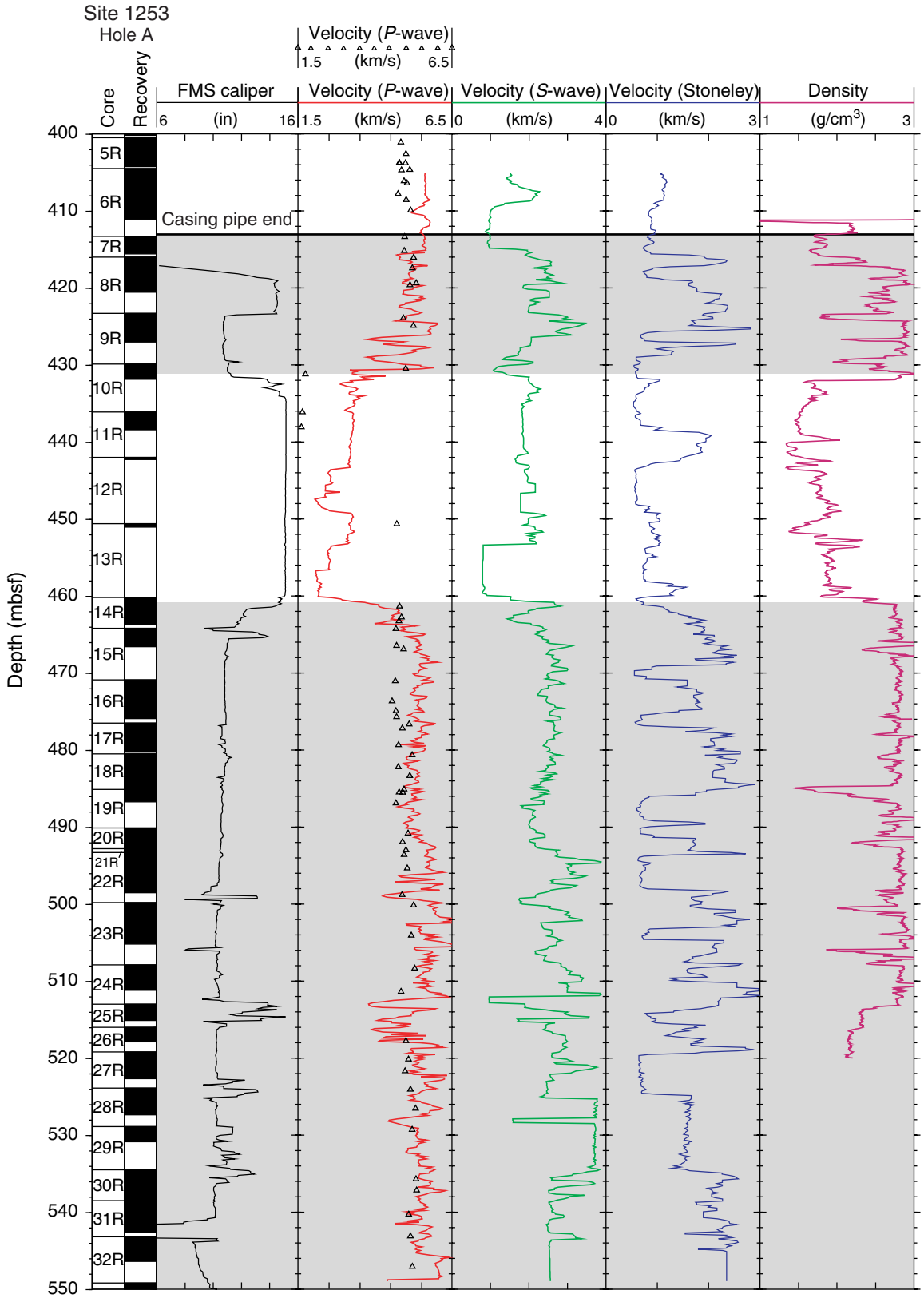

Figure F91. FMS profile for second pass, which was the deepest logging run in Hole 1253A.

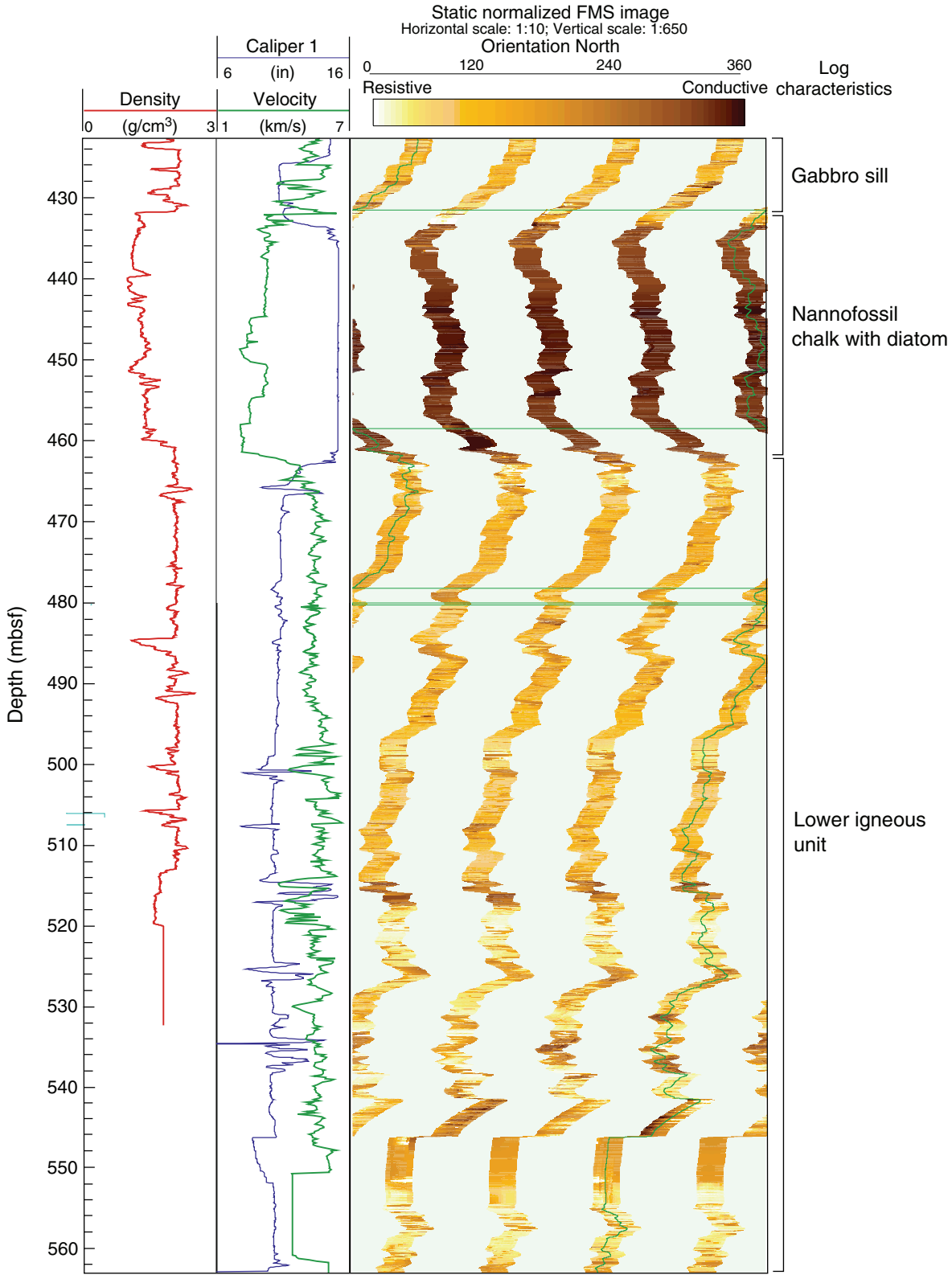

Figure F92. Dynamic and static normalized FMS images showing the (**A**) gabbro zone and (**B**) the lower igneous unit in Hole 1253A.

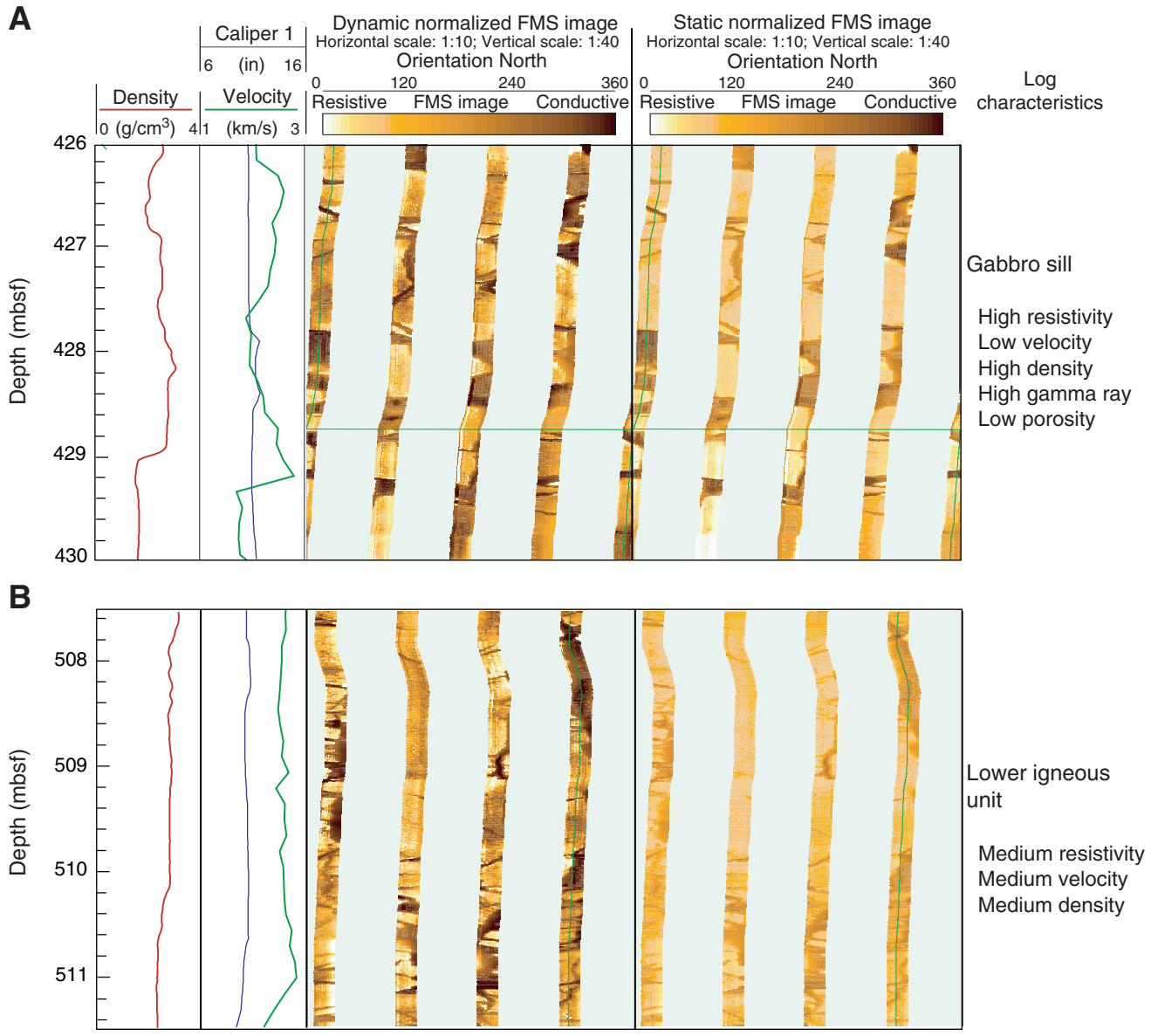

Figure F93. Dynamic and static normalized FMS images locating the (**A**) upper and (**B**) lower OsmoSamplers.

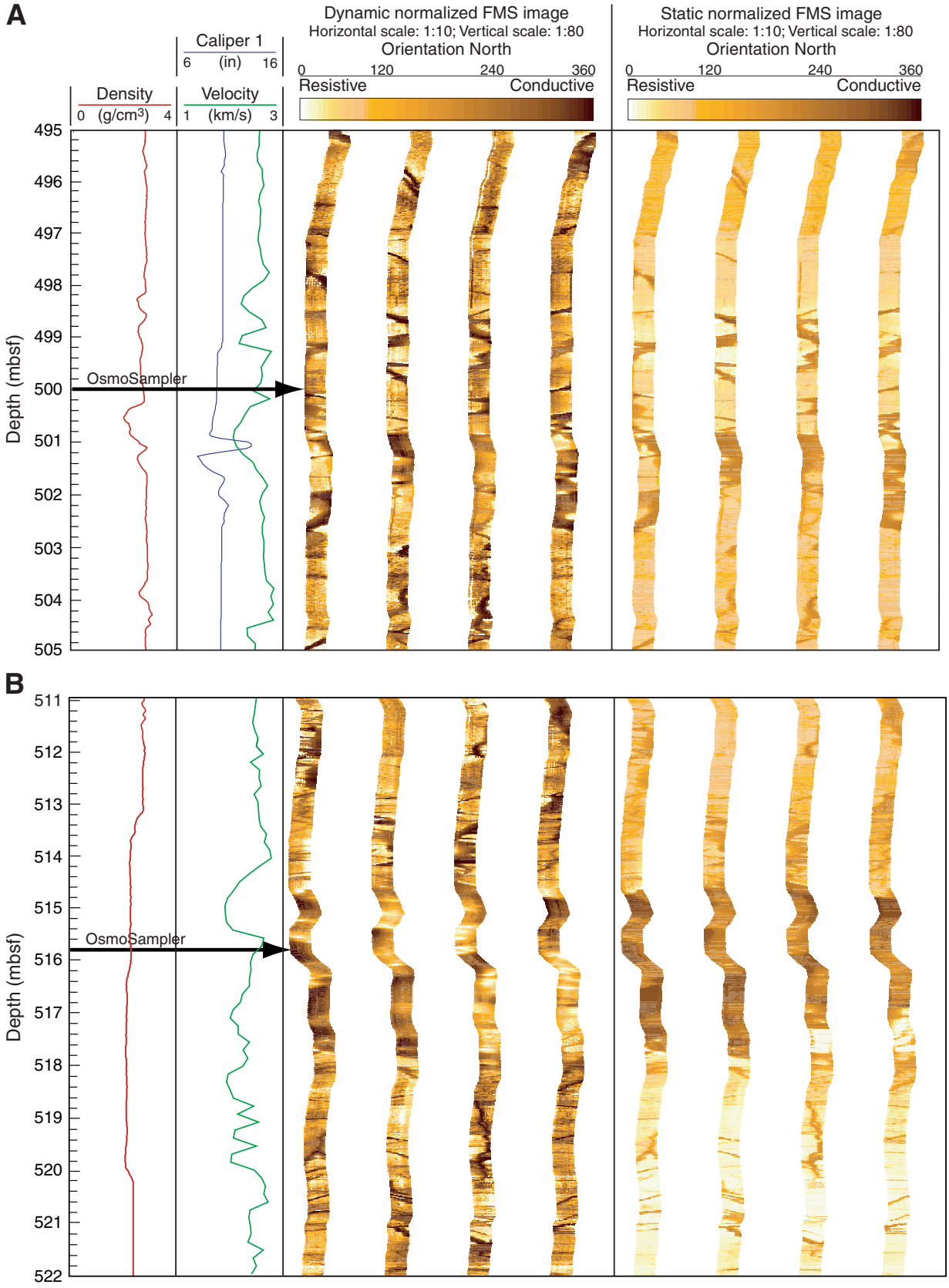

Figure F94. Magnetic field strength from the downhole logging measurements and magnetic intensity from the paleomagnetic measurements. Red = curve fit line. Inset = detailed magnetic field strength.

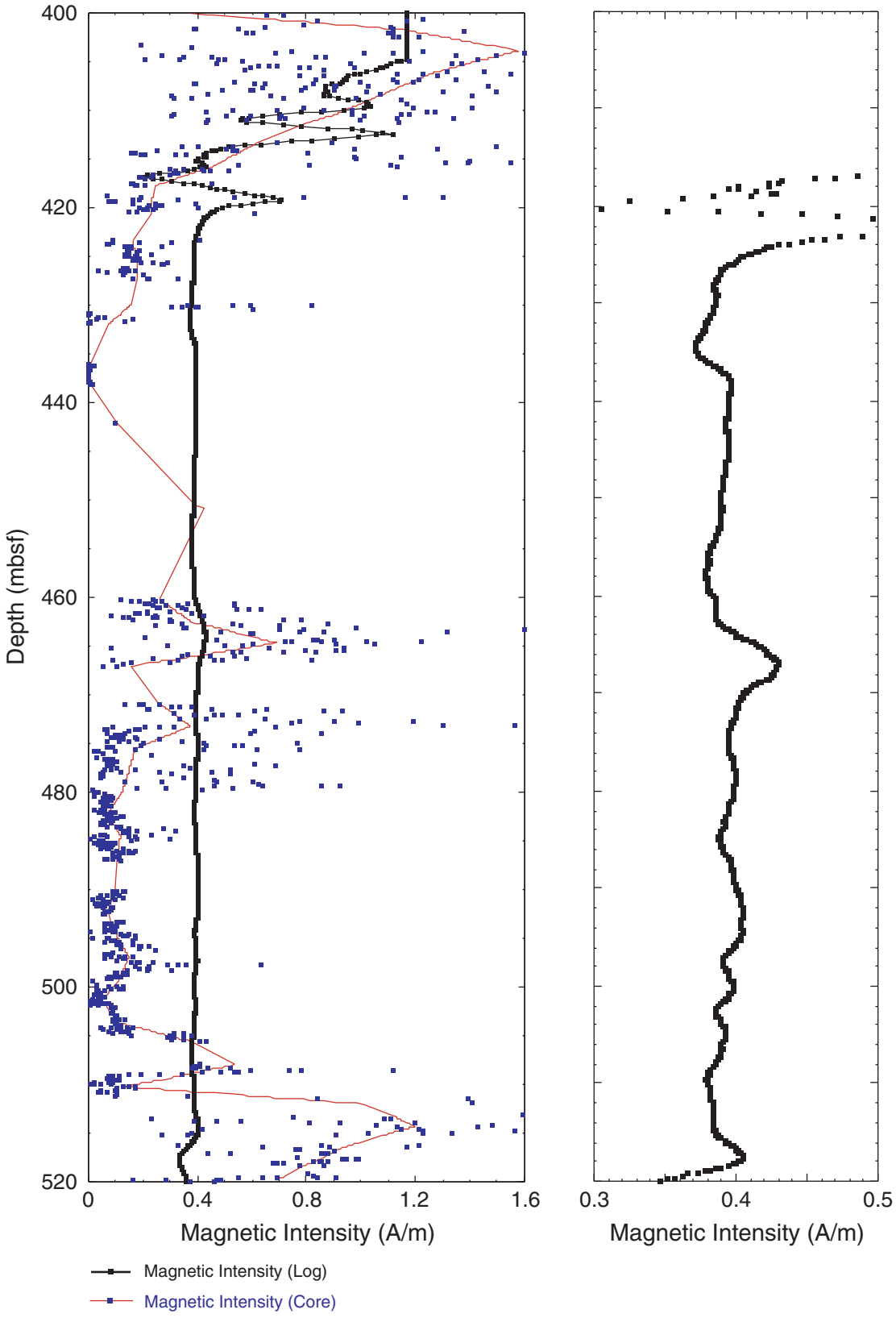

Table T1. Coring summary, Site 1253.

Hole 1253A
Latitude: 9°38.8583′N
Longitude: 86°11.4337′E
Time on site (hr): 475.25 (1430 hr, 21 Sep 2002–0945 hr, 11 Oct 2002)
Time on hole (hr): 473.25 (1630 hr, 21 Sep 2002–0945 hr, 11 Oct 2002)
Seafloor (drill pipe measurement from rig floor, mbrf): 4387.2
Distance between rig floor and sea level (m): 11.2
Water depth (drill pipe measurement from sea level, m): 4376.0
Total depth (drill pipe measurement from rig floor, mbrf): 4987.2
Total penetration (meters below seafloor, mbsf): 600.0
Total length of cored section (m): 230.0
Total length of drilled intervals (m): 370.0
Total core recovered (m): 148.65
Core recovery (%): 64.6
Total number of cores: 43
Total number of drilled intervals: 2

Core	Date (2002)	Ship local time (hr)*	Depth (mbsf) Top	Depth (mbsf) Bottom	Length (m) Cored	Length (m) Recovered	Recovery (%)	Remarks
205-1253A-								
			*****Drilled from 0.0 to 150.2 mbsf*****					DVTPP at 56.8 and 150.0 mbsf
			*****Drilled from 150.2 to 370.0 mbsf*****					
1R	24 Sep	0420	370.0	375.6	5.6	3.96	70.7	
2R	24 Sep	0535	375.6	385.2	9.6	8.89	92.6	Whirl-Pak
3R	24 Sep	0700	385.2	394.9	9.7	4.06	41.9	
4R	24 Sep	0840	394.9	400.5	5.6	5.30	94.6	Whirl-Pak; hard formation at 404 mbsf
5R	24 Sep	1220	400.5	404.5	4.0	3.75	93.8	AHC
6R	24 Sep	1745	404.5	413.3	8.8	6.61	75.1	AHC
7R	24 Sep	2215	413.3	416.0	2.7	2.28	84.4	AHC
8R	25 Sep	0340	416.0	423.3	7.3	4.56	62.5	Whirl-Pak; AHC
9R	25 Sep	0945	423.3	429.9	6.6	3.74	56.7	AHC
10R	25 Sep	1155	429.9	436.1	6.2	1.95	31.5	Drilling change at 431 mbsf
11R	25 Sep	1355	436.1	442.0	5.9	2.33	39.5	
12R	25 Sep	1515	442.0	450.6	8.6	0.28	3.3	Hard formation at 451 mbsf
13R	25 Sep	1705	450.6	460.2	9.6	0.46	4.8	
14R	25 Sep	2320	460.2	464.2	4.0	3.48	87.0	Whirl-Pak
15R	26 Sep	0415	464.2	470.9	6.7	2.37	35.4	
16R	26 Sep	0800	470.9	476.5	5.6	5.02	89.6	Whirl-Pak
17R	26 Sep	1110	476.5	480.5	4.0	3.77	94.3	
18R	26 Sep	1530	480.5	485.1	4.6	5.33	115.9	Whirl-Pak
19R	26 Sep	1910	485.1	490.1	5.0	1.63	32.6	
20R	26 Sep	2250	490.1	492.8	2.7	2.73	101.1	Whirl-Pak
21R	27 Sep	0115	492.8	493.3	0.5	0.52	104.0	
22R	27 Sep	0530	493.3	499.8	6.5	5.22	80.3	Whirl-Pak
23R	27 Sep	1055	499.8	507.9	8.1	5.40	66.7	
24R	27 Sep	1500	507.9	513.0	5.1	3.30	64.7	Whirl-Pak
25R	27 Sep	1735	513.0	516.0	3.0	2.12	70.7	
26R	27 Sep	1850	516.0	519.2	3.2	1.88	58.8	Whirl-Pak
27R	29 Sep	0015	519.2	523.9	4.7	3.47	73.8	
28R	29 Sep	0515	523.9	528.9	5.0	3.47	69.4	Whirl-Pak
29R	29 Sep	0820	528.9	534.5	5.6	1.97	35.2	Whirl-Pak; hard formation at 531 mbsf
30R	29 Sep	1300	534.5	538.5	4.0	4.14	103.5	Whirl-Pak
31R	29 Sep	1625	538.5	543.2	4.7	4.18	88.9	
32R	29 Sep	2100	543.2	549.2	6.0	3.19	53.2	Whirl-Pak
33R	30 Sep	0130	549.2	552.9	3.7	3.34	90.3	
34R	30 Sep	0730	552.9	557.9	5.0	4.40	88.0	Whirl-Pak
35R	30 Sep	1215	557.9	562.5	4.6	3.27	71.1	
36R	30 Sep	1655	562.5	566.0	3.5	3.30	94.3	Whirl-Pak
37R	30 Sep	2115	566.0	572.2	6.2	1.91	30.8	Whirl-Pak
38R	1 Oct	0125	572.2	577.2	5.0	1.89	37.8	Whirl-Pak
39R	1 Oct	0540	577.2	582.8	5.6	2.91	52.0	Whirl-Pak
40R	1 Oct	1045	582.8	585.8	3.0	1.55	51.7	Whirl-Pak
41R	1 Oct	1715	585.8	589.9	4.1	5.70	139.0	Whirl-Pak
42R	2 Oct	0225	589.9	595.4	5.5	4.42	80.4	Whirl-Pak
43R	2 Oct	1100	595.4	600.0	4.6	4.60	100.0	Whirl-Pak
				Cored totals:	230.0	148.65	64.6	
				Drilled totals:	370.0			
				Total:	600.0			

Note: * = Ship local time is Universal Time Coordinated – 5 hr. DVTPP = Davis-Villinger Temperature-Pressure Probe. Whirl-Pak = microbiology microsphere contamination testing. AHC = active heave compensation.

Table T2. Peak intensities and peak areas from X-ray diffraction analysis of bulk-powder sediment samples, Site 1253.

Core, section, interval (cm)	Subunit	Depth (mbsf)	Lithology	X-ray diffraction peak intensities (cps)						X-ray diffraction peak areas (total count)					
				Composite clay	Quartz (101)	Plagioclase (002)	Calcite (104)	Quartz (100)	Cristobalite (101)	Composite clay	Quartz (101)	Plagioclase (002)	Calcite (104)	Quartz (100)	Cristobalite (101)
205-1253A-															
1R-1, 13–29	U3C	370.13	Carbonate sediments	12	15	22	2,874	9	0	375	146	223	39,731	110	0
2R-1, 49–50	U3C	376.09	Tephra	0	17	328	477	0	46	0	220	3,865	6,611	0	627
2R-2, 85–104	U3C	377.95	Carbonate sediments	19	0	27	2,536	0	0	514	0	380	34,732	0	0
2R-3, 101–102	U3C	379.15	Tephra	14	18	85	1,175	0	31	355	170	1,043	17,478	0	453
2R-3, 133–135	U3C	379.47	Carbonate sediments	12	0	26	2,945	23	0	423	0	294	40,759	225	0
3R-1, 7–23	U3C	385.27	Carbonate sediments	9	0	16	3,222	8	13	314	0	228	45,112	79	135
3R-1, 118–119	U3C	386.38	Carbonate sediments	22	10	16	2,388	11	0	788	71	125	32,871	96	0
3R-2, 23–24	U3C	386.93	Carbonate sediments	17	16	24	2,509	8	0	573	198	128	34,766	53	0
3R-3, 39–40	U3C	388.59	Carbonate sediments	82	0	24	1,210	17	28	3,067	0	287	17,129	161	457
3R-3, 63–64	U3C	388.83	Carbonate sediments	48	46	44	476	30	80	2,178	493	327	6,790	273	1,211
4R-1, 14–15	U3C	395.04	Carbonate sediments	27	10	0	1,851	0	0	1,062	99	0	26,258	0	0
4R-1, 86–87	U3C	395.76	Tephra	60	73	467	22	29	250	1,231	692	6,329	259	311	3,829
4R-1, 132–134	U3C	396.22	Carbonate sediments	177	840	102	116	193	45	6,711	10,782	1,645	1,399	2,766	487
4R-2, 50–53	U3C	396.90	Carbonate sediments	148	3,381	46	67	672	0	5,486	42,323	823	785	9,005	0
4R-3, 26–39	U3C	398.16	Carbonate sediments	270	309	137	0	97	18	9,311	4,099	2,356	0	1,384	169
4R-3, 32–35	U3C	398.22	Carbonate sediments	220	1,403	107	0	298	32	7,626	18,168	1,681	0	4,406	384
4R-3, 90–92	U3C	398.80	Tephra	74	603	1,018	0	188	630	1,924	6,551	13,944	0	2,419	8,913
4R-3, 100–120	U3C	398.90	Carbonate sediments	163	2,983	100	32	828	55	5,361	37,036	1,434	337	10,527	578
5R-1, 0–1	U3C	400.50	Baked sediments	188	1,170	123	109	349	33	6,342	14,568	1,941	1,173	4,379	347
10R-2, 34–36	U3C	431.06	Carbonate sediments	99	0	56	1,329	12	12	3,287	0	1,083	16,158	100	73
10R-2, 59–73	U3C	431.31	Carbonate sediments	22	589	66	2,124	121	1,442	526	7,430	748	29,203	1,728	23,538
10R-2, 85–87	U3C	431.57	Tephra	44	18	216	966	0	371	1,239	118	2,539	14,717	0	6626
11R-1, 81–96	U3C	436.91	Carbonate sediments	34	0	28	2,820	0	36	929	0	482	38,644	0	626
11R-2, 26–28	U3C	437.32	Carbonate sediments	35	16	28	2,123	23	0	871	206	512	28,904	382	0
11R-2, 42–44	U3C	437.48	Tephra	30	0	83	996	0	0	697	0	1,050	14,736	0	0
25R-1, 10–12	U3C	513.10	Baked sediments	42	0	58	2,757	8	146	1,821	0	490	36,376	67	1,663
27R-1, 4–7	U3C	519.24	Baked sediments	115	662	134	430	137	51	3,589	8,474	1,533	8,710	2,051	612

Notes: cps = count per second. Numbers in parentheses are Miller indexes.

Table T3. Peak area ratios of dominant minerals.

Core, section, interval (cm)	Subunit	Depth (mbsf)	Lithology	Peak areas relative to quartz (101)			Peak area ratio
				Clay/ Quartz	Plagioclase/ Quartz	Calcite/ Quartz	Cristobalite (101)/ Quartz (100)
205-1253A-							
1R-1, 13–29	U3C	370.13	Carbonate sediments	2.57	1.53	272.13	
2R-1, 49–50	U3C	376.09	Tephra	0.00	17.57	30.05	
2R-2, 85–104	U3C	377.95	Carbonate sediments	NA	NA	NA	
2R-3, 101–102	U3C	379.15	Tephra	2.09	6.14	102.81	
2R-3, 133–135	U3C	379.47	Carbonate sediments	NA	NA	NA	
3R-1, 7–23	U3C	385.27	Carbonate sediments	NA	NA	NA	1.71
3R-1, 118–119	U3C	386.38	Carbonate sediments	11.10	1.76	462.97	
3R-2, 23–24	U3C	386.93	Carbonate sediments	2.89	0.65	175.59	
3R-3, 39–40	U3C	388.59	Carbonate sediments	NA	NA	NA	2.84
3R-3, 63–64	U3C	388.83	Carbonate sediments	4.42	0.66	13.77	4.44
4R-1, 14–15	U3C	395.04	Carbonate sediments	10.73	0.00	265.23	
4R-1, 86–87	U3C	395.76	Tephra	1.78	9.15	0.37	12.31
4R-1, 132–134	U3C	396.22	Carbonate sediments	0.62	0.15	0.13	0.18
4R-2, 50–53	U3C	396.90	Carbonate sediments	0.13	0.02	0.02	
4R-3, 26–39	U3C	398.16	Carbonate sediments	2.27	0.57	0.00	0.12
4R-3, 32–35	U3C	398.22	Carbonate sediments	0.42	0.09	0.00	0.09
4R-3, 90–92	U3C	398.80	Tephra	0.29	2.13	0.00	3.68
4R-3, 100–120	U3C	398.90	Carbonate sediments	0.14	0.04	0.01	0.05
5R-1, 0–1	U3C	400.50	Baked sediments	0.44	0.13	0.08	0.08
10R-2, 34–36	U3C	431.06	Carbonate sediments	NA	NA	NA	0.73
10R-2, 59–73	U3C	431.31	Carbonate sediments	0.07	0.10	3.93	13.62
10R-2, 85–87	U3C	431.57	Tephra	10.50	21.52	124.72	
11R-1, 81–96	U3C	436.91	Carbonate sediments	NA	NA	NA	
11R-2, 26–28	U3C	437.32	Carbonate sediments	4.23	2.49	140.31	
11R-2, 42–44	U3C	437.48	Tephra	NA	NA	NA	
25R-1, 10–12	U3C	513.10	Baked sediments	NA	NA	NA	24.82
27R-1, 4–7	U3C	519.24	Baked sediments	0.42	0.18	1.03	0.30

Notes: Numbers in parentheses are Miller indexes. NA = could not be determined because peak was absent.

Table T4. Bulk sediment analyses of selected sediments and sedimentary rocks, Site 1253.

Core, section, interval (cm)	Depth (mbsf)	Major element oxide (wt%)											Ti/Al	Trace element (ppm)							
		SiO_2	TiO_2	Al_2O_3	Fe_2O_3	MnO	CaO	MgO	Na_2O	K_2O	P_2O_5	Total		Ba	Cr	Sr	V	Y	Zr	Cu	Zn
Basal sediments:																					
205-1253A-																					
2R-2, 85–104	378.10	34.64	0.25	3.12	2.81	0.20	34.40	1.45	1.46	0.63	0.09	79.04	0.08	2225	38.3	1040	98.4	14.4	56.1		
2R-3, 133–135	379.47	26.76	0.13	1.38	1.72	0.22	42.36	0.90	1.37	0.26	0.10	75.20	0.09	1944	26.5	1219	77.0	12.0	29.7		
2R-4, 60–62	380.24	29.58	0.27	1.88	1.61	0.19	39.37	0.92	1.94	0.31	0.13	76.19	0.14	1639	26.2	1217	83.6	12.7	38.2		
3R-1, 7–23	385.40	23.36	0.13	1.95	1.74	0.38	46.96	0.90	1.12	0.39	0.09	77.00	0.07	1375	28.6	1224	74.3	12.1	51.2		
3R-1, 118–119	386.38	34.78	0.19	1.89	2.57	0.21	34.71	1.43	1.80	0.29	0.10	77.95	0.10	2266	45.0	1060	106.0	13.5	29.2		
3R-2, 23–24	386.93	37.08	0.16	1.76	1.55	0.19	34.49	0.91	1.49	0.36	0.11	78.09	0.09	2867	30.2	1096	83.1	13.5	40.4		
4R-1, 132–134	396.22	51.69	0.17	1.58	2.66	0.24	2.66	20.84	1.97	0.14	0.12	82.07	0.11	609	20.7	267	76.4	8.9	31.6		
4R-3, 26–29	398.20	52.22	0.09	1.20	2.34	0.19	0.91	26.97	1.42	0.16	0.09	85.58	0.08	132	26.0	131	69.6	8.8	33.4		
4R-3, 100–120	399.00	61.46	0.10	1.30	2.34	0.14	2.06	19.35	1.43	0.13	0.08	88.39	0.08	239	21.3	173	68.0	9.0	38.1		
5R-1, 0–1	400.50	53.87	0.14	1.55	2.73	0.16	2.85	21.84	1.67	0.15	0.07	85.04	0.09	345	30.3	251	77.1	9.2	34.1		
10R-2, 59–73	431.40	45.03	0.22	2.36	2.84	0.31	28.77	2.42	1.17	0.27	0.14	83.53	0.09	3151	39.3	761	102.1	14.5	40.4		
11R-1, 81–96	437.00	24.79	0.12	1.45	3.39	0.32	39.81	5.17	1.06	0.13	0.14	76.39	0.09	2139	27.6	1066	97.1	11.8	28.7		
Tephras:																					
205-1253A-																					
2R-1, 49–50	376.09	44.83	1.19	12.07	9.50	0.19	15.63	5.21	2.49	0.68	0.14	91.95	0.10	407	143.1	382	301.4	22.2	125.8	489.3	97.1
2R-3, 101–102	379.15	43.15	0.79	8.52	6.93	0.18	21.67	4.43	2.23	0.29	0.11	88.32	0.09	947	151.4	600	234.3	17.1	49.1	374.6	169.9
4R-1, 86–87	395.76	53.49	1.64	11.60	9.10	0.23	8.89	6.83	4.44	0.20	0.19	96.62	0.14	897	53.2	1051	394.2	40.4	125.1	611.6	80.9
4R-2, 110–111	397.50	64.77	0.27	2.87	3.10	0.26	5.99	12.87	1.98	0.13	0.17	92.41	0.09	2006	26.1	448	51.5	17.2	71.7	58.2	96.6
4R-3, 90–92	398.80	61.51	0.47	13.14	1.44	0.02	2.35	6.91	6.56	0.27	0.03	92.67	0.04	1172	5.9	1234	40.4	85.1	726.1	285.4	39.4
10R-2, 85–87	431.57	41.81	1.70	8.61	8.92	0.21	16.20	2.96	3.04	1.03	0.22	84.70	0.20	1255	18.7	621	257.4	29.8	150.5	614.6	121.2
11R-2, 42–44	437.48	48.28	0.66	6.52	6.65	0.17	13.17	5.39	2.31	0.50	0.07	83.73	0.10	1016	69.7	528	199.5	15.3	47.9	341.6	97.7
Baked sediments:																					
205-1253A-																					
25R-1, 10–12	513.10	23.06	0.15	1.71	1.94	0.39	34.85	13.10	0.55	0.05	0.14	75.94	0.09	78	9.9	880	101.2	20.9	29.9	202.8	84.1
27R-1, 4–7	519.24	55.72	0.32	4.42	6.41	0.40	6.02	17.94	2.06	0.27	0.18	93.74	0.07	366	16.5	301	126.1	19.8	52.2	247.7	105.2

Table T5. Mineralogical assemblages in igneous sections determined by X-ray diffraction, Site 1253.

Core, section, interval (cm)	Depth (mbsf)	Anorthite	Augite	Magnetite/ulvospinel	Ilmenite	Calcite	Laumontite	Mesolite	Thomsonite	Scolecite	Stilbite	Phillipsite	Saponite/smectite	Celadonite	Corrensite	Chamosite	Material
205-1253A-																	
5R-2, 43–52	402.28	X	X										X	?	?	?	Separated vein
5R-3, 88–98	404.12	X	X														Separated vein
5R-4, 14–26	404.75	X	X										X	?	?	?	Separated vein
6R-3, 33–42	406.56	X	X										X	?	?	?	Separated vein
14R-1, 28–35	460.48	X	?			?						?	X		?	?	Separated vein
16R-1, 114–117	472.04	X	X	?												?	Groundmass + vein
17R-2, 105–109	478.15	X	X	?			?	X	?	X	?				?	?	Groundmass + vein
17R-2, 108–113	478.18	X	X	?			X	X	?	?					X	?	Groundmass + vein
19R-1, 15–17	485.25	X	X	?	X		X	X	X	X					?	?	Groundmass + vein
22R-2, 55–57	494.63							X	?	X		?	X				Separated vein
22R-2, 60–62	494.68	X	X	?				?									Groundmass
25R-1, 90–91	513.90	X	X								X	X	X		X		Separated vein
25R-1, 91–93	513.91	X											X		?		Separated vein
25R-2, 90–100	515.15	X											X		?		Separated vein
27R-1, 94–98	520.14					X							X				Separated vein
27R-2, 39–40	520.71												X				Separated vein
35R-1, 34–43	558.24												X			X	Separated vein
35R-1, 40–41	558.30	X	X	?												X	Groundmass
37R-1, 24–26	566.24	X	X	?													Groundmass
37R-1, 114–115	567.14										X	X			X	X	Separated void
39R-1, 130–131	578.50					X							X				Separated vein
42R-2, 88–90	592.28	X	X	X													Groundmass
42R-2, 94–99	592.34												X				Separated vein

Note: X = identified minerals, ? = tentative indications of minerals where some main peaks in the diffractogram are missing but are believed to occur as alteration products.

Table T6. ICP-AES analyses for the gabbro sill and Subunit 4B, Site 1253. (See table notes. Continued on next page.)

Sample	Subunit	Depth (mbsf)	Major element contents (wt%)												Trace element concentrations (ppm)							
			SiO_2	TiO_2	Al_2O_3	Fe_2O_3	MgO	MnO	CaO	Na_2O	K_2O	P_2O_5	Total	LOI	Cr	Ni	Ba	Sr	V	Y	Zr	Sc
205-1253A-																						
(B) 5R-4, 60–61	4A	405.21	48.25	2.05	14.61	12.79	6.96	0.18	12.86	2.52	0.29	0.26	100.76	0.69	235.19	84.33	91.77	224.83	318.73	30.89	146.35	41.83
(A) 5R-4, 60–61	4A	405.21	47.39	1.75	14.13	12.01	6.88	0.17	12.55	2.41	0.28	0.22	97.78	0.69	235.44	92.27	91.72	213.81	316.18	29.65	139.27	38.23
(A) 6R-3, 65–67	4A	406.91	49.22	2.00	14.33	12.73	7.23	0.18	12.82	2.61	0.25	0.20	101.57	0.63	266.12	92.20	71.82	231.86	330.65	31.51	149.30	41.90
(B) 6R-3, 65–67	4A	406.91	47.64	1.55	13.79	12.14	7.09	0.17	12.49	2.44	0.23	0.21	97.76	0.63	257.07	86.65	74.34	211.39	316.61	29.87	133.23	39.98
(A) 6R-5, 38–39	4A	408.84	47.40	1.95	15.83	12.28	6.58	0.17	11.19	2.50	0.35	0.20	98.45	0.51	214.03	64.02	86.14	213.76	319.97	30.88	153.12	40.52
(B) 6R-5, 38–39	4A	408.84	47.16	1.91	15.94	11.89	6.13	0.16	11.18	2.38	0.34	0.25	97.34	0.51	218.26	59.52	81.33	205.69	301.92	26.30	150.62	42.65
(A) 6R-6, 89–90	4A	410.74	49.15	2.11	14.80	12.95	7.35	0.18	12.36	2.54	0.38	0.30	102.12	1.23	224.07	93.85	76.46	210.79	328.99	31.05	152.15	42.96
(A) 7R-1, 130–131	4A	414.60	47.67	2.58	13.46	14.06	6.65	0.18	11.10	2.95	0.25	0.25	99.14	0.81	35.56	53.97	125.34	232.30	389.80	40.05	182.97	43.03
(B) 7R-1, 130–131	4A	414.60	46.96	2.48	12.90	13.63	6.47	0.18	10.65	2.85	0.24	0.23	96.59	0.81	36.11	60.74	122.91	222.16	377.94	37.11	173.62	40.33
(A) 8R-1, 68–69	4A	416.68	47.66	2.74	14.34	14.57	6.48	0.20	10.19	2.78	0.39	0.42	99.77	0.70	30.35	32.27	117.99	204.81	448.50	38.14	185.82	44.57
(B) 8R-1, 68–69	4A	416.68	47.12	2.74	14.34	16.12	6.30	0.19	10.14	2.72	0.38	0.84	100.89	0.70	30.87	35.54	113.84	202.52	447.39	37.81	185.26	57.15
(A) 8R-2, 75–76	4A	418.13	48.64	2.29	14.28	12.87	7.78	0.19	10.88	2.44	0.31	0.18	99.86	1.32	75.67	95.58	80.35	194.58	370.00	31.43	145.76	49.52
(B) 8R-2, 75–76	4A	418.13	46.99	2.20	14.11	12.69	7.58	0.18	10.63	2.39	0.30	—	97.07	1.32	67.38	149.70	81.20	191.97	355.40	30.67	144.24	41.17
(A) 9R-2, 35–37	4A	424.21	46.64	1.87	15.13	12.24	7.00	0.17	10.89	2.27	0.46	0.28	96.94	1.39	262.38	80.49	89.13	195.30	309.80	29.07	132.85	40.58
(B) 9R-2, 35–37	4A	424.21	46.17	1.86	15.92	11.54	7.25	0.17	10.79	2.22	0.45	0.06	96.45	1.39	255.25	55.10	88.39	187.75	304.54	29.55	130.04	40.41
(A) 14R-2, 60–61	4B	462.13	48.02	1.26	15.92	11.35	8.41	0.17	13.93	2.05	0.14	0.11	101.35	1.84	365.14	131.69	16.77	155.66	295.16	20.88	64.63	42.64
(B) 14R-2, 60–61	4B	462.13	47.83	1.23	15.40	11.09	8.47	0.17	13.92	2.03	0.14	0.06	100.35	1.84	370.44	119.49	17.02	152.35	300.00	19.85	65.31	42.56
(A) 16R-3, 30–31	4B	474.03	46.81	1.11	17.59	10.11	7.87	0.16	11.96	2.10	0.15	0.06	97.92	1.91	340.02	57.82	35.05	145.25	277.49	19.84	70.99	40.84
(B) 16R-3, 30–31	4B	474.03	46.60	1.10	17.34	11.62	8.14	0.16	11.77	2.00	0.15	0.12	99.00	1.91	377.29	167.42	34.89	143.85	293.11	18.79	68.62	43.20
(A) 17R-3, 44–45	4B	478.90	47.55	1.20	18.14	10.29	6.95	0.16	12.86	2.14	0.10	0.25	99.66	1.62	343.78	70.67	26.48	164.45	311.18	22.57	71.33	43.02
(B) 17R-3, 44–45	4B	478.90	47.26	1.18	17.85	10.54	6.37	0.15	12.72	2.12	0.10	—	98.28	1.62	336.23	111.36	23.67	160.93	295.57	20.26	68.19	39.41
(A) 17R-3, 48–49	4B	478.94	46.30	2.81	13.62	16.22	6.47	0.21	9.68	3.24	0.29	0.26	99.09	1.11	21.00	45.21	71.02	186.87	521.33	42.01	158.23	42.95
(B) 17R-3, 48–49	4B	478.94	46.50	2.68	13.40	15.49	6.30	0.21	9.54	3.14	0.27	0.30	97.84	1.11	18.06	21.07	73.32	187.40	502.39	41.77	156.28	43.97
(A) 18R-1, 77–78	4B	481.27	47.74	1.65	14.39	13.25	6.71	0.18	12.14	2.62	0.17	0.16	99.02	1.69	56.74	83.29	44.80	174.94	351.67	31.63	101.12	43.22
(B) 18R-1, 77–78	4B	481.27	47.59	1.56	14.47	13.06	6.69	0.17	12.17	2.62	0.18	0.06	98.57	1.69	53.16	80.43	45.09	170.20	343.55	30.08	100.42	42.83
(A) 18R-4, 77–78	4B	484.90	48.23	1.27	16.02	11.81	8.07	0.17	14.19	2.08	0.21	0.13	102.19	1.72	353.50	112.09	29.10	157.81	310.25	21.68	72.10	43.05
(B) 18R-4, 77–78	4B	484.90	48.57	1.24	15.61	11.80	8.08	0.17	14.11	2.07	0.21	0.09	101.96	1.72	346.58	120.38	28.31	154.49	309.26	20.92	70.58	43.02
(A) 20R-1, 59–60	4B	490.69	46.77	1.14	15.03	11.25	8.26	0.17	13.70	1.82	0.16	0.06	98.35	2.54	398.03	147.15	22.11	141.84	276.39	18.08	57.21	39.50
(B) 20R-1, 59–60	4B	490.69	46.10	1.10	15.04	10.99	8.12	0.16	13.44	1.78	0.16	0.09	96.98	2.54	374.64	134.68	20.99	139.47	275.06	17.49	57.79	39.07
(A) 22R-1, 46–47	4B	493.76	48.66	1.12	15.93	11.41	8.35	0.17	14.23	1.91	0.17	0.09	102.04	1.76	429.44	127.20	30.43	152.52	279.47	19.84	61.61	41.62
(B) 22R-1, 46–47	4B	493.76	47.27	1.05	15.51	11.06	8.07	0.17	13.85	1.86	0.18	0.08	99.10	1.76	411.56	125.33	29.30	144.48	279.92	18.65	60.29	41.60
(A) 25R-1, 33–36	4B	513.33	47.71	1.52	17.48	11.89	7.55	0.19	11.39	2.38	0.27	0.14	100.53	3.16	242.51	66.43	77.79	177.51	335.73	25.20	101.23	43.55
(B) 25R-1, 33–36	4B	513.33	47.60	1.51	17.09	12.20	7.78	0.19	11.40	2.26	0.32	—	100.35	3.16	210.55	—	76.75	179.02	347.72	24.03	98.26	44.14
(A) 25R-1, 99–101	4B	513.99	47.23	1.54	16.48	12.18	7.96	0.20	11.20	2.47	0.28	0.16	99.70	3.15	201.80	45.73	101.77	189.06	337.73	28.31	102.67	42.81
(B) 25R-1, 99–101	4B	513.99	46.85	1.53	16.42	12.56	7.72	0.20	11.01	2.38	0.27	—	98.93	3.15	173.64	350.73	100.65	187.30	346.43	29.46	101.29	51.66
(A) 25R-2, 3–5	4B	514.28	47.33	1.55	16.97	11.43	7.46	0.18	11.68	2.42	0.21	0.22	99.47	2.89	219.07	80.56	77.09	182.88	352.91	25.62	97.08	45.39
(B) 25R-2, 3–5	4B	514.28	47.44	1.52	16.84	12.28	7.48	0.18	11.71	2.36	0.20	0.39	100.38	2.89	243.10	56.60	76.46	174.53	347.08	25.23	99.33	39.13
(A) 25R-2, 28–30	4B	514.53	47.53	1.59	16.63	12.02	6.93	0.17	11.40	2.35	0.18	0.16	98.97	2.63	165.75	64.84	67.95	174.77	350.84	24.46	107.57	36.76
(B) 25R-2, 28–30	4B	514.53	47.60	1.58	16.61	10.76	6.91	0.18	11.61	2.33	0.17	0.74	98.48	2.63	145.42	—	70.80	174.71	350.14	28.02	103.07	38.28
(A) 31R-4, 67–68	4B	543.41	47.67	1.62	15.06	12.58	6.42	0.18	12.53	2.29	0.16	0.14	98.65	0.75	141.99	85.39	45.86	160.77	328.53	27.06	100.23	41.97
(B) 32R-3, 29–30	4B	546.04	47.26	1.43	14.81	11.36	6.62	0.17	13.30	2.03	0.20	0.12	97.30	0.71	259.49	101.07	37.98	159.92	317.09	22.86	85.68	43.18
(A) 33R-1, 118–119	4B	550.38	48.81	1.43	15.83	10.61	7.10	0.16	14.06	2.22	0.19	0.05	100.46	1.14	369.84	106.37	38.82	175.94	336.58	23.87	85.21	45.95
(B) 33R-1, 118–119	4B	550.38	50.13	1.31	15.38	10.57	6.97	0.16	13.97	2.16	0.19	0.11	100.96	1.14	341.27	26.45	44.06	173.67	327.13	23.99	83.66	47.52
(A) 33R-2, 119–120	4B	551.89	47.33	1.36	16.75	11.46	7.22	0.17	12.34	2.04	0.20	0.20	99.08	0.44	296.92	57.12	44.27	164.81	312.50	24.88	91.21	44.28
(A) 33R-3, 46–47	4B	552.66	47.93	1.36	17.47	11.00	7.08	0.17	12.25	2.11	0.19	0.18	99.74	0.80	263.67	87.72	38.09	169.49	316.53	25.14	85.45	42.71
(B) 33R-3, 46–47	4B	552.66	47.09	1.32	17.00	10.97	6.85	0.17	12.20	2.02	0.20	—	97.82	0.80	242.33	—	52.44	166.60	307.15	24.93	87.66	36.62
(A) 35R-1, 97–98	4B	558.87	46.22	1.41	16.28	11.49	6.98	0.18	11.75	2.03	0.21	0.18	96.72	1.05	272.24	58.57	36.16	160.85	319.54	24.13	92.30	43.22
(B) 35R-1, 97–98	4B	558.87	46.73	1.41	16.13	12.24	6.78	0.17	11.83	1.96	0.21	0.34	97.83	1.05	251.43	334.26	46.02	160.81	321.98	22.54	92.56	48.28

Table T6 (continued).

Sample	Subunit	Depth (mbsf)	Major element contents (wt%)											Trace element concentrations (ppm)							
			SiO_2	TiO_2	Al_2O_3	Fe_2O_3	MgO	MnO	CaO	Na_2O	K_2O	P_2O_5	Total	LOI	Cr	Ni	Ba	Sr	V	Y	Zr	Sc
(A) 35R-2, 119–120	4B	560.35	49.21	1.40	15.46	12.03	6.73	0.17	13.82	2.15	0.12	0.15	101.25	0.78	224.83	94.28	37.41	174.30	319.41	24.16	83.56	42.99
(B) 35R-2,119–120	4B	560.35	47.64	1.56	15.61	11.98	6.73	0.17	13.81	2.14	0.13	0.13	99.90	0.78	216.59	96.04	36.79	177.21	318.09	24.29	89.53	42.57
(B) 36R-1, 114–115	4B	563.64	48.32	1.57	15.11	12.62	7.10	0.18	13.59	2.26	0.16	0.16	101.06	1.03	212.71	86.08	55.75	172.93	348.08	26.45	95.13	44.15
(A) 37R-1, 5–6	4B	566.05	46.86	1.65	14.87	11.61	6.77	0.17	12.78	2.29	0.14	0.21	97.36	1.73	214.33	89.41	43.48	177.23	360.37	29.39	91.28	45.67
(B) 37R-1, 5–6	4B	566.05	48.41	1.53	15.07	12.63	6.86	0.18	13.02	2.31	0.13	0.17	100.30	1.73	189.97	24.91	51.16	179.82	357.37	31.00	86.23	46.87
(A) 37R-1, 47–48	4B	566.47	48.94	1.60	15.10	11.99	7.21	0.16	12.38	2.68	0.36	0.16	100.59	1.56	276.42	34.61	160.72	206.50	354.61	28.34	100.44	46.10
(B) 37R-1, 47–48	4B	566.47	49.32	1.69	15.15	12.74	7.03	0.16	12.42	2.67	0.36	0.14	101.68	1.56	240.41	27.63	157.43	204.26	353.74	29.69	103.61	47.14
(A) 37R-1, 127–128	4B	567.27	48.55	1.55	15.20	12.25	7.47	0.17	12.30	2.41	0.17	0.14	100.21	2.04	264.02	32.83	107.34	178.37	335.78	27.16	92.55	43.51
(B) 37R-1, 127–128	4B	567.27	47.33	1.37	14.97	12.01	7.31	0.17	11.93	2.37	0.18	0.08	97.72	2.04	246.50	29.45	105.64	174.81	328.84	25.59	89.00	44.44
(A) 37R-2, 49–50	4B	567.90	49.11	1.60	15.38	12.43	7.34	0.18	12.79	2.38	0.16	0.12	101.49	1.66	293.77	27.17	51.49	177.22	338.23	28.23	93.03	45.64
(B) 37R-2, 49–50	4B	567.90	48.68	1.49	15.01	12.70	7.25	0.17	12.91	2.35	0.16	0.12	100.85	1.66	318.76	27.51	53.92	176.83	332.38	26.56	96.61	46.54
(B) 38R-1, 89–90	4B	573.09	46.49	1.39	14.83	11.67	6.90	0.18	12.82	2.10	0.16	0.07	96.61	1.06	255.52	86.91	25.39	148.67	312.49	25.11	84.94	41.21
(B) 39R-1, 77–78	4B	577.97	46.64	1.43	14.47	11.82	6.65	0.18	13.03	2.10	0.19	0.09	96.60	0.31	247.78	92.77	39.49	150.45	309.47	25.44	82.66	41.35
(A) 42R-3, 33–34	4B	592.77	48.89	1.68	14.87	12.97	6.97	0.19	13.74	2.27	0.22	0.11	101.88	0.29	230.09	98.49	43.47	163.90	355.45	28.86	105.53	45.30
(B) 42R-3, 33–34	4B	592.77	48.80	1.57	14.02	12.22	6.64	0.18	13.35	2.25	0.22	0.14	99.40	0.29	226.42	87.57	40.86	159.78	349.12	26.53	92.20	45.53
(B) 43R-2, 116–117	4B	597.52	48.85	1.33	15.05	11.84	6.65	0.18	13.25	2.18	0.18	0.13	99.63	0.17	250.06	100.17	35.84	159.18	322.39	24.07	89.49	43.11

Notes: LOI = loss of ignition. A and B = replicate analyses of the same sample aliquot. — = not determined.

Table T7. Normal magnetic chrons identified in upper and lower igneous units, Site 1253.

Top		Bottom	
Interval (cm)	Depth (mbsf)	Interval (cm)	Depth (mbsf)
205-1253A-			
5R-1, 15	400.65	5R-2, 35	402.20
6R-1, 5	404.55	6R-5, 55	409.01
6R-6, 5	409.89	6R-6, 130	411.14
7R-1, 5	413.35	7R-2, 5	414.82
8R-1, 5	416.05	8R-4, 100	420.57
9R-1, 5	423.35	9R-4, 115	427.36
10R-1, 5	429.95	10R-1, 55	430.45
24R-1, 55	508.45	24R-2, 55	509.91
25R-1, 65	513.65	25R-2, 105	515.30
26R-1, 5	516.05	28R-1, 75	524.65
28R-2, 55	525.80	28R-3, 75	527.65
29R-1, 70	529.60	29R2, 90	531.00
30R-1, 10	534.60	32R-1, 100	544.20
32R-2, 85	545.18	32R-4, 10	547.24
33R-1, 5	549.25	33R-3, 75	552.95
35R-1, 90	558.80	35R-1, 120	559.10
37R-1, 85	566.95	37R-2, 90	568.31
38R-1, 5	572.25	38R-2, 90	574.41
40R-1, 5	577.30	39R-3, 55	580.66
40R-1, 5	582.85	42R-3, 95	593.39

Table T8. Pore water chemical data of major constituents, Site 1253.

Core, section, interval (cm)	Depth (mbsf)	Volume (cm^3)	pH	Alkalinity (mM)	Salinity	Cl (mM)	SO_4 (mM)	Na (mM)	Mg* (mM)	K (mM)	Ca* (mM)	Na/Cl	Mg/Ca
205-1253A-													
1R-1, 13–29	370.2	45.0	7.51	2.05	35.0	559	28.00	480.81	46.20	12.00	15.73	1.30	2.94
2R-2, 85–104	378.1	45.0	7.42	1.99	35.0	560	27.21	479.27	46.78	12.15	15.54	1.27	3.01
3R-1, 7–23	385.4	40.0	7.36	2.03	35.0	560	28.56	485.07	46.35	11.79	14.63	1.26	3.17
4R-3, 100–120	399.0	29.0	7.69	2.06	34.3	551	28.09	482.18	46.22	8.63	12.87	1.21	3.59
10R-2, 59–73	432.1	27.5	8.01	2.05	35.5	563	27.81	495.82	44.41	10.45	12.65	1.15	3.51
11R-1, 81–96	437.0	32.0	7.71	ND	35.0	559	28.16	486.89	47.05	10.72	12.68	1.11	3.71

Notes: * = determined by titration. ND = not determined.

Table T9. Pore water chemical data of minor constituents, Site 1253.

Core, section, interval (cm)	Depth (mbsf)	Volume (cm^3)	B (μM)	Ba (μM)	Fe (μM)	Li (μM)	Mn (μM)	Sr (μM)	Si (μM)	NH_4 (μM)
205-1253A-										
1R-1, 13–29	370.2	45.0	436.74	2.27	0.70	10.50	8.01	189.83	948.6	82.75
2R-2, 85–104	378.1	45.0	410.08	1.60	3.60	11.27	8.72	178.60	990.6	75.25
3R-1, 7–23	385.4	40.0	439.04	1.04	4.75	13.51	11.68	169.40	946.6	70.25
4R-3, 100–120	399.0	29.0	409.59	4.84	0.47	18.00	19.76	129.39	290.6	49.00
10R-2, 59–73	432.1	27.5	386.08	3.02	43.55	17.50	18.20	138.23	474.6	57.75
11R-1, 81–96	437.0	32.0	384.36	1.29	0.64	16.95	16.86	144.30	746.6	46.50

Table T10. Composition of headspace gases, Site 1253.

Core, section, interval (cm)	Depth (mbsf)	CH_4 (ppmv)	C_2H_6 (ppmv)	C_3H_8 (ppmv)	CH_4/C_2H_6
205-1253A-					
1R-1, 29–34	370.29	3	0	0	ND
2R-3, 0–5	378.14	3	0	0	ND
3R-1, 31–35	385.51	3	0	0	ND
4R-4, 5–10	399.15	3	0	0	ND
10R-1, 72–73	430.62	21	2	0	14
11R-1, 95–96	437.05	2	0	0	ND

Notes: ppmv = parts per million by volume. ND = not determined.

Table T11. Calcium carbonate, inorganic carbon, total carbon, total nitrogen, total sulfur, and total organic carbon contents in sediments, Site 1253.

Core, section, interval (cm)	Piece	Depth (mbsf)	$CaCO_3$ (wt%)	IC (wt%)	TC (wt%)	TN (wt%)	TS (wt%)	TOC (wt%)	TOC/TN	Comments
205-1253A-										
1R-1, 13–29		370.13	59.70	7.17	7.11	0.01	0.19	0.00	ND	
1R-1, 30–31		370.30	51.14	6.14	6.26	0.02	0.00	0.12	ND	
2R-2, 74–75		377.84	35.91	4.31	4.36	0.01	0.08	0.05	ND	
2R-2, 85–104		377.95	42.10	5.05	5.12	0.00	0.06	0.07	ND	
2R-3, 133–135		379.47	31.99	3.84	7.05	0.02	0.16	3.21	ND	
2R-4, 60–62		380.24	53.75	6.45	6.46	0.01	0.07	0.01	ND	
3R-1, 7–23		385.27	64.14	7.70	7.92	0.00	0.01	0.22	ND	
3R-1, 32–33		385.52	55.69	6.69	6.62	0.00	0.14	0.00	ND	
3R-1, 118–119		386.38	44.81	5.38	5.62	0.02	0.15	0.24	ND	
3R-2, 23–24		386.93	45.39	5.45	5.54	0.02	0.06	0.09	ND	
4R-1, 132–134		396.22	1.72	0.21	0.43	0.02	0.00	0.22	ND	
4R-3, 26–39		398.16	0.64	0.08	0.04	0.00	0.03	0.00	ND	
4R-3, 100–120		398.90	0.88	0.11	0.10	0.00	0.02	0.00	ND	
4R-CC, 3–7	1	399.98	0.31	0.04	0.04	0.00	0.00	0.00	ND	Top, Subunit 4A
6R-3, 103–105	1D	407.29	0.31	0.04	0.07	0.00	0.02	0.03	ND	Gabbro (reference)
10R-1, 73–80	5B	430.63	0.15	0.02	0.04	0.00	0.00	0.02	ND	Base, Subunit 4A
10R-2, 59–73		431.31	32.90	3.95	4.69	0.00	0.11	0.74	ND	
11R-1, 81–96		436.91	57.60	6.91	6.90	0.00	0.04	0.00	ND	
12R-1, 26–28	1	442.26	0.23	0.03	0.02	0.01	0.00	0.00	ND	Top, Subunit 4B
13R-1, 48–53	8	451.08	0.17	0.02	0.02	0.01	0.00	0.00	ND	Voids
17R-1, 30–32	2	476.80	0.31	0.04	0.03	0.00	0.00	0.00	ND	Gabbro (reference)
18R-4, 120–127	4	485.33	4.50	0.54	0.54	0.00	0.00	0.00	ND	Vein
18R-5, 15–20	1	485.58	4.85	0.58	0.58	0.01	0.00	0.00	ND	Vein
20R-1, 9–14	2	490.19	3.32	0.40	0.40	0.01	0.00	0.00	ND	Vein
22R-2, 48–57	1A	494.56	0.29	0.03	0.03	0.00	0.00	0.00	ND	Vein
25R-1, 14–17	2	513.14	0.11	0.01	0.02	0.01	0.00	0.01	ND	Dropstone in Subunit 4B
25R-1, 88–91	9C	513.88	0.31	0.04	0.06	0.02	0.00	0.02	ND	Voids
27R-1, 9–10	3	519.29	0.24	0.03	0.07	0.01	0.01	0.04	ND	Dropstone in Subunit 4B
27R-1, 91–98	7C	520.11	0.31	0.04	0.05	0.01	0.00	0.01	ND	Vein
32R-3, 37–45	3A	546.12	5.38	0.65	0.68	0.00	0.20	0.03	ND	Vein
39R-1, 121–126	14	578.41	3.13	0.38	0.39	0.01	0.00	0.01	ND	Vein
42R-2, 70–84	1D	592.10	10.82	1.30	1.71	0.00	0.04	0.41	ND	Vein
43R-3, 120–127	11	598.93	0.16	0.02	0.05	0.00	0.01	0.03	ND	Vein

Notes: IC = inorganic carbon, TC = total carbon, TN = total nitrogen, TS = total sulfur, TOC = total organic carbon. ND = not determined. The accuracies for TS and TN are low ~20% (see **"Organic Geochemistry,"** p. 26, in the "Explanatory Notes" chapter).

Table T12. Seawater contamination levels in sediment cores inferred from PFT analyses, Site 1253.

Core, section, interval (cm)	Depth (mbsf)	Sample position in core	Observed contamination (µL seawater per g sediment)
205-1253A-			
2R-2, 80–85	377.90	Interior	0.62
		Middle	0.08
		Exterior	0.36
		Sample site	0.58
3R-1, 23–31	385.43	Interior	0.19
		Middle	0.67
		Exterior	0.26
		Sample site	0.59
4R-4, 0–5	399.10	Interior	0.05
		Middle	0.28
		Exterior	BDL
		Sample site	0.56
10R-2, 73–78	431.45	Interior	105.13
		Middle	23.74
		Exterior	319.05
		Sample site	1.05
11R-1, 73–79	436.83	Interior	2.56
		Middle	2129.35
		Exterior	623.16
		Sample site	4.99

Notes: The detection limit is 0.045 µL. BDL = below detection limit.

Table T13. Seawater contamination levels in gabbro cores based on the concentration of PFT observed in crushed gabbro, interior core samples, Site 1253.

Core, section, interval (cm)	Depth (mbsf)	Sample position in core	Observed contamination (µL seawater per g gabbro)
205-1253A-			
32R-2, 10–16	544.43	Interior	39.38
33R-1, 34–36	549.54	Interior	13.75
34R-2, 69–74	554.72	Interior	128.66
36R-1, 47–50	562.97	Interior	119.65
37R-1, 30–32	566.30	Interior	510.37
38R-2, 0–3	573.51	Interior	0.61
39R-1, 128–130	578.48	Interior	190.79
41R-2, 2–4	587.07	Interior	301.43
42R-2, 102–103	592.42	Interior	30.10
43R-3, 100–108	598.73	Interior	99.53

Table T14. Contamination observed in the interior of gabbro cores using fluorescent beads as bacterial mimics, Site 1253.

Core	Depth (mbsf)	Sample position in core	Microspheres/ 50 FOV	Microspheres per mL of gabbro	Delivery confirmed
205-1253A-					
32R	543.2	Outside	351	8,585	Yes
		Interior	33	807	
34R	552.9	Outside	174	4,256	Yes
		Interior	4	98	
36R	562.5	Outside	331	8,096	Yes
		Interior	2	49	
37R	566.0	Outside	68	1,663	Yes
		Interior	4	98	
38R	572.2	Outside	17	416	Yes
		Interior	1	24	
39R	577.2	Outside	839	20,522	Yes
		Interior	3	73	
41R	585.8	Outside	62	1,517	Yes
		Interior	0	0	
42R	589.9	Outside	1,643	40,188	Yes
		Interior	0	0	
43R	595.4	Outside	NA	NA	No
		Interior	3	73	

Notes: FOV = a field of view using the 100× objective with an approximate area of 3.14×10^4 μm^2. NA = not applicable.

Table T15. Logging operations summary, Site 1253.

Date (Oct 2002)	Local time (UTC – 5 hr)	Tool depth (mbsf)	Remarks
2	1100		Last core on deck
2			Circulated the hole from the bottom up with 30 bbl of sepiolite mud twice
3	2330–0640	150	Triple combo tool would not penetrate a bridge at 4537 mbrf (150 mbsf)
3			Logging operation was postponed until after 10¾-in casing into the top of the first sill
7	0145–0215		Circulated the hole from the bottom up with 50 bbl of sepiolite mud
7	0215–0230		Hole displaced with sepiolite mud
7	0230–0350		Set back top drive; bottom of pipe put at 90 mbsf
7	2130		Start logging rig-up
8	0000		Start going downhole with triple combo TAP/DIT/HLDS/APS/HNGS tool string
8	0215		Lost power to tools because of oil leaking in HLDS; changed to HLDT
8	0730		Start going downhole again with triple combo TAP/DIT/HLDT/APS/HNGS tool string
8	0901	0	Stop for 5 min at mudline for temperature calibration
8	1006	530	Tool at total depth; start logging up at 900 ft/hr
8	1033	413	Tool back into pipe
8	1127	0	End of run; tool at seafloor
8	1310		Tool back on rig floor
8	1400		Finish rig-down
8	1400		Start logging rig-up
8	1500		Start going downhole with FMS-sonic FMS/DSI/SGT tool string
8	1715	530	Tool at total depth; start logging up at 900 ft/hr
8	1740	413	Tool back into pipe; end of pass 1
8	1756	564	Tool at total depth; start logging-up pass 2 at 900 ft/hr
8	1830	413	Tool back in pipe; end of pass 2
8	1930		Tool back on rig floor
8	2030		Finish rig-down

Notes: Triple combo = triple combination. UTC = Universal Time Coordinated. See Table **T7,** p. 75, in the "Explanatory Notes" chapter for explanations of acronyms used to describe tool strings and tools.